ESRF
The European Synchrotron

ESRF HIGHLIGHTS 2014

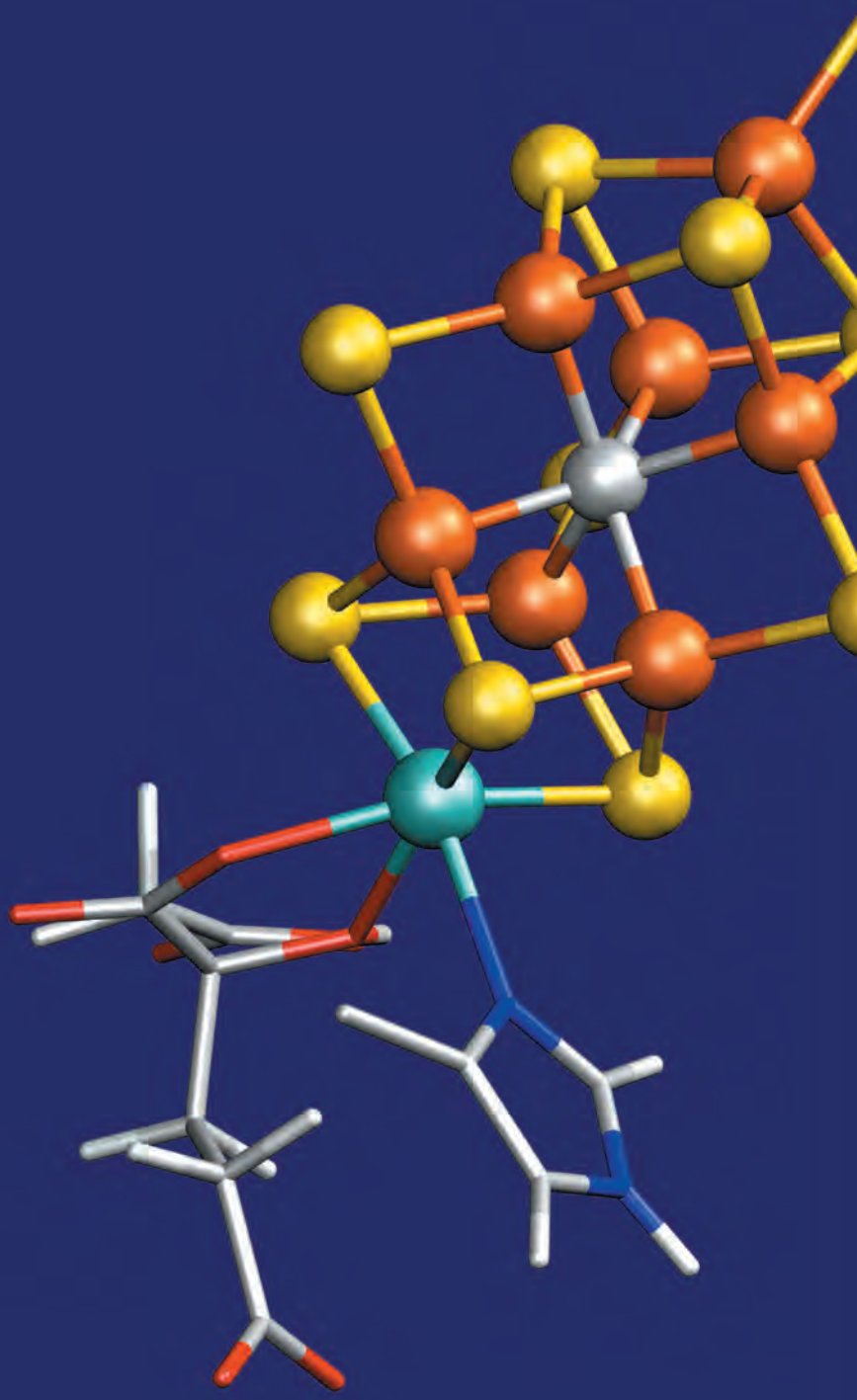

ESRF
The European Synchrotron

ESRF HIGHLIGHTS 2014

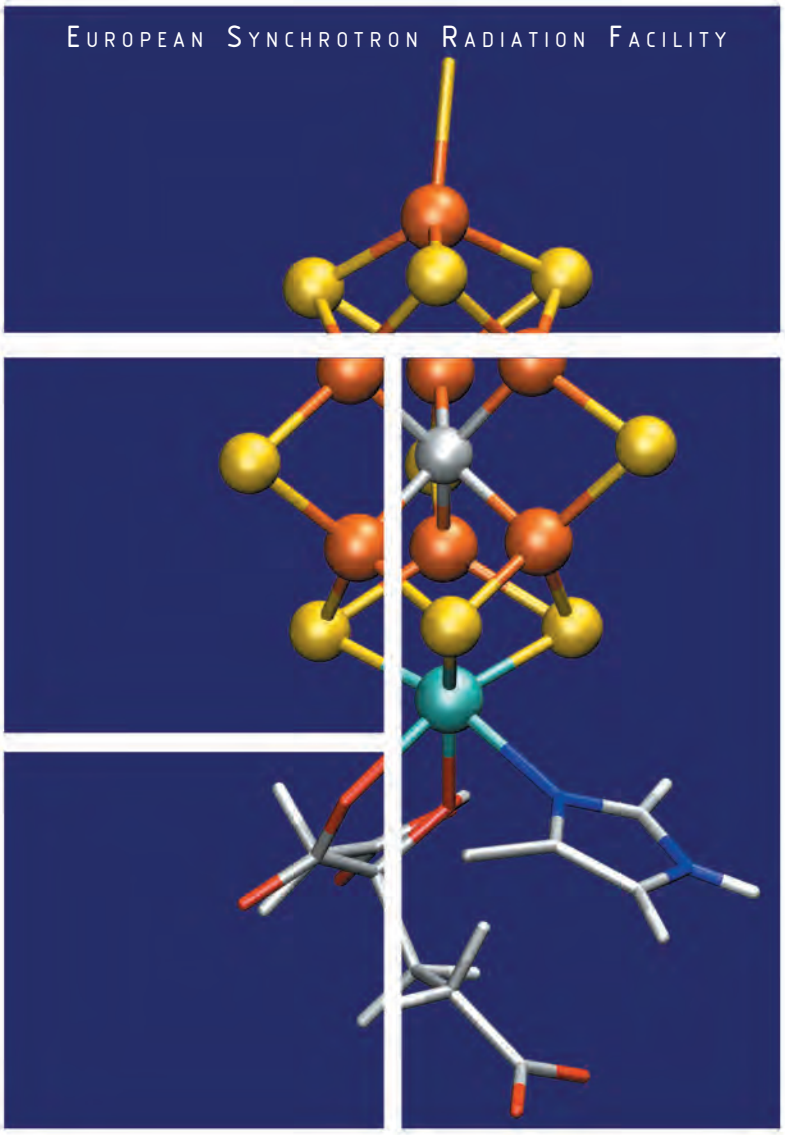

DEAR READER

Francesco Sette

Twenty years after its inauguration, the ESRF, in 2014, welcomed the Russian Federation as a new Member State. It also reached important milestones in the delivery of Phase I of the Upgrade Programme (UP) and has proudly announced the launch of Phase II. In parallel, the excellent operation of the facility throughout the year enabled the ESRF users to carry out their scientific programmes very successfully. Over 2000 proposals were submitted by ESRF users in 2014. This figure is the highest ever reached, and puts the number of proposals at more than two and a half times the available beam time.

The achievements of 2014 are the result of the hard work of thousands of people among the ESRF Users and Staff, and would not have been possible without the support provided by our partner countries. Following on from these achievements, we are now excited about the prospects for 2015, which will see the completion of UP Phase I, the start of UP Phase II construction, and full-scale user operation for the ESRF accelerators and available beamlines.

The ESRF Council endorsed the UP Phase II deliverables, timescale and budget envelope in June 2014 following the science case and construction planning described in the UP Phase II Technical Design Study report, the 'Orange Book'. At the subsequent Council meeting in December 2014, the first financial contribution to the UP Phase II budget was approved. Over the next eight years (2015-2022), the ESRF plans to bring into operation a new synchrotron X-ray source, housed in the existing buildings and replacing the present machine that has been in operation since 1992, as well as four new beamlines and an ambitious instrumentation programme. The objective is to deliver a fully renewed facility by 2023 for the benefit of scientific users from around the world, and to enable the ESRF to remain a global leader in synchrotron X-ray science for many years to come.

Alongside the preparation work for UP Phase II, in 2014, many developments took place within the context of the implementation of UP Phase I. New instruments were delivered, and in particular, I wish to highlight the restart of user operation at the new beamlines ID01, ID02, ID16A/B, ID22, ID30A and ID32. With respect to the opening of ID30A, part of the MASSIF complex at ID30, the macromolecular crystallography community will benefit from the first public experimental station in the world that is completely automated. In fact, beyond remote access, users can now send in their samples, have them analysed automatically using instructions given in the ISPyB database, and then log on to discover and review their results. This new facility has the potential to save hours, or even days of users' valuable time. It has been designed particularly for the initial screening of crystals and the collection of data sets from reasonably well-known samples. Since it opened in late October, 500 samples have already been processed. ID30A has three end stations and, with BM29, replaces the highly successful ID14 complex that was closed at the end of 2012.

UP Phase I continues to progress according to schedule, with the goal of its completion by the end of 2015. During 2015, therefore, the few remaining Phase I beamlines will be commissioned, and by early 2016 the topping-up of the storage ring will become part of normal user operation.

The new joint ESRF-ILL Science Building and the new site entrance of the EPN Science Campus, entirely financed by the French State (CPER Programme) to increase the visibility and attractiveness of the campus, was inaugurated in February 2014 by the French Minister for Higher Education and Research, the President of the Rhône-Alpes Region and the local authorities. The Science Building will foster new collaboration and closer working relations between the two facilities, their scientific user communities as well as with industry. ESRF users can now access the Science Building from the ESRF thanks to a covered footbridge. This footbridge provides access to the new library, new chemistry labs and the new facilities of the Partnership for Soft Condensed Matter (PSCM). Thanks to the CPER Programme, the ESRF has also been made more accessible to users coming from and going into town since the completion, in September 2014, of an extension of one of Grenoble's tram lines.

I wish to thank our colleagues in charge of the operation of the storage ring for the outstanding performance in beam delivery. Indeed, during 2014 they were able to establish a new world record with 99.15% beam availability with enhanced beam properties. The excellent beamline and beam delivery performance have enabled excellent scientific results. A selection of them is presented here in Highlights to record and applaud the wonderful scientific advances of the ESRF Users.

FRANCESCO SETTE,
Director General,
ESRF

STATUS OF THE UPGRADE PROGRAMME

Following the occupation of the new buildings delivered within the EX2 project, 2014 has been the peak year for the implementation of the new beamline portfolio in the new premises. The year saw the inauguration of many new beamlines with unprecedented scientific capabilities, including ID02 (**Figure 1**), ID16A, ID16B, ID22, ID30A-1, and ID32. As we are entering the final year of Phase I of the Upgrade Programme, the construction of the new beamlines is approaching completion on time, within budget and in line with or exceeding specification.

The upgrade of the current accelerator complex is also heading towards its completion, with the latest step being preparation for top-up operation in the timing modes, scheduled for routine operation in 2016. Several tests on top-up operation during machine dedicated time have helped to identify the remaining issues and devise solutions. 2014 has also seen a large effort from all Divisions of the ESRF in the preparation of the Orange Book, with the proposal for the construction of a new low emittance storage ring light source at its core. Preliminary design work and cost estimates have been concluded successfully and led to the approval of the project by Council in June 2014. Representing our Users, we thank our staff for these achievements, delivered while the facility was kept in full user operation.

Fig. 1: Inauguration of beamline ID02 (UPBL9A) at the 69th meeting of the Science Advisory Committee, November 2014. Pictured from left to right: F. Sette (Director General), Prof. K. Hämäläinen (Chairman SAC), N. Theyencheri (Scientist in charge of ID02), Dr A. Petukhov (SAC).

Upgrade of the source

2014 has seen the successful completion of several upgrades to subsections of the accelerator system.

The RF system has been renewed with the addition of solid state amplifiers and HOM-damped cavities. The manufacture of 12 additional cavities for Phase II is progressing well. All the planned straight sections have been lengthened from 5 m to 6 m, with one 7 m-long section in cell 23, enabling the installation of the RF cavities.

Following the construction of ID32, the new helical undulator will be put into place in the straight section in March 2015. Canted straight sections have been successfully installed, and only ID15 remains to be modified with this scheme, foreseen for 2015. An improved electron beam position monitoring system and a fast orbit feedback system have been successfully developed and installed.

The top-up project is progressing well, and several tests were carried out with beamlines in 2014. Feedback from the beamlines has been positive and, working with users, we have implemented improvements following their requests. The new bunch cleaning system installed in the booster this year will greatly aid top-up operation, scheduled for the beginning of 2016, once a formal agreement from the authorities has been accorded.

The technical design study for the UP Phase II, based on a hybrid 7-bend achromat lattice, has been completed and received very positive reports from the Accelerator Project Advisory Committee (APAC), the

Scientific Advisory Committee (SAC) and the Administration and Finance Committee (AFC). In June 2014 it was submitted to the Council, which approved and launched the project. We entered the execution phase on 1st January 2015 with leaders being appointed for the Accelerator Project Office and Work Packages. The lattice and engineering designs have advanced well, with some magnets already at the prototype stage.

Renewal of beamlines

The Instrumentation Services and Development Division (ISDD) and the Experiments Division (ExpD), with the assistance of the Technical Infrastructure Division (TID), deliver new and refurbished beamlines. A significant number of beamlines are still under construction or will receive their finishing touches while they are already in user operation. A total of five beamlines are still under construction with most of them returning to user operation in 2015. Significant financial and human resources are also invested in the continuous refurbishment and further development of the remaining beamlines.

The main projects for beamline renewal are as follows:

UPBL1 – Diffraction for nano-analysis. Most of the optical components, including the white beam mirrors and multilayer monochromator, double crystal monochromator and transfocator have been assembled and installed. With the completion of the installation of the nano-diffractometer, the beamline received its first user team in December 2014. The SAXS/GISAXS end-station is in the assembly phase and will be commissioned early in 2015.

Fig. 2: ID32 RIXS branch: refocusing optics, sample chamber, collimating optics and grating vessel (from right to left).

UPBL2 – High energies for interfaces and materials processing. The infrastructure for the beamline has been completed and first components installed in optics hutch OH1. The design, assembly and installation of the main optical components (transfocators, multilayer monochromator, double Laue monochromator) in OH2 is ongoing. The control infrastructure is under preparation. The large granite detector gantry has been installed and aligned.

UPBL4 – Nano-imaging and nano-analysis. The beamlines ID16A and ID16B have been installed and commissioned. Both beamlines resumed user operation in 2014 with some remaining work (cryo-cooling of the sample stage and high energy KB system (34 keV)) at the endstation of the ID16A-NI branch.

NI- nanotomography endstation: The installation of the endstation has been completed and the fixed-energy KB system (17 keV) commissioned. Most of the detectors are operational while the remaining cSAXS detector is still in the assembly phase. After reaching a beam size of 20 x 40 nm^2 the beamline was successfully opened for user operation.

NA- nano-analysis endstation: The construction of the beamline was finished with all the detectors installed and the beamline has returned to user operation. The contaminated KB system, damaged by a defective gas line, will be replaced in 2015.

UPBL6 – Hard X-ray spectroscopy (RIXS & XRS). The horizontally deflecting (focusing) mirrors are operational and five APD detectors have been installed. The beamline returned to full user operation.

UPBL7 – Soft X-ray spectroscopy (RIXS & XMCD). All components for the beamline optics have been received and installed. Existing ID08 experimental facilities have been moved to the new ID32 premises in the experimental hall extension.

XMCD branch: The assembly of the XMCD branch including the new sample preparation facility has been finished and all components have been commissioned. First user experiments have been successfully performed with the XMCD setup as well as with a user-specific setup in the open access hutch attached to the XMCD branch.
All specifications have been met.
RIXS branch: The assembly of the 11m RIXS spectrometer arm is heading towards its final steps (**Figure 2**). All components have been received with only the gratings for the spectrometer still to be delivered.

UPBL9a – Time-resolved ultra-small-angle scattering. All optical components have been installed at beamline ID02 and the new 32 m long USAXS tube including the detector wagon has been assembled and aligned in the new premises (**Figure 3**). All SAXS (**Figure 4**) and WAXS detectors have been delivered and commissioned in the beam.

UPBL9b – Pump-probe and time-resolved experiments. The design of the new optical components for beamline ID09 has been finished and the orders placed. The high heatload chopper has been delivered and a new 3 kHz chopper is in the design stage. The beamline will remain fully operational throughout the upgrade.

UPBL10 – Automated crystallographic evaluation. The new MASSIF sample handling facility including a high capacity dewar and RoboDiff setup (**Figure 5**) has been commissioned on ID30A-1 and has begun user operation. The microfocus beamline ID30A-3 has started user operation with a conventional experimental setup that will be replaced by a RoboDiff in 2015. The new Eiger 4M detector has been delivered and is being prepared for installation at the beamline. The installation of the new MAD beamline ID30B is in progress including the installation of a MD2S microdiffractometer, a new sample changer robot and a modified high

Fig. 3: ID02 detector wagon (front view) inside the USAXS tube.

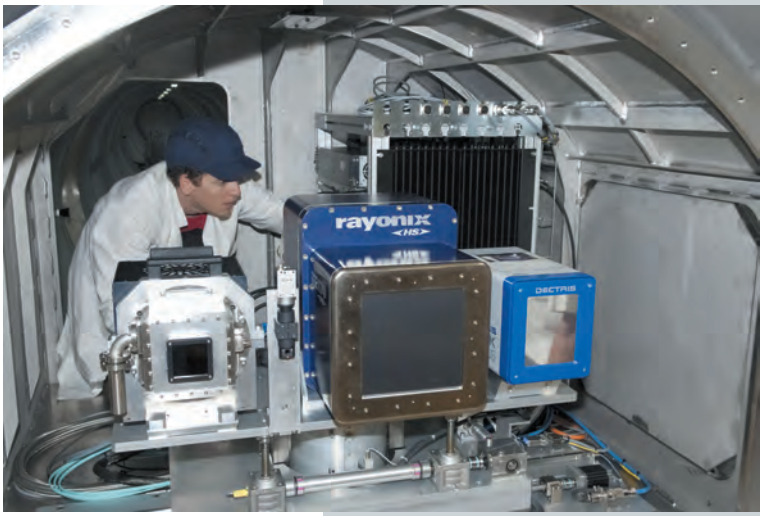

Fig. 4: Detectors inside the ID02 SAXS conveyor: FReLoN camera, beam viewer, Rayonix MX170 CCD detector, Pilatus 300K hybrid pixel array detector (from left to right).

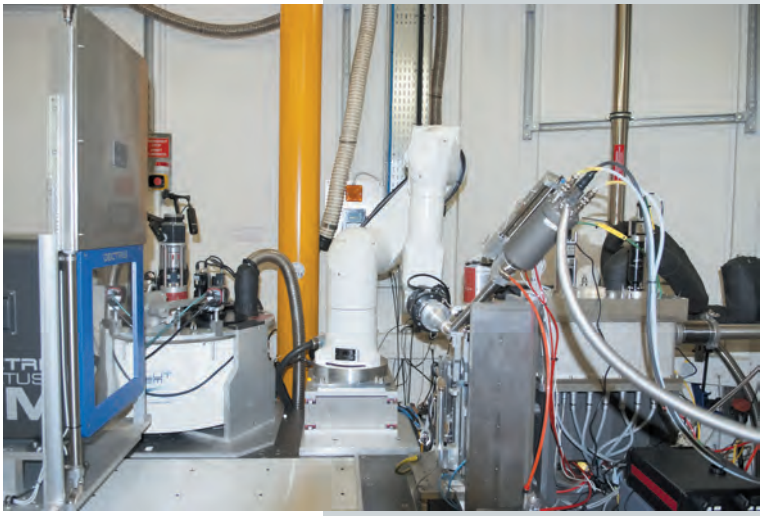

Fig. 5: Sample handling facility at ID30A-1 with high capacity dewar (left) and the new RoboDiff (centre) acting as sample changer and microdiffractometer.

capacity dewar (in collaboration with the EMBL Grenoble). The new Pilatus3 6M detector has been received and commissioned.

UPBL11 – Time-resolved and extreme conditions XAS. Work on several optical components continued while keeping the upgraded ID24 beamline fully operational. New detectors have been produced and are under commissioning.

ID22 – Powder diffraction. The installation of the new beamline optics and the transfer and refurbishment of the endstation have been completed. After a short shutdown of only four months the powder diffraction beamline successfully commenced user operation.

ID19 – X-ray imaging and palaeontology project. The upgrade and refurbishment of the beamline optics is nearly finished. The design, procurement and installation of detectors continues according to the TDR.

ID15 – High pressure, materials engineering, materials chemistry. The TDR for the two branches ID15A/B has been completed and approved. The optical design and configuration has been validated and the order for the construction of the new hutches was placed.

In the context of the Upgrade Programme, the ISDD continues to monitor its projects and associated resources, which are shared among several core activities, such as completion of the UP Phase I, daily operation of the facility and development of the in-house R&D programme for scientific instrumentation. In addition, in 2014, ISDD has focussed on defining a roadmap for UP Phase II, which includes strategic developments for future scientific instrumentation at the ESRF. This programme aims to provide engineering solutions for the best scientific exploitation of the new storage ring properties. The two main pillars of this programme are detector development and the implementation of a new model for data analysis. A special effort is foreseen to develop a new data analysis strategy and technical solutions to provide better service for ESRF users.

The year has also seen further consolidation of the project management organisation, with the implementation of an electronic system for project submission and associated approval workflow. This system is now used by both the Experiments Division and ISDD, and it is expected to be adopted by the ASD for the management of Phase II projects.

Several large-scale projects have also aimed to strengthen the ESRF's capabilities in certain strategic areas. One such highlight is a new laboratory which will be entirely dedicated to the development and production of curved X-ray analyser crystals for spectroscopy applications. Similarly, 2014 has seen the implementation of a new Fizeau interferometer in vertical geometry with semi-automated stitching capability for optical metrology and the installation of a new system for cleaning carbonaceous contamination from optical surfaces.

In 2014, ISDD and ExpD initiated an in-depth review of double-crystal monochromator (DCM) technologies for spectroscopic applications. A dedicated working group is currently reflecting on the development of high-performance DCMs to cope with future scientific needs and also to anticipate the obsolescence of our aging DCMs.

As in previous years, special effort has been devoted to developing generic solutions and frameworks (see the chapter on Enabling Technologies). Alongside the complete specifications and initial design of a new DAnCE-based encoder processing unit, several software platforms have been further integrated and standardised, which include mxCuBE, LImA, PyFAI and PyMCA.

Detector R&D activities have continued to focus on the continuation or completion of several projects launched previously, including Medipix 3, HiZPAD2, XNAP and high efficiency scintillators, whilst reflection began for the Phase II development programme.

The instrumentation beamline, BM05, continued to be a strategic tool for instrumentation developments such as detector calibration, scintillator characterisation and testing of optical components. The beamline DCM has been upgraded and a new diffractometer will soon be implemented to better serve those instrumentation programmes.

Finally, commercial activities and new partnerships continued to support the European synchrotron community with the procurement of specific instruments such as a FReLoN-based detector and IcePAP controllers.

Moving on

The extensive UP Phase I building programme was completed in 2014 with the delivery of the EX2 extensions (ID16 satellite building, Belledonne Hall, Chartreuse Hall, Lab and Office Building) in parallel with the new site entrance and joint ESRF-ILL Science Building. The availability of the new premises has inevitably triggered the relocation of a large fraction of staff which will continue throughout 2015. From the outset, the ESRF was keen to embrace a high quality environment standard for the tertiary buildings, thus contributing to sustainable development and to provide a comfortable working environment for the support laboratories of the experimental programme.

The Lab and Office Building is now fully occupied and houses 30 laboratories for some of the beamlines and the ISDD. Some of these new laboratories were built to compensate for space forfeited to the beamline refurbishment programme, with beamlines now passing through the areas previously occupied by some of the laboratories and into the EX2 extension. Others have enabled activities to be re-grouped, such is the case for the Electronics Group, which in turn has freed up space in the Central Building. Laboratories are also being modernised and relocated around the experimental hall for an optimal operation in proximity to the new and refurbished beamlines.

The chemistry and surface science laboratories have moved from the Central Building to the Science Building. The space freed up in the Central Building will be converted into offices, allowing staff in dispersed groups to be brought together. This concerns the Software, Mechanical Engineering, Detector, and Alignment groups. At the end of this operation, more than 50% of the ESRF staff will have moved and will have gained improved working conditions and/or increased synergy to carry out the demanding work ahead to operate the facility and implement Phase II of the Upgrade Programme.

R. DIMPER, P. RAIMONDI, H. REICHERT and J. SUSINI

ELECTRONIC STRUCTURE AND MAGNETISM

One of the major events of the year 2014 was the start of operation of ID32, the upgrade beamline project UBPL7 dedicated to polarisation dependent studies using soft X-rays. This 120 m long beamline replacing the former ID08 features two branches, optimised for state-of-the-art X-ray magnetic circular dichroism (XMCD) experiments and resonant inelastic X-ray scattering (RIXS) with very high energy resolution. Among the upgraded features are a variable spot size down to 10x100 μm^2 on the XMCD branch and a combined resolution of 30000 on the RIXS branch. ID32 was inaugurated on November 6 (see photo below). The first user group (Ghiringhelli *et al.*, Politecnico di Milano, Italy) worked on the high field magnet (9 T) end station on the XMCD branch to investigate chiral effects in high temperature superconductors. The second group (Ogin *et al.*, University of Exeter, UK) made use of the "free" experimental station, on the same branch, for time-resolved soft X-ray magnetic holography.

Inauguration ceremony at beamline ID32. Pictured from left to right: N. Brookes (Scientist in charge of ID32), Prof. D. McMorrow (SAC member), Prof. K. Hämäläinen (Chairman SAC), F. Yakhou-Harris (ID32), Prof. M. Takata (SAC member), F. Sette (Director General).

Another important result that marked the year 2014 was the success of the first high-power laser-shock experiment at the energy-dispersive X-ray absorption spectroscopy (XAS) beamline ID24, which was the upgrade beamline project UPBL11. For the first time at a synchrotron, iron was investigated while being dynamically compressed to extreme pressures and temperatures (~4 Mbar, 9000 K). A compact (30 J) focused laser beam was used to produce a hot compressed state in the sample, of sufficient duration to be probed with a single 100 ps X-ray pulse. The feasibility of a "single" shot scheme is very important because the reproducibility of such extreme conditions is never guaranteed. Usually, much larger, very high energy lasers are required to produce such extreme states making the experiments more costly and less accessible. The possibility of performing such experiments at a synchrotron beamline offers new opportunities to a large user community.

At beamline ID12, the high pressure programme reached a milestone early this year with the first ever measured chlorine K edge XAS at high pressure. The B1(NaCl-type) - B2(CsCl-type) structural phase transition (≈ 3 GPa) in a KCl crystal was recorded in total fluorescence yield mode through a specially-designed diamond-anvil cell featuring a fully-perforated diamond coupled to a thin 30 µm diamond window. The beam was focused in both directions by Be refractive lenses. This achievement opens exciting new opportunities for high pressure studies at low X-ray energies.

At beamline ID26, the KB mirror assembly was replaced. This, considerably improved the beam stability and increased the brilliance by a factor of 4. Following on from pioneering experiments where X-ray magnetic circular dichroism was combined with resonant inelastic X-ray scattering, a chamber was designed for permanent installation at the beamline holding phase plates to generate circular polarised light. Many samples measured at ID26 suffer radiation damage. This can be avoided by using a large amount of sample that is moved through the beam. To permit this, ID26 has developed hardware and software tools to map a large sample surface or liquid jets. Finally, ID26 is exploring the energy range from 2-5 keV in X-ray emission spectroscopy with a new instrument under design.

This year's chapter reflects the large variety of different spectroscopic and scattering methods utilised at the ESRF to investigate the electronic and magnetic structure in materials that are becoming more and more diverse. In addition to the five beamlines of the Electronic Structure and Magnetism Group (ID12, ID24, ID26, ID32 and BM23), our chapter also hosts science highlights from ID20, the new Inelastic X-ray Scattering (IXS) beamline, and from BM28, the UK CRG beamline.

The science highlight from BM28 shows how the interference between non-resonant magnetic X-ray scattering and the pure quadrupole resonance at the Fe K absorption edge in the weak ferromagnet $FeBO_3$ carries the sign of the Dzyaloshinskii–Moriya interaction. The selection from ID20 includes the investigation of high energy plasmonic excitations in transition metal dichalcogenides by IXS and the study of the electronic structure of the spin-orbit Mott insulator $CaIrO_3$, where RIXS at the Ir L_3 edge has been applied to explain its insulating behaviour.

RIXS in the soft X-ray regime has also been used for one of the last science highlights from beamline ID08 before its closure, to reveal differences between electronic excitations in electron- and hole-doped cuprates, a prerequisite for a complete understanding of the superconductivity in these systems. The second selection from ID08 shows

an interesting application of soft XCMD to investigate the magnetic properties of surface-supported molecular systems employing transition metals dopants.

XMCD with hard X-rays, the work horse of the ID12 beamline, has also been used to unveil a novel dilute magnetic semiconductor, europium nitride, showing that it exhibits surprising properties that distinguish it from other materials in this class. A second highlight from ID12 concerns observation of strong magneto-chiral dichroism at the K-edges of transition metals in paramagnetic molecular helices. This peculiar type of dichroism is due to orbital toroidal currents which are of relevance for many phenomena, ranging from multiferroicity to superconductivity.

Valence-to-core XES is highly sensitive to small variations of a transition metal's valence electronic structure induced by the ligand. In the first science highlight from beamline ID26, this technique has been used as a spectroscopic ruler for the quantitative determination of the NO oxidation state in Fe-NO complexes. Two additional highlights focus on the use of HERFD-XAS to probe the chemically active *4f* orbitals of Ce in colloidal Ce oxide nanoparticles, and the oxidation state of Mo in the active site of the enzyme nitrogenase.

Remaining within the realm of catalysis, but moving from biology to inorganic chemistry, one of the science highlights from the pre-upgrade **ID24** beamline reports on the spontaneous oscillatory behaviour in heterogeneous catalysts by means of the combination of time-resolved EXAFS with synchronous diffuse reflectance infrared Fourier transform spectroscopy (DRIFTS) and mass spectroscopy.

To conclude, the two science highlights selected from the general purpose EXAFS beamline BM23 focus on the optimisation of Ru-doped spinels used as cathodes for high voltage lithium-ion batteries, and on revealing icosahedral bonding configurations in highly undercooled metals.

S. PASCARELLI

MEASURING THE DZYALOSHINSKII–MORIYA INTERACTION IN A WEAK FERROMAGNET

The Dzyaloshinskii–Moriya interaction (DMI) plays a crucial role in several of the most topical phenomena in magnetism, including the slow magnetic rotation found in skyrmion lattices and cycloidal magnetoelectrics. The original formulation of the DMI related to the occurrence of 'weak ferromagnetism' in nominally collinear antiferromagnetic materials such as αFe_2O_3, $MnCO_3$ and $FeBO_3$ [1,2]. Unfortunately, in these archetypal twisted magnetic systems, the sign of the DM interaction has eluded experimenters because it affects only the phase of magnetic scattering, whereas experiments based on a single scattering mechanism determine only intensity (a manifestation of the famous 'phase problem' of crystallography). This meant that the DMI in such weak ferromagnets could be determined in magnitude and axial direction, but not in sign.

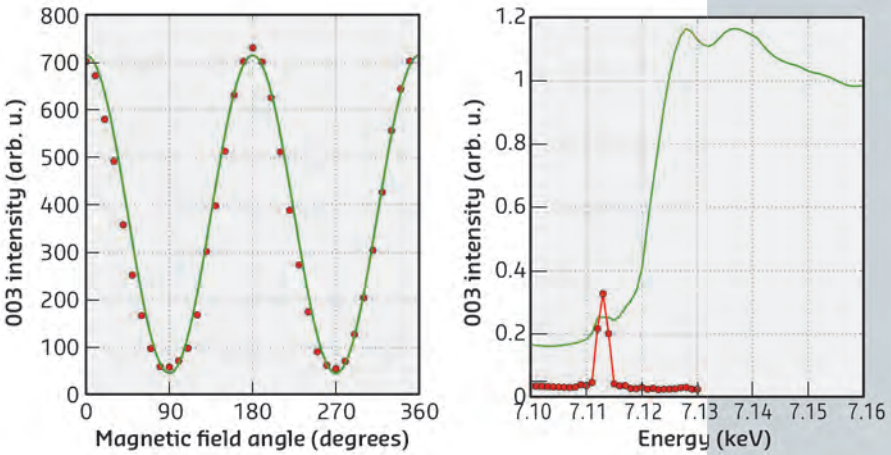

Fig. 6: Spacegroup-forbidden diffraction intensities arising from pure non-resonant magnetic scattering (left) and pure quadrupole resonant scattering (right – red line) as a function of photon field angle and energy, respectively.

Principal publication and authors
V.E. Dmitrienko (a), E.N. Ovchinnikova (b), S.P. Collins (c), G. Nisbet (c), G. Beutier (d), Y.O. Kvashnin (e), V.V. Mazurenko (f), A.I. Lichtenstein (g) and M.I. Katsnelson (f,h), *Nature Physics* **10**, 202–206 (2014).
(a) A.V. Shubnikov Institute of Crystallography RAS, Moscow (Russia)
(b) Faculty of Physics, M.V. Lomonosov Moscow State University (Russia)
(c) Diamond Light Source Ltd, Didcot (UK)
(d) SIMaP, CNRS, Grenoble-INP & UJF, Saint-Martin d'Hères (France)
(e) ESRF
(f) Department of Theoretical Physics and Applied Mathematics, Ural Federal University, Ekaterinburg (Russia)
(g) I. Institut für Theoretische Physik, Universität Hamburg (Germany)
(h) Institute for Molecules and Materials, Radboud University Nijmegen (The Netherlands)

References
[1] I. Dzyaloshinsky *J. Chem. Phys. Solids* **4**, 241-255 (1958).
[2] T. Moriya *Phys. Rev.* **120**, 91–98 (1960).
[3] V.E. Dmitrienko *et al.*, *JETP Lett.* **92**, 383–387 (2010).
[4] M.I. Katsnelson, Y.O. Kvashnin, V.V. Mazurenko and A.I. Lichtenstein *Phys. Rev. B* **82**, 100403 (2010).

Following the suggestion that the sign of the DMI might be determined by measuring interference between non-resonant magnetic X-ray scattering and the pure quadrupole resonance at the K absorption edge [3], magnetic and resonant quadruple scattering were first investigated separately on a sample of $FeBO_3$ (Figure 6). The magnetic structure was observed in the conventional way, by rotating the magnetism with respect to the X-ray probe. However, with this class of weak ferromagnets we were able to carry out such a rotation with a static crystal, using a small rotating magnet to turn the entire magnetic structure. This approach allows very high-quality data to be obtained from a rapid series of measurements. The quadrupole resonance can be seen very clearly as a sharp peak in the pre-edge region (Figure 6).

The final step was to create the conditions whereby these two scattering processes occur simultaneously and can interfere with each other. To this end, measurements of the (009) resonant quadrupole reflection were carried out at **BM28**, again rotating the magnet to manipulate the antiferromagnetic structure, causing the phase of the magnetic scattering to be reversed. This produced a remarkable jump in the energy of the resonance due to the reversal of the interference conditions on the low and high energy side of the peak (Figure 7). From the direction of the jump, we were able to determine the phase of the magnetic scattering and finally the sign of the DMI.

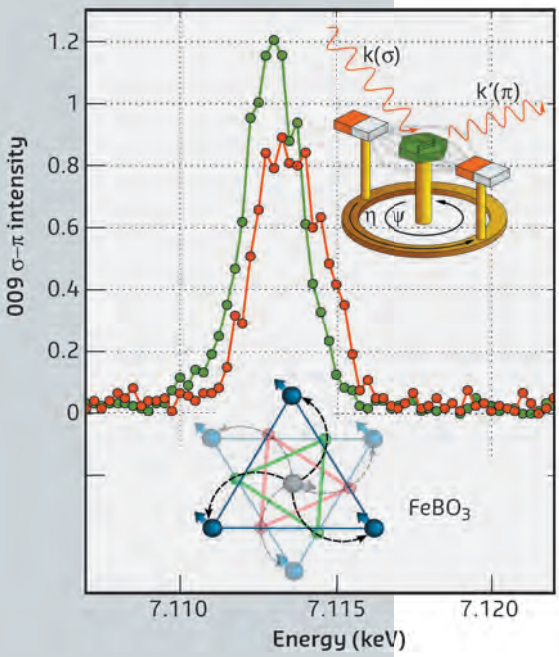

Fig. 7: The jump in the quadrupole resonance as the magnetic structure was rotated by 180 degrees. The relationship between the twisting of the magnetic moments and that of triangles of oxygen atoms between the iron planes is shown at the bottom.

Armed with these results, we could provide a thorough test of state-of-the-art first-principles calculations. A realistic simulation of the spin canting in antiferromagnets leading to weak ferromagnetism requires an accurate account of the spin-orbit coupling, Coulomb correlations and hybridisation of the atomic states. To solve this problem we have developed a method for calculating the DMI based on the local force theorem, by considering the change in energy with respect to the twisting of the magnetic moments away from collinear ordering, $D_{ij} = \delta E/\delta\phi_{ij}$. We proposed [4] a new nonlocal inter-site formulation of the DMI,

$$D_{ij} = -\frac{i}{2}\, Tr_{L,\sigma}\{N_{ji}[\hat{J}, \hat{t}_{ij}]_+\}$$

where N_{ji} is the inter-site occupation matrix, $\hat{J}$ is the total moment operator, $\hat{t}_{ji}$ is the hopping matrix and $[.,.]_+$ represents an anticommutator. Our method leads to a compact and transparent form that can take into account hybridisation, correlation and temperature effects in the system. Moreover, it can be applied to a wide range of the materials with different strengths of the spin-orbit coupling and Coulomb correlations.

The calculations of the isotropic exchange and DMI by this method have shown that weak ferromagnetism in $FeBO_3$ is fully described by the six exchange interactions between atoms belonging to the first coordination sphere. Crystal symmetry dictates that the net DMI is along the *c* axis, which means that there is weak ferromagnetism in the *ab* plane. Both the sign and magnitude of the small twisting of the spins from collinear ordering are in excellent agreement with experimental data.

In conclusion, we have applied a novel experimental technique to a classic problem – the origin of weak ferromagnetism in $FeBO_3$ – and shown that the results are in excellent agreement with a new theoretical method that can be used to model the Dzyaloshinskii-Moriya interaction in a wide range of materials.

HIGH-ENERGY PLASMONIC EXCITATIONS IN 2D TRANSITION-METAL DICHALCOGENIDES

Transition-metal dichalcogenides (TMDC) have attracted a tremendous interest in the last few years as they exhibit many interesting properties, such as the coexistence of two competing electronic orders: superconductivity and charge-density wave (CDW) as well as optical valley control and valleytronics in MoS_2 monolayers.

In particular, an intense debate has developed around the origin of CDW order and its impact on the spectroscopic properties of these materials. The dynamic density response is a key quantity that could help us to disentangle CDW and superconductivity order. It is quantified by the loss function, or equivalently the dynamic structure factor $S(q,\omega)$. Its investigation has been the subject of a very recent EELS study that has reported a negative plasmon dispersion for in-plane momentum transfers of the loss function of 2H-$NbSe_2$ [1]. This result was different from the expectations derived from the homogeneous electron gas, where the plasmon dispersion is positive. The negative plasmon dispersion was ascribed to correlation effects arising from the incipient CDW [1].

In an earlier publication [2], we presented the results of an extensive *ab initio* theoretical analysis of the loss functions of two prototypical TMDC materials, namely 2H-$NbSe_2$ and 2H-$Cu_{0.2}NbS_2$, which respectively do and do not exhibit a CDW ordered phase. We found a negative plasmon dispersion in both materials and proposed a very general and simple interpretation of the in-plane negative plasmon behaviour. Our interpretation links the peculiar anisotropic band structure of those systems with narrow d-symmetry bands crossing the Fermi level.

Our study was conducted at **ID20** using nonresonant inelastic X-ray scattering (IXS) spectroscopy. The results represent an important step towards the understanding of neutral excitations in this class of materials. In fact, at variance with the previous theoretical and experimental work that mainly focused on the low energy plasmon, we investigated the dynamic density response at higher energy up to 50 eV for momentum transfer normal to the plane of the layers. The dynamic range in energy and momentum required by this study is only accessible to IXS. Our results are summarised in **Figure 8** where we compare the measured loss function obtained by IXS with state-of-the-art time-dependent density functional theory (TDDFT) calculations performed in adiabatic local density approximation (ALDA). The agreement between theory and experiment is good enough to show that TDDFT-ALDA is able to capture the physics of the collective excitations in this class of materials. At the same time, we found that the spectra of 2H-$NbSe_2$ and 2H-$Cu_{0.2}NbS_2$ are similar not only at low energy and for in plane momentum transfer, as shown in [2], but also at higher energy and large momentum transfer normal to the plane. This result further validates our interpretation of the in-plane negative dispersion of the low energy plasmon reported in the previous work.

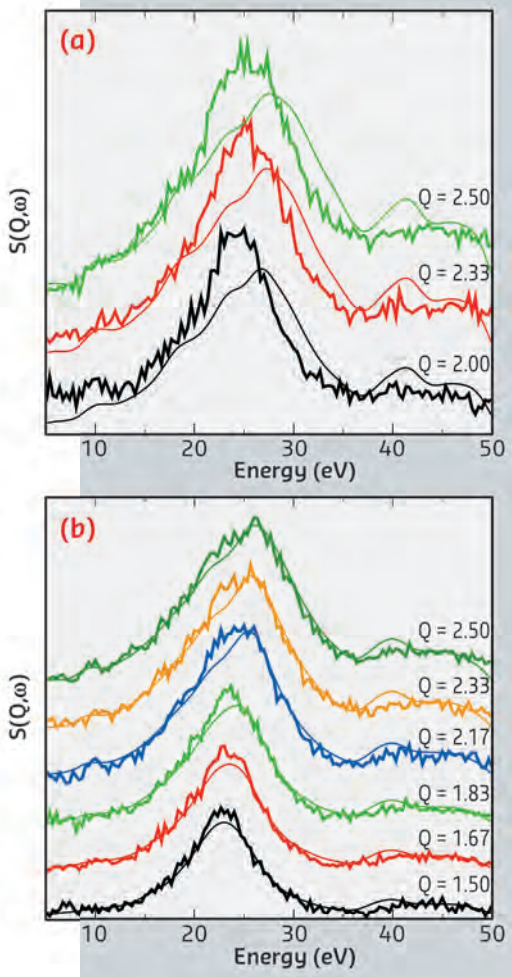

Fig. 8: Comparison between experimental (bold line) and theoretical (thin line) spectra of $Cu_{0.2}NbS_2$ (a) and $NbSe_2$ (b) at different values of momentum transfer Q (in multiple of $2\pi/c$) normal to the plane of the layers. A broadening of 1.0 eV was used in the calculations.

Principal publication and authors
P. Cudazzo (a,b), K.O. Ruotsalainen (c), C.J. Sahle (c), A. Al-Zein (d), H. Berger (e), E. Navarro-Moratalla (f), S. Huotari (c), M. Gatti (b,g,h) and A. Rubio (a,b), *Physical Review B* **90**, 125125 (2014).
(a) Nano-Bio Spectroscopy Group, Departamento Física de Materiales, Universidad del País Vasco, Centro de Física de Materiales CSIC-UPV/EHU-MPC and DIPC, San Sebastián (Spain)
(b) European Theoretical Spectroscopy Facility (ETSF)
(c) Department of Physics, University of Helsinki (Finland)
(d) ESRF
(e) École Polytechnique Fédérale de Lausanne (EPFL), Institut de Physique des Nanostructures (Switzerland)
(f) Instituto de Ciencia Molecular (ICMol), Universidad Valencia (Spain)
(g) Laboratoire des Solides Irradiés, École Polytechnique, CNRS-CEA/DSM, Palaiseau (France)
(h) Synchrotron SOLEIL, Saint Aubin (France)

References
[1] J. van Wezel *et al.*, *Phys. Rev. Lett.* **107**, 176404 (2011).
[2] P. Cudazzo, M. Gatti, A. Rubio, *Phys. Rev. B* **86**, 075121(2012).

Principal publication and authors
M. Moretti Sala (a), K. Ohgushi (b), A. Al-Zein (a), Y. Hirata (b), G. Monaco (a,c) and M. Krisch (a), *Phys. Rev. Lett.* **112**, 176402 (2014).
(a) ESRF
(b) Institute for Solid State Physics, University of Tokyo, Kashiwa (Japan)
(c) Dipartimento di Fisica, Università di Trento, Povo (Italy)

$CaIrO_3$: A SPIN-ORBIT MOTT INSULATOR BEYOND THE j_{eff} = 1/2 GROUND STATE

Spin-orbit coupling, when compared to the energy scale of other interactions, is usually neglected in the description of correlated 3d transition metal compounds. However, in compounds containing 5d elements its role grows in importance and the combined influence of electron correlation and spin-orbit coupling gives rise to novel quantum phases and transitions.

The insulating behaviour of antiferromagnetic Sr_2IrO_4, for example, is unexpected for a system with a half-filled outermost electronic shell and spatially extended orbitals. The conventional Mott mechanism often invoked to explain the insulating character of strongly correlated systems cannot be envisaged here as electron correlation is small. However, in combination with a strong cubic crystal field, spin-orbit coupling enhances the effect of electronic correlation through the formation of the so-called j_{eff} = 1/2 ground state: Sr_2IrO_4 was therefore termed a spin-orbit Mott insulator [1].

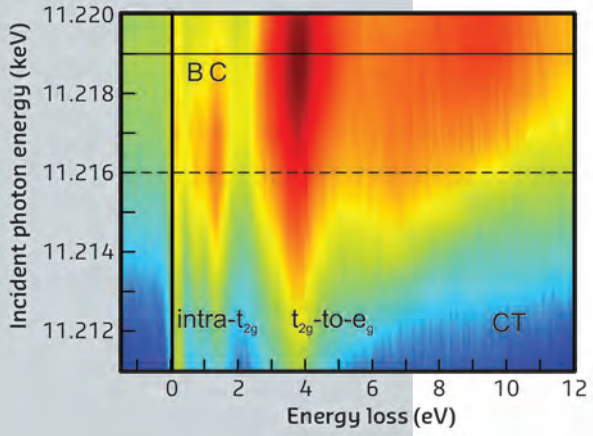

Fig. 9: Ir L_3 edge RIXS map of $CaIrO_3$.

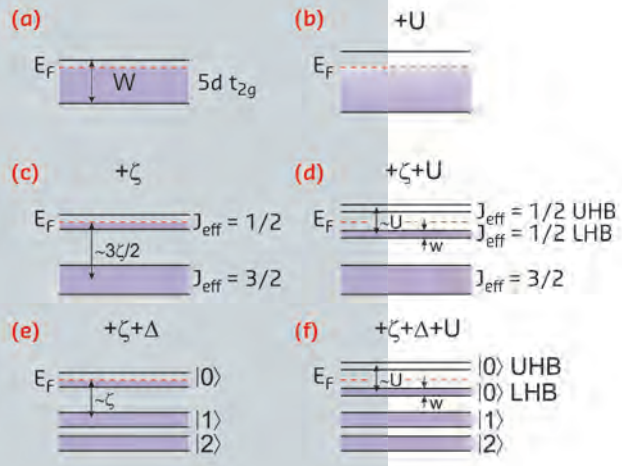

Fig. 10: Schematic band structure of $5d^5$ iridates in the absence of perturbations (a), with spin-orbit coupling (c), and spin-orbit coupling plus tetragonal crystal field splitting (e). Panels (b), (d), and (f) correspond to panels (a), (c) and (e), respectively, when the Hubbard term U is taken into account.

Whether this scenario also holds true for $CaIrO_3$ is debatable because sizeable octahedral distortions are expected to drastically lower the symmetry of the crystal field compared to Sr_2IrO_4. The robustness of the j_{eff} = 1/2 ground state against structural distortions has been mostly tested by means of resonant X-ray magnetic scattering. However, the interpretation of RXMS has been strongly debated and, in the specific case of $CaIrO_3$, a unified picture of the ground state has not yet been reached: in fact, the interpretation of experimental results [2] has been contradicted by theoretical calculations [3].

We used resonant inelastic X-ray scattering (RIXS) at the Ir L_3 edge to address the problem of the electronic structure of $CaIrO_3$. RIXS measurements were carried out at **ID20**, the new inelastic X-ray scattering beamline. Figure 9 shows a RIXS map of $CaIrO_3$. An elastic line, magnetic excitations and possibly phonons are found close to the zero energy loss line. At increasing energy losses, we assign features to intra-t_{2g} (5d t_{2g}^5 → 5d t_{2g}^5), t_{2g}-to-e_g (5d t_{2g}^5 → 5d $t_{2g}^4e_g^1$) and charge-transfer (CT) excitations, following previous RIXS studies. In this work, we focus on intra-t_{2g} excitations only, *i.e.* excitations in which electrons are promoted within the 5d t_{2g} manifold. These are composed by two peaks at 0.65 (B) and 1.22 eV (C), respectively.

To better understand the nature of these excitations and to estimate the effective tetragonal contribution to the crystal field splitting and spin-orbit coupling in $CaIrO_3$, we adopted a single-ion model [4]: the interacting Hamiltonian for one *hole* in the 5d t_{2g} states is then written as $H = \zeta \mathbf{L}\cdot\mathbf{S} - \Delta L_z^2$, in which the tetragonal crystal field splitting Δ and spin-orbit coupling ζ are treated on equal footing. The transition energies are reproduced for ζ = 0.52 and Δ = –0.71 eV. The sign of Δ is consistent with structural studies reporting a compression of the IrO_6 octahedrons and implies a minor contribution of the xy orbital to the ground state wave

function (only 10%). We conclude that the wave function of $CaIrO_3$ differs significantly from that of Sr_2IrO_4, for which xy, yz and zx orbitals are equally occupied.

How to explain the insulating behaviour for $CaIrO_3$ then? Consider the whole 5d t_{2g} manifold (**Figure 10a**): the bandwidth *W* would be too large for a reasonable Hubbard energy *U* (<*W*) to open a gap; rather, the density of states at the Fermi energy would only be slightly reduced (**Figure 10b**). Crucially, spin-orbit coupling splits the otherwise degenerate 5d t_{2g} states and a half filled j_{eff} = 1/2 band is isolated, with a bandwidth *w* < W (**Figure 10c**). As now *U* > *w*, a lower (LHB) and an upper (UHB) Hubbard band are created, and the system turns into an insulator (**Figure 10d**): this is the mechanism introduced to explain the insulating behaviour of Sr_2IrO_4. In $CaIrO_3$, however, the tetragonal crystal field is comparable to the spin-orbit coupling and three Kramers doublets are formed (**Figure 10e**). Finally, however, the action of U is similar to the pure j_{eff} = 1/2 case in view of the similar narrowing of the conduction band (**Figure 10f**). Therefore, we conclude that $CaIrO_3$ can also be classified as a spin-orbit Mott insulator.

References
[1] B.J. Kim *et al.*, *Phys. Rev. Lett.* **101**, 076402 (2008).
[2] K. Ohgushi *et al.*, *Phys. Rev. Lett.* **110**, 217212 (2013).
[3] N.A. Bogdanov *et al.*, *Phys. Rev. B* **85**, 235147 (2012).
[4] M. Moretti-Sala *et al.*, *Phys. Rev. Lett.* **112**, 026403 (2014).

SIMILARITIES AND DIFFERENCES BETWEEN ELECTRON- AND HOLE-DOPED CUPRATE SUPERCONDUCTORS UNVEILED BY INELASTIC X-RAY SCATTERING

Superconductivity is a state of matter where electrical resistance disappears completely. This phenomenon is particularly fascinating and mysterious in high-T_c superconducting cuprates, whose complicated electronic and magnetic structure has attracted great interest since their discovery more than a quarter century ago.

The parent compound of cuprate superconductors is an antiferromagnetic insulator. The material becomes a metal when either electrons or holes become mobile charge carriers through the effect of doping. The superconductivity occurs in the doped metallic state and the antiferromagnetic interaction, which causes the spin order in the parent compound, is also intimately related to the superconductivity. Therefore, both spin and charge degrees of freedom should be clarified comprehensively for a definitive understanding of the electron dynamics in the cuprates and differences or similarities between electron- and hole-doped compounds have been central in the study of the cuprate superconductors over the last few decades.

In this study, we have performed Cu L_3-edge resonant inelastic X-ray scattering (RIXS) experiments of the electron-doped superconductor $Nd_{2-x}Ce_xCuO_4$ at beamline **ID08 (now ID32)** using the AXES spectrometer. Very recently, high-resolution RIXS at the transition-metal L-edge has become a complementary technique to the conventional inelastic neutron scattering (INS) for measuring momentum-resolved spin excitations [1]. In addition, RIXS possesses sensitivity to charge excitations, which are hardly observed by neutron based techniques.

Figure 11 shows RIXS intensity maps as a function of momentum in the CuO_2 plane ($\mathbf{q}_{||}$) and energy. In the parent compound Nd_2CuO_4, spin-wave excitations with sinusoidal dispersion are predominantly observed. Charge excitations are missing in this energy region because the large charge transfer

Principal publication and authors
K. Ishii (a), M. Fujita (b), T. Sasaki (b), M. Minola (c), G. Dellea (c), C. Mazzoli (c), K. Kummer (d), G. Ghiringhelli (c), L. Braicovich (c), T. Tohyama (e), K. Tsutsumi (b), K. Sato (b), R. Kajimoto (f), K. Ikeuchi (g), K. Yamada (h), M. Yoshida (a,i), M. Kurooka (i) and J. Mizuki (a,i), *Nature Communications* **5**, 3714 (2014).
(a) Japan Atomic Energy Agency, Sayo (Japan)
(b) Tohoku University, Sendai (Japan)
(c) Politecnico di Milano, Milano (Italy)
(d) ESRF
(e) Kyoto University, Kyoto (Japan)
(f) J-PARC Center, Tokai (Japan)
(g) Comprehensive Research Organization for Science and Society, Tokai (Japan)
(h) High Energy Accelerator Research Organization, Tsukuba (Japan)
(i) Kwansei Gakuin University, Sanda (Japan)

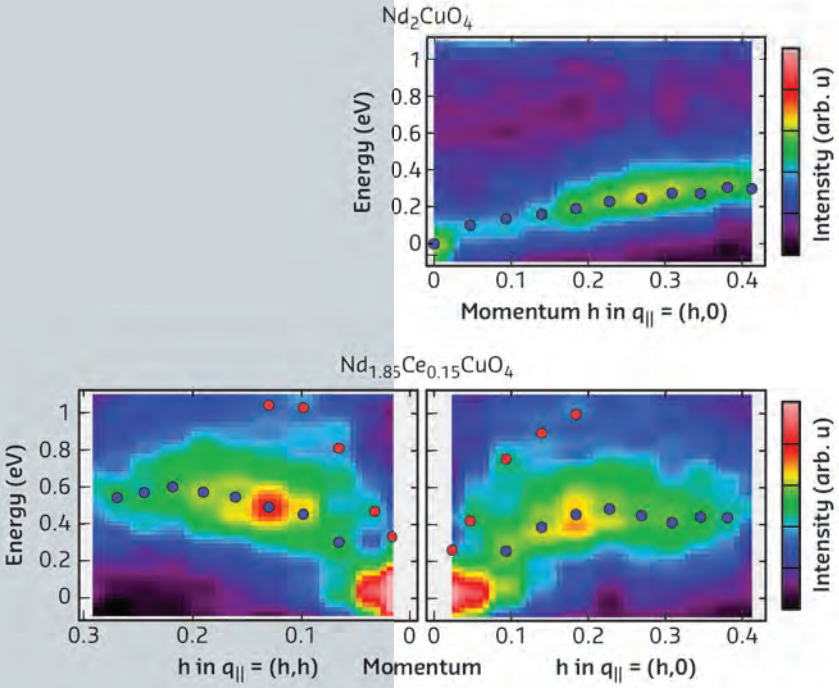

Fig. 11: Cu L_3-edge RIXS intensity map of the parent antiferromagnetic insulator Nd_2CuO_4 and the electron-doped superconductor $Nd_{1.85}Ce_{0.15}CuO_4$. Blue and red circles respectively indicate the peak positions of the spin and charge excitations obtained by fitting the spectra. The spectra were measured with a π polarised incident beam.

gap is about 2 eV. When electrons are added by partial substitution of trivalent Nd with tetravalent Ce, the spectral weight clearly moves to higher energy accompanied by the broadening of the width, as seen in the spectra of superconducting $Nd_{1.85}Ce_{0.15}CuO_4$. We also confirmed the high-energy shift of the spin excitations near the magnetic zone centre by inelastic X-ray scattering (INS). In addition, we found a distinct mode whose fast dispersion connects well to that of particle-hole excitations observed in the Cu K-edge RIXS spectra. We therefore attribute the dispersive mode to the same charge origin.

From the Cu L_3-edge RIXS, complemented by INS and Cu K-edge RIXS, we have clarified the doping evolution of the spin and charge excitations in the electron-doped cuprate superconductors. Although the spin excitations preserve their strength in the superconducting state, both in the electron- and hole-doped superconductors, they differ substantially in their dispersion relation. In **Figure 12**, we summarise the spin and charge excitations in the parent antiferromagnetic insulator and the electron- and hole-doped superconductor. A high-energy shift of the spin excitations and their mixture with the charge excitations indicate that the electron dynamics of the electron-doped cuprates has a highly itinerant character in the sub-eV energy scale. In contrast, the spectral distribution of the spin excitations also broadens but keeps its energy position almost unchanged upon hole doping [2], which means that a more localised picture is suitable. Our findings impose constraints on theoretical models and a comprehensive description of the electronic excitations in the electron- and hole-doped cuprates is a prerequisite for complete understanding of the superconductivity.

Finally, we note that while polarisation of the scattered photons was not resolved in this work, its discrimination, which is very useful for distinction between spin and charge excitations, is becoming available [4]. Furthermore, this type of experiments will soon become even more enlightening thanks to the ERIXS spectrometer installed at the new ID32 beamline, where a simultaneous increase of energy resolution (x5) and intensity (x3) is expected with respect to the experimental conditions of this work.

References
[1] L.J.P. Ament *et al.*, *Phys. Rev. Lett.* **103**, 117003 (2009).
[2] M. Le Tacon *et al.*, *Nature Phys.* **7**, 725-730 (2011).
[3] S. Wakimoto *et al.*, *Phys. Rev. B* **87**, 104511 (2013).
[4] L. Braicovich *et al.*, *Rev. Sci. Instrum.* **85**, 115104 (2014).

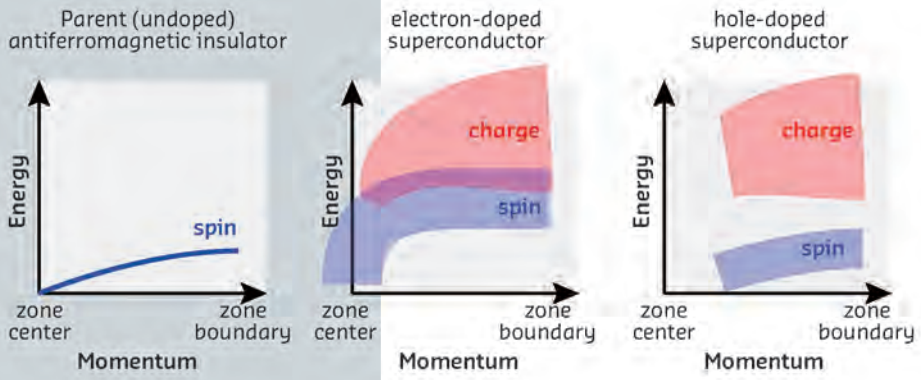

Fig. 12: Schematic of spin and charge excitations in the copper oxides. In the present work, the parent antiferromagnetic insulator and an electron-doped superconductor were studied. Excitations in hole-doped superconductors have been reported in Refs. [2,3].

TUNING THE MAGNETISM OF 3D-METAL PHTHALOCYANINE ADLAYERS BY ELECTRON DOPING

Principal publication and authors
S. Stepanow (a), A. Lodi Rizzini (b), C. Krull (b), J. Kavich (b), J.C. Cezar (c), F. Yakhou-Harris (c), P.M. Sheverdyaeva (d), P. Moras (d), C. Carbone (d), G. Ceballos (b), A. Mugarza (b) and P. Gambardella (a,b), *J. Am. Chem. Soc.* **136**, 5451-5459 (2014).
(a) Department of Materials, ETH Zürich (Switzerland)
(b) Catalan Institute of Nanoscience and Nanotechnology (ICN2), Barcelona (Spain)
(c) ESRF
(d) Istituto di Struttura della Materia, CNR, Trieste (Italy)

Thin phthalocyanine films have been incorporated in various devices including field effect transistors, light-emitting devices and photovoltaic cells. Phthalocyanines can accommodate a variety of metal ions in their centre that have particular spin configurations rendering this class of compounds also interesting for magnetic materials [1]. Due to the particular coordination geometry of the metal ions, the spin states of the complexes are sensitive to their local chemical environment. Bringing the molecules into contact with metal electrodes could therefore have significant influence on the magnetic properties of the metal centres. Another effective route for tailoring the electronic and magnetic characteristics of molecular magnets is offered by direct chemical doping.

The charging sequence of metal-phthalocyanines involves both ligand and metal orbitals and depends strongly on the nature of the central metal ion. Doping of phthalocyanine chemisorbed on a metal substrate is further complicated due to the interplay of additional substrate induced charging and screening effects that can alter the role of the charge donor towards the molecules. The step-wise attachment of electron donor Li atoms to chemisorbed CuPc and NiPc molecules was recently investigated by scanning probe microscopy and DFT calculations [2]. The effects of alkali metal doping on the magnetic properties of metal-phthalocyanines, however, have not been studied in a systematic way, neither in the bulk nor at interfaces. These effects are of particular importance for molecular electronic and spintronic applications.

This study focuses on the effect of Li doping on the electronic and magnetic states of the metal ions for a series of *3d* metal-phthalocyanine monolayers (MnPc, FePc, NiPc, CuPc) adsorbed on Ag(001). Our systematic investigation employed X-ray magnetic circular dichroism (XMCD) at beamline ID08 (now **ID32**) complemented by atomic multiplet calculations, which allowed us to accurately determine changes of the spin, electronic valence, and crystal field in electron-doped phthalocyanines. Figure 13a shows a close-packed array of CuPc. The addition of a small amount of Li atoms leads to two major types of Li-CuPc complexes where the Li atoms can reside at the ligand position (denoted *L*) or close to the metal centre (denoted *M*). The relative proportion of each type of complex depends on the Li coverage. With increasing Li coverage, the preference changes from *L*-type to the *M* configuration even though there are more ligand sites available than central positions (Figure 13b). The different Li dopant types lead to site specific electron donation either to the metal *d*-states or to the organic backbone.

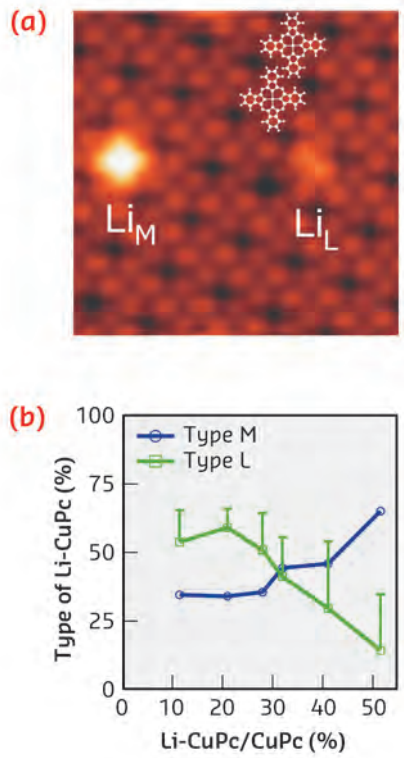

Fig. 13: STM topography of a CuPc adlayer with two doped complexes of different types (8.3 nm *x* 8.3 nm). Statistical analysis of the type of dopant as a function of Li coverage extracted from the STM data. Error bars account for undefined configurations.

References
[1] J. Bartolomé, C. Monton and I.K. Schuller, in *Molecular Magnets*, J. Bartolomé, F. Luis, J.F. Fernández (Eds.), Springer-Verlag, Berlin Heidelberg, 221-245 (2014).
[2] C. Krull, R. Robles, A. Mugarza and P. Gambardella, *Nature Mater.* **12**, 337 (2013).

Figure 14 shows the X-ray absorption and XMCD spectra of NiPc as a function of Li doping. With increasing Li concentration, the pristine non-magnetic Ni ions, which have a spin singlet d^8 configuration, become reduced and assume a d^9 configuration. A magnetic moment corresponding to S = 1/2 appears at the same time, as evidenced by the XMCD. The Li doping has the opposite effect For CuPc: the magnetic moment can be turned off by Li doping, due to the complete filling of the d-shell (from d^9 to d^{10}). In contrast, for MnPc, we observed no changes of the d^5 metal ion valence state as a function of doping, but a transition from an intermediate S=3/2 to a high S = 5/2 spin state. This transition is due to a strong reduction of the ligand field induced by Li, which is also observed for CuPc, NiPc, and FePc.

When combined with STM studies (**Figure 13** and Ref. **[2]**), these results provide a complete picture of chemically-doped metal-phthalocyanines on surfaces, in which strong correlation effects induce site-specific charging and magnetic effects. Moreover, these results demonstrate that different spin states can be realised in metal-phthalocyanine layers interfaced with metals by doping with Li atoms, offering a route to tune the magnetic properties of surface-supported molecular systems employing non-magnetic dopants.

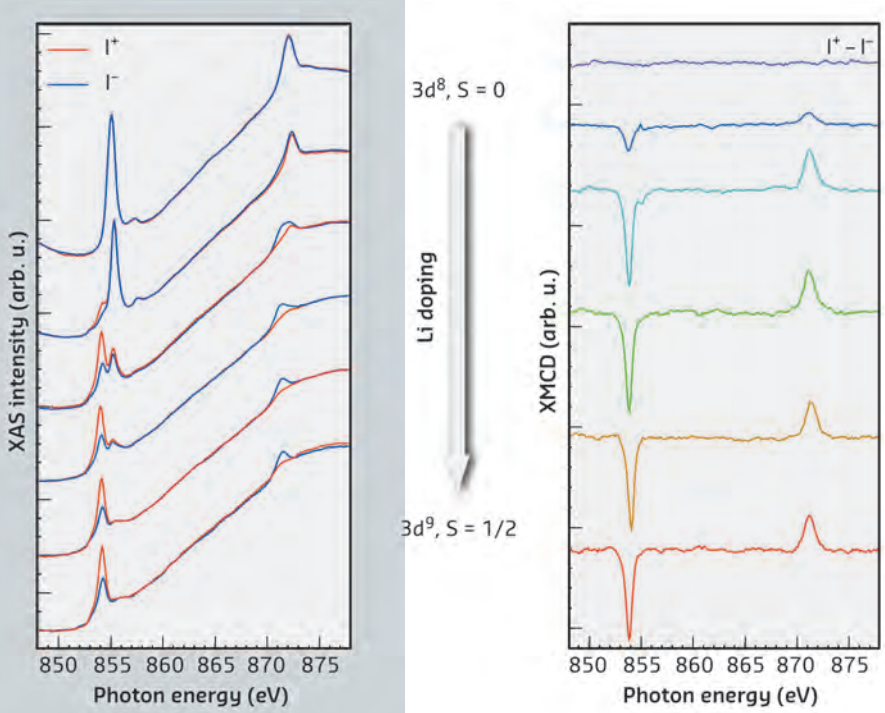

Fig. 14: Evolution of NiPc XAS and XMCD at normal incidence with subsequent Li atom deposition.

EUROPIUM NITRIDE: A NOVEL DILUTED MAGNETIC SEMICONDUCTOR

Principal publication and authors
Do Le Binh (a), B.J. Ruck (a), F. Natali (a), H. Warring (a), H.J. Trodahl (a), E.-M. Anton (a), C. Meyer (b), L. Ranno (b), F. Wilhelm (c), and A. Rogalev (c), *Phys. Rev. Lett.* **111**, 167206 (2013).
(a) The MacDiarmid Institute for Advanced Materials and Nanotechnology, Victoria University of Wellington, Wellington (New Zealand)
(b) Institut Néel, Centre National de la Recherche Scientifique and Université Joseph Fourier, Grenoble (France)
(c) ESRF

Ferromagnetism, where a material spontaneously forms a net magnetisation, is one of the oldest and most striking examples of correlated electron phenomena. Most ferromagnets are metals, but under the right conditions some semiconductors can also become ferromagnetic if they are doped with a small concentration of magnetic ions. Such so-called diluted magnetic semiconductors (DMSs) offer exciting possibilities in the field of *spintronics*, where the functionality of electronic devices is enhanced by exploiting the intrinsic magnetic moment of electrons in addition to their charge. The most well studied diluted magnetic semiconductors are formed by adding manganese to III-V semiconductors such as GaAs. Mobile charges in the semiconductor host mediate magnetic interactions

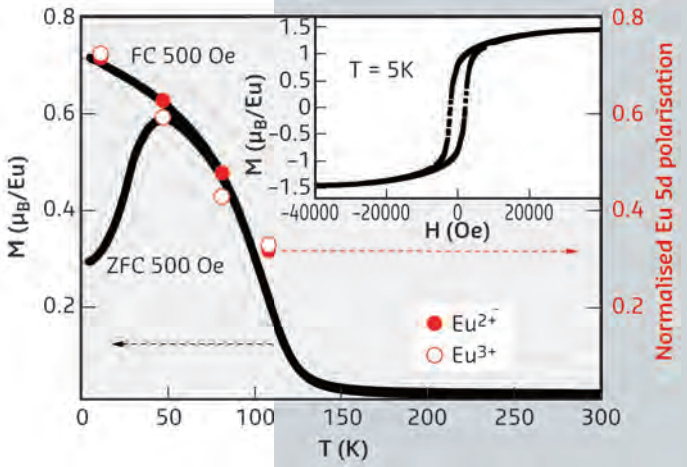

Fig. 15: Ferromagnetic response of a nitrogen deficient europium nitride film. The solid lines represent SQUID magnetometry measurements, while the red symbols represent element specific magnetisation measured by XMCD. The XMCD results prove that the ferromagnetism originates in the EuN rather than in an impurity phase.

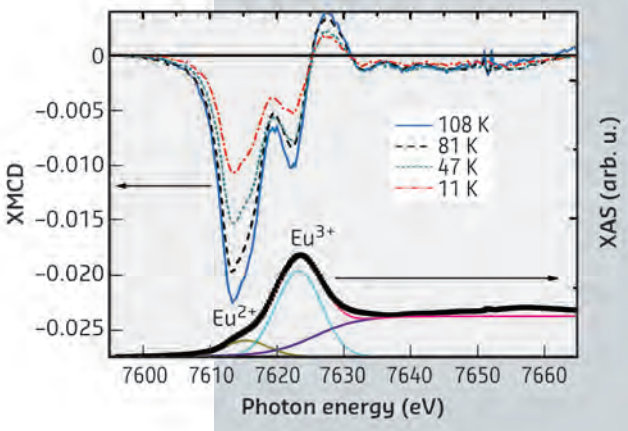

Fig. 16: X-ray absorption and XMCD results from a ferromagnetic EuN film. Magnetic polarisation of europium ions in both 2+ and 3+ charge states is evident.

between the manganese ions, allowing them to form an ordered magnetic state. Understanding the details of the interactions remains a challenge even after more than two decades of study [1], and the field remains an active research area. We have recently added a novel material, europium nitride, to the list of known DMSs, and we have shown that it exhibits some surprising properties that distinguish it from other materials in the class [2].

Europium nitride (EuN) is a member of the rare-earth nitride series, many of which are ferromagnets at low temperature. However, EuN is not expected to be magnetic because of the particular configuration of the electrons in the Eu^{3+} ions. The team at Victoria University in Wellington had already discovered that in EuN thin films prepared with a slight deficit of nitrogen some of the europium ions convert to the 2+ charge state. Eu^{2+} does carry a magnetic moment, but the moments of the individual 2+ ions had not previously been observed to order into an overall magnetic state [3]. The new research showed that, once about 20% of the europium becomes Eu^{2+}, magnetic ordering sets in below a critical temperature of 125 K (see Figure 15), which is one of the highest temperatures of confirmed DMS systems.

Proof that the magnetism is intrinsic to EuN came from X-ray magnetic circular dichroism (XMCD) results obtained at beamline **ID12**. This powerful technique independently measured the magnetic contribution from the Eu^{2+} and Eu^{3+} (see Figure 16). The magnetic signal from the Eu^{2+} component of the EuN closely follows the magnetisation of the whole sample (solid circles in Figure 15), confirming the central role of Eu^{2+} in the magnetic state. More surprisingly, a strong magnetic signal was also found on the Eu^{3+}. This proves that the Eu^{2+} remains coupled in the EuN matrix rather than forming a separate magnetic impurity phase. Furthermore, it indicates that the Eu^{3+} that forms the bulk of the material is playing far more than a passive role in the magnetism. Instead, the Eu^{3+} is acting as a magnetically polarisable background that enhances the magnetic interactions between the Eu^{2+} ions beyond that which can be provided by the small density of conduction electrons in the material. This is in striking contrast to conventional DMS systems where the host semiconductor is magnetically inert, and thus represents a new paradigm in the DMS field.

References

[1] T. Dietl and H. Ohno, *Rev. Mod. Phys.* **86**, 187 (2014); T. Jungwirth, J. Wunderlich, V. Novák, K. Olejník, B.L. Gallagher, R.P. Campion, K.W. Edmonds, A.W. Rushforth, A.J. Ferguson and P. Němec, *Rev. Mod. Phys.* **86**, 855 (2014).

[2] Do Le Binh, B.J. Ruck, F. Natali, H. Warring, H.J. Trodahl, E.-M. Anton, C. Meyer, L. Ranno, F. Wilhelm and A. Rogalev, *Phys. Rev. Lett.* **111**, 167206 (2013).

[3] B.J. Ruck, H.J. Trodahl, J. Richter, J. Criginski-Cezar, F. Wilhelm, A. Rogalev, V. Antonov, Do Le Binh, F. Natali and C. Meyer, *Phys. Rev. B* **83**, 174404 (2011).

Principal publication and authors
R. Sessoli (a), M.-E. Boulon (a), A. Caneschi (a), M. Mannini (a), L. Poggini (a), F. Wilhelm (b) and A. Rogalev (b), *Nature Phys.* **11**, 69–74 (2015).
(a) Department of Chemistry 'University of Florence (Italy)
(b) ESRF

STRONG MAGNETO-CHIRAL DICHROISM IN A PARAMAGNETIC MOLECULAR HELIX OBSERVED BY HARD X-RAYS

Chirality is a phenomenon constantly in front of us [1], as are our hands from which its name originates (χείρ=hand). It is well known that when inversion symmetry is absent and a structure is non superimposable on its mirror image, a sample absorbs right and left circularly polarised light differently giving rise to natural circular dichroism (NCD). When a magnetised sample interacts with circularly polarised light, another variety of dichroism, magnetic circular dichroism (MCD), can be observed. A chiral magnetised object interacts in a different way with *unpolarised* light depending on the sample chirality, the magnetisation vector, and the direction of propagation of light. This non-reciprocal phenomenon called magneto-chiral dichroism (MχD) has been observed for the first time only in 1997 with visible light [2] and even more recently with X-rays [3]. This effect is in fact one of the few phenomena that is simultaneously parity odd and time-reversal odd. XMχD has been considered as a possible origin of the homochirality of life on earth, in alternative to the parity-violating electroweak nuclear interactions [1]. There are very few examples of MχD in literature, most of them reporting a very weak effect. Here we report on detection of very strong magneto-chiral dichroism in paramagnetic chiral complexes in the hard X-ray range.

Two molecular helices crystallising in enantiopure trigonal crystals and comprising cobalt(II) or manganese(II) ions bridged by stable organic radicals (see **Figure 17**) have been investigated at the K-edge of the transition metal ions by exploiting the unique capabilities of the **ID12** beamline. All three dichroic spectra were measured on pairs of opposite enantiomers, using single crystals with a volume of the order of mm^3. The results for the cobalt derivatives are reported in **Figure 17**. By using both enantiomers, we were able to check the change of sign for XNCD and XMχD signals as well as the change in sign on reversal of the magnetic field for XMCD and XMχD. It appears clearly from **Figure 17** that the spectral shapes of the three dichroic contributions are very different, the magneto-chiral dichroism being significant only where electric quadrupolar transitions from 1*s* to 3*d* orbitals of the cobalt atoms are involved. It is also interesting to notice that the intensity of the magneto-chiral dichroism is indeed larger than the magnetic one, in contrast to the

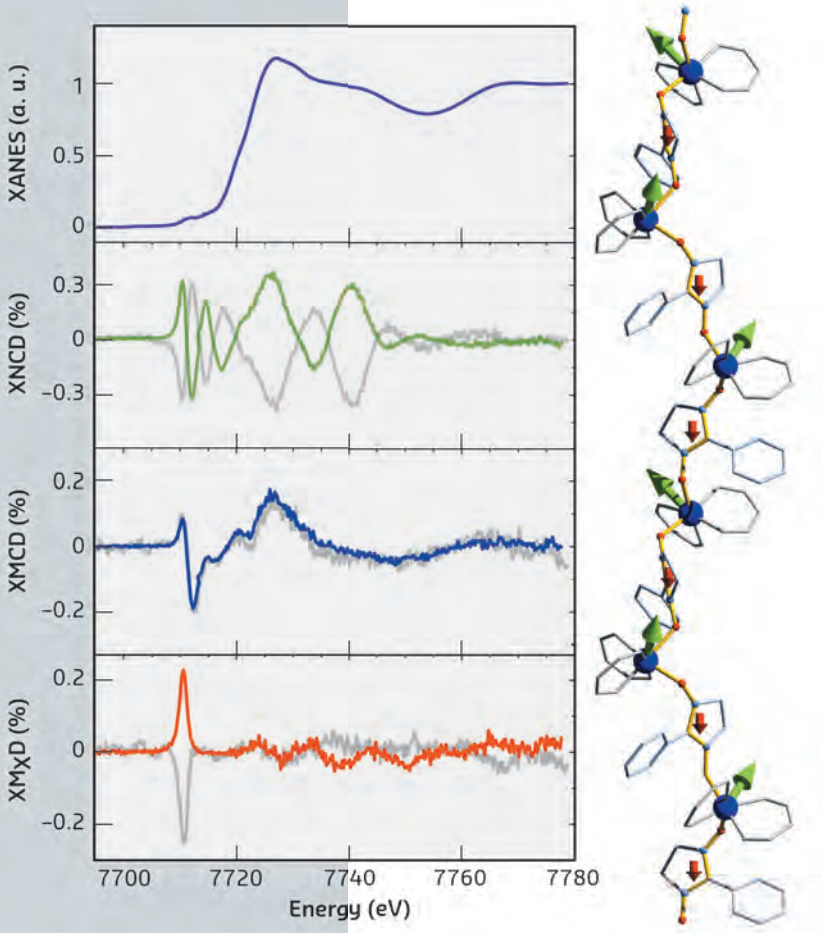

Fig. 17: View of the helix formed by cobalt(II)-hexafluroacetylacetonates and nitronyl-nitroxide radicals (Co in blue; methyl groups, fluorine and hydrogen atoms omitted for clarity). The arrows indicate the non-collinear spin structure of the chain. The XANES and the three dichroic signals (XNCD, XMCD, and XMχD) normalised to the XANES intensity at the edge jump, are shown in the four panels respectively (in colour for the depicted helicity, in grey for the other enantiomer).

assumption that MχD is weak being the product of two other weak effects (NCD and MCD).

The novelty of the investigation also resides on the possibility of investigating two isostructural helices differing for their magnetic properties. In fact, while the cobalt(II) ions have strong magnetic anisotropy due to the orbital magnetic moments resulting in a non-collinear magnetic helix, the manganese(II) derivative, comprising spin-only d^5 ions, is a pure Heisenberg spin chain. For the latter, the same hard X-ray investigation revealed comparable natural and magnetic dichroisms, but a vanishingly small magneto-chiral contribution. The combination of magnetic anisotropy with helical structure resulting in a non-collinear spin arrangement seems to be the key for a strong X-ray MχD.

The magneto-chiral dichroism has an unusual symmetry, which is odd with respect to both parity and time-reversal symmetry but invariant with respect to their product. It is closely related to the anapole moment, which in this particular case originates from the toroidal orbital currents of the cobalt atoms, as depicted in **Figure 18**. The more usual orbital currents generating the magnetic moment detected by XMCD are also shown. Orbital toroidal currents are of relevance for many phenomena, ranging from multiferroicity to superconductivity **[4]**, while the combination of chirality and magnetism could be a viable route to store information in protected magnetic structures like skyrmions **[5]**.

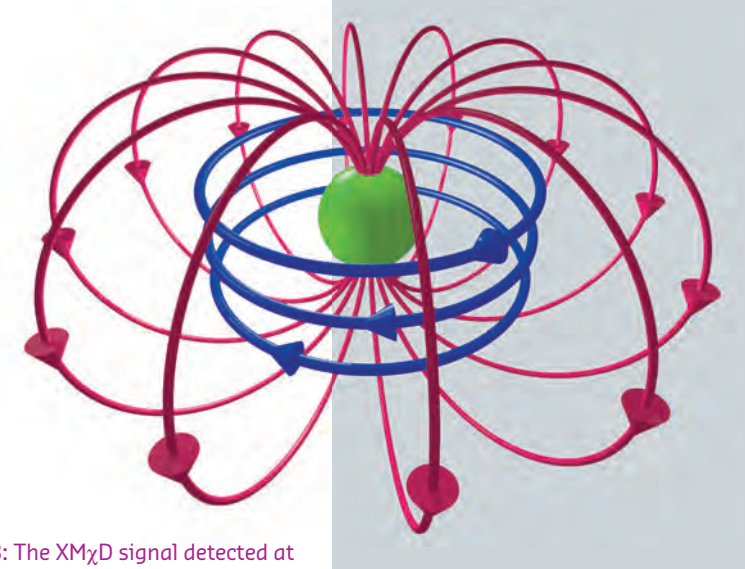

Fig. 18: The XMχD signal detected at the K-edge of the cobalt atom provides information on the orbital toroidal currents (drawn in red), or orbital anapole, while XMCD is indicative of the orbital dipolar moment (in blue).

References
[1] G.H. Wagnière, *On Chiralty and the Universal Asymmetry*. (Verlag Helvetica Chimica Acta, Zürich, 2007).
[2] G. Rikken and E. Raupach, *Nature* **390**, 493-494 (1997).
[3] J. Goulon, A. Rogalev, F. Wilhelm, C. Goulon-Ginet, P. Carra, D. Cabaret and C. Brouder, *Phys. Rev. Lett.* **88**, 237401 (2002).
[4] V. Scagnoli, U. Staub, Y. Bodenthin, R.A. de Souza, M. García-Fernández, M. Garganourakis, A.T. Boothroyd, D. Prabhakaran and S.W. Lovesey, *Science* **332**, 696-698 (2011).
[5] S. Mühlbauer, B. Binz, F. Jonietz, C. Pfleiderer, A. Rosch, A. Neubauer, R. Georgii and P. Böni, *Science* **323**, 915-919 (2009).

A NOVEL SOLUTION FOR THE DETERMINATION OF NO OXIDATION STATE IN Fe-NO COMPLEXES

To understand how the metal iron utilises its intrinsic reactivity and redox propensity for the stabilisation of nitric oxide in the form of Fe-NO complexes, an extensive study of the electronic structure of Fe-NO complexes was carried out using a variety of spectroscopic methods **[1-4]**. The comparable energy levels of NO π* orbitals and Fe 3d orbitals, however, complicate the Fe-NO bonding interaction and puzzle the quantitative assignment of the oxidation state of Fe-bound nitric oxide as NO^+, NO radical, or NO^-. With regard to the utilisation of valence-to-core X-ray emission spectroscopy (V2C XES) for quantifying small-molecule activation such as N_2 in iron-dinitrogen complexes, we developed V2C XES as a spectroscopic ruler for the quantitative determination of NO oxidation state in Fe-NO complexes, which was circumvented by invention of Enemark-Feltham notation **[5]**.

XES displays the dipole-allowed transitions from metal p orbitals to metal

Principal publication and authors
T.-T. Lu (a), T.-C. Weng (b) and W.-F. Liaw (c), *Angew. Chem.* **53**, 11562 (2014).
(a) Department of Chemistry, Chung Yuan Christian University (Taiwan)
(b) SLAC National Accelerator Laboratory (USA)
(c) Department of Chemistry, National Tsing Hua University (Taiwan)

References

[1] T.-T. Lu *et al.*, *Inorg. Chem.* **50**, 5396 (2011).

[2] J.L. Hess, C.H. Hsieh, S.M. Brothers, M.B. Hall and M.Y. Darensbourg, *J. Am. Chem. Soc.* **133**, 20426 (2011).

[3] S. Ye, F. Neese, *J. Am. Chem. Soc.* **132**, 3646 (2010).

[4] J.E.M.N. Klein *et al.*, *Angew. Chem.* **53**, 1790 (2014).

[5] J.H. Enemark and R.D. Feltham, *Coord. Chem. Rev.* **13**, 339 (1974).

1s orbital after ionisation of a metal 1s electron. The XES valence-to-core region, in particular, reveals the ligand np/ns → metal 1s transitions, which are enhanced by ~5% contribution of Fe 4p orbitals into the valence orbitals. XES spectra of complexes $[Fe^{II}(SPh)_4]^{2-}$, $[(NO)Fe(SPh)_3]^-$, $[(NO)_2Fe(SPh)_2]^-$, and $[(NO)_2Fe(OPh)_2]^-$ were collected at beamline **ID26**. As shown in **Figure 19**, a broad transition peak at 7107.5 eV is observed in the normalised Fe K-valence spectrum of complex $[Fe^{II}(SPh)_4]^{2-}$, as opposed to three distinctive V2C transition peaks at ~7098 eV, ~7103 eV, and ~7110 eV exhibited by nitrosyl iron complexes $[(NO)Fe(SPh)_3]^-$, $[(NO)_2Fe(SPh)_2]^-$, and $[(NO)_2Fe(OPh)_2]^-$. Presumably, the two additional V2C transition peaks in the lower energy region result from the incorporation of nitric oxide.

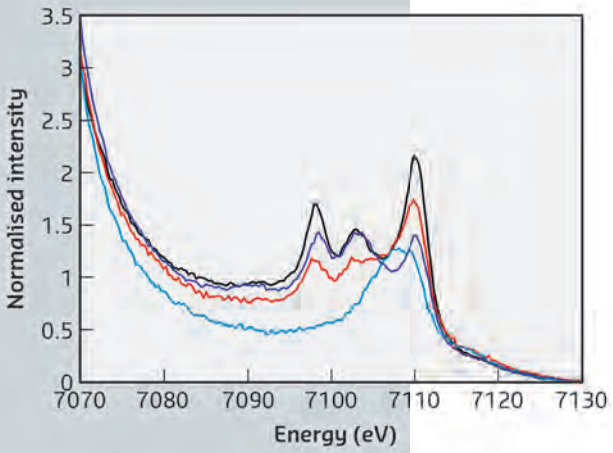

Fig. 19: Comparison of the normalised Fe K-valence XES spectra of complexes $[Fe^{II}(SPh)_4]^{2-}$ (blue), $[(NO)Fe(SPh)_3]^-$ (red), $[(NO)_2Fe(SPh)_2]^-$ (black), and $[(NO)_2Fe(OPh)_2]^-$ (purple).

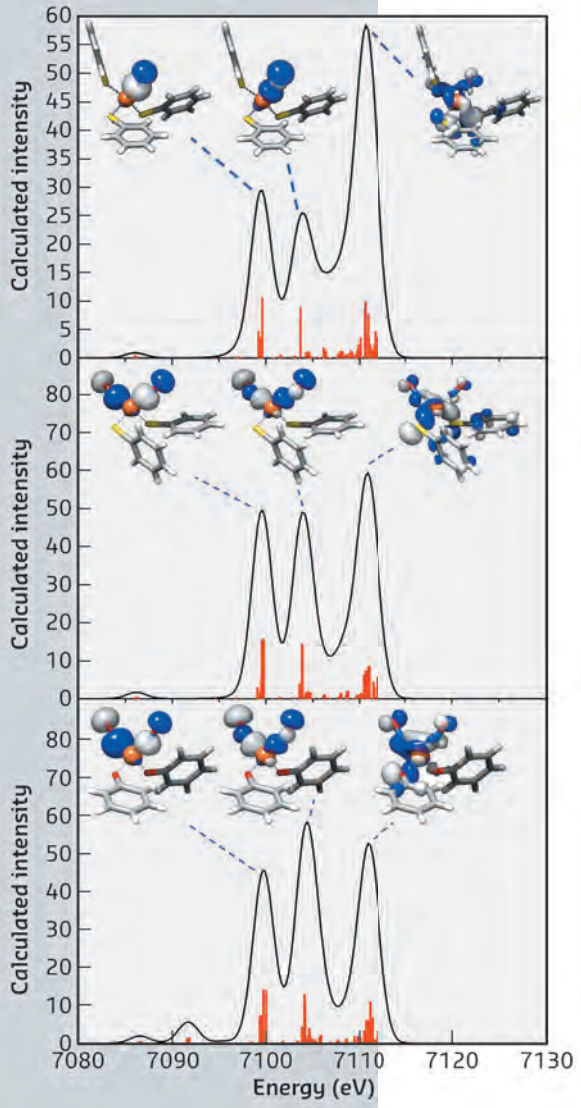

Fig. 20: DFT calculated valence-to-core XES spectra of complexes $[(NO)Fe(SPh)_3]^-$ (top), $[(NO)_2Fe(SPh)_2]^-$ (middle), and $[(NO)_2Fe(OPh)_2]^-$ (bottom) and the corresponding molecular orbitals for each of the transitions. Calculated peaks are displayed in the vertical lines.

Theoretical calculation was further pursued to verify the nature of these spectral transitions. DFT calculated V2C XES spectra of all Fe-NO complexes resemble the experimental V2C features. DFT calculation provides a computational validation for the dominant contribution from NO σ_{2s}^* and σ_{2p} orbitals, respectively, to these XES V2C features (**Figure 20**). That is, V2C XES probes the energy difference between the σ_{2s}^* and σ_{2p} orbitals of Fe-bound nitric oxide. To test the application of this energy difference, $\Delta E_{\sigma 2s^*-\sigma 2p}$ of NO, to identify the oxidation state of nitric oxide, DFT calculation of $\Delta E_{\sigma 2s^*-\sigma 2p}$ of NO^+, NO radical and NO^- was carried out to establish the linear relationship between $\Delta E_{\sigma 2s^*-\sigma 2p}$ of NO and its oxidation state. The correlation between $\Delta E_{\sigma 2s^*-\sigma 2p}$ of NO and its oxidation state follows the equation: $\Delta E_{\sigma 2s^*-\sigma 2p}$ = -0.550 × (oxidation state of NO) + 5.079. Negative correlation between $\Delta E_{\sigma 2s^*-\sigma 2p}$ of NO and its oxidation state suggests that the addition of electrons into NO π* orbitals weakens N-O bonding interaction, raises the energy level of the σ_{2p} orbital, while reducing that of the σ_{2s}^* orbital, therefore resulting in an increase in the energy separation between these two orbitals.

Based on the $\Delta E_{\sigma 2s^*-\sigma 2p}$ exhibited by Fe-NO complexes $[(NO)Fe(SPh)_3]^-$, $[(NO)_2Fe(SPh)_2]^-$, and $[(NO)_2Fe(OPh)_2]^-$, the oxidation state of these nitrosyl iron complexes are –0.58±0.18, –0.77±0.18, and –0.95±0.18, respectively. This finding suggests that binding of nitric oxide toward non-heme iron, for the sake of the storage and transport of nitric oxide, affords Fe-NO complexes and stabilises NO via partial reduction. We aim to expand this spectroscopic method to quantify NO oxidation state in a variety of Fe-NO complexes and to bring insights into Fe-NO bonding interaction modulated by its geometric structure and supporting ligands in the near future.

ABSENCE OF Ce^{3+} SITES IN CHEMICALLY ACTIVE COLLOIDAL CERIA NANOPARTICLES

Principal Publication and authors
J.-D. Cafun (a), K.O. Kvashnina (a), E. Casals (b,c), V.F. Puntes (b,c) and P. Glatzel (a), *ACS Nano* **7**, 10726–10732 (2013).
(a) ESRF
(b) Institut Català de Nanotecnologia (ICN), Bellatera (Spain)
(c) Universitat Autònoma de Barcelona (UAB), Bellaterra (Spain)

Materials based on ceria (CeO_2) have a capacity to store and release oxygen in their intrinsic *n*-type fluorite structure. This provides them with unique redox properties that are widely used and offers potential for promising applications in the areas of catalysis, fuel cells, and biomedicine. Developing tailored CeO_2 materials for industrial applications involves a clear understanding of the chemical activity of CeO_2. This ultimately depends on the electronic structure, which can be controlled at the nanoscale by the morphology.

Reducing the size of CeO_2 to the nanoscale enhances the chemical activity. The generally advocated mechanism states that particle miniaturisation results in an increase in the surface to bulk ratio and thus produces a significantly non-stoichiometric $CeO_{2-\delta}$ owing to surface oxygen vacancies. Electrons left behind by O-vacancy formation are believed to reduce Ce^{4+} to Ce^{3+} ions, resulting in a higher level of catalytically active Ce^{3+} ions at the surface that are responsible for the increased chemical activity of nanoceria when compared to bulk ceria. This ionic description of the catalytic activity is commonly supported by experiments performed under conditions that are very different from the environment of the working catalyst and may even change the chemical state of ceria (*e.g.* high vacuum). The electronic structure of ceria nanoparticles critically depends on the reaction environment, thus experiments need to be performed under *in situ* / *operando* conditions to fully reproduce the environment under which activity is observed.

We monitored the electronic structure of ceria nanoparticles using high energy resolution fluorescence-detected hard X-ray absorption spectroscopy (HERFD-XAS) at beamline **ID26**. This technique allows spectral features to be observed beyond the limitation of the L_3 edge lifetime broadening [1]. In the case of rare earth systems, HERFD-XAS reveals the fine structure of the chemically active *4f* orbitals and thus provides a direct, *in situ* probe of the Ce chemical state (**Figure 21**).

A simple ionic picture has been shown to be insufficient to describe inner-shell spectroscopic data of ceria and a multi-configuration approach is necessary. The electronic structure of Ce in bulk CeO_2 with formal valence state of IV can be described as a mixture of f^0 and $f^1\underline{L}$ contributions (where $\underline{L}$ denotes a hole in a ligand orbital) thus considering orbital mixing and sharing of electron density between Ce and O. Such formalism implies that the system remains in a singlet spin state (S = 0) independent of the f^0 and $f^1\underline{L}$ mixing ratio because the Ce f electron is spin paired with a ligand electron. The resulting spectral shape is very different from a system with two distinct f^0 (Ce^{4+}) and f^1 (Ce^{3+}) sites where the spectrum presents the sum of the two sites. Oxygen deficient $CeO_{2-\delta}$ may be described

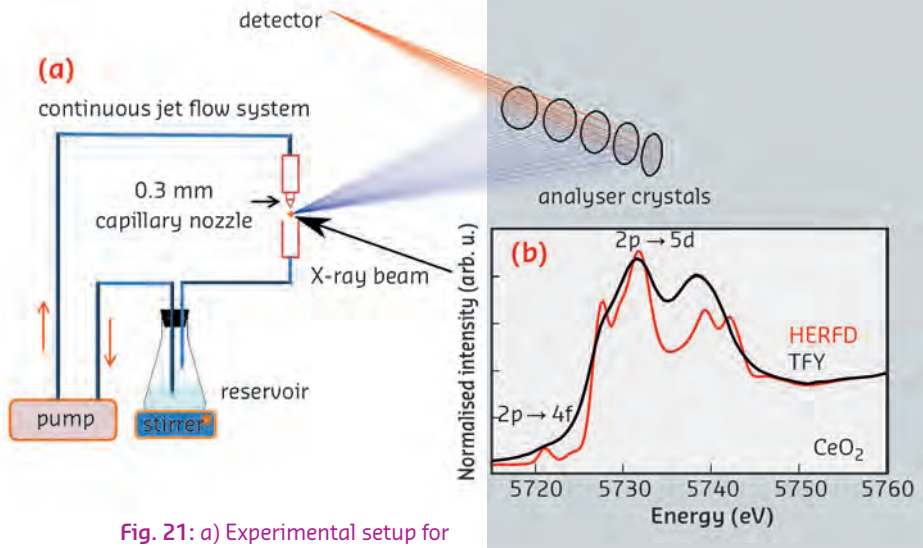

Fig. 21: a) Experimental setup for HERFD-XAS of colloidal nanoparticles. The suspension is circulated and the spectra are recorded on a free liquid jet. b) Comparison between conventional total fluorescence yield (TFY) with HERFD Ce L_3-edge spectra in bulk CeO_2. The electronic transitions are assigned to the spectral features.

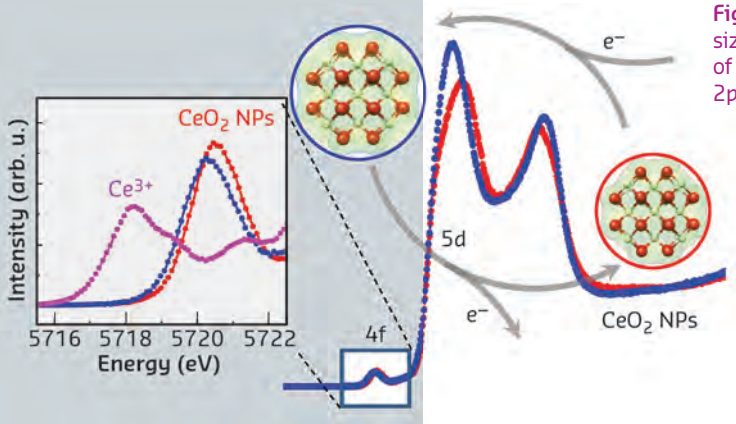

Fig. 22: Spectral changes in ceria nanoparticles (NPs) with average size of 3 nm after synthesis in ethanol (blue) and in the presence of H_2O_2 (red). The inset shows a magnification of the 2p → 4f transitions and a comparison to Ce^{3+} in $Ce(NO_3)_3$.

by an increased $f^1\underline{L}$ contribution in presence of strong orbital mixing and an unchanged singlet spin state. Such a description, however, contradicts the generally accepted view of a Ce^{3+} site with a local, unpaired spin moment in chemically active nanoceria [2].

We tested the catalytic activity of the ceria NPs by monitoring the decomposition of hydrogen peroxide (H_2O_2). This reaction mimics the activity of catalase, a common enzyme in organisms that balances the level of reactive oxygen species and thus protects cells. The 3 nm nanoparticles show rapid (< 1 minute) and significant changes in the HERFD-XAS (**Figure 22**) that are accompanied by an increase in the Ce-O inter-atomic distance. The pre-edge peak remains as one strong resonance, leading us to conclude that Ce is in a singlet state over the whole course of reaction. The changing intensity ratio between the two strong *5d* absorption peaks can be rationalised as a change in the f^0 and $f^1\underline{L}$ contributions to the ground state electronic structure.

Thus, the picture of a delocalised electron distribution emerges where the entire NP participates in the reaction as opposed to single Ce^{3+} sites. The challenge now is to find a quantum chemical theoretical description of the electron structure that accounts for the particle morphology and is able to model X-ray absorption data.

References
[1] K. Hämäläinen, D.P. Siddons, J.B. Hastings and L.E. Berman, *Phys. Rev. Lett.* **67**, 2850-2853 (1991).
[2] F. Esch, S. Fabris, L. Zhou, T. Montini, C. Africh, P. Fornasiero, G. Comelli and R. Rosei, *Science* **309**, 752-755 (2005).

HERFD XAS REVEALS A Mo(III) IN THE NITROGENASE ACTIVE SITE

Principal publication and authors
R. Bjornsson (a,b), F.A. Lima (a,c), T. Spatzal (d,e), T. Weyhermüller (a), P. Glatzel (f), E. Bill (a), O. Einsle(d), F. Neese (a) and S. DeBeer (a,g). *Chem. Sci.* **5**, 3096–3103 (**2014**).
(a) Max-Planck-Institut für Chemische Energiekonversion, Mülheim and der Ruhr (Germany)
(b) Present address: Science Institute, University of Iceland, Reykjavik (Iceland)
(c) Present address: Centro Nacional de Pesquisa em Energia e Materiais, Brazilian Synchrotron Light Laboratory – LNLS, Campinas (Brazil)
(d) Institute for Biochemistry, Albert-Ludwigs-Universität Freiburg (Germany)
(e) Present address: Howard Hughes Medical Institute and Division of Chemistry and Chemical Engineering, California Institute of Technology, Pasadena (USA)
(f) ESRF
(g) Department of Chemistry and Chemical Biology, Cornell University, Ithaca (USA)

The conversion of inert nitrogen to ammonia represents a process that is fundamental for all life on earth. While both plants and animals require bioavailable ammonia for incorporation into proteins and DNA, neither plants nor animals possess enzymes that are capable of effecting this conversion. As such, we rely on diazotrophs (bacteria and archaea that are able to fix atmospheric nitrogen gas using the enzyme nitrogenase) as the biological source of ammonia. The enzyme active site that is responsible for catalysis is an $MoFe_7S_9C$ cluster, known as FeMoco (**Figure 23**). The long-time enigmatic cluster was only recently revealed to contain a central carbon atom, and many details of the electronic structure remain unknown [1]. However, understanding the iron oxidation state, the molybdenum

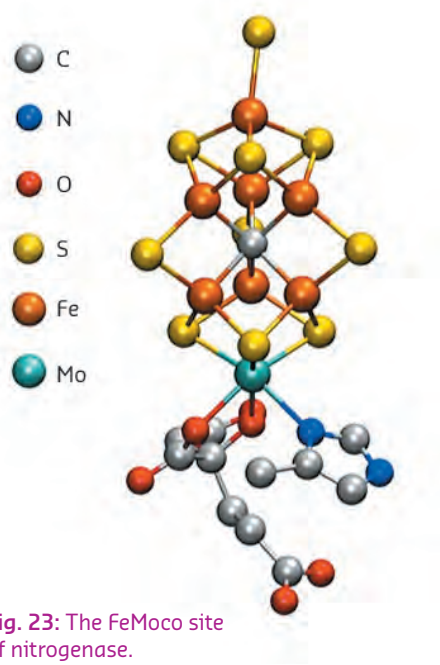

Fig. 23: The FeMoco site of nitrogenase.

oxidation states, and the spin coupling within this complex biological cofactor is essential for understanding the mechanism and is a prerequisite for rational bio-inspired catalytic design.

Recently, using high-energy resolution fluorescence detected Mo K-edge X-ray absorption spectroscopy (HERFD XAS) at beamline **ID26**, we were able to show that the nitrogenase contains a Mo(III) centre in the FeMoco active site (**Figure 24**). Previous Mo K-edge studies were unable to make a clear assignment of the Mo oxidation state in this cluster, due in large part to the significant core hole lifetime broadening at the Mo K-edge. By using HERFD XAS at beamline **ID26**, we were able to overcome many of the limitations of standard XAS measurements.

Furthermore, by using a time-dependent density functional approach to calculate the Mo K-edges [2], we were able to verify the Mo(III) assignment and to also show that the Mo(III) is in an unusual spin-coupled configuration. This finding represents the first example of Mo(III) in biology. The implications that this electronic configuration has for nitrogenase reactivity are part of ongoing research efforts in our laboratory.

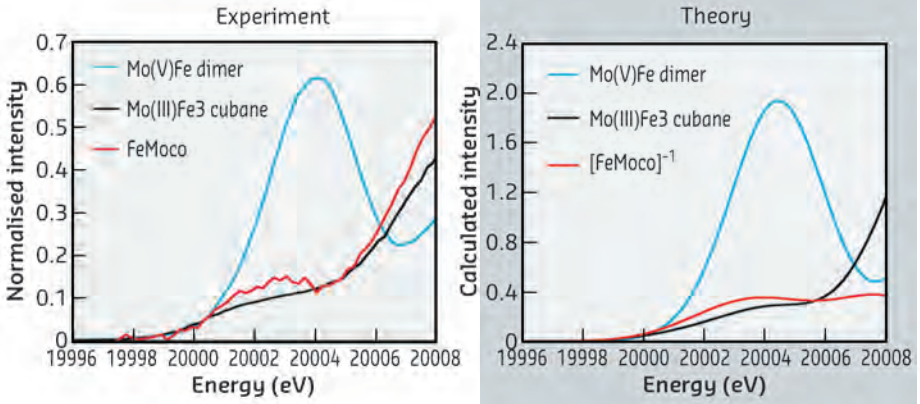

Fig. 24: A comparison of experimental and calculated HERFD Mo K-edge XAS data for FeMoco and reference model complexes.

References
[1] K.M. Lancaster, M. Roemelt, P. Ettenhuber, Y. Hu, M.W. Ribbe, F. Neese, U. Bergmann and S. DeBeer, *Science* **334**, 974-977 (2011).
[2] F.A. Lima, R. Björnsson, T. Weyhermüller, P. Chandrasekaran, P. Glatzel, F. Neese and S. DeBeer, *Phys. Chem. Chem. Phys.* **15**, 20911 (2013).

WHAT DRIVES OSCILLATIONS IN CO OXIDATION BY O_2 OVER RH/AL_2O_3 CATALYSTS?

Principal publication and authors
S.J.A. Figueroa (a,b) and M.A. Newton (a), *J. Catal.* **312**, 69 (2014).
(a) ESRF
(b) Now at Brazilian Synchrotron Light Source (LNLS), Campinas (Brazil)

Spontaneous oscillatory behaviour in heterogeneous catalysis is of considerable interest from fundamental and applied points of view; anticipating and controlling such behaviour is important to process engineering, as it may be highly problematic to process control and efficiency.

Previous studies of oscillations in CO oxidation over Rh/Al_2O_3 systems have resulted in differing opinions as to their source. Shanks and Bailey [1] concluded that oscillations arose from temperature fluctuations within the reactor, whereas Ioannides *et al.* [2] preferred redox processes within the Rh phase as their preferred explanation, though no technique directly sensitive to the oxidation state of the Rh was applied.

To resolve this situation a 5wt%Rh/Al_2O_3 catalyst was investigated during CO oxidation catalysis using synchronous application of Rh K edge dispersive EXAFS (at beamline **ID24**), diffuse reflectance infrared spectroscopy (DRIFTS) and mass spectrometry (MS), at sub-second time resolution. [3]

Figure 25a shows CO_2 production at varying temperatures when a stoichiometric ($2CO:O_2$) flow of reactive gas is passed over the Rh/Al_2O_3 catalyst. Rapid variations in CO_2 evolution that vary in period/magnitude are observed. **Figure 25b** shows (I) DRIFTS during the oscillatory behavior at 433K and (II) the difference between the maximum and minimum levels of CO_2 production. Linear, bridged and geminal carbonyls are observed but no relation to the oscillatory

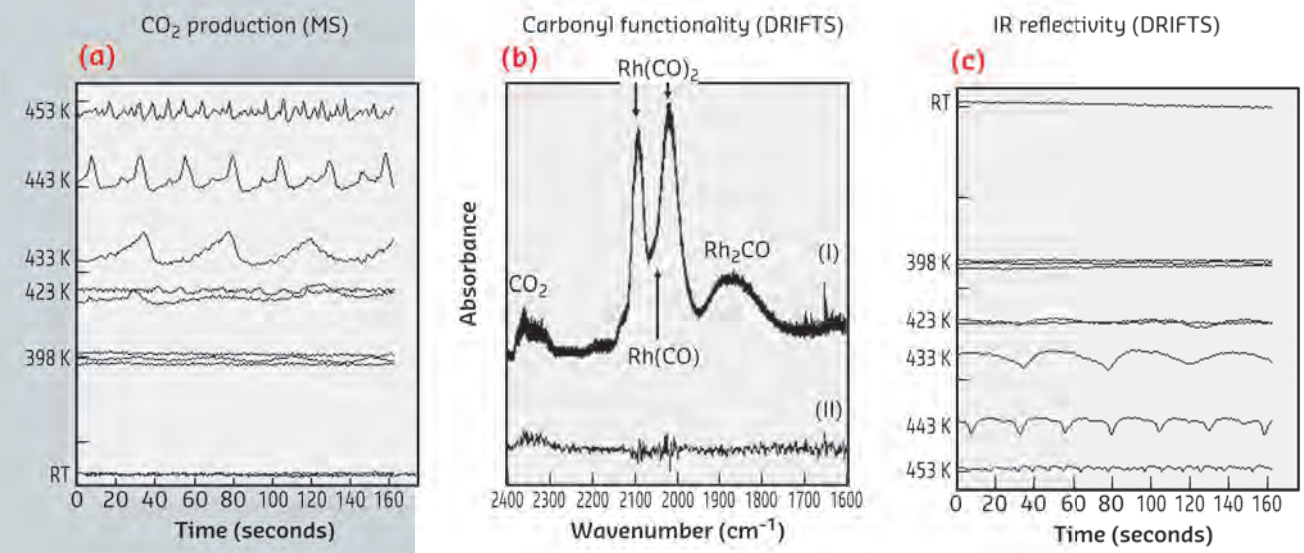

Fig. 25: a) Oscillations in CO_2 (MS) as a function of temperature. b) DRIFTS showing (I) carbonyl speciation present during oscillatory behaviour at 433K, and (II) the difference in spectra taken at points of maximal and minimal levels of CO_2 production. c) Temporal variation in overall infrared reflectivity.

behaviour observed. These species do show that Rh is present in at least two forms, reduced nanoparticles (Rh(CO) and $Rh_2(CO)$) and $Rh^I(CO)_2$ centres, but cannot inform us as to whether redox (Rh(0) to Rh (3+)) bi-stabilities are directing these events.

Figure 25c shows changes in infrared reflectivity (DRIFTS). Here we do observe variations that precisely match those observed in MS. These changes may have two origins: variations in surface temperature, or changes in the reflectivity of the Rh arising from a change from metallic nanoparticles to more oxidic entities. A precise correlation between these variations and the temperature of the sample can be established. However, this does not rule out variations (0 to +3) in the oxidation state of the Rh as the underlying source of the oscillations.

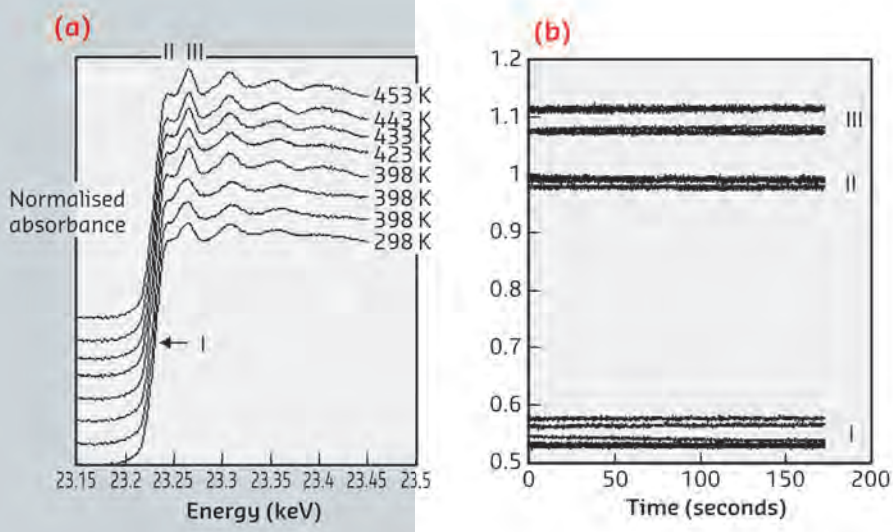

Fig. 26: a) Rh K edge XAFS at t=0 seconds within the CO oxidation experiment as a function of temperature. b) Temporal variation observed at the three points indicated in (a) within the XAFS envelope.

Figure 26 shows Rh K edge XAFS obtained at 0 seconds for each temperature. The XAFS envelope is different at each temperature reflecting changes in the balance between Rh in a metallic state and ($Rh^I(CO)_2$). However, the temporal variation of the Rh K edge position (I), the Rh white line (II) – both very sensitive to the Rh^0/Rh^{3+} ratio- and a second XANES feature (III) that indexes the Rh(0) nanoparticulate state (**Figure 26b**) again show no relationship to the oscillatory CO_2 production.

As such, neither the carbonyl functionality (DRIFTS) nor the oxidation state of the Rh (XAFS) are the sources of the oscillations. Furthermore, the relationship between the temperature of the sample (**Figure 25**) and the production of CO_2 shows that this cannot be the cause of the oscillations but rather a result of them. Therefore we have to search for another explanation that is invisible to both the DRIFTS and the Rh K edge EXAFS.

Previous studies [5] have shown that, alongside adsorbing molecular CO, in the regimes of Rh particle size and temperature investigated here, Rh nanoparticles also dissociate CO to yield adsorbed atomic carbon; a speciation invisible to infrared and Rh K edge XAFS. Also, the probability of CO dissociation as a function of temperature matches, in terms of onset and magnitude as a function of temperature, the oscillations in CO_2 production we observe.

Therefore, the evidence points to a unique mechanism based upon CO dissociation. This leads to an accumulation and periodic ignition of adsorbed carbon as the source of the oscillatory phenomena.

References
[1] B.H. Shanks and J.E. Bailey, *J. Catal.* **110**, 197 (1988).
[2] T. Ioannides, A.M. Efstathiou, Z.L. Zhang and X.E. Verykios, *J. Catal.* **156**, 265 (1995).
[3] M.A. Newton, *Topics in Catalysis* **52**, 1410 (2009).
[4] V. Matolin, M.H. Elyakhloufi, K. Masek and E. Gillet, *Catal. Letts.* **21**, 175 (1993).

RATE CAPABILITY ENHANCEMENT BY Ru DOPING IN HIGH VOLTAGE LITHIUM-ION BATTERY CATHODE MATERIAL $LiNi_{0.5}Mn_{1.5}O_4$

Lithium-ion batteries are the most common energy storage systems commercialised so far for applications in electric vehicles or hybrid electric vehicles. The application of Li-ion batteries in electromobility demands high volumetric as well as gravimetric energy and power densities which

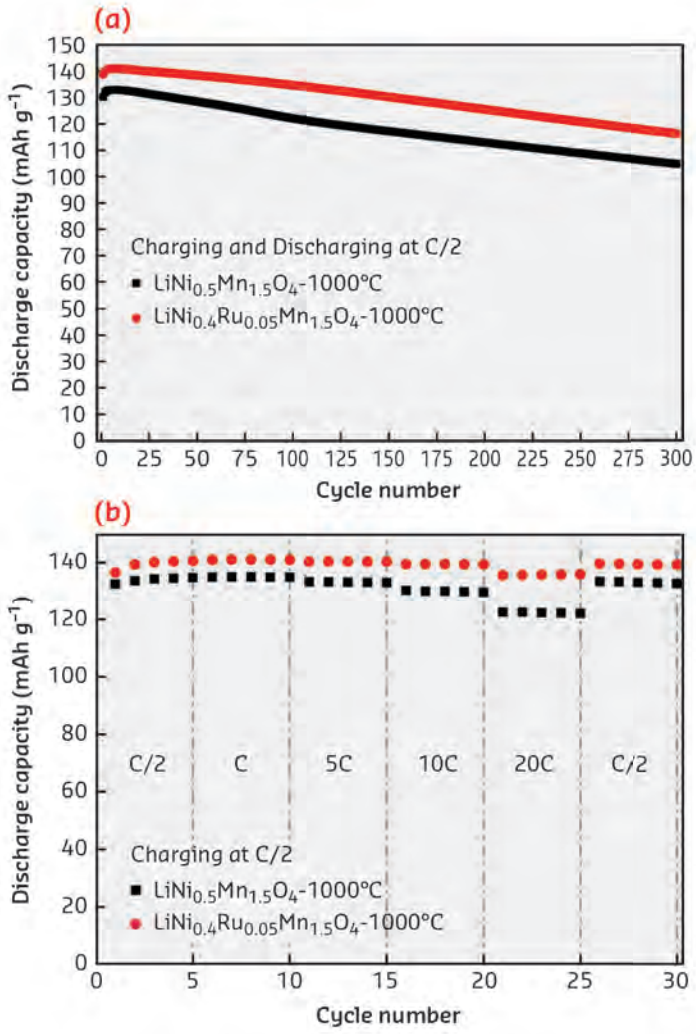

Fig. 27: a) Cycle number vs. discharge capacity plots at C/2 charge-discharge rate. b) Cycle number vs. discharge capacity plots at C/2 charge rate and varied discharge rates for Ru-doped and un-doped LNMO samples cycled between 3.5-5.0 V at room temperature.

Principal publication and authors
N. Kiziltas-Yavuz (a), A. Bhaskar (a), D. Dixon (a), M. Yavuz (a,b), K. Nikolowski (a,c), L. Lu (d), R. Eichel (e,f) and H. Ehrenberg (a,b), *J. Power Sources* **267**, 533-541 (2014).
(a) Karlsruhe Institute of Technology (KIT), Institute for Applied Materials - Energy Storage Systems (IAM-ESS), Eggenstein-Leopoldshafen (Germany)
(b) Helmholtz Institute Ulm (HIU) Electrochemical Energy Storage, Karlsruhe (Germany)
(c) Fraunhofer Institute for Ceramic Technologies and Systems IKTS, Dresden (Germany)
(d) National University of Singapore, Dept. of Mechanical Engineering (Singapore)
(e) Forschungszentrum Jülich, Institut für Energie- und Klimaforschung (IEK-9) (Germany)
(f) RWTH Aachen University, Institut für Physikalische Chemie (Germany)

References
[1] C.M. Julien and A. Mauger, *Ionics.* **19**, 951-988 (2013).
[2] A. Bhaskar, D. Mikhailova, N. Kiziltas-Yavuz, K. Nikolowski, S. Oswald, N.N. Bramnik and H. Ehrenberg, *Progress in Solid State Chemistry* **1**, 1-21 (2014).

are factors often determined by the positive electrode or cathode materials [1]. Nowadays, most of the commercial lithium-ion batteries employ layered $Li(Ni,Co,Mn)O_2$ and spinel-type $LiMn_2O_4$ (working at ~4 V) as cathode and graphite as anode. However, the spinel type cathode materials possess high cycling stability in comparison to the layered counterpart. Spinels have a general formula AB_2O_4, where the oxygen atoms occupy 32*e* site ($Fd\bar{3}m$ space group) and form a face-centred cubic close packing. The A cations occupy tetrahedral 8*a* site, whereas the B cations are located in octahedral 16*d* site. The unoccupied octahedral 16*c* site together with the 8*a* tetrahedral site forms a three dimensional pathway for the lithium-ion diffusion in these materials. Ni-doped Mn spinel with the composition $LiNi_{0.5}Mn_{1.5}O_4$ (LNMO) is considered as highly promising cathode material due to its large reversible capacity obtained at a high operating voltage of around 4.7 V where the reversible $Ni^{2+} \leftrightarrows Ni^{4+}$ redox reactions take place [2]. In this work, we have proved that doping of the LNMO with Ru further increases the rate capability and cycling stability. The Ru doped spinel (LNRMO) with the composition $LiNi_{0.4}Ru_{0.05}Mn_{1.5}O_4$ was prepared by citric acid-assisted sol-gel method with heat treatment at 1000°C for the final compound. The material has an initial capacity of ~139 mAh g^{-1} and capacity retention of 84% after 300 cycles at C/2 charging-discharging rate between 3.5-5.0 V vs. Li/Li^+. The achievable discharge capacity at 20C for a charging rate of C/2 is ~136 mAh g^{-1} (~98% of the capacity delivered at C/2). These results are summarised in **Figure 27**. The Ru doping inside the spinel material was confirmed by XAS studies carried out at beamline **BM23**. From the XANES analysis of the Ru K edge data, Ru was found to be in +4 oxidation state. The EXAFS analysis shows that Ru has a nearest coordination bond distance of 2.02 Å and 2.94 Å with oxygen and transition metal Ni or Mn. This conclusively proves that the Ru exists inside the spinel lattice (**Figure 28**).

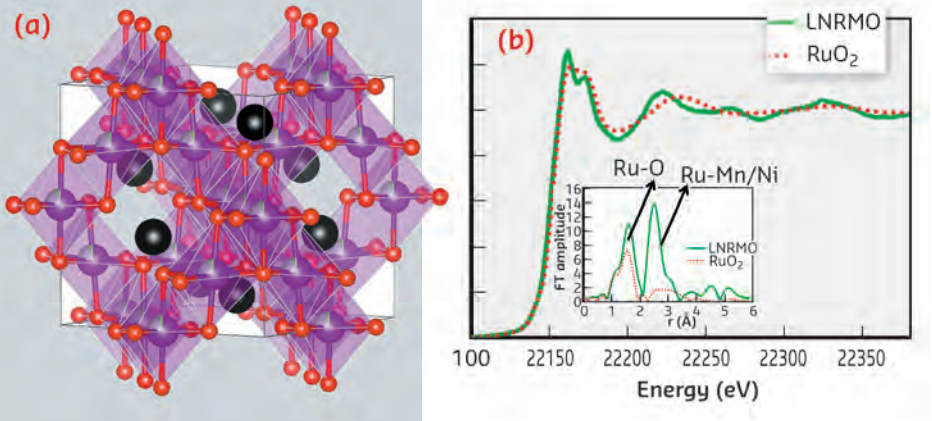

Fig. 28: a) Atomic cluster of $LiNi_{0.4}Ru_{0.05}Mn_{1.5}O_4$ spinel (Red: oxygen; purple: Ni, Mn and Ru, black: Li). b) The Ru K-edge XANES of LNRMO compared to the reference RuO_2, reveals that the oxidation state of Ru is +4. The Fourier transform of the EXAFS clearly shows a strong second peak confirming Ru bonding to the transition metal (Mn/ Ni).

Principal publication and authors
A. Di Cicco (a), F. Iesari (a), S. De Panfilis (b), M. Celino (c), S. Giusepponi (c) and A. Filipponi (d), *Phys. Rev. B* **89**, 060102(R) (2014).
(a) Università di Camerino (Italy)
(b) IIT, Roma (Italy)
(c) ENEA Casaccia (Italy)
(d) Università dell'Aquila (Italy)

LOCAL FIVEFOLD SYMMETRY IN LIQUID AND UNDERCOOLED Ni

Perfect crystal structures can contain pyramids, cubes, or hexagons, but not pentagons. The five-fold symmetry of a pentagon is indeed impossible to replicate over and over in space to make a conventional crystal. Most solid metals actually form closely packed cubic crystals, but in the 1950s, calculations showed that metals such as copper, gold, silver, and lead might form liquids with local five-fold symmetry, in the form of icosahedral structures. The presence of such close-packed fivefold configurations, favoured by energetic considerations, was considered as a possible explanation for the peculiar undercooling properties of liquid metals. Crystal nucleation is hampered by the positive liquid-crystal interfacial energy, resulting in the

possibility of bringing a liquid sample into a metastable (undercooled) molten state below the melting temperature. However, five-fold ordering in metals is not entirely unprecedented. Quasicrystals are metal alloys that have a peculiar semi-crystalline five-fold symmetry that never quite repeats itself. The determination of the local structure in liquid matter is quite a challenging task. Most techniques (X-ray and neutron diffraction) can only find the relative positions of two atoms at a time, which makes it difficult to pin down the five-fold symmetry prediction. On the other hand, X-ray absorption spectroscopy (XAS) is a technique particularly sensitive to short range ordering and able to determine also three-body distributions. In this work, we used the ESRF XAS beamline [1] (now **BM23**) to perform XAS measurements combined with complementary techniques, such as fixed energy X-ray absorption temperature scans and X-ray diffraction. Reaching extremely high temperatures, we have investigated the short-range structure in solid and liquid Ni, following a previous study on liquid Cu [2] and other metals. Samples were prepared from a submicrometric Ni and alumina (Al_2O_3) powder mixtures with a 1:20 mass ratio that were suspended in alcohol, filtered, and pressed into 100-μm-thick, 13-mm-diameter pellets. The furnace consisted of a 130-mm-diameter cylindrical Pyrex glass vessel with a suitable window for X-rays. The pellets were placed inside the crucible of the furnace and the heat treatments were performed under high-vacuum conditions (P = 10^{-5} mbar). Temperature was monitored using a high-temperature pyrometer. X-ray absorption at fixed energy as a function of temperature is shown in **Figure 29**. Upon cooling, the absorption remains stable about 300 K below the melting point, showing the deep undercooling properties of small metal particles. The relatively broader decrease in absorption is associated with the progressive nucleation of the broad mass droplet distribution in the sample. Analysis of this part of the scan using previous methods allows us to extract the Ni nucleation rate in a relatively wide temperature range (**Figure 29**, inset). High quality EXAFS spectra have been collected in the solid phase at 1493 K, in the stable liquid phase at 1733 K and in the undercooled liquid phase at 1493 K. The extracted signals are compared in **Figure 30**.

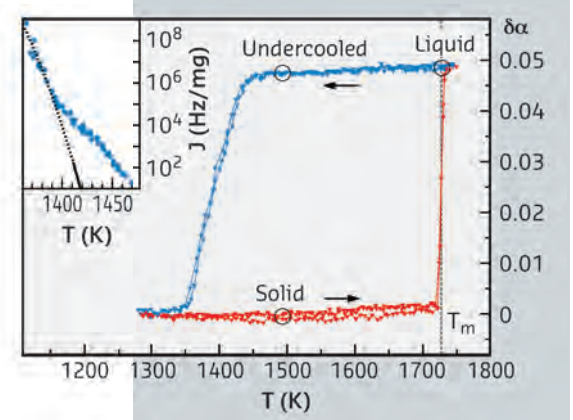

Fig. 29: X-ray absorption temperature scans of the Ni sample. The change in the absorption coefficient at E = 8.338 keV is plotted with respect to the solid Ni absorption level during repeated thermal cycles. Inset: temperature dependence of the Ni nucleation rate from the cooling scan.

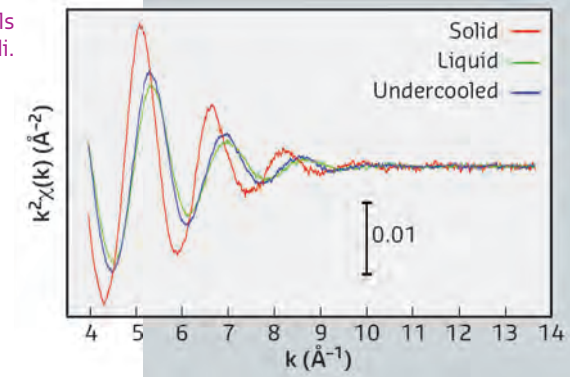

Fig. 30: EXAFS extracted signals for different phases of Ni.

Using a sophisticated data-analysis technique, known as Reverse Monte Carlo (RMC), coupled with GNXAS multiple-scattering calculations, it has been possible to create a model structure for the liquid reproducing our experimental data with some constraints. Moreover, *ab initio* computer molecular-dynamics (MD) simulations provided further insights to the determination of the local structure. From both RMC and MD configurations we were able to calculate different physical quantities, such as bond angle distribution functions. Two different approaches have been used to analyse the local geometry: the common-neighbour analysis (CNA) and the calculation of spherical harmonic invariants, giving consistent results. The fractions of fivefold nearly icosahedral configurations found were in the range 14-18% for Ni in the liquid undercooled phase and 11-14% for liquid Ni just above the melting temperature. The emerging picture for the liquid structure is that of a mixture of nearly icosahedral structures embedded in a disordered network mainly composed of fragments of highly distorted icosahedra, structures reminiscent of the crystalline phase and other configurations.

References
[1] A. Filipponi, M. Borowski, D.T. Bowron, S. Ansell, S. De Panfilis, A. Di Cicco and J.P. Itié, *Rev. Sci. Instr.* **71**, 2422 (2000).
[2] A. Di Cicco, A. Trapananti, S. Faggioni and A. Filipponi, *Phys. Rev. Lett.* **91**, 135505 (2003).

SOFT CONDENSED MATTER

This chapter presents a selection of articles related to Soft Matter Science published during the past year. A particular emphasis in this edition is on the *self-assembly* that is at the origin of many fascinating features exhibited by soft matter systems. From simple surfactant molecules to highly tailored complex organic molecules and biomolecules, scattering experiments once again have proved to be unique for unravelling the complex pathways and mechanisms of self-assembly processes. Indeed, advanced modelling and computer simulations were essential for the extraction of quantitative information from these scattering experiments, which again proved to be a winning combination in the investigation of complex systems. Such studies, driven primarily out of fundamental curiosity, are now approaching closer to the engineering of smart materials and devices pertinent to modern technology. Needless to say that only a small fraction of the exciting results published during the year made it into this chapter. To mention a few notable omissions: the millisecond dynamics of protein upload in multicompartment lipid cubic nanocarriers (B. Angelov *et al.*, *ACS Nano* **8**, 5216, 2014); pressure induced re-entrant phase separation in concentrated protein solutions (J. Moeller *et al.*, *Phys. Rev. Lett.* **112**, 028101, 2014), nanoscale structure of Si/SiO_2/organics interfaces (H.-G. Steinrueck *et al. ACS Nano* **8**, 12676–12681, 2014), etc.

On the technical front, very impressive progress has been made during the year. The upgrade beamline project UPBL9a was successfully completed at ID02 and the new beamline reopened for Users in July with unique capabilities for ultra low angle scattering. The upgrade beamline was officially inaugurated during the ESRF Science Advisory Committee meeting on the 06 November. The sister project UPBL9b at ID09 is progressing well, the combined time-resolved X-ray emission spectroscopy and wide-angle scattering setup has been commissioned. New focusing optics and an area detector are expected to be in place by 2016, when the beamline will become fully dedicated to time-resolved experiments. A new diffractometer for liquid scattering will be installed at the soft interfaces station of ID10. In addition, a notable step has been made in the three-dimensional analysis of highly-organised surface structures by means of grazing-incidence small-angle scattering (E.A. Chavez Pandura *et al.*, *ACS Appl. Mater. Interfaces* **6**, 2686, 2014). X-ray photon correlation spectroscopy has made new inroads into the probing of atomic dynamics in glasses (B. Ruta *et al.*, *Nature Communications* **5**, 3939, 2014), a publication summarised in the chapter on Dynamics and extreme conditions. At ID13, a pioneering serial protein crystallography experiment was performed by an international team (P. Nogly *et al.*, IUCr J., 2, doi: 10.1107/S2052252514026487,(2015)). Furthermore, ID13 has received a state-of-the-art Eiger 4M detector from Dectris that is expected to revolutionise nanodiffraction experiments.

Also during the year, ID09B had a successful beamline review in May. The scientific staff of the Structure of Soft Matter Group have relocated to the Science Building, sharing the third floor with the Large Scale Structures Group of the ILL. The Partnership for Soft Condensed Matter (PSCM) has attracted several collaborative partners from academia and their contracts are currently being finalised. New services offered to soft matter industrial customers using techniques such as SAXS, WAXS and microdiffraction are yielding good dividends. Finally, the local organisation for the next International Soft Matter Conference in 2016 (ISMC2016) is advancing well. This meeting, under the auspices of the SOFTCOMP network of excellence will be jointly organised by the ESRF and ILL together with Grenoble University, CEA and CNRS.

T. NARAYANAN

Inside view of the 34 m detector tube at ID02. The detector wagon at the far end travels along the rails.

FROM SPHERES TO WORMS: MONITORING TRANSFORMATION KINETICS OF SURFACTANT MICELLES USING TIME-RESOLVED SAXS

Principal publication and authors
G.V. Jensen (a), R. Lund (b), J. Gummel (c), T. Narayanan (c) and J.S. Pedersen (a), *Angew. Chem. Int. Ed.* **53**, 11524–11528 (2014).
(a) Department of Chemistry and Interdisciplinary Nanoscience Center (iNANO), Aarhus University (Denmark)
(b) Department of Chemistry, University of Oslo (Norway)
(c) ESRF

Since their discovery about a century ago, surfactant micelles have been a topic of great interest in both academic and technological research. Surfactant molecules consist of distinct hydrophobic and hydrophilic parts that, in water, lead to aggregation into a wide variety of interesting and highly dynamic nanostructures. The shape and size of the micelles depend on the type of surfactant and conditions such as temperature and solvent composition. Due to the widespread applications ranging from detergents and additives in daily products to advanced applications in biotechnology and nanotechnologies [1], insight into their fundamental behaviour is still highly relevant.

Equilibrium structures of surfactant micelles have been studied extensively, but the pathways of transitions between different morphologies are still not well understood. Micelle kinetics usually takes place in the millisecond and even sub-millisecond regime. This makes it exceedingly difficult to monitor the structural evolution in real time, due to the lack of methods with both nanostructural resolution and millisecond temporal resolution.

Here we use the high brilliance of the ID02 beamline to monitor the kinetics of the transformation from spherical to worm-like micelles induced by adding sodium chloride (NaCl) to an aqueous solution of the archetypical anionic surfactant, sodium dodecyl sulphate (SDS). In aqueous solution SDS forms small spherical or ellipsoidal micelles due to the repulsion between the charged head groups which favours a large surface curvature. By adding salt, the repulsions are screened, and a smaller curvature is favoured, leading to a transition into flexible, "worm-like" cylinders (**Figure 31a**). Using a stopped-flow apparatus for rapid mixing, combined with the small-angle X-ray scattering (SAXS) setup at ID02, we were able to follow the structural details of the process

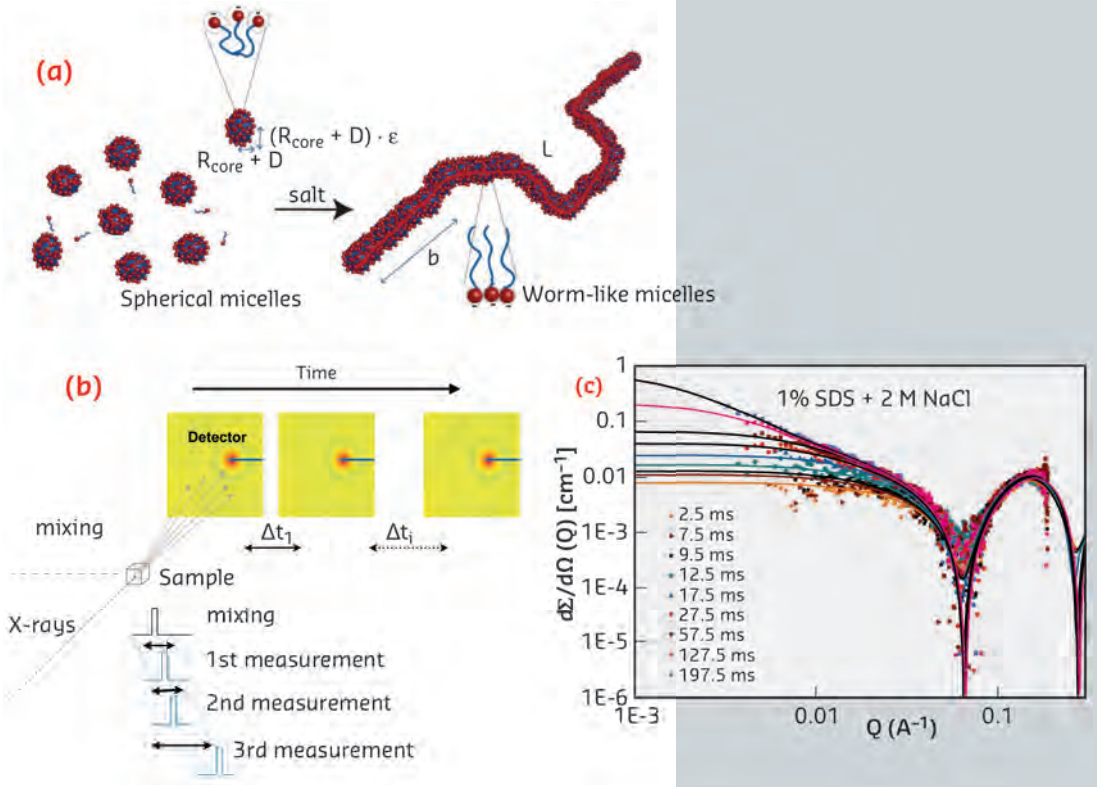

Fig. 31: a) Transition from spherical to worm-like SDS micelles upon addition of salt. b) Experimental setup where the X-ray pulse is synchronised with the sample mixing. Using a stroboscopic-type sampling, millisecond time resolution was obtained. c) Scattering curves: Intensity vs. modulus of the momentum transfer vector, Q, as a function of time. The data are described using a model for core-shell ellipsoids and worm-like cylinders (lines).

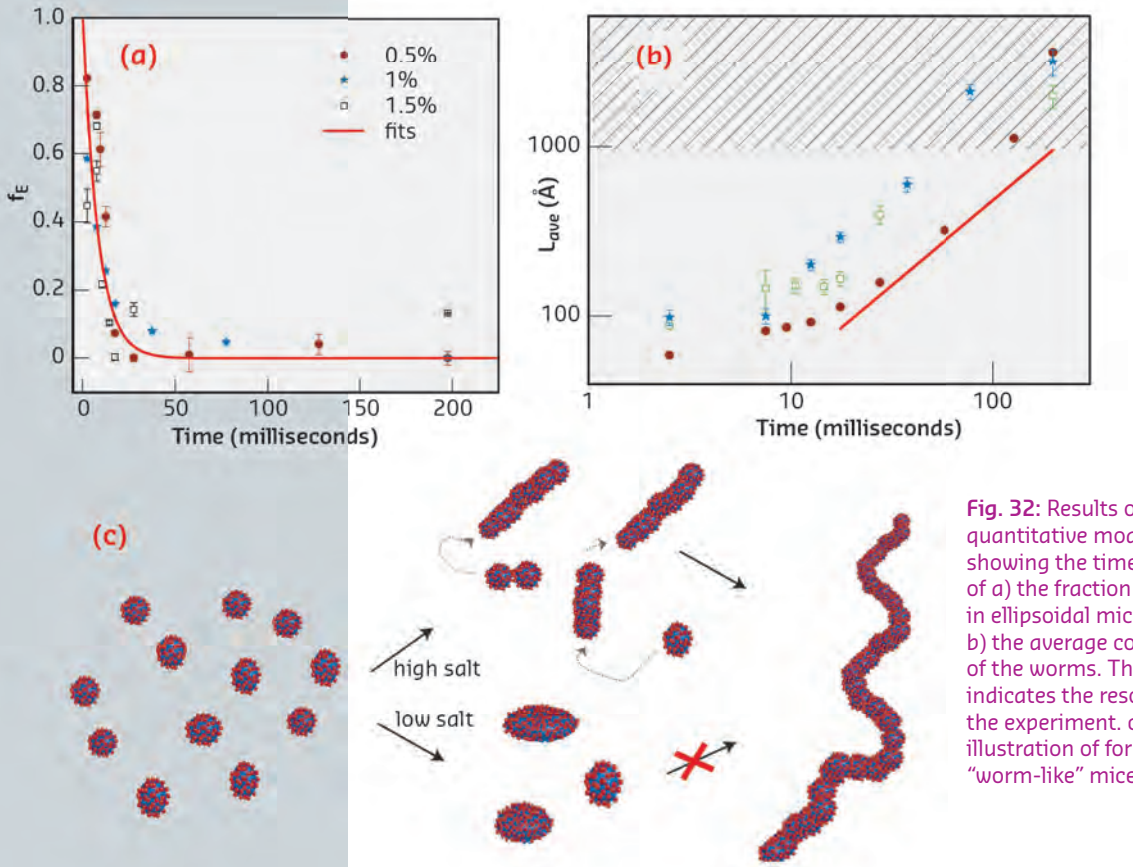

Fig. 32: Results of the quantitative model fit analysis showing the time dependence of a) the fraction of surfactant in ellipsoidal micelles, and b) the average contour length of the worms. The hatched area indicates the resolution limit of the experiment. c) Schematic illustration of formation of "worm-like" micelles.

over time. The time gap between data frames was limited by the detector read-out time, and a stroboscopic-type sampling was employed to capture the rapid kinetic process (**Figure 31b**). By repeating the mixing sequence several times, varying the delay between the time of mixing and collection of the first data frame, we obtained sampling with only a few milliseconds increment.

Figure 31c depicts the scattering curves obtained after mixing a 1% SDS solution with 2 M NaCl (1:1). The intensity rapidly increases, accompanied by a Q^{-2} behaviour at low Q at later times, demonstrating formation of worm-like micelles. To quantify the results, the data were analysed using a model consisting of a linear combination of ellipsoidal and worm-like core-shell particles [2]. The result, in terms of fraction of surfactant in ellipsoidal micelles and contour length of the worm-like micelles, is plotted in **Figure 32**.

The fraction of ellipsoids approximately follows a single exponential decay, $\varphi_{ell}(t) \sim \exp(-t/\tau_E)$, with a time constant of about τ_E = 10 ms (**Figure 32a**). This decay is followed by growth in the contour length of the worms. Interestingly, the growth approximately follows a linear law $L_{ave} \sim t$ (**Figure 32b**). This resembles step-wise growth polymerisation reactions where a linear relationship between mean molecular weight and time is observed [3]. In such reactions, the polymers grow through addition reactions at the chain ends, indicating that a similar mechanism applies here. This suggests a growth mechanism of micelle fusion at the cylinder ends, where the curvature and surface energy is highest (**Figure 32c**). At a lower NaCl concentration of 1 M, the repulsion between the surfactant head groups is less well screened. The micelles do not undergo a transition into worms, but a slight elongation (within ~10 ms) is observed (**Figure 32c**).

In conclusion, by time-resolved SAXS, we have been able to shed new light on an old classical surfactant system and obtain insight into morphological transition of micelles. Through a quantitative analysis, we deduced that the kinetic pathway of the transition from spherical to worm-like micelles involves successive fusion events, bearing similarities to classical polymerisation reactions.

References
[1] D. Attwood and A.T. Florence, *Surfactant systems, their chemistry, pharmacy and biology*, Chapman and Hall, New York (1983).
[2] J.S. Pedersen and P. Schurtenberger, *Macromolecules* **29**, 7602 (1996).
[3] P.J. Flory, Principles of polymer chemistry, Cornell University Press (1953).

NON-EQUILIBRIUM COLLECTIVE DYNAMICS IN PHOTO-EXCITED LIPID MEMBRANES

Principal publication and authors
T. Reusch (a), D.D. Mai (a), M. Osterhoff (a), D. Khakhulin (b), M. Wulff (b) and T. Salditt (a), *Physical Review Letters* **111**, 268101 (2013).
(a) Institut für Röntgenphysik, Georg-August-Universität Göttingen (Germany)
(b) ESRF

All living systems are intrinsically out of thermal equilibrium. Their metabolism results in a multitude of local force centres on a molecular scale. 'Active' molecular transport in cells, motor proteins, and shape transformations of biological membranes are just some of the most prominent examples. From a fundamental point of view, the understanding of how a local energy release may change the properties of a soft biomolecular assembly remains elusive in many cases. We wanted to investigate how a system with long-range non-covalent interactions relaxes back to the equilibrium state after it has been driven out of equilibrium by external forces and the extent to which collective modes of many interacting biomolecules are involved.

For the important case of membranes, considered to be Nature's most important interface, non-equilibrium fluctuations can be expected to be driven by active proteins or external forces. We have now shown that photo excitation of fluorophor-labelled lipids in a membrane can lead to a very characteristic collective response and have studied the pathway and time scales on which structural dynamics evolves.

In the experiment, we monitored the shape fluctuations in a stack of phospholipid bilayers mainly composed of the model lipid DOPC (1,2-dioleoyl-sn-glycero-3-phosphatidylcholine), deposited on a quartz surface in solution. To excite the system, a short picosecond laser pulse was used, matched in wavelength to the absorption band of fluorescently labelled lipids (Texas-red), which were mixed into the membranes, as routinely used for optical fluorescence experiments. After energy uptake, the system's response was probed by well defined picosecond X-ray pulses. The characteristic diffraction pattern of the membrane stack (non-specular diffuse scattering) was then recorded as a function of time delay, from a few picoseconds to several microseconds, before the procedure was repeated to gain sufficient statistics. **Figure 33** summarises the experiment schematically.

From the data, we extracted the temporal evolution of the height correlation functions describing the lipid bilayer undulations after excitation (**Figure 34**). The results indicate that pulsed laser illumination even at quite moderate peak intensities of about 10^5 W/cm^2 leads to significant changes of the in plane membrane correlation length by up to 50% as well as the excitation of transient conformal undulation modes of a well defined lateral wavelength. The

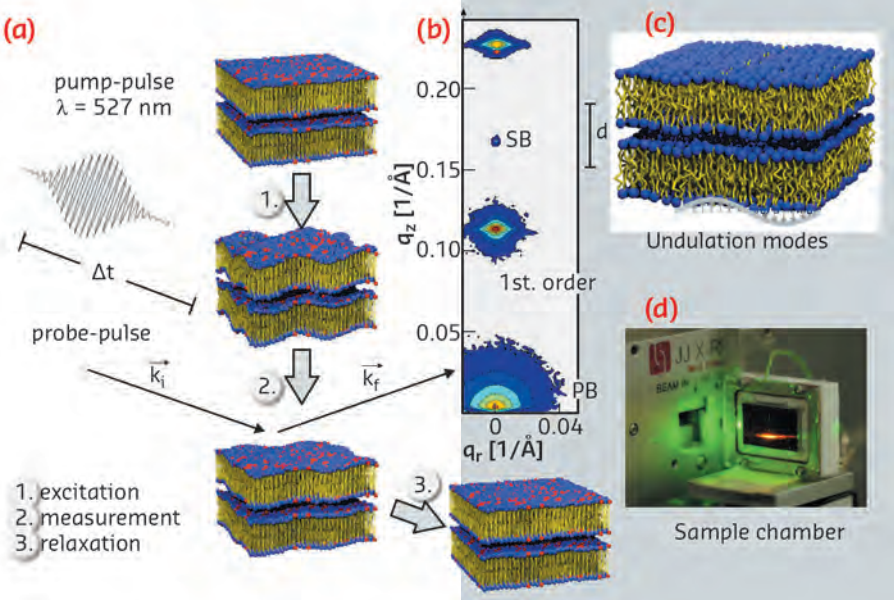

Fig. 33: a) Schematic of the laser pump/X-ray probe experiment at beamline ID09B on the multilamellar lipid stack in the fluid phase. The temporal evolution of membrane undulations was studied in response to a short pulse excitation, by recording the diffuse scattering pattern and line-shape analysis of the individual lamellar reflections. b) Example of a lamellar diffraction pattern with primary beam (PB), specular beam (SB), and the two first lamellar diffraction orders. c) From the two-dimensional distribution, the temporal evolution of the lateral and vertical correlation functions are extracted. d) Sample chamber for oriented Texas-Red labelled lipid multilayers fully immersed in solution.

observed phenomena evolve on nano- to microsecond timescales after optical excitation, and can be described in terms of a modulation instability in the lipid multilamellar stack.

In simple terms, the energy uptake at the molecular level leads to non-thermalised local vibrations which can be regarded as "local heat", before the long-range undulation modes have equilibrated. In such a transient state, the lipid molecules tend to expand their inter-molecular distances, but on short time scales this motion is quenched. For compensation, the membranes buckle, opening up a faster relaxation mechanism than the thermal expansion of the entire system. The results may have important implications for many other optical fluorescence experiments, in which it is tacitly assumed that the supra-molecular structural state of the sample remains unchanged, apart perhaps from more or less negligible heat generation. After all, the excitation of embedded fluorophores in biomolecular assemblies is a very common tool in biomolecular and life science. Similar collective dynamic effects may thus occur in many photo labelled soft matter sample systems, effectively driving the structure away from thermal equilibrium.

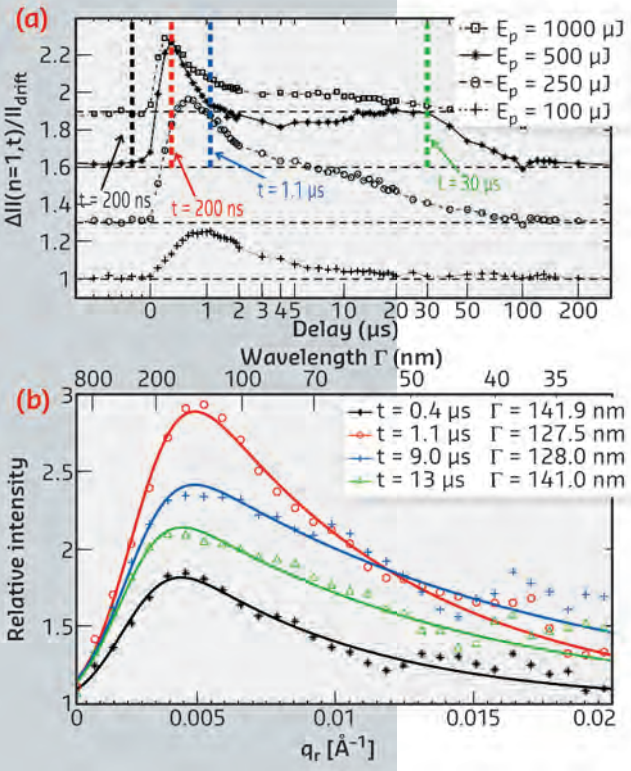

Fig. 34: a) Evolution of the diffuse scattering intensity as a function of time after excitation. The increase reflects the transient increase in membrane undulations. b) A characteristic undulation mode with a wavelength band centred around 130 nm appears, reaching its maximum about 1 µs after excitation.

Importantly, the non-equilibrium effects do not directly manifest themselves on the molecular length scale, but rather on mesoscopic scales via collective mechanisms. In the present example, local molecular energy uptake by absorption of photons in the membrane leads to peculiar long-range mesoscopic changes observable over microseconds before the sample has reached equilibrium again. The energy dissipation pathway involves a characteristic sequence of modes at length scales of a few hundred nanometres. We speculate that this may be a quite general phenomenon, not only applicable to optical excitation, but also to other excitation mechanisms and local force centres occurring in active states of biomolecular and soft matter.

Principal publication and authors
S.-H. Lim (a), H.-S. Jang (a), J.-M. Ha (a), T.-H. Kim (b), P. Kwasniewski (c), T. Narayanan (c), K. S. Jin (d) and S.-M. Choi (a), *Angew. Chem. Int. Ed.* **53**, 12548 (2014).
(a) Department of Nuclear and Quantum Engineering, KAIST (Rep. of Korea)
(b) Korea Atomic Energy Research Institute (Rep. of Korea)
(c) ESRF
(d) University of Science and Technology (Rep. of Korea)

TWO-DIMENSIONAL BINARY SUPERLATTICE OF A SINGLE-WALLED CARBON NANOTUBE/CYLINDRICAL-MICELLAR SYSTEM

Binary or multicomponent superstructures of nanoparticles, are of great interest for potential applications such as optical and electronic devices, sensing, and energy storage as well as their own scientific merit [1]. Their synthesis may provide new emerging properties through synergetic coupling between different types of nanoparticles. Exciting progress has been made in the fabrication of binary spherical-nanoparticle superlattices with various symmetries by using an interplay of entropy and van der Waals,

electrostatic, and other interactions. However, systematic experimental studies on the formation of binary superlattices by mixtures of two different types of 1-D nanoparticles have been very rare, and the reported structures have been limited to simple liquid-crystalline structures. Here, a highly-ordered and highly-aligned binary superlattice of 1-D nano-objects is demonstrated.

One approach to the synthesis of highly-ordered binary 1-D nanoparticle superlattices is to first find conditions under which 1-D nanoparticles of one type self-assemble into a highly ordered superlattice, and then to add another type of 1-D nanoparticles into the preformed superlattice so that the second type of 1-D nanoparticles can collectively self-assemble with the first type of 1-D nanoparticles. Hydrophilically functionalised single-walled nanotubes (p-SWNTs [2]) with a diameter of 5 nm were added to a solution of the nonionic surfactant $C_{12}E_5$ in water with a fixed $C_{12}E_5$/water mixing ratio (45:55 by weight) at which the $C_{12}E_5$/water solution shows a highly ordered hexagonal phase (hexagonally packed cylindrical micelles with a diameter of 4.44 nm) at low temperature. Small-angle X-ray scattering (SAXS) measurements from the $C_{12}E_5$/water (45:55) and p-SWNT/$C_{12}E_5$/water (10:45:55) systems performed at beamline **ID02** (Figure 35) show that a new sharp peak appeared at q = 0.715 nm^{-1}, which has a ratio of 1:√3 with the peak at q=1.242 nm^{-1}. In fact, all the SAXS peaks of p-SWNT/$C_{12}E_5$/water are directly coupled to each other with specific peak-position ratios (1:√3:2:√7:3:√12:√21). The new scattering peaks in the p-SWNT/$C_{12}E_5$/water system arise from correlations between p-SWNTs, which was confirmed by a contrast-matched small-angle neutron scattering experiment. The coupled peak-position ratios and the origin of new peaks in the SAXS intensity indicate that the mixture forms a highly ordered intercalated hexagonal binary superlattice of p-SWNTs and $C_{12}E_5$ cylinders, in which a hexagonal array of p-SWNTs is embedded in a honeycomb lattice of $C_{12}E_5$ cylinders.

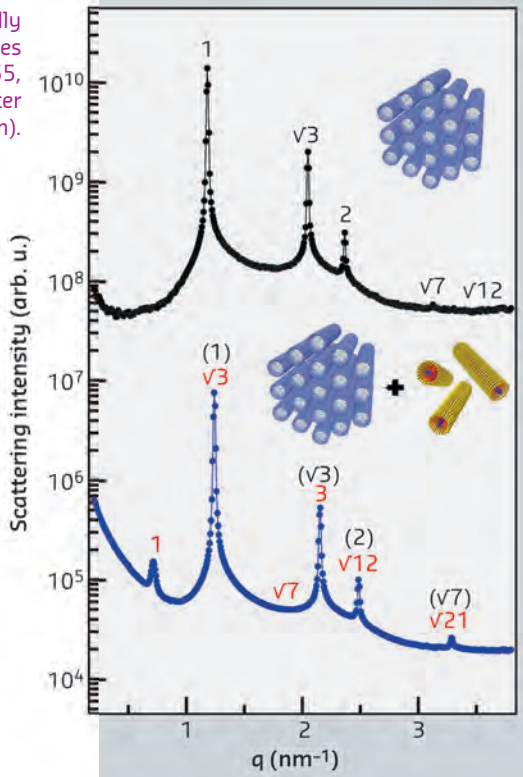

Fig. 35: a) Azimuthally averaged SAXS intensities of $C_{12}E_5$/water (45:55, top), p-SWNT/$C_{12}E_5$/water (15:45:55, bottom).

To unequivocally identify the structure, we carried out additional SAXS measurements at beamline **ID02** for the mixture under an oscillatory shear (Figure 36 a,b). The p-SWNT/$C_{12}E_5$/water loaded in a temperature-controlled shear cell was slowly cooled down from the isotropic phase (30°C) to the intercalated hexagonal phase (19°C) under an oscillatory shear with a shear stress of 500 Pa and an oscillation frequency of 5 Hz. The 2-D SAXS patterns measured along the radial direction are highly anisotropic; all the scattering peaks were found along the direction perpendicular to the flow direction. The 2-D SAXS pattern measured along the tangential direction shows clear six-fold symmetries. These results unarguably confirm that the p-SWNT/$C_{12}E_5$/water indeed forms the intercalated hexagonal binary superlattice (Figure 36c). When p-SWNTs are added to the hexagonally packed $C_{12}E_5$ cylindrical-micellar system, some $C_{12}E_5$ cylinders are replaced with p-SWNTs in such a way that the free-volume entropies for both p-SWNTs and $C_{12}E_5$ cylinders are

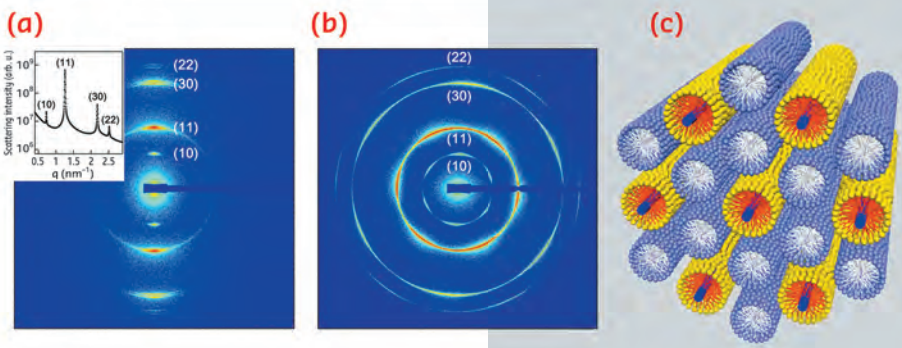

Fig. 36: SAXS Intensities of p-SWNT/$C_{12}E_5$/water aligned by an oscillatory shear, measured along the radial (a) and tangential (b) directions. c) Schematic illustration of the intercalated hexagonal binary superlattice of p-SWNT/$C_{12}E_5$/water.

References
[1] J.J. Urban, D.V. Talapin, E.V. Shevchenko, C.R. Kagan and C.B. Murray, *Nat. Mater.* **6**, 115 – 121 (2007).
[2] T.H. Kim, C. Doe, S.R. Kline and S.M. Choi, *Adv. Mater.* **19**, 929 – 933 (2007).

maximised, resulting in the intercalated hexagonal binary superlattice. The alignment was maintained for more than 24 hours. Although there have been many examples of highly oriented SWNT systems, most of which had no specific symmetry in the cluster of SWNTs, this structure is the first example of a highly oriented SWNT superstructure with hexagonal symmetry. The understanding obtained in this study may provide new insight for engineering highly-ordered binary superlattices of 1-D nanoparticles with new synergetic functionalities such as metallic, semiconducting, and magnetic nanorods, which are of great current interest.

SOLVENT EFFECTS PROMOTE TRIPLE HELIX FORMATION IN AMPHIPHILIC DISCOTICS

Principal publication and authors
M.A.J. Gillissen (a,b), M.M.E. Koenigs (a,b), A.J.H. Spiering (a), J.A.J.M. Vekemans (a), A.R.A. Palmans (a,b), I.K. Voets (a,b) and E.W. Meijer (a,b), *J. Am. Chem. Soc.* **136**, 336-343 (2014).
(a) Laboratory of Macromolecular and Organic Chemistry, TU Eindhoven (The Netherlands)
(b) Institute of Complex Molecular Systems, TU Eindhoven (The Netherlands)

Self-assembling synthetic molecules in water is of great interest for the development of functional soft matter and finds applications in regenerative medicine and sensors. Defining rules for effective self-assembly in water with the ability to control the shape and function of the supramolecular structures formed is, however, less trivial. A delicate balance between hydrophobic effects and other non-covalent interactions is often required but not easy to achieve.

With the help of small-angle X-ray scattering (SAXS) at beamline ID02, in combination with circular dichroism (CD) spectroscopy and cryogenic transmission electron microscopy (cryo-TEM), we have now unravelled how the self-assembly behaviour in water of an amphiphilic discotic molecule (**Figure 37**, middle) is affected by the presence of isopropanol (IPA), added to enhance its solubility. The molecular structure of the discotic amphiphile is designed to form bundled structures in H_2O (**Figure 37**, right) and incorporates both hydrophilic/hydrophobic peripheral side chains and a core that strongly aggregates via π–π interactions. In pure IPA, the hydrophobic effect is absent and only π–π interactions are operative, resulting in one-dimensional helical fibres (**Figure 37**, left).

The behaviour of the discotic amphiphile was investigated as a function of solvent composition in IPA–H_2O mixtures and temperature. Remarkably, three distinct structural regimes were detected with all techniques (**Figure 38**). SAXS showed that a 1D helical fibre was present at high IPA concentration, evidenced by a scattering curve typical for long elongated objects with a homogenous electron length density (regime III). The addition of water induced the formation of small, bundled aggregates, showing a signature scattering curve for core–shell assemblies with a low aspect ratio (regime II). At high water content, long, one-dimensional core–shell assemblies are formed, consisting of 3-4 fibres in the cross-section. Because the discotics have a flexible propeller shape and are never completely flat, the most likely conformation is a triple helix of helices. The results obtained by SAXS measurements were corroborated by cryo-TEM measurements: short fibres were observed for regime II and long fibres for regimes I and III. CD spectroscopy showed strong Cotton effects in all three regimes, confirming the presence of helical aggregates.

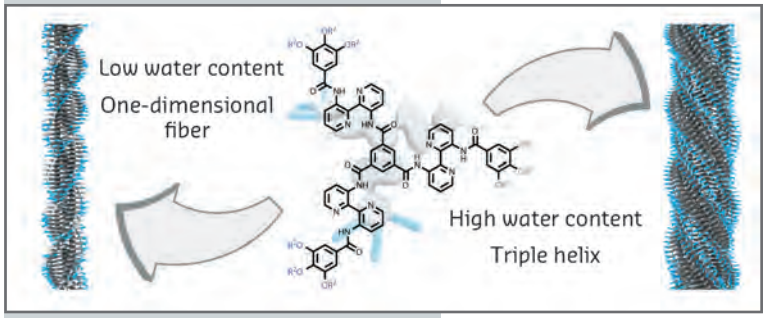

Fig. 37: Self-assembly of an amphiphilic discotic into (left) one-dimensional helical fibres at low water content and (right) triple helical structures at high water content.

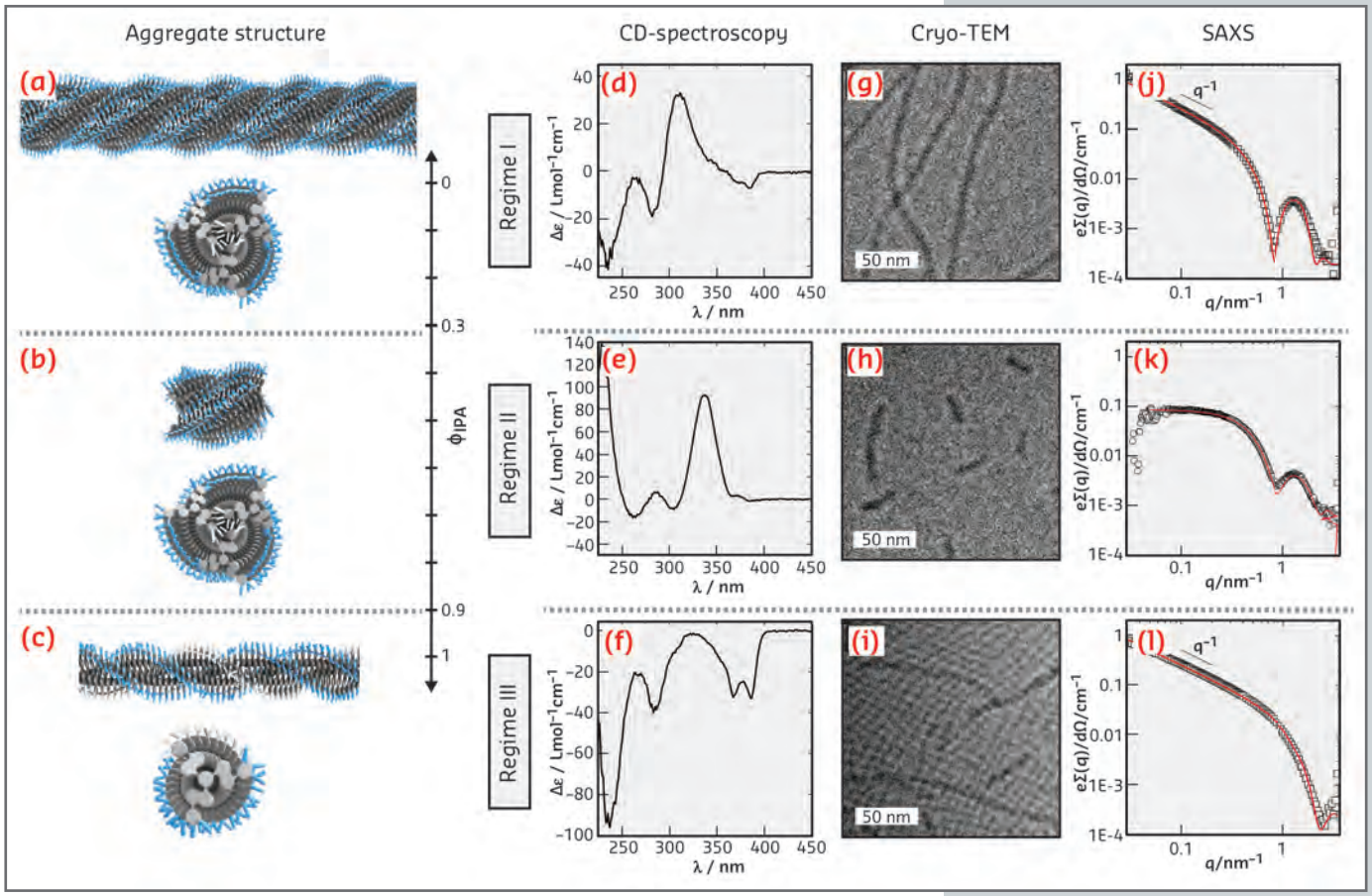

Fig. 38: a-c) Schematic depiction of the three regimes in self-assembly of the discotic amphiphile in IPA–H_2O. CD-spectra of c = 3x10^{-4} M and T = 0°C for: d) f_{IPA} = 0.25; e) f_{IPA} = 0.5; f) f_{IPA} = 1; Cryo-TEM images at c = 3x10^{-4} M for g) f_{IPA} = 0.25;) f_{IPA} = 0.75; i) f_{IPA} = 1; SAXS profiles (symbols) and form factor fits (lines) in IPA–H_2O mixtures at c = 3×10^{-4} M and T = 20°C for: j) f_{IPA} = 0.25; k) f_{IPA} = 0.5; l) f_{IPA} = 1.

The most noteworthy finding of this research is that the boundaries of the three regimes coincide with the two extrema (ϕ_{max} and ϕ_{min}) that are present in the excess enthalpy of mixing phase diagram of IPA–H_2O mixtures [1]. This suggests that the solvent mixing thermodynamics drive the observed morphological transitions, as also suggested by Trappe and co-workers for the phase behaviour of poly(*N*-isopropylacrylamide) in IPA–H_2O mixtures [2]. To confirm that the boundary between regime II and III is indeed coupled to excess enthalpy of mixing, we performed a temperature-dependent experiment at ϕ_{IPA} = 0.95. At 80°C, ϕ_{max} is well below 0.95 while at 0°C ϕ_{max} shifts to values larger than 0.95. This means that cooling a solution of the discotic amphiphile in ϕ_{IPA} = 0.95 should induce a change in the nature of the aggregates typical for regime III to an aggregate typical for regime II. Indeed, the CD spectrum at 10°C is typical for regime III, while it is typical for regime II at 0°C.

The above findings demonstrate that the self-assembly of the discotic amphiphile discussed here in IPA–H_2O mixtures is intricately linked to the mixing behaviour of the IPA–H_2O solvent mixture. This finding is highly important since the nanostructures obtained upon self-assembly in water can be greatly influenced by the preparation method. Frequently, samples are prepared by the direct injection into water of solutions of small self-assembling units in a "good" solvent such as an alcohol or THF. Understanding how the solvent composition influences the aggregate structure helps us to unravel the pathways by which the final structures are formed in water.

References

[1] a) F. Franks and D.J.G. Ives, *Q. Rev. Chem. Soc.* **20**, 1 (**1966**);
b) T. Katayama, *Kagaku Kogaku Ronbun*. **26**, 361 (1962); c) R.F. Lama, B.C.Y. Lu, *J. Chem. Eng. Data* **10**, 216 (1965).

[2] I. Bischofberger, D.C.E. Calzolari, P. De Los Rios, I. Jelezarov and V. Trappe, *Scientific Reports* **4**, 4377 (2014).

Principal publication and authors
F. Liu (a), M. Prehm (b), X.B. Zeng (a), C. Tschierske (b) and G. Ungar (a), *J. Am. Chem. Soc.* **136**, 6846–6849 (2014).
(a) Department of Materials Science and Engineering, University of Sheffield (UK)
(a) Institute of Chemistry, Organic Chemistry, Martin-Luther-University Halle-Wittenberg, Halle (Germany)

SKELETAL CUBIC, LAMELLAR, AND RIBBON PHASES OF BUNDLED THERMOTROPIC BOLAPOLYPHILES

Ordered periodic structures can self-assemble on several different length scales. Crystals form by ordered packing of atoms, *i.e.* units on the 0.1 nm scale. Block copolymers can form regular lattices of the different polymer blocks typically of 10-100 nm size and colloidal particles, such as polystyrene beads or inorganic glassy spheres (such as in opal), can form "colloidal crystals" with periodicities between a fraction of a µm to several µm. The most prominent periodic self-assembled systems in the 1-10 nm range can be classified as liquid crystals (LC) in a broader sense. They contain molecules typically combining two or more poorly compatible chemical groups (amphiphilic or polyphilic) as well as combining both flexible and rigid units of rod-, disk-, or wedge-like shape. This expanding field of soft matter science has produced some very intriguing structures, growing in complexity year after year. The challenge is to learn how to design molecules that will assemble into pre-determined superstructures, which could be used in molecular electronic and optical devices, sensors, actuators, membranes and other smart molecular materials.

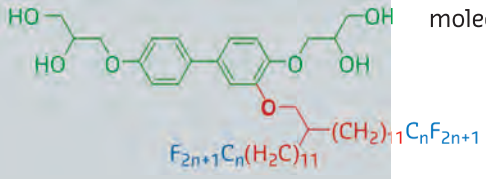

Fig. 39: Structure of the T-shaped polyphilic molecules.

In the work highlighted here, a series of T-shaped polyphilic molecules composed of a rigid linear aromatic core with a polar glycerol group at each end and one "swallow-tail" partially fluorinated side-chain of different lengths *n* (see **Figure 39**) were synthesised and their LC phases were investigated by small-angle grazing incidence X-ray scattering (GISAXS) at beamline **BM28**, as well as by other techniques.

Similar molecules with smaller side-groups show a remarkable series of honeycomb-like LC phases with the aromatic rods as the "wax" and the side-chains as "honey". However, here we find that, as the side-groups increase in size, the honeycomb cells open up, resulting in a structure of alternating rigid aromatic and flexible fluoroalkyl layers (**Figure 40g**). As temperature is raised, the flexible side-chains expand faster than the rigid cores, and the growing mismatch results in the aromatic layers (green) being shredded into parallel ribbons (symmetry *c*2*mm*). Interestingly, the molecules are highly aligned along the ribbon axis, forming a nematic LC phase self-confined within these 2-3 nm wide channels (**Figure 40h**).

As the temperature is increased further, birefringence is lost (**Figure 40c**) as the structure becomes cubic (*Ia*$\bar{3}$*d*, **Figure 39**). This phase is of the cubic type known as "double gyroid" bicontinuous, also found in some lipid-water systems, block copolymers and some LC systems. It consists of two infinite interpenetrating networks that never touch. However, unlike in

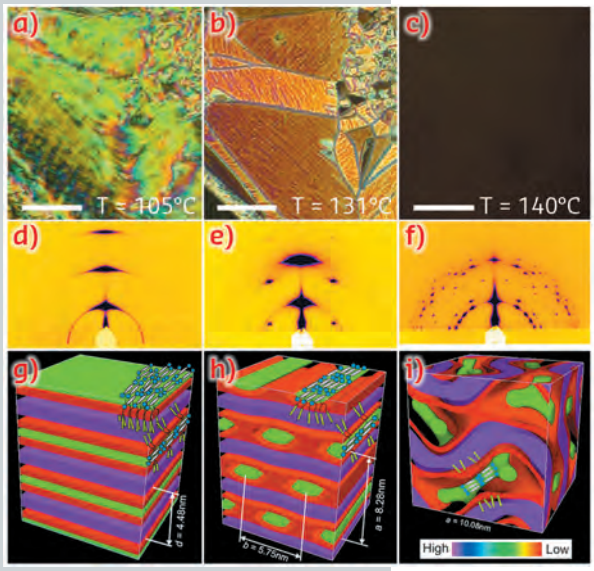

Fig. 40: (a-c) Texture as seen between crossed polarisers in the (a) lamellar phase at 105°C; (b) ribbon phase at 131°C and (c) Cubic *Ia* $\bar{3}$*d* phase at 140°C. Scale bar: 50 µm. (d-f): GISAXS patterns from a thin film in the (d) lamellar, (e) ribbon and (f) cubic phase.
(g-i): Histogrammatic electron density maps with added schematic molecules for (g) lamellar, (h) ribbon, and (i) cubic phase. Discrete solid colours are allocated to three different density ranges, purple for the highest, green for the middle and red for the lowest; they correspond roughly to chemical group colours in the chemical formula.

any other bicontinuous phase, the molecular rods are parallel to the segments of the networks. Also, the distance between the network junctions is exactly two molecular lengths and is fixed.

This new mode of molecular self-assembly promises potential 3-D semiconductors for applications such as organic photovoltaic materials that need no alignment. For alignment is often hard to achieve and is required in the alternative anisotropic systems such as columnar LCs. This work also shows how a single appropriately designed organic compound can display molecular layers, wires and networks just by changing temperature. If required, each of these could be stabilised and fixed by chemical cross-linking.

CRYSTAL STRUCTURE OF CONJUGATED POLYMERS: A COMBINED SCATTERING AND ATOMISTIC SIMULATION APPROACH

Principal publication and authors
A.A.Y. Guilbert (a), J.M. Frost (a), T. Agostinelli (a,b), E. Pires (c), S. Lilliu (c,d), J.E. Macdonald (c) and J. Nelson (a), *Chemistry of Materials* **26**, 1226-1233 (2014).
(a) Centre for Plastic Electronics, Department of Physics, Blackett Laboratory, Imperial College London (UK)
(b) Plastic Logic Ltd., Cambridge (UK)
(c) School of Physics and Astronomy, Cardiff University (UK)
(d) Masdar Institute of Science and Technology, Abu Dhabi (United Arab Emirates)

Organic photovoltaics (OPV) is a promising technology with the potential to deliver a cheap, lightweight, flexible and large area solution for niche applications in electricity generation. In polymer OPV devices, light is harvested by a low-bandgap conjugated polymer with an absorption band closely matching the solar spectrum. Upon photo-excitation of the polymer, a coulombically bound electron-hole pair, called an exciton, is formed. Exciton dissociation into free charge carriers occurs when a second material with higher electron affinity, typically a fullerene derivative, is blended with the polymer to form the so-called bulk-heterojunction. This blend can be solution processed, leading to thin films around 100 nm, and subsequently sandwiched between two electrodes with different work functions to complete the device.

Device performance is strongly affected by the microstructure of the polymer-fullerene blends, which in turn is influenced by the processing conditions and the chemical structure of the blend components. For instance, the nature of the side chains attached to the conjugated backbones to solubilise the polymer and side chain attachment can strongly influence polymer packing, and thus influence both the polymer crystallisation and the polymer:fullerene phase separation.

We studied a number of cyclopentadithiophene-co-benzothiadiazole polymer derivatives differing in the heteroatom (carbon or silicon, see **Figure 41**) that links the side chains to the cyclopentadithiophene unit and in the structure of the side chains (2-ethylhexyl, 3,7-dimethyloctyl and hexadecyl). Previous studies had shown that the photocurrent produced by a solar cell could be greatly increased by substituting the carbon heteroatom with a silicon atom or by processing the carbon analogue with additives. This effect had been assigned to a higher tendency of the silicon-substituted polymer to crystallise leading to more pronounced phase separation in the blend.

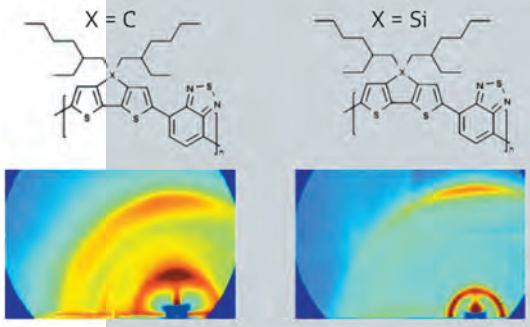

Fig. 41: GIWAXS 2D diffraction pattern of a) poly[2,1,3-benzothiadiazole-4,7-diyl-[4,4-bis(2-ethylhexyl)-4H-cyclopenta[2, 1-b:3,4-b']-dithiophene-2,6-diyl]] (C-PCPDTBT) and b) poly(4,4-dioctyldithieno(3,2-b:2',3'-d)silole-2,6-diyl-alt-(2,1,3-benzo-thiadiazole)-4,7-diyl) (Si-PCPDTBT). Adapted with permission from A.A.Y. Guilbert *et al.*, *Chemistry of Materials* **26**, 1226-1233 (2014). Copyright (2014) American Chemical Society.

Grazing-incidence wide-angle X-ray scattering (GIWAXS) offers us the possibility to investigate the crystalline structure of such conjugated polymer in thin films. **Figure 41** displays the GIWAXS pattern for the carbon and silicon analogue taken with a MAR SX-165 area detector at **BM28** – the XMaS beamline. The silicon analogue, which displays a better defined diffraction pattern, shows a higher tendency to crystallise than the carbon analogue. From the patterns, we notice that the crystals of the two analogues are oriented differently with respect to the substrate. By substituting the carbon atom with a silicon atom, the π–π stacking distance (the distance between the flat, conjugated backbones of the polymers when stacked on top of one another cofacially) decreases at the cost of increasing the lamellar stacking distance (the lateral distance between polymer backbones, arranged in a sheet). This is illustrated in **Figure 42**.

To bridge the gap between chemical structure and crystal structure, we combine GIWAXS with molecular dynamics simulations (MD). From the quantum chemical calculations, it appears that cis and trans conformations between the cyclopentadithiophene and benzothiadiazole units are more likely and that the side chains of the silicon analogue are more flexible. We built a crystal structure with polymers in the trans configurations, a π–π stack featuring a two-fold axis parallel to the main chain axis simply translated to create the lamellar stack (See **Figure 42**). Then, we scanned the energy surface of this structure while varying the π–π stacking and lamellar stacking distances (for each configuration, the side chains are relaxed by performing a MD simulation at 300 K in a NPT ensemble, see **Figure 42**). No difference can be observed for the carbon and silicon, but both display two minima. The π–π stacking and lamellar stacking distances of one of the minima agrees very well with the distances extracted from the GIWAXS pattern of the silicon analogue. The other minimum displays a lamellar stacking in agreement with the carbon analogue but the π–π stacking is overestimated. In further studies of structures with longer and less bulky side chains, we found only one minimum corresponding to the short π–π stacking distance and long lamellar distance and in good agreement with previous reports.

We propose that the greater side chain flexibility of the silicon bridged polymer enables that material to find the minimum with the shorter π–π stacking distance, which should enable improved hole transport, leading to the higher hole mobilities that have been observed and to easier photocurrent generation in a solar cell. These studies confirm that structural characterisation using GIWAXS combined with molecular modelling can help to explain difference in performance of organic electronic materials in terms of their chemical structure and packing tendency.

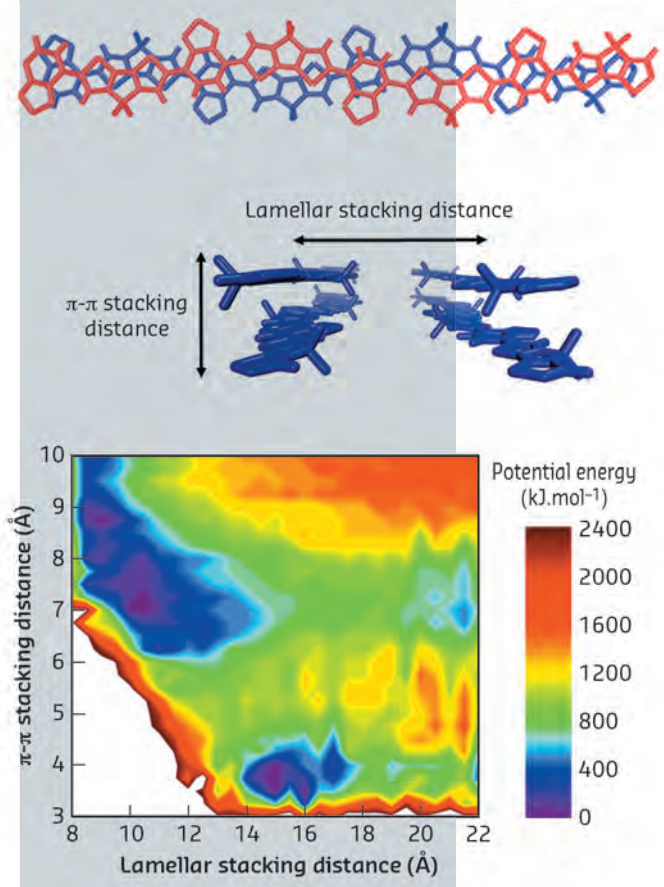

Fig. 42: Structure used for potential energy surface calculations showing the π–π stack and the lamellar stack. Calculated potential energy surface (PES) for C-PCPDTBT. The step size is 0.25 Å for the π–π stacking and 0.5 Å for the lamellar stacking. The PES is not shown for Si-PCPDTBT since no noticeable differences can be observed. Adapted with permission from A.A.Y. Guilbert *et al.*, *Chemistry of Materials* **26**, 1226-1233 (2014). Copyright (2014) American Chemical Society.

INVESTIGATING THE LOCAL STRUCTURE OF A π–π CONJUGATED NETWORK BY X-RAY NANODIFFRACTION AND CROSS CORRELATION

Principle publication and authors
C. Gutt (a), L. Grodd (a), E. Mikayelyan (a), U. Pietsch (a), R. J. Kline (b) and S. Grigorian (a), *J. Phys. Chem. Lett.* **5**, 2335–2339 (2014).
(a) Fachbereich Physik, Universität Siegen (Germany)
(b) Materials Science and Engineering Division, National Institute of Standards and Technology, Gaithersburg (USA)

Poly(3-hexylthiophene) (P3HT) is one of the most widely used semicrystalline polymers in organic electronics. Cast P3HT thin films are typical semicrystalline where well-ordered crystalline nanodomains with sizes of about 5-10 nm are embedded in a disordered host matrix. Considerable effort has been made to understand the charge transport mechanism in terms of the size and orientation of these nanodomains and their degree of crystallinity. It was found that the P3HT films, with edge-on orientation of thiophene moieties with π–π stacking direction along the substrate plane, are a favourable way of achieving high charge mobility in organic field-effect transistor (OFET) devices [1].

The majority of structural investigations of organic thin films has been performed using the grazing incidence X-ray diffraction (GIXD) technique, where the large footprint accounts for spatial averaging over more than ten thousand crystalline nanodomains. This drawback of GIXD in terms of sample averaging has been overcome by using an X-ray nanobeam in transmission geometry (**Figure 43**) at the **ID13** nanofocus beamline. We employed nanobeam X-ray diffraction using an X-ray spot size of 150 nm to investigate the local structure of P3HT thin films.

P3HT drop-cast films on rectangularly shaped grids with 15 nm thick Si_3N_4 membranes (Dune Sciences, Inc.) were measured by using a mesh scan technique with a step size of 180 nm. From this we obtained 121 scattering patterns.

The (020) diffraction ring associated with the π–π stacking of the thiophenes is the most prominent signal visible at q = 16 nm^{-1} and originates from the edge-on orientation of the nanocrystals. The broadening of the peaks confirms the size of the nanocrystals of 5–10 nm as deduced by the Debye–Scherrer formula. Due to the small spot size of 150 nm, the X-ray diffraction pattern becomes sensitive to the local crystalline structure and the local angular or orientational order of the crystallites can be traced by the use of X-ray cross-correlation analysis (XCCA) [2].

In comparison to integrated profiles, which do not show any pronounced spatial variation over the whole nanomesh, the correlation functions elucidate the variety of local structures existing in P3HT.

At certain spots, the angular correlations with 2-fold symmetry (**Figure 44a**) and pronounced 4-fold symmetries (**Figure 44b**) are found, while other positions show no sign of orientational variation with flat correlation functions C(Δ) (**Figure 44c**). Despite 2-fold symmetry being a typical motif in the arrangement of P3HT crystals (even on larger length scales), the 4-fold symmetry oscillations provide an enhanced local degree of ordering and cannot be resolved in conventional GIXD measurements.

At each spot on the sample, both the magnitude and the direction (the phase) were deduced for the L = 2 Fourier component of the scattering intensity.

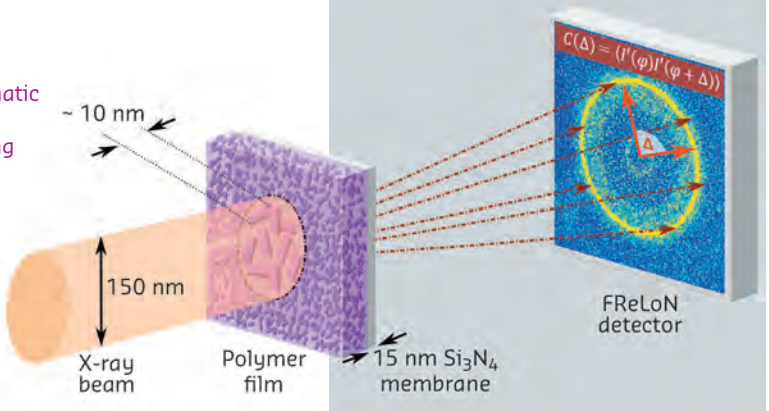

Fig. 43: Schematic setup of the X-ray scattering experiment employing transmission geometry.

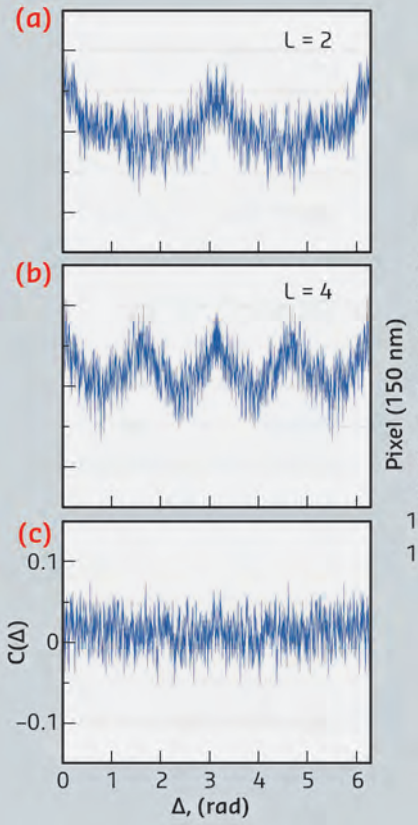

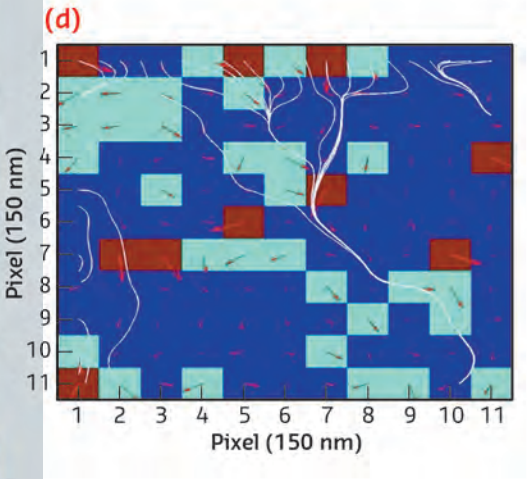

Fig. 44: Correlation functions C(Δ) at four different positions on the sample showing different symmetries: (a) 2-fold, (b) 4-fold, (c) flat correlation at the (020) Bragg peak position $q = 16\ nm^{-1}$, (d) Stream lines (white) of the Fourier component L = 2.

The arrows in **Figure 44a** have length associated with the magnitude of the Fourier component and direction given by the phase. The colour of the pixels represent the magnitude binned into three intervals: strong (brown), medium (green) and weak (blue), respectively.

We observe a strong spatial variation without gradual transition from spot to spot in the correlation functions. The overall appearance of C(Δ) is different at each spot, indicating that the structural motifs are short-range with length scales below the spot size. One key aspect for π–π conjugated polymers is the question of connectivity through the nanoscale complex network. **Figure 44d** visualises a form of connectivity by displaying streamlines through the different angular order maps. The streamlines indicate how distant parts of the sample can be connected along the orientational order direction. **Figure 44d** shows that for L = 2 Fourier component it is difficult to connect over long distances when angular disorder is present. The P3HT system possesses a complex interplay between order and disorder, and the understanding of such interconnectivity remains a manifold task.

Our X-ray study reveals the complex nanoscale structure of the crystals in P3HT where spatially resolved investigation provides strong variations of the structural order on a local scale. The diffraction patterns confirm that a high degree of angular order can exist in the polymer network within an X-ray spot size of 150 nm. The XCCA technique allows us to determine local features on the scale of the working device, avoiding the averaging procedures. The present approach investigating the ordering and interconnectivity of the π–π conjugated network at the 150 nm level has particular potential for the optimisation of organic electronic devices.

References
[1] H. Sirringhaus *et al.*, *Nature* **401**, 685 (1999).
[2] P. Wochner *et al.*, PNAS **106**, 11511 (2009).

GLASS–GLASS TRANSITION DURING AGEING OF A COLLOIDAL CLAY

Principal publication and authors
R. Angelini (a,b), E. Zaccarelli (c,b), F.A. de Melo Marques (d), M. Sztucki (e), A. Fluerasu (f), G. Ruocco (b,d) and B. Ruzicka (a,b), *Nat. Commun.* **5**, 4049 (2014).
(a) CNR-IPCF, UOS Roma (Italy)
(b) Physics Department, Sapienza University, Roma (Italy)
(c) CNR-ISC, UOS Sapienza, Roma (Italy)
(d) Center for Life NanoScience, IIT@ Sapienza, Roma (Italy)
(e) ESRF
(f) Brookhaven National Laboratory, Upton, New York (USA)

Colloidal suspensions are characterised by a variety of microscopic interactions, which generate unconventional phase diagrams encompassing fluid, gel and glassy states and offer the possibility to study new phase and/or state transitions. Glass–glass transitions in particular have rarely been found, especially at ambient conditions. Here, through a combination of dilution experiments, X-ray photon correlation spectroscopy (XPCS) at beamline **ID10**, small-angle X-ray scattering (SAXS) at beamline **ID02**, rheological measurements and Monte Carlo (MC) simulations, we provide evidence of a spontaneous glass–glass transition in a colloidal system consisting of aqueous Laponite suspensions.

Figure 45 shows a dilution experiment that allowed us to distinguish between two different glasses: the first glass melts upon addition of water within three days, i-j, while the second glass no longer melts upon addition of water after three days, k-l. The former is dominated by repulsion, a Wigner glass

[1], while for the latter an additional mechanism must have been involved, probably due to attraction [2]. These results suggest that a previously unreported transition occurs in such Laponite glass at weight concentrations C_w = 3.0% around a critical time $t_c \approx 3$ days.

To further investigate this transition, XPCS measurements were performed on rejuvenated samples and the intensity autocorrelation functions shown in Figure 45m have been fitted through the expression $g_2(Q,t)-1=B\cdot\exp[-(t/\tau)^{\beta}]^2$ where τ is an 'effective' relaxation time whose distribution is measured by the exponent β. Two different behaviours were again observed upon varying the rejuvenation time, t_R: samples rejuvenated before t_c show a stretched behaviour ($\beta < 1$) while samples rejuvenated after t_c exhibit a compressed behaviour ($\beta > 1$) (inset of Figure 45m) [3].

To complement these observations, we also investigated the structure of rejuvenated samples. Measurements of static structure factors $S^M(Q)$ are shown in Figure 45n: two different behaviours were found for samples rejuvenated before t_c (black curves) and after t_c (red curves) showing a shift of the main peak to larger wave vectors (inset of Figure 45n) and a moderate increase of the low Q signal, that is, of the compressibility.

To gain information on the macroscopic differences between the two glasses, we performed oscillatory rheological measurements at different times before and after t_c. Interestingly, a significant change of the storage modulus G'(ν) is found (Figure 45o): for times below 3 days G'(ν) ≈10^3 Pa, however, for times above 3 days, G'(ν) is roughly one order of magnitude higher (G'(ν) ≈10^4 Pa) as found in systems with depletion interactions when passing from a repulsive to an attractive glass. This result thus supports the existence of two glasses with significantly different elastic properties and suggests a crucial role of attraction for the occurrence of the spontaneous glass–glass transition.

To clarify the nature of the attraction, we have carried out Monte Carlo simulations of a simple model of Laponite platelets that combines both repulsive and attractive ingredients, see Figure 46. The simulated static structure factor $S^{sim}(Q)$ of platelets interacting via electrostatic repulsion and a long-range orientational attraction at fixed C_w=3.0% on varying attraction strength mimics the effect

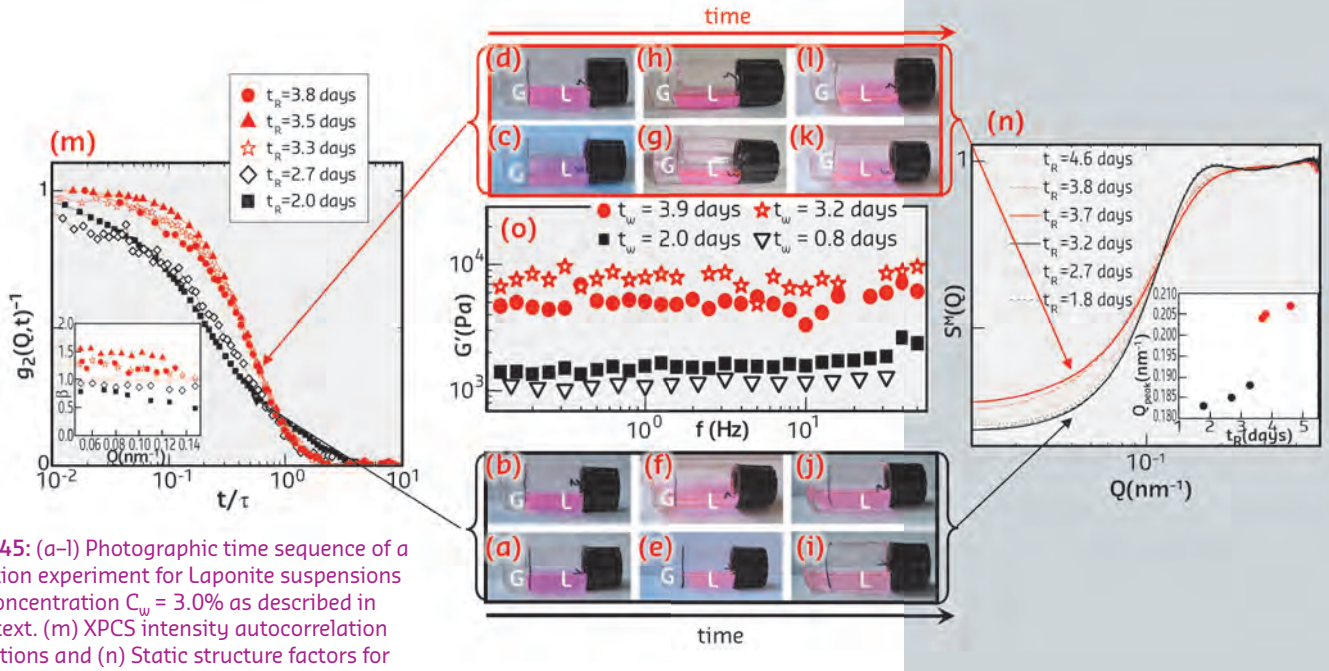

Fig. 45: (a–l) Photographic time sequence of a dilution experiment for Laponite suspensions at concentration C_w = 3.0% as described in the text. (m) XPCS intensity autocorrelation functions and (n) Static structure factors for rejuvenated aqueous Laponite suspensions at the indicated rejuvenation times t_R. In the insets, the β exponent as a function of Q and the peak position as a function of t_R are shown. (o) Frequency dependence of the storage modulus G'(ν) at the indicated waiting times t_w.

References
[1] B. Ruzicka *et al.*, *Phys. Rev. Lett.* **104**, 085701 (2010).
[2] B. Ruzicka *et al.*, *Nature Mater.* **10**, 56 (2011).
[3] R. Angelini *et al.*, *Soft Matter* **9**, 10955 (2013).

of time taking place in the ageing of Laponite suspensions, producing a qualitative similar behaviour for the structure factors as in the experiments.

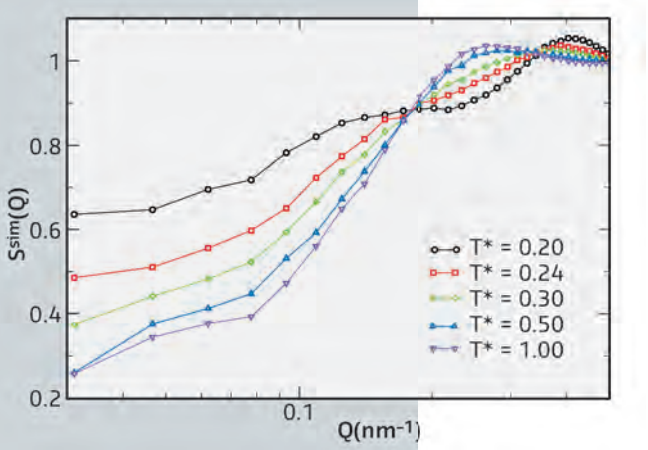

Fig. 46: Simulated static structure factor of Laponite platelets at fixed C_w = 3.0% with varying attraction strength that mimics the effect of time in the ageing of Laponite suspensions.

All of the above observations, providing information on the microscopic structure (SAXS) and dynamics (XPCS) as well as on the macroscopic properties (dilution experiments and rheological measurements) and on the microscopic interactions (MC simulations), indicate that two different glassy states are distinguishable with evolving waiting time: the first is dominated by long-range screened Coulombic repulsion (Wigner glass), while the second is stabilised by orientational attractions (disconnected house of cards - DHOC glass), occurring after a much longer time.

Principal publication and authors
M. Koifman Khristosov (a), L. Kabalah-Amitai (a), M. Burghammer (b,c), A. Katsman (a) and B. Pokroy (a), *ACS Nano*, **8**, 4747–4753 (2014).
(a) Technion Israel Institute of Technology (Israel)
(b) ESRF
(c) Ghent University (Belgium)

FORMATION OF CURVED MICROMETRE-SIZED SINGLE CRYSTALS

One remarkable outcome of biogenic crystal growth is the formation of unfaceted sculptured single crystals with rounded shapes and even crystals that are highly porous. This is in contrast to crystal growth by classical methods, which produce facets dictated by the atomic structure and minimisation of the surface energy, leading to specific low surface energy facets. Drawing inspiration from nature in regard to the growth of unfaceted single crystals, we demonstrate that single crystals of gold can indeed also exhibit curved surfaces. This occurs during crystal growth without the need for any top-down fabrication steps. These single crystals grow from a confined volume of a droplet of a eutectic composition melt, which forms *via* the dewetting of nanometric thin films. We can control crystal curvature by controlling the process environment, including several parameters, such as the contact angle and the curvature of the drops by changing the surface tension of the liquid drop during crystal growth.

By controlling the shape and size of the droplet, we aim to tailor the shape and size of the single crystal growing within it. The mechanism we employed for the formation of such droplets was the dewetting phenomenon in nanometric thin films. To induce dewetting into liquid droplets, a thin film needs to be brought to its melting point. A eutectic system such as gold-germanium seemed an ideal choice for this purpose owing to the relatively low temperature at which the liquid state can be achieved (T_E = 361°C). If a eutectic film of Au-Ge is deposited on a non-wetting surface such as SiO_2, it dewets on reaching the eutectic temperature (**Figure 47a**) and produces liquid droplets within which Au single crystals form (**Figure 47b**).

Energy dispersive spectroscopic (EDS) examination of the single crystals proved that they are gold. To confirm that these crystals are indeed single throughout their entire volume, we prepared cross-sections of these droplets using a focused ion beam (FIB) (**Figure 47c**). This enabled us to observe that each crystal was faceted inside the droplet and possessed a curved surface confined by the droplet's surface. Moreover, the 3D curvature of

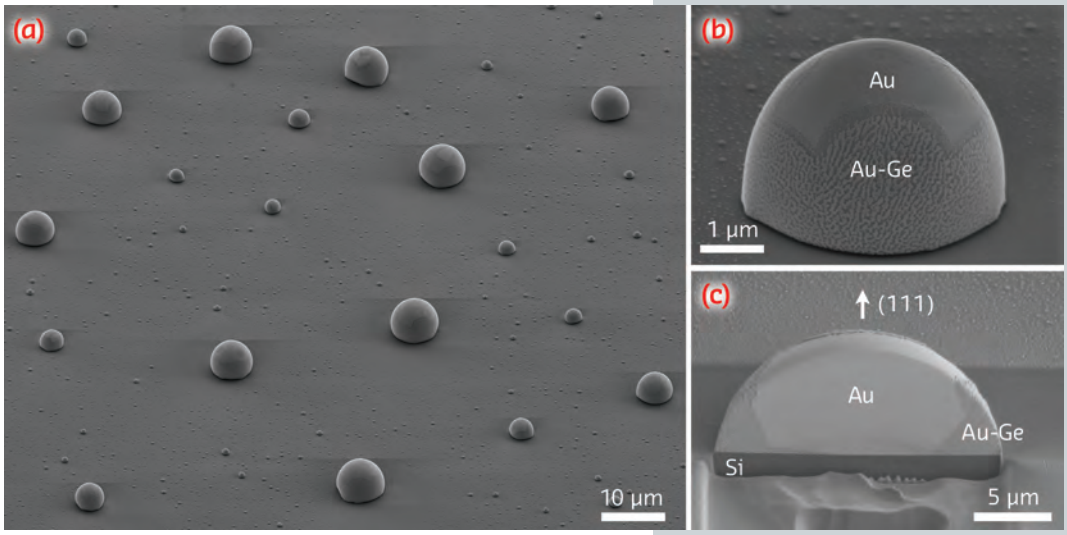

Fig. 47: HRSEM micrographs of Au-Ge droplets after dewetting. a) A large area view of the dewetted surface revealing several droplets. b) A side view of a curved gold single crystal within a micro droplet. c) A droplet cross-section obtained by FIB reveals facets inside the droplet but a curved shape on the surface.

these single crystals was identical to that of the droplets.

To obtain a crystallographic proof that these crystals were single, we used sub-micrometre scanning synchrotron diffractometry at beamline **ID13**, on a FIB-sectioned crystal of gold (**Figure 48a**). At each point of the scanned area (1793 scanning points) the same thermal diffuse scattering pattern of a bulk single crystal was observed (**Figure 48b**). We also verified this by averaging all the 1793 diffraction images from the different locations of the crystal and found that this integrated image remained identical to any one of the individual diffraction images (**Figure 48c-d**). Furthermore, a single crystal Kossel line pattern emerging from Bragg-type diffraction of gold X-ray fluorescence radiation generated by the primary beam was clearly visible in the averaged pattern (**Figure 48e**).

The energetic mechanism that permits the formation of such curved single crystals is that the free energy of a liquid/solid gold interface is yet lower than the free energy of vacuum/solid gold interface. That is why the gold crystals favour the energetic curved surfaces within the droplet, rather than breaking out of the droplet and exposing their facets.

In conclusion, using a relatively simple method such as the dewetting from thin films, and exploiting thermodynamic process such as crystallisation from an eutectic melt, we have demonstrated a method for creating a single curved crystal that grows in the confined space of its own melt, replicating the 3D shape of the droplet.

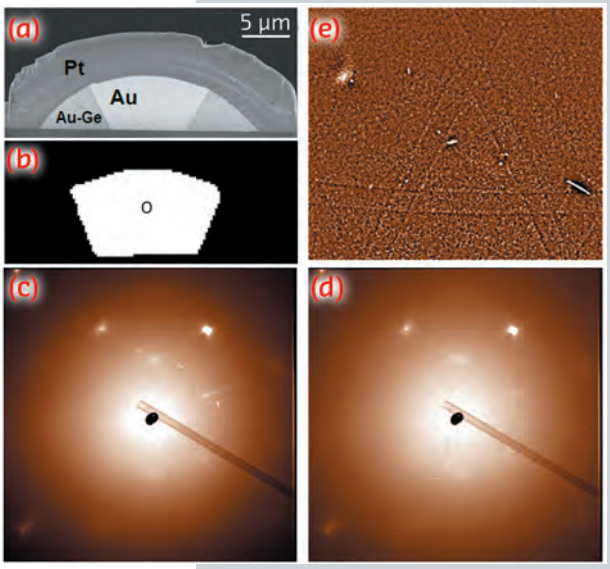

Fig. 48: a) Cross-section of a FIB-prepared droplet that was used for the high-resolution X-ray scan. b) A binary mask derived from mapping of average intensity by simple thresholding in each diffraction pattern, representing the X-ray fluorescence background of the scanned gold crystal. c) Average diffraction pattern of all corrected images of the area in (b) (1793 diffractions). Nano-beam Kossel lines can be observed due to the Au-Fluorescence. d) Corrected (spatial distortion and flat field) diffraction pattern of scan point which was taken from the centre of the single crystal, marked with a circle on (b), for reference. e) High pass filtered version of the average image enhancing the Kossel-lines.

X-RAY IMAGING

The articles presented in this chapter illustrate the broad range of scientific topics encountered at the X-ray imaging beamlines, from medicine and life science to palaeontology, nanowires, stardust or historical artefacts. All the examples share a common property: the heterogeneity (and often complexity) of the samples. However, they usually differ in terms of size, composition and structure. While ID17, the biomedical beamline, offers a beam large enough to image objects the size of organs (for example **Figure 49**, imaging the complete human knee), the NINA project (nano-imaging and nano-analysis, upgrade beamline project UPBL4) provides two new beamlines, ID16A and ID16B, designed to deliver the ultimate nanometric resolution. Accordingly, the five X-ray imaging beamlines offer our users a very wide range of accessible lateral resolution and corollary sample sizes, as well as an extended set of imaging and analytical tools.

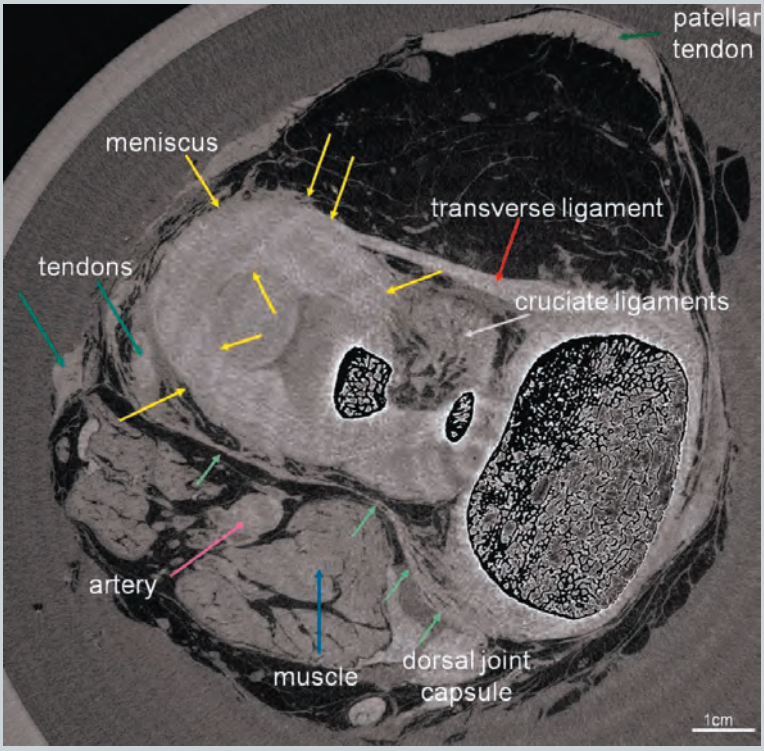

Fig. 49: Axial section of a full human knee *in vitro* imaged at ID17 using propagation-based phase contrast imaging. The image reveals an unprecedented visualisation of the various soft tissue structures (from [1]).

This year, the NINA project has reached fruition. ID16B, the nano-analysis beamline, welcomed its first users in April. Two beam modes can be used: pink beam and monochromatic beam and various techniques are available using a nanobeam focused down to around 50 × 50 nm^2: 2D and 3D fluorescence, 2D and 3D diffraction, 3D phase contrast imaging and 2D X-ray excited optical emission (XEOL). The very first papers based on these pioneering experiments have recently been accepted. As an example, Laforce *et al.* reports, the 3D nano fluorescence imaging of meteoric nanoparticles in the journal *Analytical Chemistry* [2]. Nano-X-ray absorption spectroscopy (XAS), one important deliverable of the beamline project, still requires additional development and commissioning, but should be available in 2015. At ID16A, the nano-imaging beamline, the first users arrived in October. They were very pleased to test a focused beam as small as 35 nm vertical by 20 nm horizontal at 17 keV with a flux as high as 10^{12} photons/s. The two main imaging configurations, X-ray fluorescence analysis and magnified phase tomography, are now regularly being put to good use, either on their own or in combination during a single experiment. The beamline will add three major capabilities in 2015: a high energy focusing mirror operating at 34 keV, ptychographic imaging for ultimate resolution and cryogenic sample preservation.

At an intermediate submicrometric scale, ID21, the spectromicroscopy beamline, offers complementary tools to the NINA beamlines with an X-ray microscope in the tender X-ray domain (2-9 keV) for 2D X-ray fluorescence (XRF) and XAS, a FTIR microscope for molecular mapping, including a side branch that should soon provide users with a stable and easy to use instrument for 2D µXRF and µXRD mapping. This is currently the main project at ID21, which is being implemented without any impact on the regular operation of the main branch. In 2014, major achievements included producing the first monochromatic beam in July 2014 (fixed energy at 8.5 keV) and the first focused beam in November 2014 (0.9 µm vertical × 2.0 µm horizontal). Commissioning will continue in March 2015 and the first XRD users are scheduled for June 2015. In parallel to these developments, discussions have been initiated to consider the future of the infrared beamline and the possibility of reaching the nanometre scale.

Finally, at the opposite end of the beam size scale, the paleontology facility project aims at improving X-ray coherent imaging capabilities for large samples. Important instrumental developments are underway at ID17 and ID19 to enlarge the field of view and simultaneously increase the lateral resolution. A new multi-modal monochromator (Bragg, Laue and soon multi-layer) has been installed at ID19, covering an energy range as large as 18-200 keV. Different developments in optics and detectors are on-going to further increase the field of view, and the general versatility of the various imaging configurations. At ID17, a new Bragg-Bragg coherence-preserving monochromator has been commissioned and it now allows the full exploitation of the available energy range (40-100 keV) with a flat and uniform incoming field.

Going to ultra-fast imaging is another major objective for the coming years, in particular within Phase II of the upgrade programme. Feasibility tests at ID15 and ID19 have already demonstrated that the pulsed time-structure of the ESRF's synchrotron light can be used to capture snapshot images of ultra-fast processes such as crack propagation, shown in Figure 50. Using the isolated X-ray flash from a single-bunch of electrons in the storage ring, which is as short as 140 ps, allows access to a completly new time domain for hard X-ray imaging [3].

M. COTTE

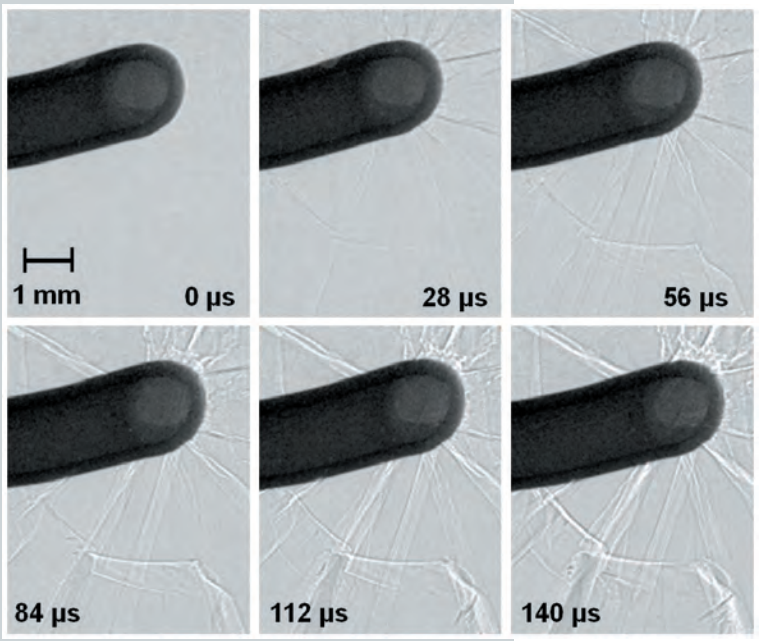

Fig. 50: Time series recording crack propagation in a glass plate initiated by an accelerated bolt. The pictures were acquired *via* single-bunch imaging at beamline ID19 (from [3]).

References
[1] A. Horng, E. Brun, A. Mittone, S. Gasilov, L. Weber, T. Geith, S. Adam-Neumair, S.D. Auweter, A. Bravin, M.F. Reiser and P. Coan, Cartilage and soft tissue imaging using X-rays: propagation-based phase-contrast computed tomography of the human knee in comparison with clinical imaging techniques and histology, *Investigative Radiology* **49**, 627-34 (2014).
[2] B. Laforce *et al.*, Nanoscopic X-ray fluorescence imaging of meteoritic particles and diamond inclusions, *Analytical Chemistry* **86**, 12369–12374 (2014).
[3] A. Rack *et al.*, Exploiting coherence for realtime studies by single-bunch imaging, *Journal of Synchrotron Radiation* **21**, 815-818 (2014).

IMPACT OF MANGANESE ON PRIMARY HIPPOCAMPAL NEURONS IN RODENTS

X-ray fluorescence (XRF) imaging was used to map the spatial distribution of manganese in neurons to help in an assessment of the safety of manganese enhanced magnetic resonance imaging (MEMRI).

Manganese is an increasingly important contrast agent for MRI, which is now widely used to image the internal body structures of rodents and non-human primates. Mn^{2+} is an MRI contrast agent [1] and, as a divalent ion, Mn^{2+} can substitute calcium (Ca^{2+}) by entering active neurons through Ca^{2+} channels [2] and can participate in axonal transport [3]. The unique ability of Mn^{2+} to image brain cytoarchitecture and connectivity makes MEMRI particularly effective for studying neurodegenerative diseases. However, at high doses, manganese is toxic for neurons and glial cells.

We have addressed the impact of Mn^{2+} on cells in culture: mouse hippocampal neurons (HN) and Neuro2a neuroblastoma cells (N2a, a neuron-like cell) using several different approaches. Here we summarise the main results obtained in HN cells.

XRF microscopy, carried out at the ID21 and ID22NI (now at ID16B) beamlines, showed that HN cells not exposed to exogenous $MnCl_2$ naturally contain 5 µg/g of Mn, a result in line with a previous study [4]. A 24h exposure to a Mn^{2+} concentration leading to 50% lethality (100 µM) yielded an intracellular Mn concentration of 248 µg/g for HN cells.

In control HN and HN exposed to moderate concentration of Mn^{2+} (20 µM), phosphorus (P) and zinc (Zn, not detected for N2a) were mostly

Principal publication and authors
A. Daoust (a,b), Y. Saoudi (a,b), J. Brocard (a,b), N. Collomb (a,b), C. Batandier (c), M. Bisbal (a,b), M. Salomé (d), A. Andrieux (a,b), S. Bohic (a,b,d) and E.L. Barbier (a,b), *Hippocampus* **24**, 598–610 (2014).
(a) Inserm, U836, Grenoble (France)
(b) Université Joseph Fourier, Grenoble Institut des Neurosciences (France)
(c) Laboratoire de Bioénergétique Fondamentale et Appliquée, Grenoble (France)
(d) ESRF

Acknowledgements
The authors acknowledge the support of the Grenoble MRI Facility (IRMaGe) and the ESRF for provision of synchrotron radiation beamtime (respectively, exp. MD-458, MD-548). AD received a stipend from the Région Rhône-Alpes – Cluster HVN.

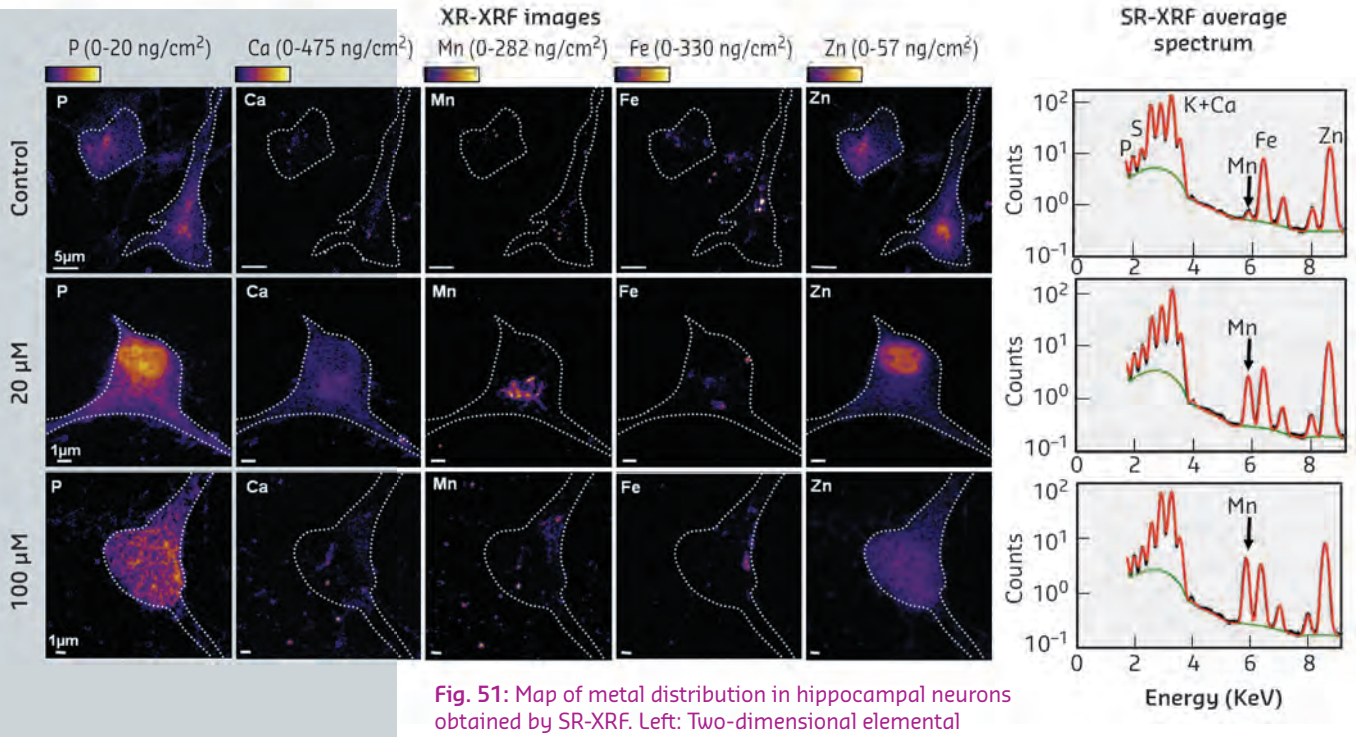

Fig. 51: Map of metal distribution in hippocampal neurons obtained by SR-XRF. Left: Two-dimensional elemental distribution in HN 24 h after adding different concentrations of Mn^{2+} to the culture medium: 0 (control), 20, and 100 µM of Mn^{2+}. Cell contours appear as a white dotted line. The colour scale is in mg of element per g of dry weight. Right: Normalised XRF spectra, averaged over the entire map. The green line corresponds to the baseline and the red line to the fit.

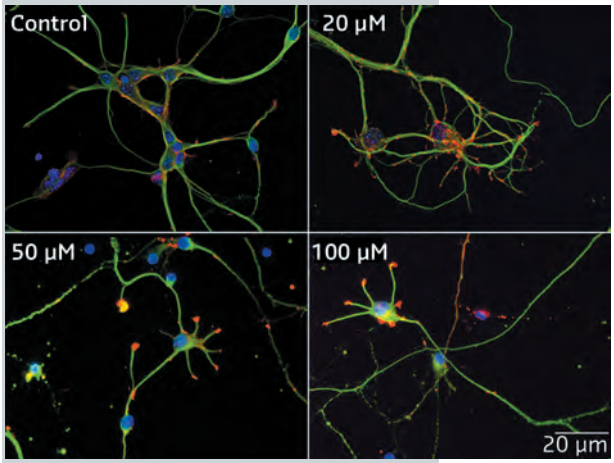

Fig. 52: Impact of Mn^{2+} on the morphology of hippocampal neurons. After 48 h in culture, HN were exposed to Mn^{2+} for 24 h. Four concentrations of Mn^{2+} were used: 0 (control), 20, 50, and 100 µM. Immunofluorescence labelling: neuronal fibrillar actin (red), tubulin (green) and nucleus (blue). The reduction in neuritic length as Mn^{2+} concentration increases is readily visible.

found in the cell nucleus (**Figure 51**). After adding a high concentration of Mn^{2+} to the culture medium (100 µM), the distributions of P and Zn became much more heterogeneous. In control HN, Ca and Fe were barely detectable whereas, after adding a moderate concentration of Mn^{2+} to the culture medium (20 µM), Ca and Fe were clearly visible and localised in the perinuclear, Mn^{2+} rich, region. At a higher Mn^{2+} concentration (100 µM), Ca and Fe were redistributed throughout the cytoplasm. Note that the distribution of Zn and Cu in HN did not change upon addition of Mn^{2+}.

Immunofluorescence studies of HN neurons revealed that concentrations of Mn^{2+} below LC50 (90 µM) shortened neuritic length and decreased mitochondria velocity after 24 h of incubation (**Figure 52**). Similar concentrations of Mn^{2+} also facilitated the opening of the mitochondrial permeability transition pore in isolated mitochondria from rat brains.

This study reports a number of new observations on the impact of Mn^{2+} on cultured HN. When cells are exposed to a concentration of Mn^{2+} below the LC50, Mn is preferentially localised around the nucleus, most likely in the Golgi apparatus or in the endoplasmic reticulum, and in discrete spots in neurites. When neurons are exposed to a concentration of Mn^{2+} above the 50% lethality level, the distribution of Mn becomes more diffuse within the cell, suggesting a mechanism of cell detoxification. Exposure of cultured HN to Mn^{2+} also induced a shortening of neurites, and a decrease of mitochondria velocity. Altogether, these data support the use of primary neuronal cultures as a model to study Mn^{2+}-induced toxicity in the brain. Future experiments should be performed on co-cultures of astrocytes and neurons to better mimic brain anatomical conditions.

References
[1] A.P. Koretsky and A.C. Silva, *NMR Biomed* **17**, 527–531 (2004).
[2] K. Narita, F. Kawasaki and H. Kita, Brain Res **510**, 289–295 (1990).
[3] R.G. Pautler, NMR Biomed. **17**, 595–601 (2004).
[4] A. Daoust, E.L. Barbier and S. Bohic, *NeuroImage* **64**, 10-18 (2013).

CHEMISTRY AND STRUCTURE OF CONTEMPORARY INTERSTELLAR DUST PARTICLES COLLECTED BY THE STARDUST SPACECRAFT

The interstellar region contains several percent of the whole mass of the galaxy. New stars and planetary systems will be generated from this so-called interstellar matter, (**Figure 53**). It contains the basic ingredients of all known space objects including our own Earth. Samples of this unique extra-solar system matter were brought back to Earth during NASA's stardust mission in order to study it in the best-suited laboratories around the world including the most powerful synchrotron sources.

Fig. 53: Infrared image of the dust rich horsehead nebula, a star forming region (image credit NASA, ESA, HST).

The stardust spacecraft collected dust particles from the interstellar medium over several months. The micrometre to sub-micrometre sized, fast flying grains were collected within Aerogel tiles, a transparent, high purity solid silicon oxide glass foam, developed to slow down and capture these grains with minimum damage. Thin slices of Aerogel containing impact tracks were cut from the trays. The tiny particles were studied *in situ*, in the Aerogel, applying nano synchrotron X-ray fluorescence (XRF) and diffraction (XRD) techniques at the nanofocussing beamline ID13 **[1]**, and the ID22NI nanoprobe (now at to ID16B) and ID22 microprobe (now closed) beamlines **[2]**.

At ID13, analyses by synchrotron XRF microscopy of the elemental composition of eight candidate impact features extracted from the Stardust Interstellar Dust Collector (SIDC) were performed, coupled with scanning XRD **[1,3]**. Six of the features were unambiguous tracks, and two were crater-like features. Five of the tracks are so-called "midnight" tracks - that is, they had trajectories consistent with an origin either in the interstellar dust stream or as secondaries from impacts on the Sample Return Capsule (SRC). Synchrotron XRD analyses of these stardust *i*nterstellar preliminary examination (ISPE) candidates **[3]** revealed that two of these particles contain crystalline materials: the terminal particle of track 30 contains olivine and spinel, and the terminal particle of track 34 contains olivine. The terminal particle of track 30, Orion, shows elemental abundances, normalised to Fe, that are close to chondritic type CI values, and a complex, fine-grained structure (**Figure 54**). The terminal particle of track 34, Hylabrook, shows abundances that deviate strongly from CI, but shows little fine structure and is nearly homogenous. An additional track, with a trajectory

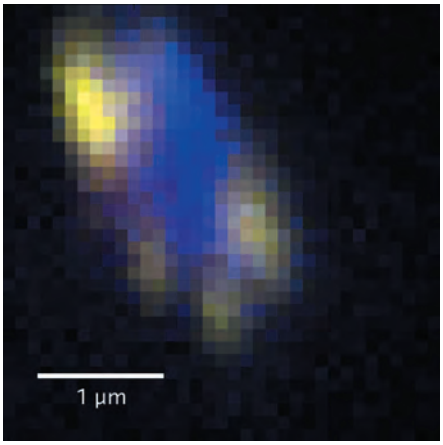

Fig. 54: Tricolour RGB = (Fe, Ni, Ca) high-resolution (100 nm per pixel) map of Orion (reproduced with permission from **[1]**).

Principal publication and authors
A.J. Westphal (a), R.M. Stroud (b), H.A. Bechtel (c), F.E. Brenker (d), A.L. Butterworth (a), G.J. Flynn (e), D.R. Frank (f), Z. Gainsforth (a), J.K. Hillier (g), Frank Postberg (g), A.S. Simionovici (h), V.J. Sterken (i,j,k,l), L.R. Nittler (m), C. Allen (n), D. Anderson (a), A. Ansari (o), S. Bajt (p), Ron K. Bastien (f), N. Bassim (b), J. Bridges (q), D.E. Brownlee (r), M. Burchell (s), M. Burghammer (u), H. Changela (u), P. Cloetens (u), A.M. Davis (w), R. Doll (x), C. Floss (x), E. Grün (y), P.R. Heck (o), P. Hoppe (z), B. Hudson (aa), J. Huth (z), A. Kearsley (bb), A.J. King (w), B. Lai (cc), J. Leitner (z), L. Lemelle (dd), A. Leonard (x), H. Leroux (ee), R. Lettieri (a), W. Marchant (a), R. Ogliore (ff), W.J. Ong (x), M.C. Price (s), S.A. Sandford (gg), J.-A. Sans Tresseras(u), S. Schmitz (d), T. Schoonjans (t), K. Schreiber (x), G. Silversmit (t), V.A. Solé (u), R. Srama (hh), F. Stadermann (x),†, T. Stephan (w), J. Stodolna (a), S. Sutton (cc), M. Trieloff (g), P. Tsou (ii), T. Tyliszczak (c), B. Vekemans (t), L. Vincze (t), J. Von Korff (a), N. Wordsworth (jj), D. Zevin (a) and M.E. Zolensky (n), 30714 Stardust@home dusters (kk), *Science* **15**, 786-791 (2014).
(a) Space Sciences Laboratory, University of California at Berkeley (USA)
(b) Materials Science and Technology Division, Naval Research Laboratory, Washington (USA)
(c) Advanced Light Source, Lawrence Berkeley Laboratory, Berkeley (USA)
(d) Geoscience Institute, Goethe University Frankfurt, (Germany)
(e) State University of New York at Plattsburgh (USA)
(f) Jacobs Technology/ESCG, NASA Johnson Space Center (JSC), Houston (USA)
(g) Institut für Geowissenschaften, University of Heidelberg (Germany)
(h) Institut des Sciences de la Terre, Observatoire des Sciences de l'Univers de Grenoble (France)
(i) Institut für Raumfahrtsysteme (IRS), University of Stuttgart (Germany)
(j) IGEP, TU Braunschweig (Germany)
(k) Max Planck Institut für Kernphysik, Heidelberg (Germany)
(l) International Space Sciences Institute, Bern (Switzerland)
(m) Carnegie Institution of Washington (USA)
(n) Astromaterials Research and Exploration Science, NASA JSC, Houston (USA)
(o) Field Museum of Natural History, Chicago (USA)
(p) Deutsches Elektronen-Synchrotron, Hamburg (Germany)
(q) Space Research Centre, University of Leicester (UK)
(r) Department of Astronomy, University of Washington, Seattle (USA)
(s) University of Kent, Canterbury (UK)
(t) University of Ghent (Belgium)

(u) University of New Mexico, Albuquerque (USA)
(v) ESRF
(w) University of Chicago (USA)
(x) Washington University, St. Louis (USA)
(y) Max-Planck-Institut für Kernphysik, Heidelberg (Germany)
(z) Max-Planck-Institut für Chemie, Mainz (Germany)
(aa) 615 William Street, Apt 405, Midland, Ontario (Canada)
(bb) Natural History Museum, London (UK)
(cc) Advanced Photon Source, Argonne National Laboratory, Lemont (USA)
(dd) LGL-TPE, Ecole Normale Superieure de Lyon (France)
(ee) University Lille 1 (France)
(ff) University of Hawai'i at Manoa, Honolulu (USA)
(gg) NASA Ames Research Center, Moffett Field (USA)
(hh) IRS, University Stuttgart (Germany)
(ii) Jet Propulsion Laboratory, Pasadena (USA)
(jj) Wexbury, Farthing Green Lane, Stoke Poges, South Buckinghamshire (UK)
(kk) Worldwide. List of individual dusters is at http://stardustathome.ssl.berkeley.edu/sciencedusters.

References
[1] F.E. Brenker, A. Westphal, L. Vincze *et al.*, *Meteoritics & Planetary Science* **49**, 1594–1611 (2014).
[2] A.S. Simionovici, L. Lemelle *et al.*, *Meteoritics & Planetary Science* **49**, 1612–1625 (2014).
[3] Z. Gainsforth *et al.*, *Meteoritics & Planetary Science* **49**, 1645–1665 (2014).

consistent with secondary ejecta from an impact on one of the spacecraft solar panels, contains abundant Ce and Zn. This is consistent with the known composition of the glass covering the solar panel.

In addition eight interstellar candidate impact features were studied by hard X-ray, quantitative, XRF elemental imaging and XRD on the ID22NI nanoprobe and ID22 microprobe beamlines [2]. Three features were unambiguous impact tracks, and the other five were identified as possible, but not definite, impact features. Overall, an absolute quantification of elemental abundances in the $15 \leq Z \leq 30$ range was produced by means of corrections of the beam parameters, reference materials, and fundamental atomic parameters. Seven features were ruled out as interstellar dust candidates (ISDC) based on compositional arguments. One of the three tracks, previously studied at ID13, contained two physically separated, micrometre-sized terminal particles, the most promising ISDCs, Orion (see above) and Sirius. We found that the Sirius particle was a fairly homogenous Ni-bearing particle and contained about 33 fg of distributed high-Z elements ($Z > 12$). The measurements at ID22NI show that Orion is a highly heterogeneous Fe-bearing particle and contains about 59 fg of heavy elements located in hundred nanometre phases, forming an irregular mantle that surrounds a low-Z core.

To date, only a small number of the particles captured by the Stardust Interstellar Dust Collector and returned to Earth have been extracted and analysed. Of these, seven have features consistent with an origin in the contemporary interstellar dust stream. The interstellar dust candidates are readily distinguished from debris impacts on the basis of elemental composition and/or impact trajectory. The seven candidate interstellar particles are diverse in elemental composition, crystal structure, and size. The presence of crystalline grains and multiple iron-bearing phases, including sulfides, in some particles, indicates that individual interstellar particles differ from any other representative model of interstellar dust inferred from astronomical observations and theory.

Principal publication and authors
B. Enders (a), M. Dierolf (a), P. Cloetens (b), M. Stockmar (a), F. Pfeiffer (a) and P. Thibault (a,c), *Appl. Phys. Lett.* **104**, *171104 (2014).*
(a) Physics Department, Technische Universität München, Garching (Germany)
(b) ESRF
(c) Current address: Physics & Astronomy Department, University College London (UK)

ROBUST LENSLESS IMAGING WITH A HIGH-FLUX INSTRUMENT

In the last decade, coherent diffractive imaging (CDI) has shown great promise as a dose-efficient and high-resolution complement to traditional (lens-based) X-ray microscopy. In contrast to conventional microscopy where an objective lensing system catches the diffracted X-ray photons to form a direct image on the detector, the X-ray photons are allowed to freely propagate to the detector forming a diffraction image. A computer algorithm is used to reconstruct an image of the specimen's transmission from the traces left in such an indirect measurement. Ptychography is a CDI variant where the specimen is scanned transversally through the X-ray beam, collecting a diffraction image at each scan point [1,2]. Unlike traditional X-ray microscopy or other CDI techniques, ptychography can deliver quantitative amplitude and phase images of extended specimen beyond the resolution limit of lenses.

However, the benefits of diffraction imaging usually come at the cost of requiring "clean" diffraction data for the algorithms to work properly. Commonly this requirement is met by strong spectral and spatial filtering for beam purity in combination with a photon counting, pixel-array detector for an ideal measurement. While the first measure drastically reduces the available photon flux, the latter cannot distinguish single photon events at

high flux. Ironically, this very need to reduce flux translates directly into lower achievable resolution [3].

An experiment was carried out at the nano-imaging endstation of the former ID22 beamline (now ID16-NI) to investigate the robustness of ptychography in a configuration that allows for high-flux experiments, under conditions that were previously considered insufficient: a broad-bandwidth X-ray beam focused by a pair of crossed multilayer-coated Kirkpatrick-Baez mirrors and an integrating scintillator-based FReLoN detector (Figure 55). As can be seen in the diffraction image (D in Figure 55), the acquired diffraction data was degraded by a large halo around the central beam (bluish in the image). The high dynamic range in the diffraction signal caused this degradation by amplifying even faint effects like diffuse air scattering or a point spread in the scintillator coupled to the CCD.

Consequently, conventional ptychographic algorithms struggled when reconstructing sample transmission (Figure 56b) and illuminating wavefront (Figure 56a) from these data. The illumination contains speckly noise and the phase image of the spoke-pattern of the sample is blurred.

Next, the mixed states approach [4] was applied, which is one of the latest algorithmic developments for the treatment of ptychographic data. It permits a number of concurrent modes to form the illumination and thereby emulates some deficiencies of the detector and the beam, *e.g.* partial coherence. These modifications alone allowed reconstruction of the sample in high detail and quality (Figure 56d) and the main mode (Figure 56c) now shows the shape expected for the illumination in the sample plane.

Furthermore, an analysis of the illumination modes revealed that the algorithm not only corrects for lower coherence and detector point spread (Figure 56, e and f), but also attempts to correct for an inhomogeneous response of the four detector quadrants in algorithmically less constrained parts of the illumination frame (Figure 56g).

Our work proves that mere adjustments in the data analysis steps can lead to dramatic improvements in image quality. With its newly demonstrated robustness, ptychography will be widely applicable with relaxed experimental requirements, paving the way to high-throughput, high-flux and high-resolution diffractive imaging.

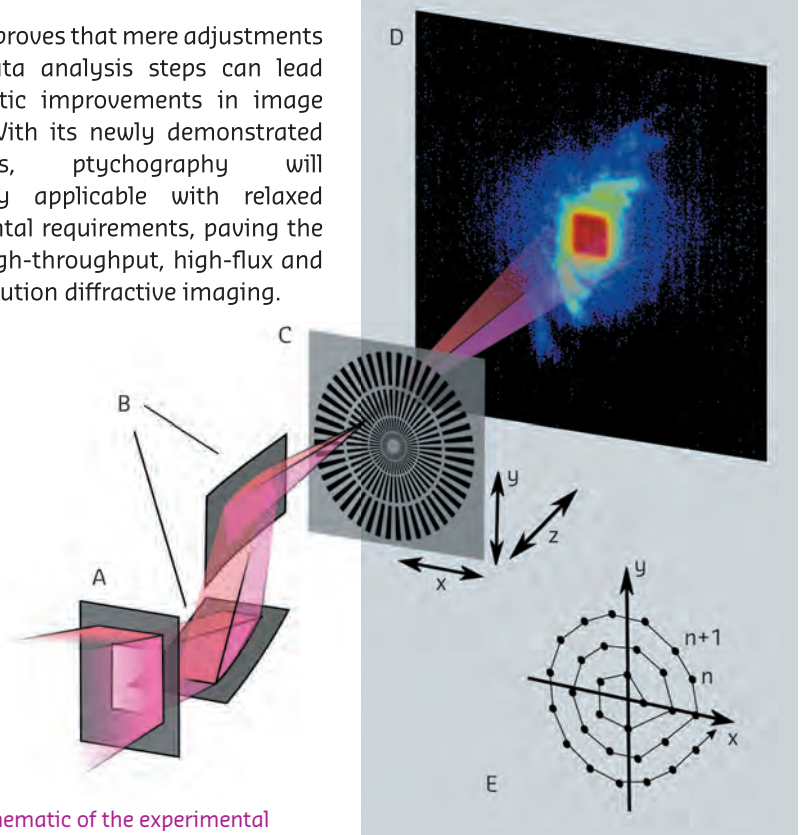

Fig. 55: Schematic of the experimental setup (not to scale) used for ptychography at the former ID22NI endstation. The X-ray beam enters through an aperture (A) and is focussed by two multilayer Kirkpatrick-Baez mirrors (B). The sample (C) is placed close to the focus and the diffraction patterns are recorded downstream by a CCD coupled to a scintillator (D). To avoid artifacts, the sample is scanned along a circular pattern (E).

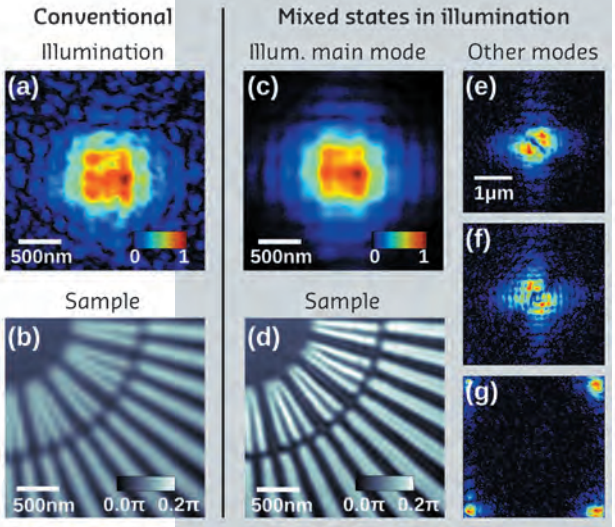

Fig. 56: Conventional reconstruction (left) compared with mixed-states approach (right). Conventional reconstruction: (a) modulus of the retrieved illumination wavefront (in a.u.) and (b) phase (in rad) of the reconstructed sample transmission function. Mixed state reconstruction: (c) showing the reconstruction of the main mode of the illumination and (d) phase of the sample transmission function. (e)-(g) an assortment of other modes reconstructed in the Illumination, where (e) and (f) can be associated with the detector point spread function or partial coherence while (g) is related to the inhomogeneous response of the four quadrants of the detector.

References

[1] P. Thibault *et al., Science* **321**, 379 (2008).
[2] M. Dierolf *et al., Nature* **467**, 436 (2010).
[3] M. Howells *et al., Journal of Electron Spectroscopy and Related Phenomena* **170**, 4 (2009).
[4] P. Thibault and A. Menzel, *Nature* **494**, 68 (2013).

REVEALING PHASE SEPARATION IN SINGLE InGaN NANOWIRES

Principal publication and authors
J. Segura-Ruiz (*a*, *b*), G. Martinez-Criado (*a*), C. Denker (*c*), J. Malindretos (*c*), A. Rizzi (*c*), *Nano Lett.* **14**, 1300–1305 (2014).
(a) ESRF
(b) Present address: Institut Laue-Langevin, Grenoble (France)
(c) IV. Physikalisches Institut, Georg-August-Universität Göttingen, (Germany)

Semiconductor materials are evolving toward the development of more complex alloys and nanoscale heterostructures. Unexpected properties and improved functionalities can be achieved with the combination of these two approaches. For instance, the ternary alloy $In_xGa_{1-x}N$ has an absorption edge that can be modified between 0.7 to 3.4 eV. This range covers most of the solar spectrum, making this material an excellent candidate for the development of high efficiency multijunction solar cells and light-emitting diodes. Nanometric-sized structures such as nanowires confer additional advantageous properties that can enhance the performance of the nanodevices. For instance, nanowire-shaped semiconductors absorb light in a much more efficient manner [1], and allow the possibility to build core–shell structures that further improve the performance of solar cells [2], and light-emitting devices [3].

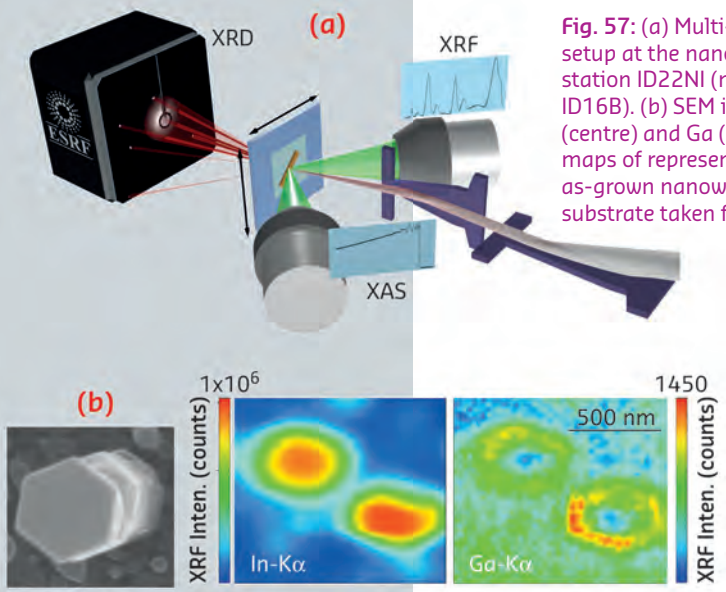

Fig. 57: (*a*) Multi-technique setup at the nanoimaging station ID22NI (now at beamline ID16B). (*b*) SEM image (left), In (centre) and Ga (right) Kα XRF maps of representative single as-grown nanowires on the Si substrate taken from the top.

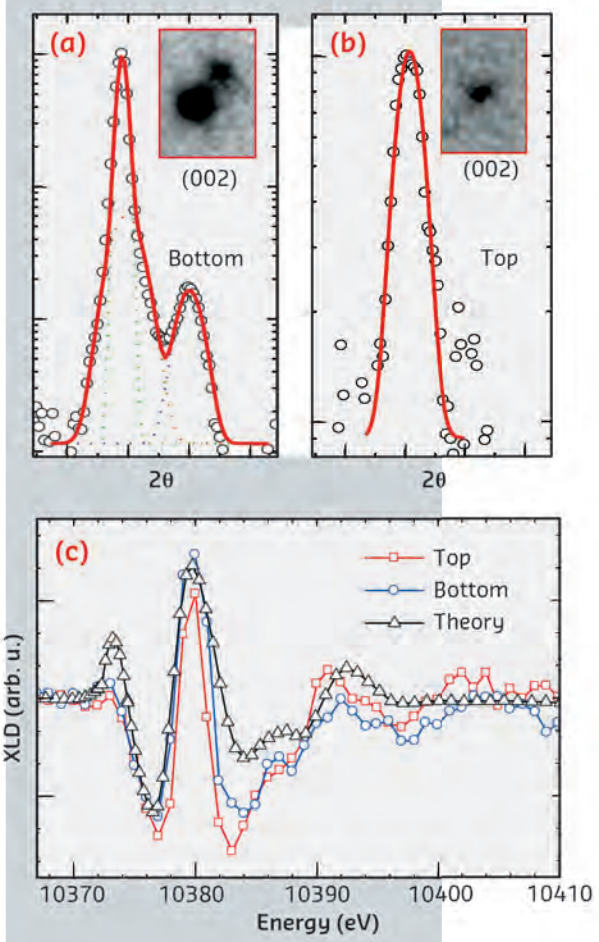

Fig. 58: (*a*) InGaN (002) XRD reflection (open circles) acquired at the bottom (*a*) and top (*b*) of a single nanowire along with the best multi-Gaussian fits (solid line). Different Gaussian contributions are plotted with dotted lines. The insets show the corresponding CCD images. (*c*) XLD spectra around the Ga K-edge measured at the top (squares) and bottom (circles) of a single nanowire, and the calculated spectrum (triangles) for wurtzite GaN.

Characterisation of these complex nanoscale structures requires the combination of several techniques, preferably with a high spatial resolution to avoid the averaging that could hide local details. In this work, we have used the hard X-ray nanoprobe at beamline ID22NI (now at ID16B) to characterise self-assembled single $In_xGa_{1-x}N$ nanowires using a multi-technique approach and nanometric resolution.

Figure 57a shows a schematic view of the setup at the X-ray nanoprobe, which integrates X-ray fluorescence (XRF), X-ray diffraction (XRD) and X-ray absorption spectroscopy techniques. This multi-technique approach allows the simultaneous study of the composition, long- and short-range order of the samples, with a very high lateral spatial resolution. As-grown and dispersed nanowires placed onto thin membranes were scanned with both, pink ($\Delta E/E \sim 10^{-2}$, flux of $\sim 5 \times 10^{12}$ ph/s, 55 × 55 nm^2 spot size) and monochromatic ($\Delta E/E \sim 10^{-4}$, flux of $\sim 5 \times 10^{10}$ ph/s, 105 × 110 nm^2 spot size) beams. XRF maps of the nanowires show an axial and radial elemental heterogeneity with Ga accumulation in the bottom and in the outer region of the nanowire, examples are displayed in **Figure 57b**.

Nano-XRD and nano-XRF maps were performed simultaneously on single dispersed nanowires, using a 28 keV

monochromatic beam. Figure 58 shows the XRD spectra of the InGaN (002) reflection acquired at the bottom (a) and top (b) of a single nanowire. A closer inspection of the (002) reflection shows at least three Gaussian contributions to this XRD peak at the bottom, and single Gaussian-like XRD peak at the top. These different contributions to the (002) diffraction peak are observed even in the original CCD images, shown in the insets of Figure 58a and b. Finally, X-ray linear dichroism (XLD) spectra around the Ga K-edge measured at the top and bottom of a single nanowire, and the calculated spectrum for wurtzite GaN are shown in Figure 58c. Both XLD spectra of the nanowire exhibit the strong anisotropy of the X-ray absorption, typical for the wurtzite GaN matrix. This confirms that despite the elemental modulation, the tetrahedral order around the Ga absorbing atoms remains along the nanowires.

In conclusion, a large phase separation at the bottom, and a single phase at the top of the nanowires were revealed. We anticipate that this methodology will contribute to a greater understanding of the underlying growth concepts, not only of nanowires, but also of many nanostructures in materials science.

References

[1] J. Wallentin, N. Anttu, D. Asoli, M. Huffman, I. Åberg, M.H. Magnusson, G. Siefer, P. Fuss-Kailuweit, F. Dimroth, B. Witzigmann, H.Q. Xu, L. Samuelson, K. Deppert and M.T. Borgström, *Science* **339**, 1057–1060 (2013).

[2] M.D. Kelzenberg, S.W. Boettcher, J.A. Petykiewicz, D.B. Turner-Evans, M.C. Putnam, E.L. Warren, J.M. Spurgeon, R.M. Briggs, N.S. Lewis and H.A. Atwater, *Nat. Mater.* **9**, 239–244 (2010).

[3] G. Martínez-Criado, A. Homs, B. Alén, J.A. Sans, J. Segura-Ruiz, A. Molina-Sánchez, J. Susini, J. Yoo and G.-C. Yi, *Nano Lett.* **12**, 5829–5834 (2012).

TUNING THE OXYGEN DOPING LEVEL IN THE Bi-2212 SUPERCONDUCTOR BY X-RAY NANO-BEAM IRRADIATION

Principal publication and authors

A. Pagliero (a), L. Mino (b), E. Borfecchia (b), M. Truccato (a), A. Agostino (b), L. Pascale (b), E. Enrico (c), N. De Leo (c), C. Lamberti (b, d), and Gema Martínez-Criado (e), *Nano Lett.* **14**, 1583 (2014).

(a) Depart. of Physics, NIS Centre of Excellence, University of Turin, Torino (Italy)

(b) Depart. of Chemistry, NIS Centre of Excellence, University of Turin, Torino (Italy)

(c) INRIM, National Institute of Metrological Research, Torino (Italy)

(d) Southern Federal University, Rostov-on-Don (Russia)

(e) ESRF

The search for higher speed and lower power consumption has driven the semiconductor industry to produce increasingly smaller integrated circuits. This trend has stimulated deep innovation in the lithographic techniques based on the use of short wavelength radiation. Nevertheless, so far, hard X-rays-based lithography with $\lambda \approx 0.1$ nm has been hampered by problems in the fabrication of suitable masks with both sufficiently high contrast in their absorbing power and small enough features. Another appealing possibility is represented by direct-writing techniques allowing the modification of substrate properties without any photoresist. Focused-electron-beam- and focused-ion-beam-induced deposition and etching, along with the scanning-probe lithography, are the most frequently used techniques, and all enabling nanometric spatial resolution [1]. A few examples of X-ray direct-writing-lithography have been reported recently, but in all cases patterning was limited to organic or organometallic materials. Since these processes are essentially based on molecular photodissociation, the limitation to this kind of materials seemed to be intrinsic to the use of X-rays. Nevertheless, it has also been shown that 12.4 keV X-rays are able to induce persistent changes in the transition temperature (T_c) of La_2CuO_{4+y} superconducting cuprates by means of photon-induced displacement of light atoms in their crystal structure [2].

In our study, we have explored the application of X-ray direct-writing lithography to the $Bi_2Sr_2CaCu_2O_{8+\delta}$ (Bi-2212) superconductor, with typical $T_c \approx$ 80-90 K. As Bi-2212 crystals below T_c are able to emit and sense THz radiation [3], an obvious application could be the production of these devices. The possibility of direct-writing X-ray lithography is even more interesting because of the expected increasing availability of hard X-ray sources with extreme brilliance and power, such as X-ray free electron lasers (XFELs).

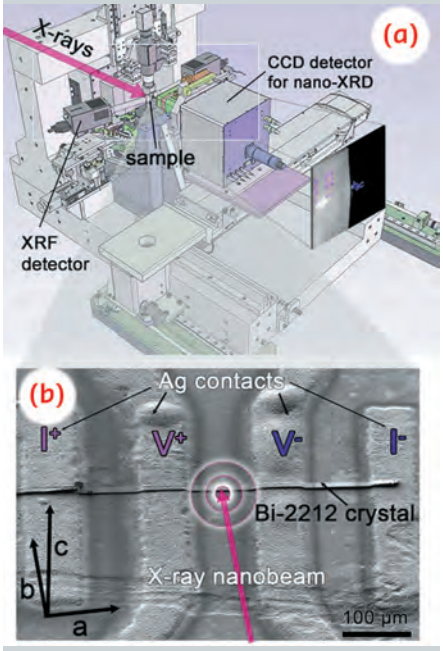

Fig. 59: a) Scheme of the experimental setup used at beamline ID22NI (now at ID16B). b) SEM micrograph of the typical chip used for electrical measurements of the Bi-2212 micro-crystals. Current and voltage electrodes used for the four-probe technique are labelled as I^+, I^-, V^+ and V^-. The arrow indicates the nanobeam direction during irradiation.

References
[1] S.J. Randolph *et al.*, *Crit. Rev. Solid State Mat. Sci.* **31**, 55 (2006).
[2] N. Poccia *et al.*, *Nat. Mater.* **10**, 733 (2011).
[3] L. Ozyuzer *et al.*, *Science* **318**, 1291 (2007).
[4] I. Piñera *et al.*, *Phys. Stat. Sol. A* **204**, 2279 (2007).

In particular, we investigated the effect of localised hard X-ray irradiation of Bi-2212 micro-crystals using the 117 × 116 nm^2 nanoprobe available at the ID22NI beamline (now at ID16B) (**Figure 59a**). The structural modifications induced by the X-ray nanobeam were monitored using nano-XRD, while the corresponding changes in the electrical properties were measured by the four-probe method (**Figure 59b**) after each irradiation session. We have clearly proven that irradiating this material by 17 keV X-rays (doses in the order of 10^{12} Gy) results in an elongation of the *c*-axis and in an increase of both the critical temperature and the normal state resistivity (**Figure 60**). This highlights a modification in the material's oxygen doping level, moving from an over-doped state towards a progressively more under-doped state.

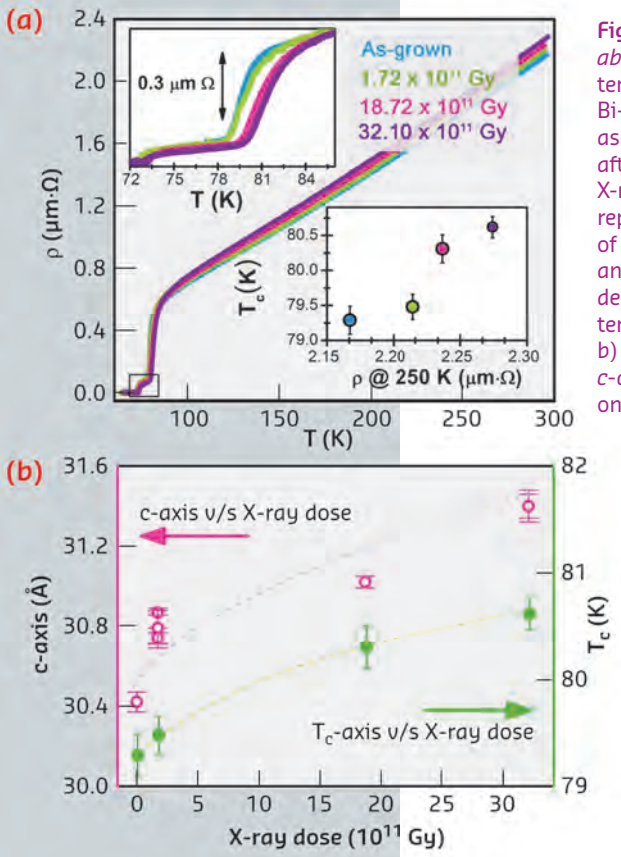

Fig. 60: a) Four-probes *ab*-plane resistivity vs. temperature curves for Bi-2212 micro-crystals in as-grown conditions and after increasingly higher X-ray doses. The insets report a magnification of the transition region and the T_c vs. resistivity dependence at room temperature.
b) Dependence of the *c*-axis length and of the T_c on the X-ray dose.

Moreover, modelling our different experimental conditions using the finite element method (FEM) allowed us to exclude heating induced by the X-ray nanobeam as the major cause for the change in the doping level. Conversely, a significant role could be played by the photoelectrons acting as a possible source of knock-on for the O atoms in the BiO layers, due to their low displacement threshold energy, which has already been predicted for the O atoms in the CuO chains of YBCO **[4]**.

Our results suggest that the use of hard X-rays as a novel direct-writing, photoresist-free lithographic process is an attractive possibility to overcome the current limitations in the fabrication of miniaturised devices with potential nanometric resolution and 3D capability.

THE *in vivo* RADIOSENSITISING EFFECTS OF NANOPARTICLE-BASED MRI CONTRAST AGENTS

Principal publications and authors
I. Miladi (a), C. Alric (a), S. Dufort (b), P. Mowat (a), A. Dutour (c), C. Mandon (a), G. Laurent (d), E. Bräuer-Krisch (e), N. Herath (f), J.L. Coll (g), M. Dutreix (f), F. Lux (a), R. Bazzi (d), C. Billotey (a), M. Janier (a), P. Perriat (h), G. Le Duc (e), S. Roux (d) and O. Tillement (a). *Small* **10**, 1116-1124 (2014);
G. Le Duc (e), S. Roux (d), A. Paruta Tuarez (a), S. Dufort (b), E. Brauer-Krisch (e), A. Marais (a), C. Truillet (a), L. Sancey (a), P. Perriat (h), F. Lux (a) and O. Tillement (a), *Cancer Nanotechnology* **5**:4 (2014).
(a) Institut Lumière Matière, Université de Lyon (France)
(b)Nano-H S.A.S, Saint Quentin-Fallavier (France)
(c) Centre Léon Bérard, Lyon (France)
(d) Institut UTINAM, Université de Franche-Comté, Besançon (France)

Radiotherapy is commonly used in cancer treatment, either alone or in combination with surgery and/or chemotherapy, since X-rays induce lethal alterations of the tumour. However, the sparing of the surrounding healthy tissue remains a challenge because the similarities in the atomic composition of the tumour and the surrounding tissues do not favour a preferential absorption of the therapeutic beam. For this reason, the use of radiosensitisers composed of heavy elements (high atomic number, Z), combined with a preferential accumulation in the tumour tissues, has been proposed in order to increase the ratio between the dose deposited in the tumour and the dose deposited in the surrounding healthy tissues **[1]**. In this context, gadolinium plays an important role because of its high relaxivity value and because of its relatively high atomic number value

(Z = 64), highlighting its potential for MRI guided radiation therapy [2].

Studies using gold nanoparticles coated with gadolinium chelates have already been carried out and the design of the particles optimised to allow both MRI monitoring (owing to the gadolinium chelates) and radiosensitisation (due to the gold core, Z = 79). The delay between the administration of the nanoparticles and the radiotherapy session was determined from the data collected by MRI (Figure 61) prior to irradiation. Although better results are expected by refining the biodistribution of the nanoparticles inside the tumour, the lifespan of the rats bearing glioma was enhanced by combining microbeam radiation therapy (MRT) and nanoparticle injection resulting in lifespans extended by 473%, which compares favourably to the 222% obtained when MRT was used without nanoparticles.

The potential for image guided radiotherapy of gadolinium based nanoparticles was compared to routinely used gadolinium chelates, by using a glioma model implanted in the rat brain. Viewed by MRI imaging, a high and relatively constant concentration was conserved by the tumour while the nanoparticles were rapidly cleared from healthy tissues. This is far better than for gadolinium chelates which are rapidly eliminated from the tumour. Another advantage of this protocol is that the same injection can be used for both MRI and radiotherapy. When radiotherapy was carried out at beamline ID17 using identical experimental conditions, the combination of gadolinium nanoparticles and radiotherapy allowed the median survival time of rats bearing glioma to be doubled when compared to the use of only gadolinium chelates. These results are shown in Figure 62.

To conclude, two kinds of gadolinium based nanoparticles were used both in MRI and radiotherapy in order to develop the concept of image guided radiotherapy, *i.e.* in order to use the same contrast media on images as a dose media during radiotherapy. The long time of residence of the nanoparticles (when compared to chelates) within the tumour allows a radiotherapy session to be carried out when the ratio between the gadolinium content of the tumour versus the surrounding healthy tissues is optimal. This time delay can be assessed by MRI prior to the radiotherapy. Finally, both gadolinium and gold/gadolinium based nanoparticles were proven to enhance the lifespan of rats bearing glioma when compared to radiotherapy alone.

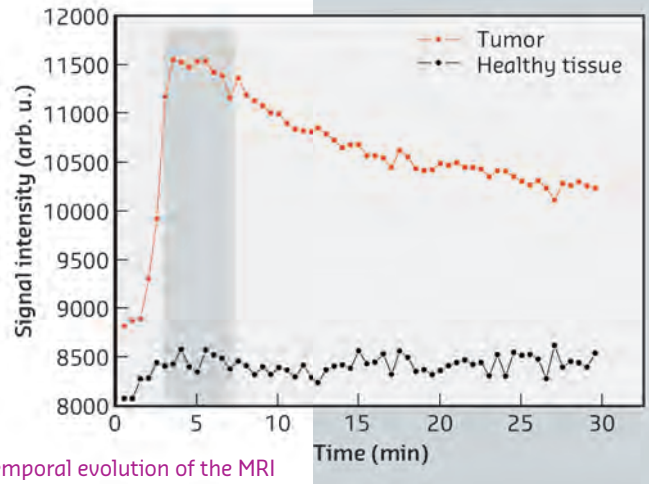

Fig. 61: Temporal evolution of the MRI signal in tumour (red squares) and in an equivalent surface in normal tissue in the left hemisphere (black circles) after intravenous injection of gadolinium chelate coated gold nanoparticles. The grey area represents the time interval during which the difference of signal intensities is the highest.

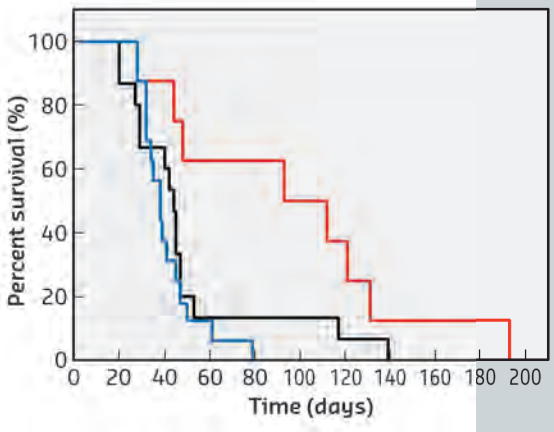

Fig. 62: Survival curves of 9LGS bearing rats treated by MRT only (black curve, n = 15 rats), treated by MRT 20 minutes after injection of DOTAREM® (blue curve, n = 16 rats), and of AGuIX nanoparticles (red curve, n = 8 rats). The irradiation was performed 10 days after tumour implantation.

(e) ESRF
(f) Institut Curie, Orsay (France)
(g) Institut Albert Bonniot, Grenoble (France)
(h) MATEIS, INSA, Lyon (France)

References
[1] J.F. Hainfeld, D.N. Slatkin and H.M. Smilowitz, *Phys. Med. Biol.* **49**, 309-315 (2004).
[2] D. Francis, G.M. Richards, A. Forouzannia, M.P. Mehta and D. Khuntia. *Expert. Opin. Pharmacother.* **10**, 2171-2180 (2009).

Principal publication and authors
S. Layachi (a), L. Porra (b,c), G. Albu (d), N. Trouillet (e), H. Suhonen (c), F. Peták (f), H. Sevestre (e), P. Suortti (b), A. Sovijärvi (g), W. Habre (d) and S. Bayat (a), *J Appl Physiol* **115**, 1057-1064 (2013).
(a) Université de Picardie Jules Verne and Amiens University Hospital (France)
(b) Department of Physics, University of Helsinki (Finland)
(c) ESRF
(d) Geneva Children's Hospital, University Hospitals of Geneva, and Geneva University (Switzerland)
(e) Department of Pathology, Amiens University Hospital (France)
(f) Department of Medical Physics and Informatics, University of Szeged (Hungary)
(g) Department of Clinical Physiology and Nuclear Medicine, Helsinki University Central Hospital (Finland)

WHY LUNG VENTILATION IS UNEVENLY DISTRIBUTED IN ASTHMA: NEW INSIGHT FROM SYNCHROTRON K-EDGE SUBTRACTION IMAGING

Asthma, the most common chronic disease in children, is characterised by chronic inflammation of the airways. Exposure to an allergen in sensitised asthmatics triggers the expression and release of mediators including cytokines, chemokines, adhesion molecules, inflammatory enzymes and receptors by inflammatory cells, which leads to bronchial smooth muscle constriction and an increased resistance of the bronchi to air flow. Allergen exposure also causes transient increases in eosinophils, T-cells, mast cells and neutrophils in the lung and inflammatory cell infiltration of airway walls. In the Brown Norway rat, a strain genetically predisposed to allergic hypersensitivity, allergen provocation produces patchy inflammatory cellular infiltrates in the walls of both airways and pulmonary blood vessels. Eosinophils are thought to play a central role in allergic inflammation in asthma, however, the relationship between eosinophilic infiltration and regional lung function is poorly understood.

Bronchoconstriction in asthmatic subjects leads to a significant heterogeneity in the distribution of inhaled air within the lung, and the appearance of ventilation defects [1]. This phenomenon is important not only because it contributes to abnormal respiratory mechanics and gas exchange, but also because it can significantly impact the distribution of inhaled drugs commonly used in the treatment of asthma. We have previously shown that both the route (inhaled vs. blood-born) and nature (allergic vs. non-specific) of airway challenge play a significant role in determining the heterogeneity of airway constriction [2]. However, the exact mechanisms causing such striking regional differences in lung ventilation in allergic asthma remain elusive.

We studied the relationship between the spatial distribution of the cellular effectors involved in asthma and the emergence of defects in regional ventilation following allergen exposure. For this purpose, we used *in vivo* high-resolution K-edge subtraction (KES) synchrotron imaging at the ID17 beamline, during xenon inhalation in ovalbumin (OVA)-sensitised Brown-Norway rats at baseline and repeatedly following OVA challenge.

The KES technique allows simultaneous imaging of the airway structure and quantitative measurements of the regional tissue density and the concentration of inhaled Xe gas [2]. This technique allowed us to measure

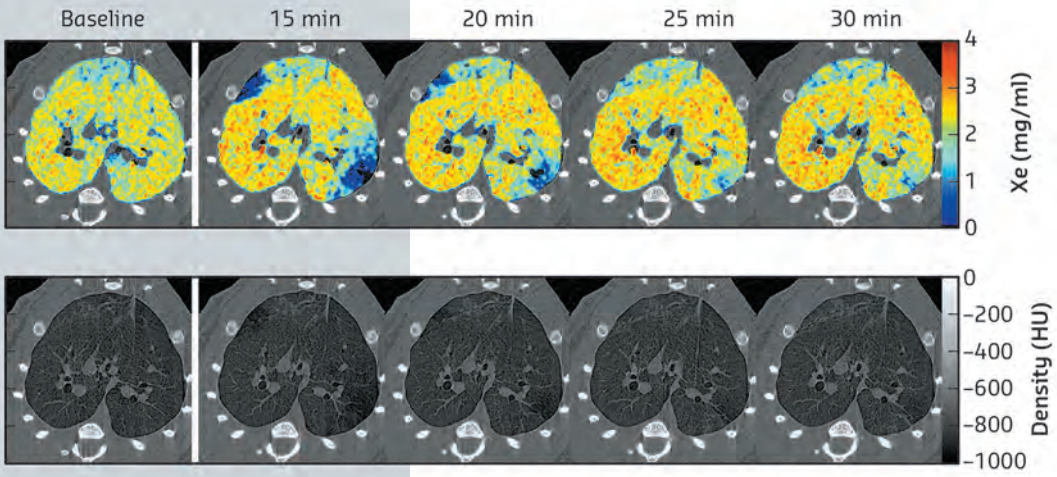

Fig. 63: High resolution K-edge subtraction images for one representative animal. Upper row: quantitative Xe-images. Following OVA, transient clustered areas of poor ventilation emerge (blue). Lower row: tissue-density KES images.

both airway narrowing and the distribution of inhaled Xe gas within the pulmonary alveoli. Histological slices of the lung anatomically matched to the computed-tomography images were stained and digitised. Total cells, CD68+ and eosinophils were counted in the walls of bronchi and vessels randomly selected within and outside of ventilation defects, delineated based on the Xe-KES images. Following OVA challenge, we observed transient ventilation defects (**Figure 63**), and increases in airway resistance and tissue elastance. Eosinophil (**Figure 64**), CD68+ and total cell counts were significantly higher in the bronchial and vascular walls within vs. outside of the ventilation defects. Furthermore, airway constriction during OVA-induced bronchoconstriction was correlated with eosinophil and total cell densities in the airway walls within the poorly-ventilated zones.

The bronchial tree is a branching structure leading to terminal acini (clusters of alveoli) where gas exchange occurs. Previously, computational modelling studies have shown that due to feedback between regional tidal expansion and airway constriction, even a uniform constriction of airway smooth muscle above a critical level can lead to self-organised emergence of patchy areas of ventilation defects resulting from clustered peripheral airway narrowing and closure [3]. This led to the theory that the appearance of ventilation defects may emerge from the complex dynamic system behaviour of the lung.

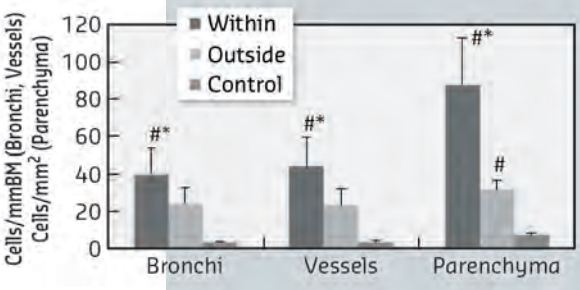

Fig. 64: Eosinophil cellular densities in airway wall, vessel wall and parenchyma, within and outside the ventilation defects, defined based on the regional concentration of Xe. Data are mean ± SE in 6 sensitised and challenged rabbits and 3 controls. *: $p < 0.05$ vs. outside of VD, #: $p < 0.05$ vs. control.

Our findings further the understanding of uneven ventilation and show that in asthma, airway inflammation is locally heterogeneous, and that this phenomenon is involved in determining the heterogeneity of regional airway constriction and that of regional ventilation following exposure to an allergen. Moreover, the global response to an allergen that causes central airway narrowing is strongly correlated to airway wall infiltration by inflammatory cells such as eosinophils. These findings bring significant new insight to the current understanding of the emergence of heterogeneous airway constriction, and have important implications for the treatment strategies for allergic asthma.

References
[1] A.R. Sovijarvi, L. Poyhonen, L. Kellomaki and A. Muittari, *Thorax* **37**, 516-520 (1982).
[2] S. Bayat, L. Porra, G. Albu, S. Layachi, F. Petak, P. Suortti, Z. Hantos, A.R.A. Sovijarvi and W. Habre, *Am J Respir Crit Care Med* **181**, A5029 (2010).
[3] J.G. Venegas, T. Winkler, G. Musch, M.F. Vidal Melo, D. Layfield, N. Tgavalekos, A.J. Fischman, R.J. Callahan, G. Bellani, and R.S. Harris. *Nature* **434**, 777-782 (2005).

MORPHOLOGICAL EVOLUTION OF THE GROWING MOLLUSC SHELL REVEALED BY X-RAY COMPUTED MICROTOMOGRAPHY

Living organisms form complex mineralised biocomposites that perform a variety of essential functions. These biomaterials are often multifunctional, being responsible for not only structural support and mechanical strength, but also provide optical, magnetic or sensing capabilities. This remarkable diversity in functionality is accomplished despite a relatively narrow range of constituent inorganic materials. Hence, a significant effort has been directed to study the process of biomineralisation – to understand how organisms assimilate elements from the environment in which they live and incorporate them into living tissues. Many studies have focused on the biological and chemical aspects

Principal publication and authors
B. Bayerlein (a), P. Zaslansky (b), Y. Dauphin (c), A. Rack (d), P. Fratzl (a) and I. Zlotnikov (a), *Nature Materials* **13**,1102–1107 (2014).
(a) Department of Biomaterials, Max Planck Institute of Colloids and Interfaces, Potsdam (Germany)
(b) Charité Universitätsmedizin BSRT and Julius-Wolff Institute, Berlin (Germany)
(c) Micropaléontologie, UFR TEB, Université P. & M. Curie, Paris (France)
(d) ESRF

of the interaction between inorganic precursors and macromolecular components resulting in controlled growth of different biominerals. In contrast, thermodynamic constraints that govern many aspects of microstructure formation and morphology of the mineralised tissues are much less understood.

Mollusc shells are widely used as model systems to investigate the biomineralisation process of calcium carbonate ($CaCO_3$) by living organisms. For example, the shell of *Pinna nobilis* has two juxtaposed mineralised layers with completely different properties and therefore, provides two different examples of calcium carbonate assemblies within the same organism: a calcitic layer exhibits an elongated prismatic microstructure and an aragonitic layer exhibits a 'brick-and-mortar' nacreous microstructure. In the prismatic layer, the mineral prism building blocks are surrounded by a 1 µm think organic interprismatic matrix defining the shape of individual prisms. The biomineralisation process of the entire prismatic layers is initiated on the organic layer covering the shell (periostracum) and propagates towards the inside of the shell by the secretion of a mixture containing the precursors for calcite formation [1]. The microstructure of the layer, a few millimetres in thickness, evolves as an assembly of growing prisms and the interprismatic matrix as a function of the growing thickness of the layer. Hence, the growth history of the prismatic layer is recorded in its microstructure and can be accessed by an appropriate imaging technique, interpreting the coordinate perpendicular to the layer as a measure of time.

The thickness of the organic interprismatic matrix surrounding the calcitic prisms matches well the resolving power accessible at **ID19**, the microtomography beamline. To study the shell geometry, a combination of absorption- and phase-contrast enhanced imaging modes was used to resolve the organic/calcite prism boundaries and to reconstruct the microstructure of the prismatic layer. The analysis of the 3D microtomography data was performed in the scope of classical grain growth and coarsening theories while considering the growth as a two-dimensional problem where the time parameter was replaced by the direction of the structural evolution [2]. We focused on mean field considerations, where the growth kinetics of a single prism is described by an average behaviour of the entire prismatic layer and topological considerations of space filling.

Figure 65a shows a representative microtomography cross section, exhibiting a honeycomb-like microstructure in the plane perpendicular to the growth direction of the prismatic layer. A representative 3D rendering of a segment of the layer, reconstructed from a continuous set of 2D sections similar to the one presented in **Figure 65a**, is shown in **Figure 65b**. These data clearly demonstrate that the average area (cross-section) of the prisms increases during growth, in an effort to decrease the total interface area between the prisms and the adjoining organic matrix. In complete agreement with the predictions from classical grain growth theories based on mean field and on topological considerations, some of the prisms are seen to shrink and disappear while others grow in their

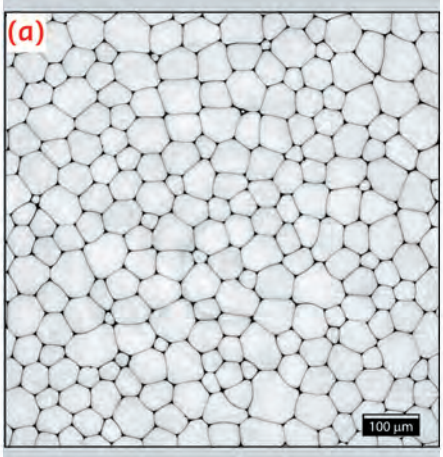

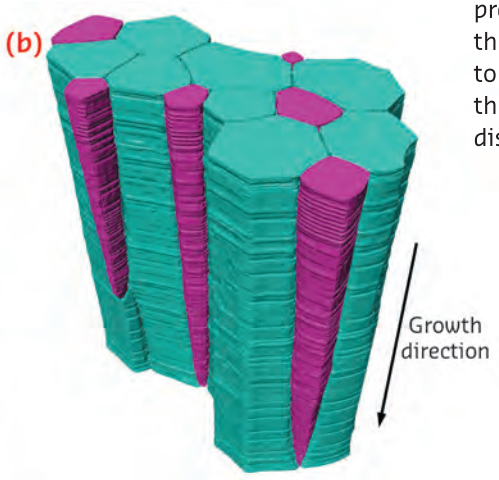

Fig. 65: a) Representative 2D microtomography section obtained perpendicular to the growth direction of the prismatic layer. b) Representative 3D microtomography section of the prismatic layer of *Pinna nobilis*. Growing prisms are colour-coded blue, shrinking prisms are colour-coded purple.

cross-sectional area (purple and blue prisms in Figure 65b, respectively). Moreover, the data reveal that the grain size distribution renormalised by its mean value is time invariant during microstructural evolution, so that the coarsening process can be considered statistically self-similar.

This quantitative description of the structural development of the calcitic prismatic layer in *P. nobilis* using high-resolution microtomography and based on the comparison with well-known theories of grain growth is a fundamental step towards a better understanding of various aspects of biomineralisation. The results show how the living organism uses thermodynamic boundary conditions to define the morphology of its calcite shell.

References
[1] F. Marin, P. Narayanappa and S. Montreuil, in *Molecular Biomineralization* Vol. 52, W.E.G. Müller (Ed.), Springer Verlag, 353-395 (2011).
[2] H.V. Atkinson, *Acta Metall.* **36**, 469-491 (1988).

COARSENING AND BREAK-UP REVEALED BY X-RAY MICROTOMOGRAPHY OF PHASE-SEPARATED GLASSES

Principal publication and authors
D. Bouttes (a), E. Gouillart (b), E. Boller (c), D. Dalmas (b) and D. Vandembroucq (a), *Physical Review Letters*, **112**, 245701 (2014).
(a) Laboratoire PMMH, UMR 7636 CNRS/ESPCI/University Paris 6 UPMC/ University Paris 7 Diderot (France)
(b) Surface du Verre et Interfaces, UMR125 CNRS/Saint-Gobain, Aubervilliers (France)
(c) ESRF

In their molten state, some silicate glasses spontaneously phase-separate: they form domains of different compositions [1, 2]. Such domains can take different shapes, such as droplets or interconnected channels. The physics is then very similar to an emulsion of oil and water, with the microstructure gradually coarsening to reduce the interfacial energy. In the case of a silicate glass, the liquid state is obtained at temperatures generally higher than 700°C, and by cooling it below this temperature one can "freeze" the system. The domains formed in the liquid state then become a microstructure in the solid, and can be used to tune some physical properties. Using X-ray tomography at **ID19**, we were able to visualise the formation of this microstructure in a barium borosilicate glass in three dimensions (3D), and observe the effect of the time spent in liquid state.

With X-ray tomography, one reconstructs 3D images of the absorption of a sample from several hundreds of radiographs. The high intensity flux at ID19, together with a setup suited for ultrafast acquisition, allows fast scans. Moreover, a dedicated furnace is used such that the same sample can be heated for some time at a given temperature then quenched to be scanned, then heated again, and so on (Figure 66).

After image processing, we were able to observe the intricate geometry of one of the two phases (Figure 67). At the beginning of the heat treatment, the system is bicontinuous, which means that there is only one domain for each phase, and these domains are interpenetrating. The geometry is similar to a sponge, where there is only one "solid" part, that is contiguous (otherwise it would collapse), and only one "void" part (otherwise the water could not fill it all). In fact, it is possible to produce a "glass sponge" by leaching one of the two separated phases with acid, which, for example, is used to produce porous glass membranes.

During the heat treatment, we were able to measure how the typical size

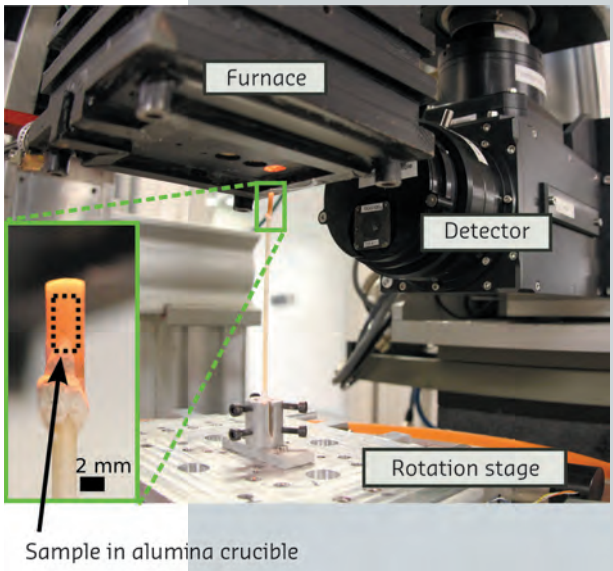

Fig. 66: Experimental setup at ID19. The sample, a 2 mm cylinder, is placed in an alumina crucible mounted on a rotation stage. A furnace, mounted on a vertical translation stage, is lowered over the sample for the heat treatments. In this image the X-rays would be arriving from the left.

References
[1] A.J. Bray, Theory of phase-ordering kinetics. *Advances in Physics*, **43**(3), 357-459 (1994).
[2] O.V. Mazurin and E.A. Porai-Koshits (Eds.). Phase separation in glass, Elsevier (1984).

of the domains increases in order to reduce the interfacial area where the two immiscible phases are in contact. General predictions suggest that this coarsening should be self-similar. This means that the geometry of the domains is statistically the same at any time provided that all lengths are divided by a characteristic length scale, which itself grows with time. The experiments confirmed this theoretical prediction, up to a limit: the coarsening is slowed down by the fragmentation of the less viscous phase into disconnected droplets. This important fragmentation mechanism was identified for the first time thanks to the possibility of following the same sample at different heat treatment times.

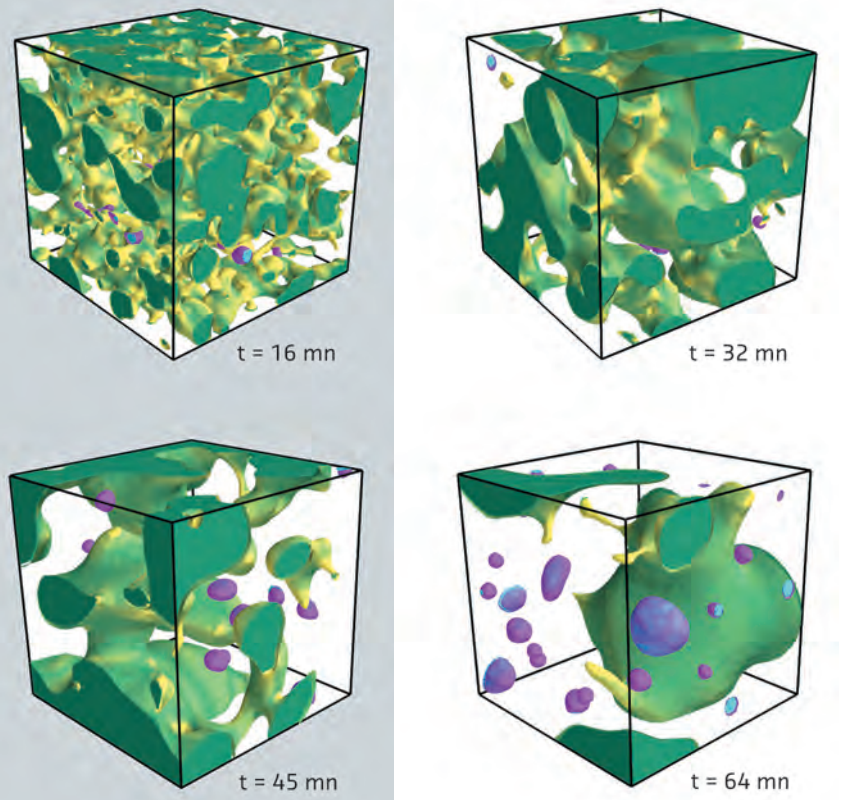

The experimental setup at ID19 has recently been improved with a new camera and rotation stage. The acquisition time has been reduced from a few minutes to a few seconds to obtain 3D images with micrometric resolution. This has triggered new studies, which are ongoing, to investigate the origin of the unexpected fragmentation. It is now possible to follow *in situ* the coarsening (without quenching to room temperature). In particular, the dynamics of evolution of domain shapes are considered, and point towards hydrodynamics effects. Such understanding of microstructure formation could lead to new ways of building tailored microstructures in phase-separated glasses.

Fig. 67: 3D rendering of the barium-rich phase during coarsening. The largest domain, in green, is percolating. Other domains, in purple, are isolated droplets. The shades of colour represent the mean curvature value. The lateral size of the cubes is 140 µm.

DIRECT THREE-DIMENSIONAL IMAGING OF POLYMER–WATER INTERFACES BY NANOSCALE HARD X-RAY PHASE TOMOGRAPHY

Principal publication and authors
Y. Cheng (a), H. Suhonen (b,c), L. Helfen (a,b), J. Li (a,d), F. Xu (a,b), M. Grunze (a,d), P.A. Levkin (a,d) and T. Baumbach (a), *Soft Matter* **10**, 2982-2990 (2014).
(a) Karlsruhe Institute of Technology (Germany)
(b) ESRF
(c) Presently at: University of Helsinki (Finland)
(d) Department of Applied Physical Chemistry, University of Heidelberg (Germany)

Surfaces with special wettability can exhibit unique properties like self-cleaning or cell repellency and therefore attract much research interest in the quest to improve coating technology. Superhydrophobic and superoleophobic surfaces, in particular, have been studied intensively in recent years due to their extraordinary liquid repellent properties. Slippery liquid-infused porous surfaces (SLIPS) based on lubricant-infused porous polymer substrates [1] were found to have particularly good anti-bacterial and marine anti-biofouling properties. Visualisation of such surfaces and their interfaces to water or aqueous solutions have been attempted *via* confocal laser-scanning and *via* cryo-FIB/SEM microscopy but artefacts due to the required staining or freezing processes cannot be excluded.

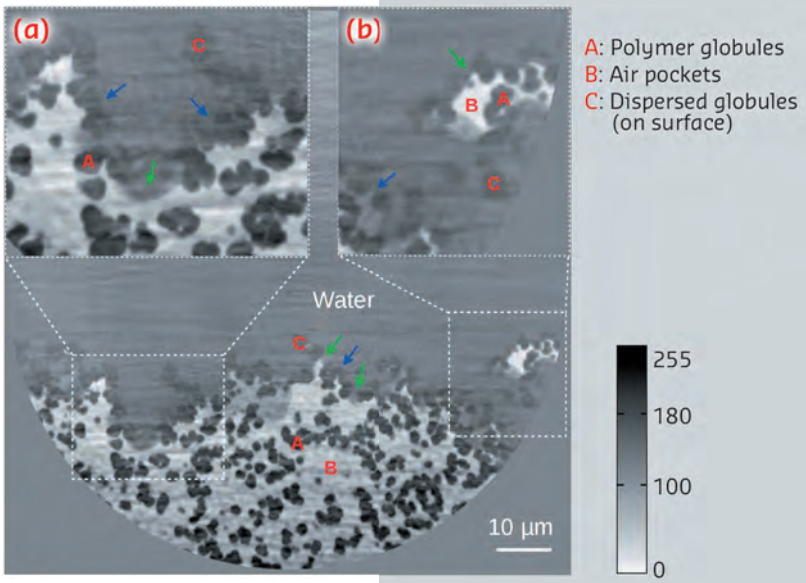

Fig. 68: Cross-section of the microporous BMA-EDMA surface on a glass substrate at an effective pixel size of 50 nm. Insets (a) and (b) are enlargements of the white dashed selections. Red colour labels A, B and C denote polymer globules, air pockets and dispersed globules, respectively. Air was trapped by the structured BMA-EDMA polymer. The coexistence of the Wenzel state (blue arrows) and Cassie–Baxter state (green arrows) was observed. A volume of 0.1×0.05×0.01 mm^3 was rendered in 3D via grey level segmentation, see **Figure 69a**.

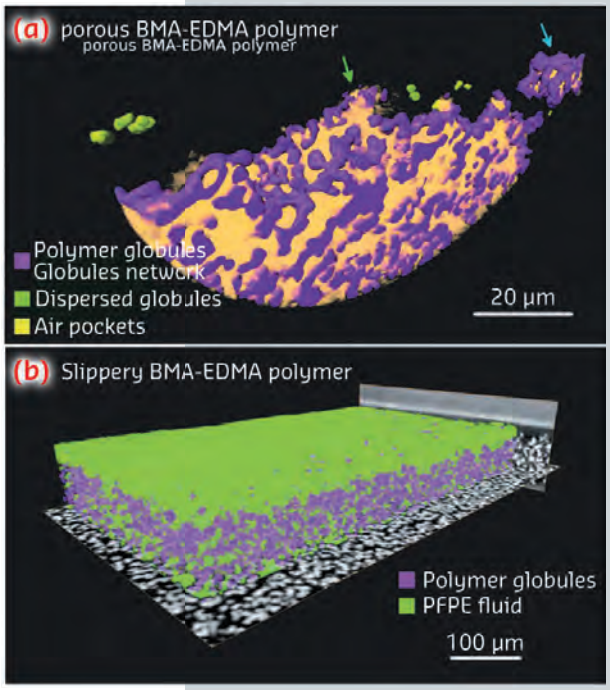

Fig. 69: a) Volume rendering of the local mass density of the porous BMA-EDMA surface, voxel size 50 nm. Blue and green arrows indicate Wenzel and Cassie–Baxter states, respectively. b) Rendering of the slippery BMA-EDMA surface with a voxel size of 0.32 µm.

To better understand such surfaces in their natural state, we investigated their structure on the micro- and nanoscale by three-dimensional (3D) hard X-ray phase tomography. To have a representative interface area, several mm thick samples were needed and therefore hard X-rays were used. Since water, lubricant (oil) and polymers provide weak absorption contrast, we used holotomography at the nano-imaging endstation ID22NI (now at ID16) for propagation-based phase imaging of such interfaces. Multilayer-coated Kirkpatrick–Baez (KB) optics provided a tightly focused spot (50×50 nm^2 H×V, FWHM) of monochromatic X-rays (E = 29.6 keV, $\Delta E/E \approx 10^{-2}$). The sample was placed downstream of the focus in the slightly diverging beam, and, by varying the source-specimen and specimen-detector distances, the geometrical magnification *M* and thus the spatial resolution of the imaging setup could be adjusted. Fresnel diffraction patterns acquired with different *M* and effective propagation distances *D* in this so-called projection microscopy set-up allow retrieval of the phase shift introduced by the specimen with a high sensitivity that allows us to distinguish between water, polymer and oil after tomographic reconstruction of the specimen's electron density.

As the material for our study, we chose porous poly(butyl methacrylate-co-ethylene dimethacrylate) (BMA-EDMA) surfaces, as described in [2]. The substrates of 5×25 mm^2 surface area were imaged inside a polypropylene tube of 8 mm diameter that was filled with water. Each scan at all four propagation distances took around 45 minutes.

The 2D distribution of the electron density on a tomographic cross-section through the substrate is shown in **Figure 68**. Water, air and polymer globules of the porous structure can be distinguished. The visualisation of the structure (see also **Figure 69**) allows us to identify regions which coexist and follow two existing models that explain the hydrophobicity of a porous surface, namely the Wenzel state [3], where the increased surface area of the rough interface is responsible for its hydrophobicity or the Cassie–Baxter state [4] where gas trapped between the rough surface and water favours hydrophobicity.

Figure 69 shows 3D visualisations of such interfaces at two different spatial resolutions in the nm-scale (a) and on the (sub-)µm scale. For the oil-infused surface in (b), such 3D

References
[1] T.-S. Wong, S.H. Kang, S.K.Y. Tang, E.J. Smythe, B.D. Hatton, A. Grinthal and J. Aizenberg, *Nature* **477**, 443–447 (2011).
[2] P.A. Levkin, F. Svec, J.M.J. Fréchet, *Adv. Funct. Mater.* **19**, 1993-1998 (2009).
[3] R.N. Wenzel, *Ind. Eng. Chem.* **28**, 988–994 (1936).
[4] A.B.D. Cassie and S. Baxter, *Trans. Faraday Soc.* **40**, 546–551 (1944).

data sets can be used to determine features such as the infusion quality or the spatial fluctuation of the thickness of the lubricant – here perfluoropolyalkylether (PFPE) oil – *e.g.*, due to the anisotropic pressure imposed by the surrounding water environment.

Summarising, we have demonstrated non-invasive direct 3D imaging of surface–water interfaces on hydrophobic porous BMA-EDMA and slippery BMA-EDMA surfaces with hard X-ray phase-contrast nanotomography. The method provides isotropic volumetric structural characterisation of complex interfaces as well as bulk materials from sub-µm to nm scales whilst preserving the ambient conditions and representative specimen sizes. These advantages are of central importance to help understand the correlations between surface properties and their physical micro- or nanostructures which are needed to identify present limitations of such coatings.

HOW CAN LOCAL ENVIRONMENTAL CONDITIONS INFLUENCE THE SECONDARY STRUCTURE OF AN AMYLOID BETA PEPTIDE?

Principal publication and authors
A. Accardo (a), V. Shalabaeva (a), M. Cotte (b), M. Burghammer (b), R. Krahne (a), C. Riekel (b) and S. Dante (a), *Langmuir* **30**, 3191–3198 (2014).
(a) Istituto Italiano di Tecnologia, Genova (Italy)
(b) ESRF

Extracellular amyloid plaques are a hallmark material for the study of Alzheimer's disease. The neurotoxicity of their main components, the amyloid β peptides (Aβs), may be mediated by their direct interaction with the neural lipid membrane. In order to shed more light on conformational and structural processes of amyloidosis involving membranes, we focused our attention on the Aβ(25–35) and Aβ(1-42) species in the presence of a phospholipid mixture that mimics the phospholipid composition of the neural membranes, *i.e.*, a lipid mixture made of POPC (1-palmitoyl-2-oleoylphospatidylcholine) and POPS (1-palmitoyl-2-oleoylphospatidylserine).

The investigation was supported by a multi-technique approach based on a combination of micro-Raman (µRaman), synchrotron radiation (SR) micro-Fourier-transform infrared spectroscopy (µFTIR) at ID21 and micro X-ray diffraction (µXRD) at ID13. In order to enhance the sensitivity of these probes, we deposited droplets with Aβ and phospholipid suspensions on highly hydrophilic nanostructured substrates. Ring-like solid residues were formed almost immediately due to the strong heterogeneous evaporation rate on hydrophilic substrates (**Figure 70a,b**). The aid of micro-fabricated supports for structural studies had already been successfully exploited in previous experiments **[1]**. As detected by µFTIR, the outer rim of Aβ-25-35 residue (**Figure 71a,b**) was characterised by β-sheet material

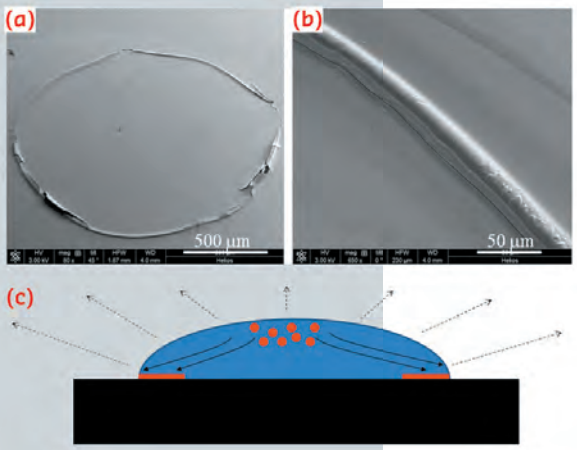

Fig. 70: a,b) SEM micrographs of Aβ(25–35) ring-like residues; c) Sketch of an evaporating droplet on a hydrophilic substrate. The evaporation rate is stronger near the contact line, provoking a radial convective motion of the solute from the centre toward the contact line.

(peak at 1634 cm^{-1}), while the inner zone (Figure 71c) contained peptide in α-helical conformation (1657 cm^{-1}). The high evaporation flux at the triple contact line resulted in an accumulation of solute while the inner regions were depleted (Figure 70c). Therefore, the convective flow and the enhanced peptide concentration in proximity to the external rim, have been shown to result in self-assembly of β-amyloid fibrils. At the inner rim, the lower amount of material was not sufficient for the α/β transition and the peptide remained arrested in a α-helical conformation. The Aβ(25–35)/POPC/POPS mixture showed, on the contrary, the exclusive presence of β-sheet material without any trace of α-helices indicating that the presence of phospholipids plays an active role in the fibrillation process, as already suggested by previous studies [2]. As a control, μFTIR experiments on Aβ(1–42) in the presence and absence of POPC/POPS revealed in both cases the presence of parallel β-sheet material. Complementary information on the crystalline fractions of the lipid and peptide system was obtained by micro small and wide angle X-ray scattering (μSAXS/WAXS). The pure Aβ(1–42) pattern (Figure 71d) showed β-sheet features with a 4.2 Å peak characteristic of the distance between hydrogen-bonded strands and a 10 Å peak due to the β-sheet stacking. In contrast, the Aβ(25–35) rim showed only a very weak signature of a peak in the range of 10 Å, suggesting stacking disorder (Figure 71e) and was further confirmed by a more detailed analysis of the peak profile by fitting Gaussian functions (Figure 71g). A composite peak with d ~4.7/4.1 Å (Figure 71g) agreed with the possible coexistence of a β-phase (4.1 Å) together with an α-phase (~4.7 Å).

Based on these results, we were able to demonstrate the presence of an α/β transition from the internal rim of the coffee-ring residues to the external rim in the pure Aβ(25–35) case, probably due to the convective flow inside the droplet sitting on highly hydrophilic substrates that enhances the local concentration of the protein at the external edge of the drying drop. In contrast, the presence of POPC/POPS lipids in the protein did not result in α-helical structures and introduced the presence of pure β-type material. An integrative μXRD analysis of the same residues confirmed the μFTIR experiments. Further work could help to clarify the role of enzymes, such as acetylcholinesterase, and of different lipid systems in the amyloidosis of the analysed peptides and of other Aβ fragments.

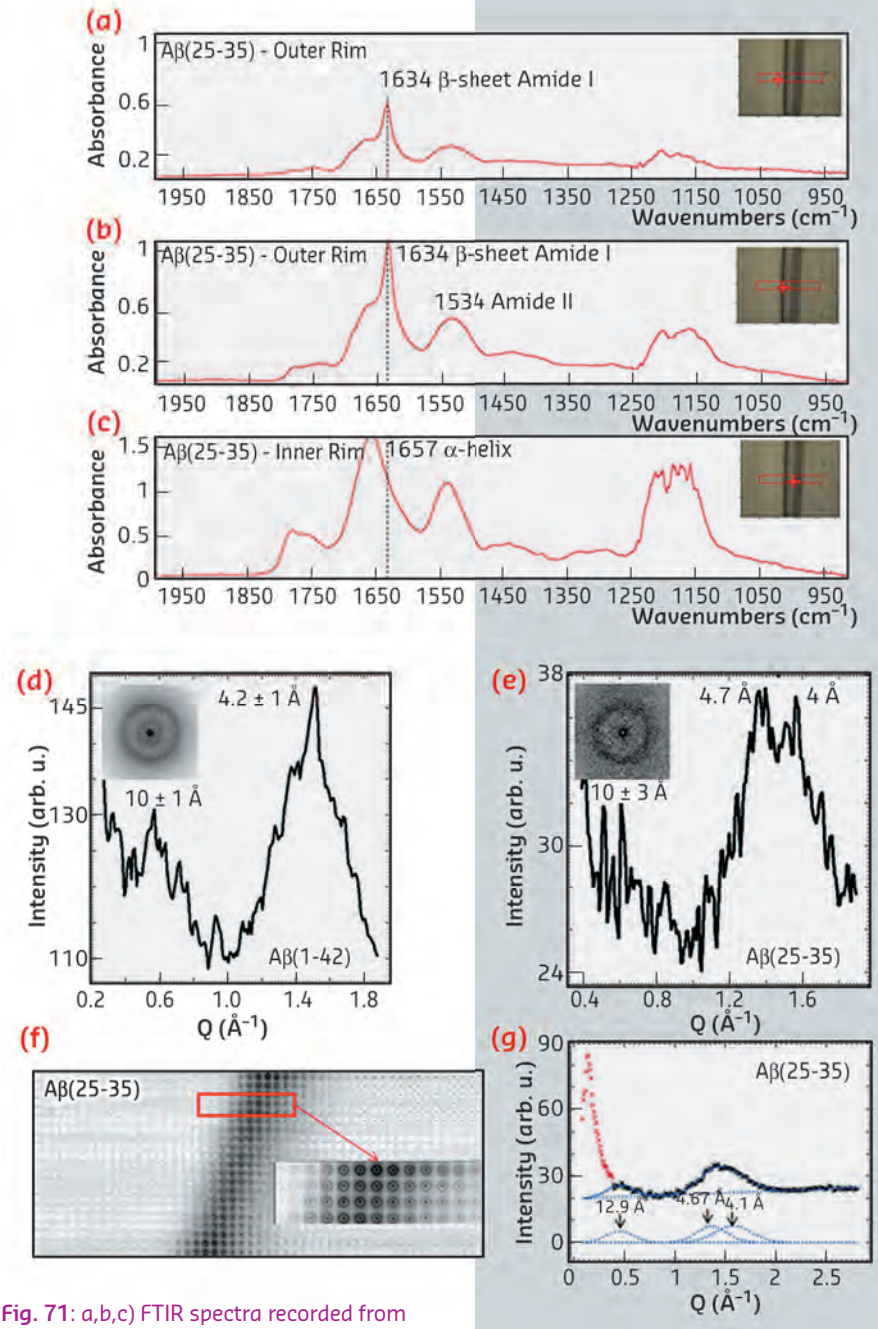

Fig. 71: a,b,c) FTIR spectra recorded from several regions of the Aβ(25–35) residue dried on highly hydrophilic BaF_2 surfaces. Typical μXRD mesh scan and relative azimuthal averages of the Aβ(1–42) (D) and Aβ(25–35) (e) droplet rims. (f) XRD mesh-scan of the Aβ(25–35) solid rim. (g) Peak fitting of the Aβ(25–35) XRD pattern of Figure 71e.

References

[1] A. Accardo, E. Di Fabrizio, T. Limongi, G. Marinaro and C. Riekel, *Journal of Synchrotron Radiation* **21**, 643-653 (2014).

[2] A.M. Sheikh and A. Nagai, *FEBS Journal* **278**, 634–642 (2011).

Authors
E. Pouyet (a,b), M.Cotte (a,c), A.Nevin (d) and D. Saviello (e).
(a) ESRF
(b) ARC-Nucléart - CEA/Grenoble (France)
(c) Laboratoire de Physique des Solides, UMR 8502 Université Paris Sud, Orsay (France)
(d) Consiglio Nazionale delle Ricerche – Istituto di Fotonica e Nanotecnologie (CNR-IFN), Dipartimento di Fisica, Politecnico di Milano (Italy)
(e) Dipartimento di Chimica Materiali e Ingegneria Chimica, Politecnico di Milano (Italy)

Micro-FTIR STUDY OF THE POLYMER DEGRADATION IN DESIGN OBJECTS

Recent developments in analytical chemistry are being put to good use in the study of artwork. Some analyses can be carried out directly on the objects, while in some cases, micro-fragments can be sampled, allowing a more accurate analysis of the material's composition, at the micrometre scale. Care is needed in the preparation of these tiny fragments to reveal as much detail as possible of their intrinsic structure (usually multi-layer) and to preserve the chemical and physical properties of the sample. New preparation strategies have been recently developed at beamline ID21 for thin sections from painting fragments [1]. We report here their application to the study of the degradation of acrylonitrile-butadiene-styrene (ABS) polymer in historical Italian design objects [2].

ABS has been widely used over the last 50 years as a plastic material in industrial applications. It is present in many design objects and household items such as telephones, domestic appliances, lamps, musical instruments, some of which are now being exhibited in international museums. However, as observed with paintings, ABS suffers from photo-ageing, which leads to the alteration of its physical properties, chemical modifications such as crosslinking and chain scission, colour changes (yellowing and discolouration) and worsening of mechanical performance. The objective of this study was to characterise and assess the depth of alteration in terms of chemical modifications on two types of samples: artificially photo-aged ABS blocks and fragments from historical Italian design objects from the 1960's [2] (**Figure 72**).

Fourier transform infrared spectroscopy (FTIR) is well suited to the characterisation of such materials since it probes molecular groups and allows the disappearance of the reactive groups and the formation of degradation products to be followed. In-depth analysis of such phenomena has already been reported, but limited by an in-depth resolution of about 100 µm [3]. The goal of the present study was to study transversal sections of the polymers with synchrotron-based micro-FTIR (at ID21), in order to locate the different components constituting the polymers, at the micrometre scale. This required the preparation of thin-sections (2 µm), sliced perpendicularly to the block surface. The sample fragment, smaller than 1 mm^3 and representative of the entire stratigraphy, was clamped between two sheets of polycarbonate or polyether ether ketone foil, PEEK, (3 × 6 x 1 mm^3). Thin-sections of different thicknesses were obtained using a microtome, at room temperature.

This method produced very thin samples with high surface quality while avoiding the use of embedding media and polishing or grinding; it solves the risk of chemical and analytical interference, both for IR and X-ray analyses.

On such a section, both the internal pristine polymer and the superficial products formed during photoageing can be identified and localised, in a single FTIR map. The visible image (**Figure 73a**) and UV fluorescence images (**Figure 73b**) highlight a luminescent upper layer of about 45 µm on the surface of an artificially aged block. In **Figure 73c**, three FTIR

Fig. 72: Italian design objects made of ABS. (left) Grillo (Marco Zanuso and Richard Saper for Siemens), 1965; (right) E63 (Umberto Riva for Francesconi) 1963, Private Collection.

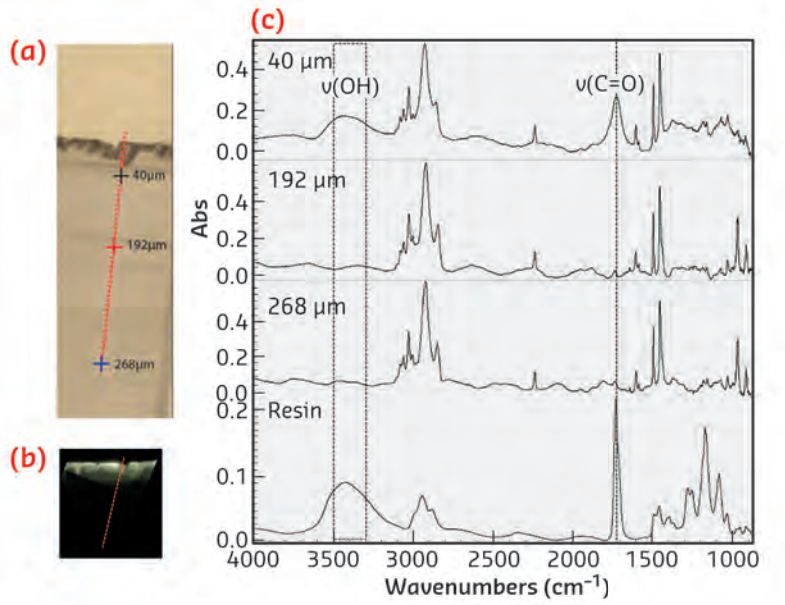

spectra from three different depths are shown: 40, 194 and 268 µm. When comparing surface and bulk areas, the spectra from the most external parts of the sample show a clear increase of the signal relative to C = O stretching in the region 1800-1600 cm^{1} and the appearance of an intense and broad signal relative to O-H stretching centred at 3436 cm^{-1}. These bands were attributed to ketones, aldehydes, esters, α,β-unsaturated carbonyl, carboxylic acids and alcohols. The depth of oxidation in samples was also evaluated, for samples aged for different amounts of time. µFTIR highlighted a selective and progressive gradient of degradation, greatest at the surface of the sample and which decreases in-depth. The oxidation compounds tend to form a passivation layer, limiting further oxidation of the bulk ABS [2].

To illustrate the strength of this sample preparation protocol, **Figure 73c** includes the spectrum of a standard embedding resin (Historesin, Leica), showing strong overlaps with FTIR bands characteristic of the chemical bonds formed during photo-ageing. Identification and precise localisation of these degradation compounds would have been difficult or even impossible using a standard resin embedding protocol.

Fig. 73: SR µFTIR study of the oxidation of an ABS model film (sample exposed to UV-irradiation for 1000 hours); a) Visible light microscope image of a 2 µm thin-section, b) UV light microscope images of 1000 hour aged ABS sample on the left, and of pure resin thin-section (2 µm) on the right c) FT-IR spectra acquired at different positions corresponding to three different depths from the sample surface and one spectrum characteristic of the absorption of an embedding resin, prepared as a 2 µm thin-section.

References
[1] E. Pouyet *et al.*, *Analytica Chimica Acta* **822**, 51-59 (2014).
[2] D. Saviello *et al.*, *Analytica Chimica Acta* **843**, 59-72 (2014).
[3] J.G. Bokria and S. Schlick, *Polymer* **43**, 3239-3246 (2002).

DYNAMICS AND EXTREME CONDITIONS

This year's highlights in dynamics and extreme conditions include the study of fundamental phenomena such as dynamics in glasses and clathrates, and magnetism at very high pressures beyond 200 GPa. This chapter also comprises work on the synthesis and *in situ* characterisation of novel materials at extreme conditions, the investigation of correlated electron systems, and unique insights into the structure and dynamical phenomena of Earth's interior. In addition, the chapter hosts a contribution on the atomic motion in network glasses revealed by coherent X-rays from beamline ID10A. Experiments performed at the Dynamics and Extreme Conditions Group's beamlines resulted in about 100 publications in peer reviewed journals with 20 papers in high-impact journals.

Besides user operation, the beamline teams and support groups were highly active in developing and implementing new instruments and facilities.

The technical design report for the hard X-ray microscope (HXRM) project at beamline ID06 has been completed, and the project has entered its implementation phase. In parallel, proof-of-concept experiments were conducted, and first results were recently published in *Nature Communications* (H. Simons *et al.*, *Nat. Commun.* **6**, 6098 (2015), doi: 10.1038/ncomms7098).

The large volume press (LVP at ID06) continued to operate at 30% of the standard allocation time for an ESRF beamline. Deformation experiments are now possible up to 10 GPa and 1700 K, with strain rates of 10^{-6} to 10^{-4} sec^{-1} and 35% maximum total strain. Two-stage X-ray transparent anvils were successfully commissioned, allowing fully open 2D solid-angle diffraction up to 20 GPa and 2000 K. Furthermore, new detection and data acquisition schemes are under development.

The technical design report for the move of ID09A to ID15B has been completed, and the current planning foresees the closure of the high-pressure branch of ID09 at the end of 2015. ID15B will be available for user operation from scheduling period II/2016 onwards.

New capabilities at ID27 comprise a Soller slit system interfaced to the CO_2 laser heating bench for the collection of high quality X-ray diffraction patterns at high pressures and temperatures, and the full remote control of the rotational-tomography Paris-Edinburgh cell (rotoPEC) for diffraction and imaging applications.

At the Nuclear Resonance Beamline (ID18), the portfolio of available Mössbauer isotopes was expanded to include the Ru-99 resonance (at 89 keV) and the Os-187 resonance (at 9.8 keV). The synchrotron Mössbauer source (SMS) setup took up nearly half of the available beamtime in 2014, focusing on investigations of magnetic and electronic properties under extreme conditions, including double sided laser heating capabilities.

The new inelastic X-ray scattering beamline, ID20, has reached all its target performances, and has been 100% available for user operation since 1 March 2014. As a consequence, the UPBL6 project was officially closed on 31 December 2014.

The high-throughput diffuse scattering diffractometer project, a side-station of beamline ID28, was officially launched in February 2014, and is well under way. First commissioning experiments are expected to take place towards the end of 2015.

External funding has become a significant complement to the investment and staff capacity of the group. The HXRM project at ID06 profits from collaboration with Technical University of Denmark (DTU), Norwegian University of Science and Technology (NTNU) and Utrecht University. A BMBF grant under the leadership of the Bayerisches Geoinstitut Bayreuth aims at the further development of high-pressure sample environment in materials at extreme conditions at ID18. Further support for ID18 has been received in the framework of the Helmholtz Russia Joint Research Group ("Sapphire ultra optics for synchrotron radiation"; FZ Jülich) and the XNAP collaboration for the development of a two-dimensional counting pixel X-ray detector based on silicon avalanche photodiodes. A further BMBF grant, led by the Goethe-Universität Frankfurt am Main, supports the installation of the high-throughput diffractometer for diffuse scattering studies as a side-station to beamline ID28. A second grant for ID28 (ANR-DPG grant; Goethe-Universität and ESRF) is dedicated to the understanding of the role of dynamic disorder in carbonates. Finally, ID27 profits from the ANR Blanc grant MOFLEX "Structure and dynamics of simple molecular fluids under extreme conditions of pressure and temperature", coordinated by IMPMC Paris and CEA Bruyères.

This year's achievements would not have been possible without a vibrant user community and the continuous support and effort of all the other ESRF divisions. The advent of the ESRF Upgrade Phase II provides a further stimulus for a sustained R&D programme. The significantly higher photon flux density will allow studies to be carried out on much smaller sample volumes at much higher pressures and temperatures, and on much shorter time scales. The increased coherence of the X-ray beam at high energies will allow new techniques to be used at extreme conditions such as imaging methods using phase contrast, coherent diffraction, and ptychography. For further details, please consult the chapter on matter at extreme pressures and temperatures in the recently published Orange Book.

M. KRISCH

FUNDAMENTAL PHENOMENA

ROLE OF DISORDER IN THE THERMODYNAMICS AND ATOMIC DYNAMICS OF GLASSES

In the late 1950s, the low-temperature thermal conductivity of glasses was found to be several orders of magnitude smaller and the heat capacity several times bigger [1] than those of crystals. The anomalously low thermal conductivity was soon successfully explained by phonon scattering caused by disorder. However, the understanding of the excess of the heat capacity demanded longer studies.

The excess of the heat capacity in glasses at ~10 K was found to be associated with a similar excess of the vibrational excitations in the ~1 THz frequency range of the density of states (DOS) *g(E)* [2]. In the reduced DOS presentation, $g(E)/E^2$, these states form a distinct peak (the so-called 'boson' peak) at a position where the reduced DOS of the corresponding crystals is nearly flat. This excess of heat capacity and the corresponding excess of vibrational states are universally observed for all glasses and with all relevant experimental techniques. Nevertheless, the results of numerous studies still do not converge to a unified answer on *how disorder causes*

Principal publication and authors
A.I. Chumakov (a), G. Monaco (b, a), A. Fontana (b, c), A. Bosak (a), R.P. Hermann (d, e), D. Bessas (d, e, a), B. Wehinger (a), W.A. Crichton (a), M. Krisch (a), R. Rüffer (a), G. Baldi (f), G. Carini Jr. (g), G. Carini (h), G. D'Angelo (h), E. Gilioli (f), G. Tripodo (h), M. Zanatta (i, c), B. Winkler (j), V. Milman (k), K. Refson (l), M. T. Dove (m), N. Dubrovinskaia (n), L. Dubrovinsky (n), R. Keding (o) and Y.Z. Yue (p), *Physical Review Letters* **112**, 025502 (2014).
(a) ESRF
(b) University of Trento (Italy)
(c) University of Rome (Italy)
(d) Jülich Centre for Neutron Science and Peter Grünberg Institut (Germany)
(e) University of Liege (Belgium)
(f) IMEM-CNR, Parma (Italy)
(g) IPCF-CNR, Messina (Italy)
(h) University of Messina (Italy)
(i) University of Perugia (Italy)
(j) Goethe-University, Frankfurt (Germany)
(k) Accelrys, Cambridge (UK)
(l) STFC Rutherford Appleton Laboratory, (UK)
(m) Queen Mary University of London (UK)
(n) University of Bayreuth (Germany)
(o) Max Planck Institute for the Science of Light, Erlangen (Germany)
(p) Aalborg University (Denmark)

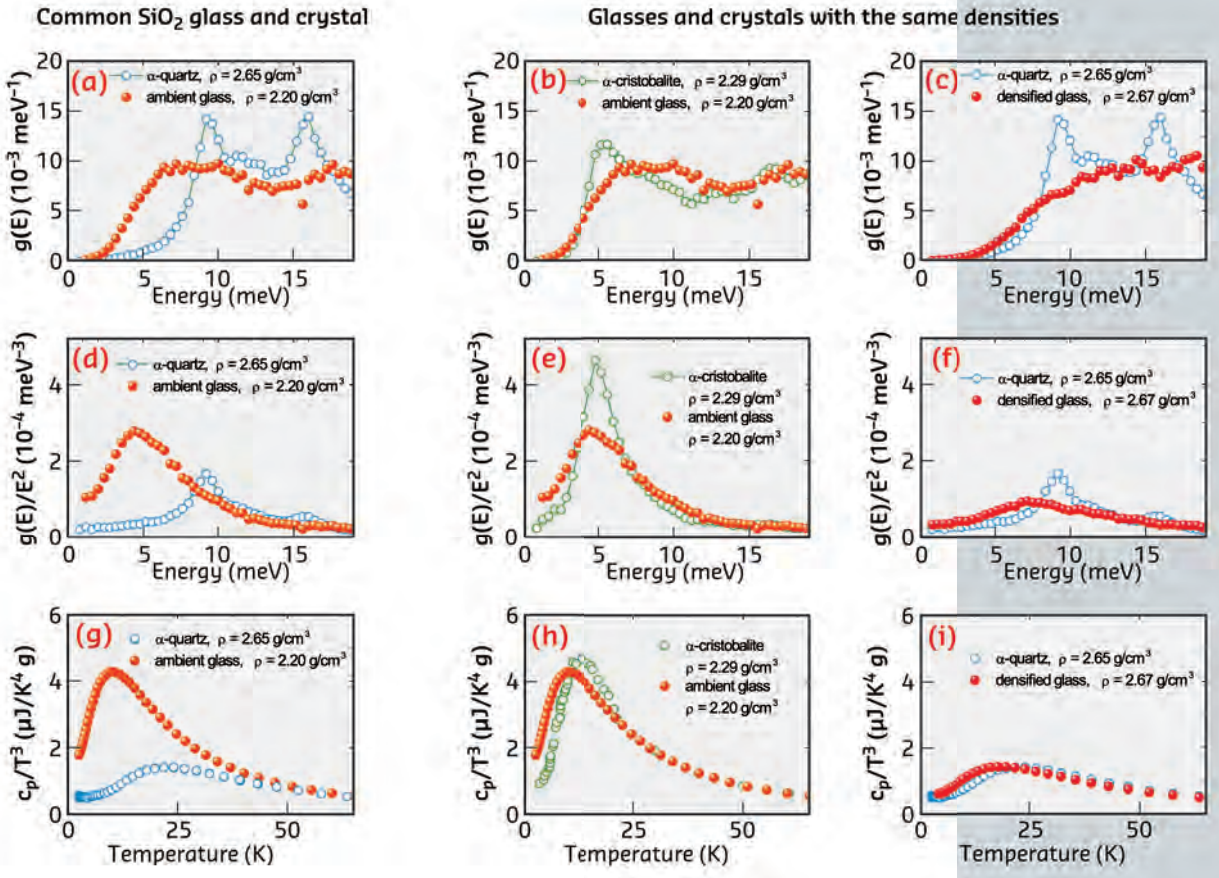

Fig. 74: The density of states *g(E)* (a–c), the reduced density of states $g(E)/E^2$ (d–f), and the heat capacity c_p/T^3 (g–i) for various glassy and crystalline polymorphs of SiO_2. The left panels (a, d, g) compare the most common glassy and crystalline polymorphs and reveal a noticeable difference in the displayed properties. The middle and the right panels compare the glassy and crystalline polymorphs with matched densities, namely, the low-density (b, e, h) and high-density (c, f, i) polymorphs. They demonstrate that the atomic dynamics and thermodynamics of the glassy and crystalline polymorphs with matched densities do not differ much from each other. From Ref. [3].

these features. Recent experiments conducted at beamlines **ID18** and **ID28** have now revealed that disorder actually *is not responsible*.

The studies were performed on SiO_2, which exists in various glassy and crystalline polymorphs with different structures and densities. The density (ρ) of the most common SiO_2 glass (ambient silica glass, ρ = 2.20 g / cm^3) is smaller than the density of the most common crystal (α-quartz, ρ = 2.65 g/cm^3). However, SiO_2 also exists in a lower density crystalline form (α-cristobalite, ρ = 2.29 g/cm^3). The density of this crystal is nearly the same as the density of the ambient glass. Furthermore, SiO_2 exists also in a higher-density glassy form (densified silica glass, ρ = 2.67 g/cm^3). The density of this glass is nearly the same as the density of α-quartz. Thus, SiO_2 offers a suitable 2×2 matrix of (dis)order versus density, which allows for a model-independent evaluation of the relative role played by structural disorder and density.

The measured DOSs revealed that SiO_2 glasses have the same number of low-energy states and the same number of excess states as SiO_2 crystals. For the most common glass, these states are located at lower energy than for the typical crystal and provide the higher heat capacity (left column of **Figure 74**).

For glasses and crystals with matched densities (middle and right columns of **Figure 74**), the excess states are located in the same energy region and provide the same heat capacity. Furthermore, the boson peak of glasses appears as a smooth counterpart of the van Hove acoustic singularity of the corresponding crystals.

Thus, being responsible for the anomalous *thermal conductivity* of glasses, disorder does not greatly affect the *frequency spectrum* of the atomic vibrations and the *heat capacity*. The usually lower heat capacity of glasses is caused by their usually lower *density*.

References
[1] R.C. Zeller, R.O. Pohl, *Phys. Rev. B* **4**, 2029 (1971).
[2] U. Buchenau, N. Nücker and A.J. Dianoux, *Phys. Rev. Lett.* **53**, 2316 (1984).
[3] A.I. Chumakov and G. Monaco, *J. Non-Cryst. Solids* **407**, 126-132 (2015).

LOCALISATION OF PROPAGATING PHONONS IN A PERFECTLY CRYSTALLINE SOLID

Principal publication and authors
S. Paìlhès (a), H. Euchner (b), V.M. Giordano (a,f), R. Debord (a), A. Assy (c), S. Gomès (c), A. Bosak (d), D. Machon (a), S. Paschen (e), M. de Boissieu (f), *Phys. Rev. Lett.* **113**, 025506 (2014).
(a) Institute of Light and Matter, UMR5306 Université Lyon 1-CNRS, Université de Lyon, Villeurbanne (France)
(b) Institute of Materials Science and Technology, Vienna University of Technology (Austria)
(c) Centre de Thermique de Lyon CETHIL UMR5008, UCBL, INSA de Lyon, CNRS (France)
(d) ESRF
(e) Institute of Solid State Physics, Vienna University of Technology (Austria)
(f) SIMAP, UJF, CNRS, INP Grenoble, St Martin d'Hères (France)

The energy loss due to thermal conversion processes has triggered the search for new functional materials allowing for more efficient energy consumption. Promising candidates are ultra-low thermal conductivity materials that can be made use of in thermoelectric converters for waste heat recovery as well as in thermal barrier coatings. In non-metallic crystalline solids, heat is mainly carried by atomic motion, in the form of propagating waves. In a quantum mechanical picture, the atomic vibrations can be described by means of the free motion of bosonic quasiparticles, known as phonons.

Cage-like structures encapsulating guest atoms or molecules such as clathrates, skutterudites, β-pyrochlore and zeolites are known to exhibit anomalously low thermal conductivities. The encaged atoms were formerly considered as independent oscillators and the observed suppression of the thermal conductivity was then rationalised by considering the inelastic resonant scattering of heat carrying phonons with these oscillators. However, in 2008, a study of phonons in skutterudites demonstrated that this intuitive picture of resonant scattering by loosely bound guest atoms is not applicable, putting into question the current understanding of the anomalous heat properties in these materials **[1]**.

We have investigated the mechanism at the origin of the low thermal conductivity in cage based materials by mapping the phonon states in the simplest representative intermetallic clathrate, Ba_8Si_{46} (see **Figure 75**), using Inelastic X-ray Scattering (IXS) at beamline **ID28**. Phonons propagating along the main crystallographic directions were studied and the corresponding IXS cross sections

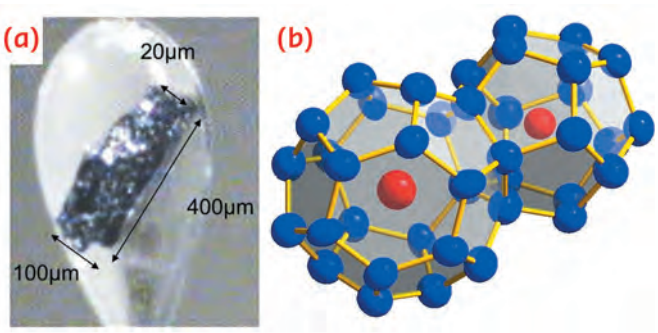

Fig. 75: a) Ba_8Si_{46} microcrystal grown at 5 GPa and 1000°C. **b)** Representation of face sharing $BaSi_{20}$ and $BaSi_{24}$ cages as building units of type-I clathrates. Atoms are represented by their atomic displacement ellipsoids obtained from single crystal X-ray diffraction.

were simulated by *ab initio* density functional theory (DFT) calculations. In **Figure 76**, raw data of constant Q-scans, along the [100] direction, are shown together with the corresponding simulated IXS spectra, convoluted with the instrumental resolution function. A surprisingly good agreement between the experimental and the simulated energy profiles can be observed for both the position and the energy width of the phonons. For phonon wave vectors close to the Brillouin zone centre (q –> 0), all phonon spectra consist of a main peak at energies distinctly below the optical (op) guest excitations, which stems from the acoustic (ac) branch and follows a linear dispersion. No energy broadening was needed to fit the acoustic and optic phonon profiles. The main effect that was observed in our experimental data was an abrupt decrease of the intensities of the acoustic phonons for wave vectors higher than a critical wave vector, q_c, concomitant with an increase of the intensities of the guest phonons. This was accompanied by a strong bending of the dispersion relation of the acoustic excitations, with its slope approaching zero. qc was interpreted as the limit of the acoustic regime above which the acoustic character of the modes vanishes. The abrupt changes of the acoustic intensities were remarkably well reproduced by the *ab initio* simulation.

In conclusion, the filling of the cages with guest atoms leads to the suppression of host propagative phonons, which are highly efficient at carrying heat, over a wide range of energies and wave vectors in phase space. The guest-host interaction can be understood as a purely harmonic process, *i.e.* it is not dominated by phonon-phonon scattering. The acoustic phonons preserve a very long lifetime and their propagative nature, until a critical wave vector is reached: at this point the character of the acoustic phonons changes, resulting in modes with an increasing contribution of the guest atoms. A careful theoretical analysis provides evidence that the guest modes are not propagative. These modes release their energy locally in an isotropic manner, leading to a change from a propagative to a diffusive energy transport mechanism, which may, in turn, be responsible for the low lattice thermal conductivity.

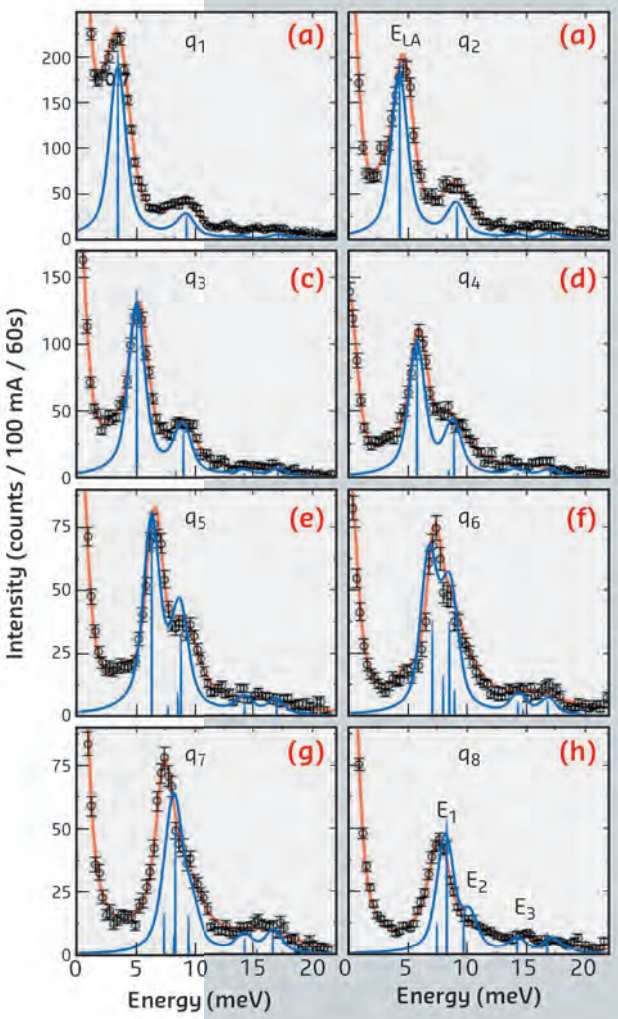

Fig. 76: a-h) Example of constant Q-scans for photons propagating along the 001 direction. Orange lines are fits of the data. Blue profiles correspond to the *ab inito* simulated IXS spectra, convoluted with the instrumental resolution function. The blue vertical lines indicate the simulated phonon positions without the convolution.

References
[1] M. Marek Koza, M.R. Johnson, R. Viennois, H. Mutka, L. Girard and D. Ravot, *Nature Materials* **7**, 805 (2008).

Principal publication and authors
B. Ruta (a), G. Baldi (b), Y. Chushkin (a), B. Rufflé (c), L. Cristofolini (d), A. Fontana (e), M. Zanatta (f) and F. Nazzani (g), *Nat. Commun.* **5**, 3939 (2014).
(a) ESRF
(b) IMEM-CNR Institute, Parma (Italy)
(c) Université Montpellier 2, Laboratoire Charles Coulomb UMR 5221 (France)
(d) Physics and Earth Sciences Department, Parma University (Italy)
(e) Dipartimento di Fisica, Trento University (Italy)
(f) Dipartimento di Fisica e Geologia, Universitá di Perugia (Italy)
(g) Department of Physics, University of Fribourg (Switzerland)

ATOMIC MOTION IN NETWORK GLASSES REVEALED BY COHERENT X-RAYS

The remarkable properties of glasses are related to their out-of-equilibrium state in which relaxations occur on time scales that were believed to be too long to be observed. Thanks to the use of coherent X-rays, it has been possible to investigate the atomic motion of a silicate glass and discover the existence of unexpected atomic rearrangements even in the deep glassy state, contrary to the common belief of a fully arrested state. These results modify our conception of the glassy state, suggest more experiments, and ask for a new microscopic theory of glass dynamics.

Glasses are essential materials in present day science and technology. The optimisation of the properties of materials for technological applications is often the result of a trial-and-error approach, as a basic understanding of many of their properties is still lacking. One of the challenges for glasses is that their intrinsic non-equilibrium nature poses formidable challenges both for experiments and theory. While important progress has been made in the understanding of the dynamics of their high temperature phases, the so called glass-forming liquid phase, a microscopic theory of glasses is still missing due to the extreme difficulty of probing the structural relaxation of a glass far below the glass transition temperature T_g, both with experiments and simulations [1].

Thanks to the instrumental developments in the collection of sparse scattering signals [2] and to an increased flux and coherence of X-ray beams, X-ray photon correlation spectroscopy (XPCS) has recently emerged as a very powerful technique able to follow the evolution of the dynamics at the atomic length scale in crystalline and amorphous materials [3].

We used XPCS at **ID10** to follow the temporal and temperature evolution of the relaxation dynamics for the first time in a prototypical network glass, a sodium silicate, at both the mesoscopic and atomic length scales. We revealed the existence of collective atomic motion in the glassy state. This is in contradiction with the common idea of an ultraslow arrested out-of-equilibrium state: upon cooling the system from the melt to the glassy state, the structural relaxation time strongly departs from the supercooled liquid behaviour and displays a weak temperature dependence characterised by relaxation times of about 10^3 s even in the deep glassy state (**Figure 77**). This fast atomic motion is accompanied by the absence of any detectable physical ageing, not even in the glass transition region, in disagreement with macroscopic studies and theoretical approaches (**Figure 77**) [1]. Indeed, current phenomenological models for relaxation in glasses, such as the TNM model [1], assume that the physical ageing takes place on a timescale comparable to the structural relaxation time, which is usually the case for macroscopic observables. In contrast to macroscopic studies, the microscopic dynamics remains stationary in the glassy state, even in those cases where

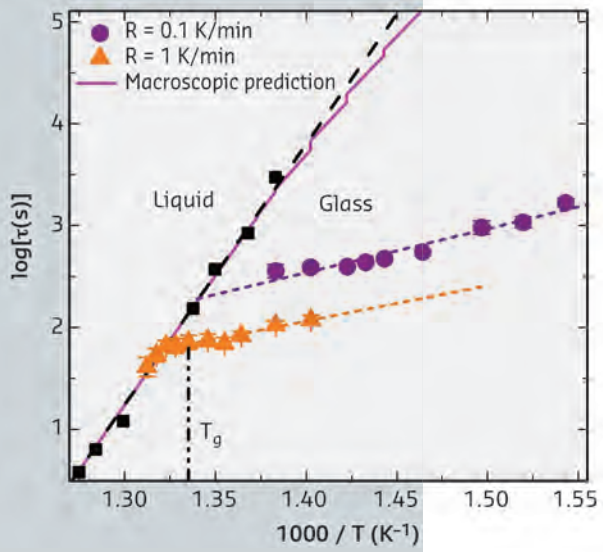

Fig. 77: Arrhenius plot of the relaxation times measured with XPCS at Q_{max} = 1.53 Å^{-1} (coloured symbols) by cooling from the ultraviscous liquid with different cooling rates R. Black symbols are macroscopic data taken from the literature. The dashed lines are Arrhenius fits while the full line is the macroscopic prediction of the TNM model [1].

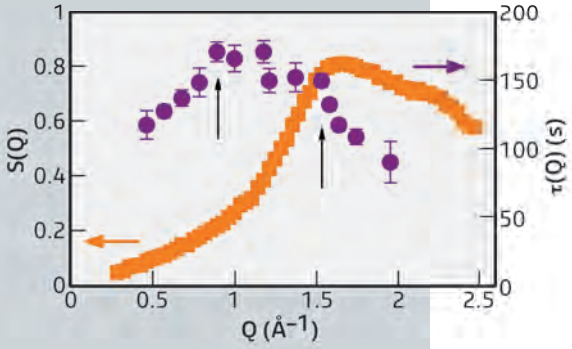

Fig. 78: Wave vector dependence of the relaxation times (circles) measured in a silicate glass cooled down to ambient temperature with a rate of 100 K/s from the high temperature melt. The data are reported together with the corresponding static structure factor (squares).

the annealing time is much longer than the structural relaxation time derived from a simple extrapolation of the supercooled liquid relaxation times. These results indicate that a different physical mechanism, unpredicted by previous experimental and theoretical studies, is responsible for the relaxation dynamics at the microscopic level.

Some insight into this novel dynamics can be gained by inspecting its dependence on the scattering vector. The relaxation time (τ) shows a broad peak with two contributions: a shoulder close to the position of the maximum of the static structure factor; a maximum in the pre-peak region, at lower scattering vectors, and corresponding to the mesoscopic scale (Figure 78). While the first is reminiscent of the de Gennes-like narrowing, also observed in coherent neutron scattering experiments of supercooled liquids, the second corresponds to the characteristic distance between the sodium diffusion channels in the network, in agreement with a high temperature simulation in molten silicates.

This observed complex microscopic dynamics calls for a reexamination of phenomenological models and highlights the need for a new microscopy theory for network glasses.

References
[1] L. Berthier and G. Biroli. *Rev. Mod. Phys.* **83**, 587-645 (2011).
[2] Y. Chushkin, C. Caronna and A. Madsen, *J. Appl. Cryst*. **45**, 807-813 (2012).
[3] B. Ruta *et al. Phys. Rev. Lett.* **109**, 165701 (2012).

CORRELATED ELECTRON SYSTEMS

HYPERFINE SPLITTING AND ROOM-TEMPERATURE FERROMAGNETISM OF Ni AT MULTIMEGABAR PRESSURE

High pressure generally leads to the suppression of ordered magnetism in the solid state. The critical pressure where magnetism disappears depends on the material. Here we observed ferromagnetism in Ni metal at room temperature up to 260 GPa, the highest pressure where magnetism has been reported.

The critical pressure at which a material becomes non-magnetic is of importance for the fundamental understanding of the origin of its magnetism. In particular, this is important for simple 3d-transition metals Fe, Co and Ni due to their technological use. Fe and Co become nonmagnetic above 16 [1] and 120 [2] GPa, respectively. In these cases, however, the collapse of ferromagnetism is associated with structural transitions of the crystal structure. In contrast for Ni, no structural transition is observed at least up to 200 GPa [3]. Thus, Ni is a good candidate to study solely the effect of pressure on the magnetic properties. It was shown recently by X-ray absorption spectroscopy that Ni stays ferromagnetic up to 200 GPa [3]. Theoretical calculation so far did not predict the critical pressure at which the magnetic moment is quenched. The calculations show that the ferromagnetic state is persistent up to 300 GPa at 0 K [4] and the Curie temperature is expected to decrease to room temperature at about 160 GPa [5] or at 300 GPa [6].

In this work, the magnetic properties of Ni metal under high pressure were investigated by nuclear forward scattering (NFS), using the 67.4 keV nuclear transition in ^{61}Ni. The measurements performed at beamline ID18 revealed the presence of magnetic hyperfine splitting of Ni metal at room temperature up to 260 GPa (see Figure 79), which confirm that Ni stays ferromagnetic up to this pressure. The magnetic hyperfine field shows a peculiar pressure dependence, reported in Figure 80. It slowly increases up to its maximum value around 225 GPa and then decreases towards higher pressures. This result seems to be in contradiction to the observed and theoretically predicted continuous decrease of the magnetic moment, which is supposed to be proportional to the magnetic hyperfine field.

Principal publication and authors
I. Sergueev (a), L. Dubrovinsky (b), M. Ekholm (c), O.Yu. Vekilova (d), A.I. Chumakov (e), M. Zajac (e), V. Potapkin (e,b), I. Kantor (e), S. Bornemann (f), H. Ebert (f), S.I. Simak (d), I.A. Abrikosov (d) and R. Rüffer (e), *Physical Review Letters* **111**, 157601 (2013).
(a) Deutsches Elektronen-Synchrotron, D-22607 Hamburg (Germany)
(b) Bayerisches Geoinstitut, Universität Bayreuth (Germany)
(c) Swedish e-Science Research Centre (SeRC), Department of Physics, Chemistry and Biology (IFM), Linköping University (Sweden)
(d) Department of Physics, Chemistry and Biology (IFM), Linköping University (Sweden)
(e) ESRF
(f) Department of Chemistry, Ludwig-Maximilians-Universität München (Germany)

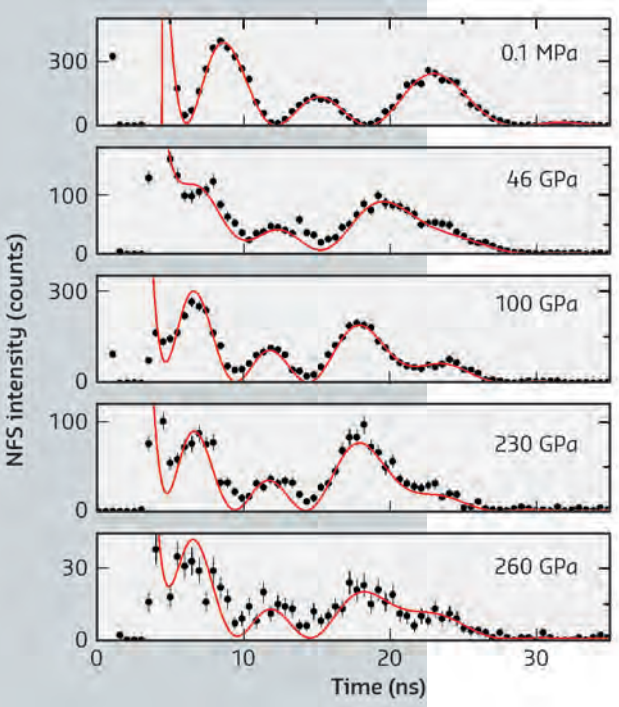

Fig. 79: Time evolution of the nuclear forward scattering for Ni measured at room temperature and different pressures. The solid lines show the best fit to the data. The oscillation period of the signal is inversely proportional to the magnetic hyperfine splitting.

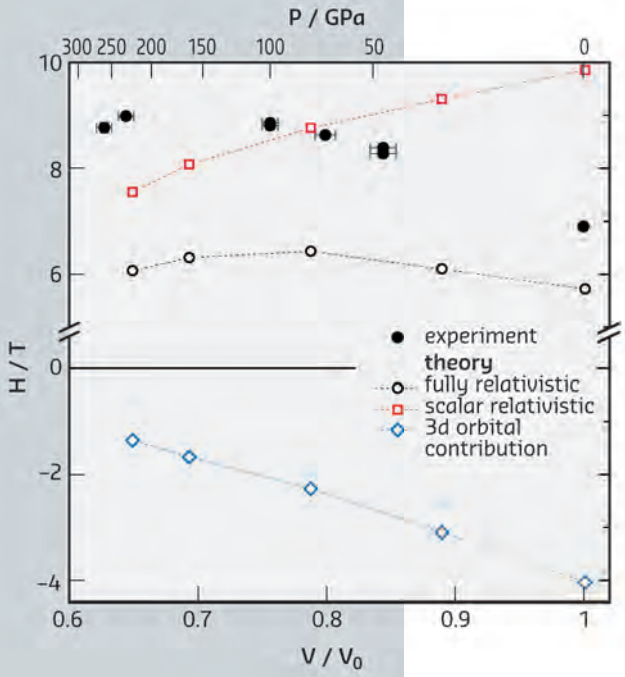

Fig. 80: Pressure dependence of the hyperfine magnetic field in Ni from experiment and theory, calculated using fully relativistic *ab initio* calculations. Positive and negative contributions to the calculated field are shown as scalar relativistic calculations (mainly due to the Fermi contact interaction) and 3d orbital contribution.

The theoretical explanation of this behaviour reveals the importance of relativistic effects. In fact, the hyperfine field consists of two main contributions of different signs: a positive contribution due to the Fermi contact interaction and a negative contribution due to the orbital magnetic moment of the 3d electrons induced by spin-orbit coupling. The magnitude of both contributions decreases with pressure, similar to the magnetic moment but with different slopes. Thus, the sum of the two contributions, that determines the total hyperfine field, increases up to 100-180 GPa, reproducing well the experimentally observed behaviour.

This work demonstrates a breakthrough in the technique that enables magnetism to be studied in Ni containing compounds at high and ultra-high pressures. The efficiency of the method significantly benefits from the application of high pressure because of the hardening of the material and, consequently, a substantial increase in the Lamb-Mössbauer factor. Thus, the highest pressure observed in this work is not limited by the NFS technique but by the mechanical stability of the diamond anvil cells used. Recent advances in high pressure technology [7] as well as the decrease of the X-ray source size with the future upgrade of the ESRF would allow the technique to study Ni and Ni containing compounds at pressures even above 500 GPa.

References
[1] O. Mathon *et al.*, *Phys. Rev. Lett.* **93**, 255503 (2004).
[2] R. Torchio *et al.*, *Phys. Rev. B* **84**, 060403 (2011).
[3] R. Torchio *et al.*, *Phys. Rev. Lett.* **107**, 237202 (2011).
[4] T. Jarlborg, *Physica C* **385**, 513 (2003).
[5] S. Shang *et al.*, *J. Appl. Phys.* **108**, 123514 (2010).
[6] V. G. Tissen, *Sov. Phys. Solid State* **25**, 11 (1983).
[7] L. Dubrovinsky *et al.*, *Nature Communications* **3**, 1163 (2012).

MATERIALS SYNTHESIS

DIVERSE CHEMISTRY IN THE MAGNESIUM/CARBON SYSTEM

Magnesium and carbon, both of which form numerous compounds with other elements, have a remarkably low affinity for one another. At ambient pressure, only the reaction of Mg or MgO with hydrocarbons leads to the formation of metastable carbides with reasonable yields, and pure Mg and carbon do not react to form stable compounds at any temperature. With experimental data obtained at beamline **ID06LVP**, we have demonstrated that thermodynamically stable Mg-C compounds are indeed possible under high-pressure conditions (above 5 GPa and 1300 K). The new compound synthesised, β-Mg_2C_3, crystallises in the monoclinic *C2/m* space group, and contains rare allene-derived C_3^{4-} anions that are isoelectronic with CO_2.

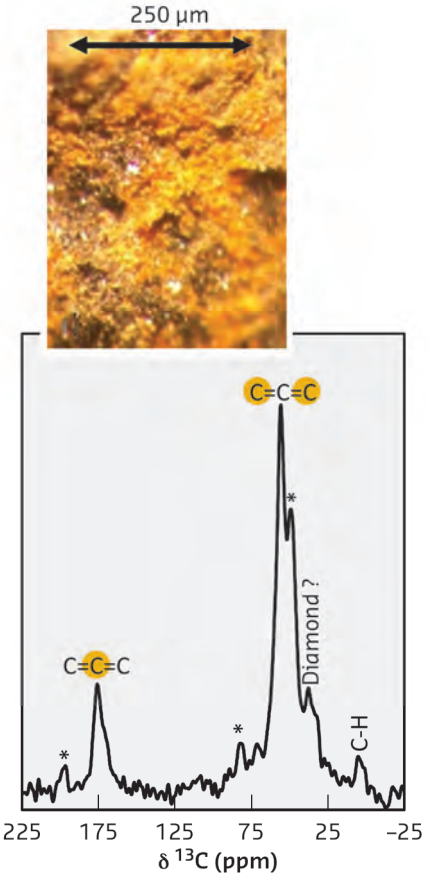

Fig. 81: ^{13}C MAS NMR spectrum of β-Mg_2C_3 recovered from 9 GPa showing two unique carbon environments. Inset: optical microscope picture of the golden-yellow powder.

A bright golden-yellow powder of this new Mg-C compound was recovered from high-pressure, high-temperature experiments (**Figure 81**). Mass spectrometry analysis of the hydrolysis products showed allene, C_3H_4, indicative of the presence of C_3^{4-} anions within the structure. In addition, ^{13}C NMR analysis confirmed the presence of two structurally distinct carbon atoms in an approximate 1:2 ratio, and Raman spectra indicated carbon stretching modes from [C=C=C]. The crystal structure –clearly distinct from previously reported compounds– was, however, impossible to solve using the available powder X-ray diffraction data.

To resolve the structure of this new magnesium carbide, two important steps were taken. First, potential Mg_2C_3 structures were predicted using USPEX, an *ab initio* structural evolution algorithm. Second, *in situ* high-pressure synthesis was performed at beamline ID06 using the recently-commissioned large-volume press. The *in situ* synthesis allowed the nearly phase-pure synthesis of the new compound, and high-resolution X-ray diffraction patterns obtained allowed conclusive comparison with theoretical models.

Remarkably, the high-pressure Mg_2C_3 structure predicted via USPEX was a perfect match to the experimental X-ray diffraction data (**Figure 82**). Thus, the structure of β-Mg_2C_3 was solved. Unlike α-Mg_2C_3,

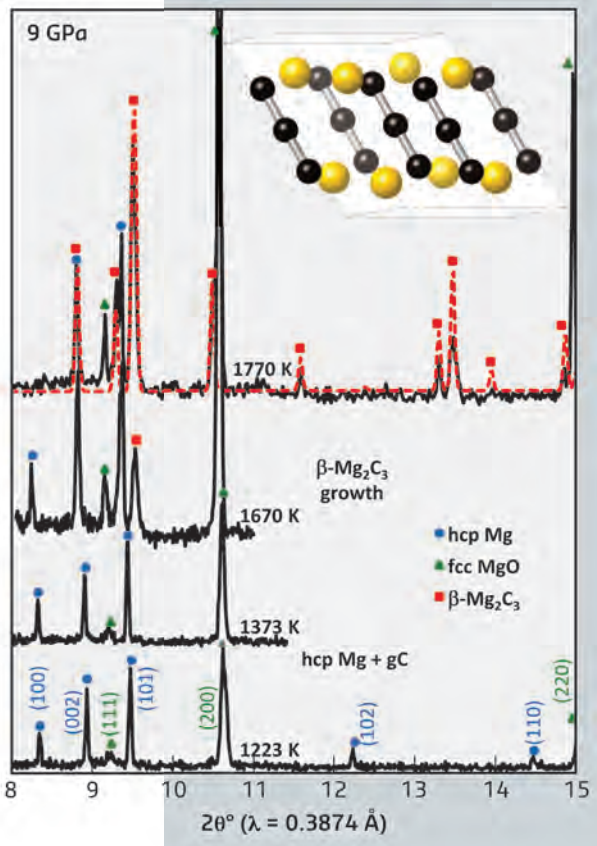

Fig. 82: *In situ* diffraction data collected during HPHT synthesis at ID06. Crystal structure of β-Mg_2C_3 showing C_3^{4-} ions aligned along the c-axis.

Principal publication and authors
T.A. Strobel (a), O.O. Kurakevych (a, b), D.Y. Kim (a), Y. Le Godec (b), W. Crichton (c), J. Guignard (c), N. Guignot (d), G.D. Cody (a) and A.R. Oganov (e-h), *Inorg.Chem.* **4**, 53, 7020–7027 (2014).
(a) Geophysical Laboratory, Carnegie Institution of Washington, Washington DC (USA)
(b) Institut de Minéralogie, de Physique des Matériaux et de Cosmochimie, UPMC,CNRS, Paris (France)
(c) ESRF
(d) SOLEIL, Gif-sur-Yvette (France)
(e) Department of Geosciences, SUNY, Stony Brook, NY (USA)
(f) Institute for Advanced Computational Science, SUNY, Stony Brook, NY (USA)
(g) Moscow Institute of Physics and Technology, Dolgoprudny City (Russian Federation)
(h) Northwestern Polytechnical University, Xi'an (China)

which contains alternating layers of C_3^{4-} chains oriented in opposite directions, all C_3^{4-} chains within β-Mg_2C_3 are nearly aligned along the crystallographic c-axis.

After exploring pressure as an additional dimension for the chemistry of the Mg–C system, four magnesium carbides are now known: (1) tetragonal MgC_2, (2) orthorhombic α-Mg_2C_3, (3) monoclinic β-Mg_2C_3, and (4) cubic Mg_2C [1]. Taking into account that, at ambient pressure and at pressures up to ~5 GPa, the elements do not interact at any temperature, it is quite astonishing to observe such rich chemistry.

Finally, these results indicate that the Mg-C system should be completely revised under high pressure [2]. The phase behaviour in this system is important for the production of structurally-perfect diamonds with high growth rates as compared to other known metal-carbon systems, and also for the synthesis of unique nitrogen-free and boron-doped semiconductive diamonds. With these new results, we now have a much deeper understanding of Mg-C thermodynamics under extreme conditions.

References
[1] O.O. Kurakevych, T.A. Strobel, D.Y. Kim and G.D. Cody, *Angew. Chem. Int. Ed.* **52**, 8930-8933 (2013).
[2] O.O. Kurakevych, Y. Le Godec, T.A. Strobel, D.Y. Kim, W.A. Crichton and J. Guignard, *J. Phys. Chem. C* **118**, 8128–8133 (2014).

A NEW CRYSTAL PHASE OF FERROCENE

Principal publication and authors
D. Paliwoda (a,b), K. Kowalska (a), M. Hanfland (b) and A. Katrusiak (a), *J. Phys. Chem. Lett.* **4**, 4032–4037 (2013).
(a) Faculty of Chemistry, Adam Mickiewicz University, Poznan (Poland)
(b) ESRF

In 1951 the serendipitous discovery of ferrocene, $FeC_{10}H_{10}$, bis(cyclopentadienyl)iron(II), the first and one of the most stable metallocenes, ignited the 'explosion' of organometallic chemistry [1,2]. Since then, thousands metallocenes and their derivatives have been synthesised and used as catalysts in chemical laboratories and in technological processes [3,4]. The proposed sandwich-like structure of the ferrocene molecule, consisting of two parallel cyclopentadienyl (*Cp*) rings with Fe^{2+} ion sandwiched in-between, was soon confirmed by spectroscopic and X-ray diffraction studies. The structure of ferrocene has been determined independently in several laboratories, but its molecular conformation and interactions remained unclear. Under normal conditions, ferrocene polymorph I is monoclinic with staggered cyclopentadienyl rings, *i.e.* their torsion angles τ equal to 36° + *n*·72° (τ is defined as torsion C-c*Cp*···c*Cp'*-C', where unprimed and primed symbols refer to two *Cp*-rings of one molecule, c*Cp* and c*Cp'* are the rings centroids, and *n* is an integer). The staggered conformation is energetically unfavoured and high-resolution neutron-diffraction measurements revealed structural models with *Cp*-rings disordered in two or three sites (Figure 83). Below 164 K, ferrocene I transforms into the triclinic form II, where the *Cp*-rings of two independent molecules are each distorted by about 9° off the energetically favoured eclipsed conformation (τ = 0°, Figure 83). Dunitz *et al.* [5] crystallised ferrocene below 98 K and obtained its orthorhombic polymorph III with the *Cp*-rings eclipsed at τ equal to 0°. These results suggested that the unfavoured staggered conformation in ferrocene I is promoted by intermolecular interactions. However, under normal conditions, these crystal cohesion forces are too weak to completely stabilise the molecular rings at the unfavourable staggered conformation. The intermolecular interactions of

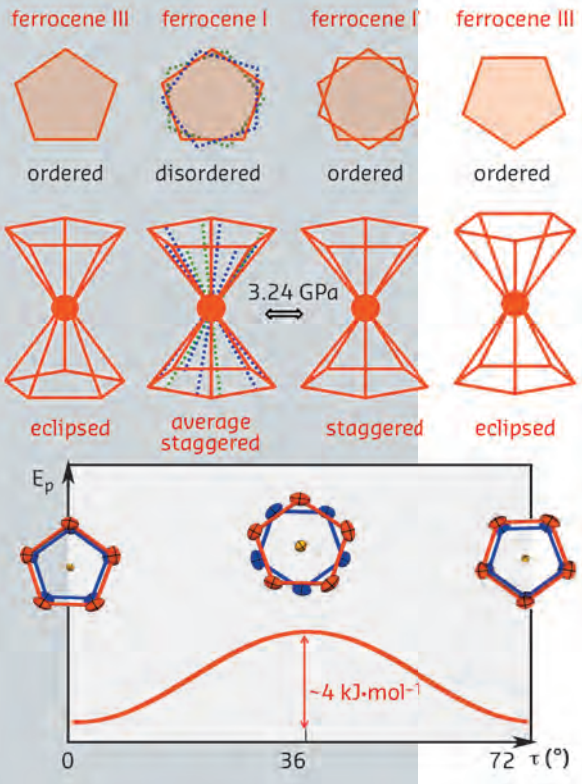

Fig. 83: Schematic illustration of the conformers of ferrocene molecule and their potential energy function (E_p). The torsion angle τ describes the mutual orientation of the cyclopentadienyl rings (*Cp*), as defined in the text. The dotted green and blue lines in the drawing of the molecule in phase I indicate the positions of disordered *Cp*-rings.

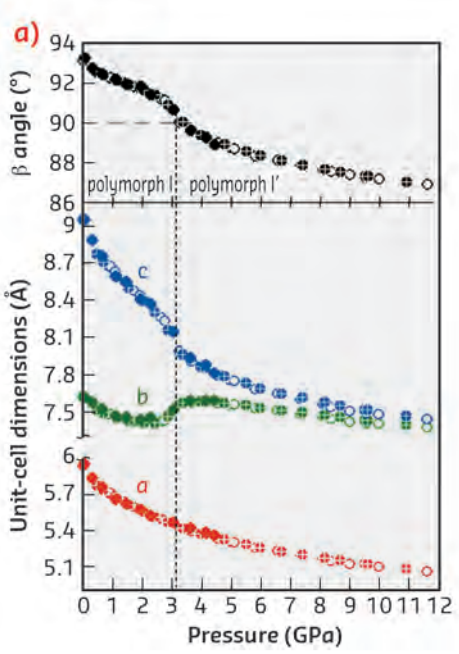

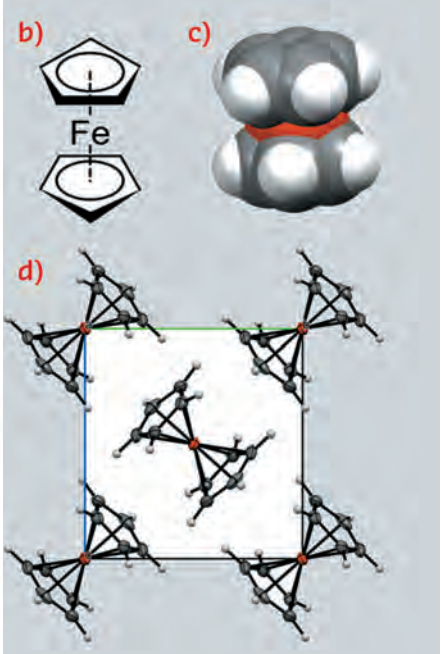

Fig. 84: a) Unit-cell dimensions of ferrocene phases I and I' compressed up to 11.6 GPa. The vertical dashed line marks the transition between phases I and I' at 3.24 GPa. The filled circles represent laboratory data, crossed circles and empty circles indicate the compression and decompression runs measured at beamline ID09A, respectively; b) structural formula of the molecule in the staggered conformation, used in most chemistry textbooks; c) space-filling model of the ferrocene molecule in phase I; and d) molecules of ferrocene located at the inversion centres in the monoclinic polymorph I'.

ferrocene I have been enhanced by high pressure in our single-crystal X-ray diffraction experiment performed at beamline **ID09A**. We found that ferrocene I undergoes an isostructural phase transition at 3.24 GPa (**Figure 84**), preserving the crystal unit cell and symmetry of space group $P2_1/n$. Therefore, this new high-pressure phase of ferrocene has been denoted as phase I'. In its structure, the molecules are 'pushed' by intermolecular forces into the staggered conformation and the disorder of *Cp*-rings is eliminated. This result is consistent with the occurrence of the average staggered conformers unfavoured by 4 kJmol^{-1} in ferrocene I. In contrast, this pressure-induced phase transition is in many respects different to most other order-disorder phase transitions. Usually in high-temperature phases molecules or ions are disordered, in two or more equivalent or nearly equivalent sites. On lowering temperature, the disorder in the structure is eliminated when *Cp*-rings reside in only one of the sites. Thus, below 164 K the disordered ferrocene I transforms into ferrocene II with two independant molecules ordered. We were able to show that high pressure has a very different effect on the crystal structure, and that in ferrocene I' it does not favour any of the disordered sites, but the average and the least energetically-favoured conformation. We were also able to explain the U-turn shaped compression of the unit-cell parameter b, by the compensation of the shortest intermolecular distances in the compressed structure. However, several intriguing observations could be made about the measured data. The discontinuities in unit-cell parameters occur when angle β, obtuse in ferrocene I, passes through 90° and it becomes acute in phase I'. The β = 90° coincides with the point of structural transformations when the first and second shortest intermolecular contacts between the centres of molecules in ferrocene I become equal and then reversed in phase I'. In these respects, the structure of ferrocene phases I and I' resembles a mechanical box with meshing gears regulated by their positions and distances. Our study shows that a lot of information is still missing for a complete understanding of the basic properties of prototypical compounds at their molecular level, and that high pressure studies provide a new perspective for their investigation.

References
[1] T.J. Kealy and P.L. Pauson, *Nature* **168**, 1039–1040 (1951).
[2] P.L. Pauson, *J. Organomet. Chem.* 637–639, 3–6 (2001).
[3] H. Werner, *Angew. Chem. Int. Ed.* **51**, 6052–6058 (2012).
[4] G.B. Kauffman, *J. Chem. Educ.* **60**, 185–186 (1983).
[5] P. Seiler and J.D. Dunitz, Acta *Crystallogr. Sect B* **38**, 1741–1745 (1982).

$(N_2)_6NE_7$: A HIGH PRESSURE VAN DER WAALS INSERTION COMPOUND

Through increased pressure, two different atomic or molecular species that interact via weak van der Waals forces can auto-organise to form stoichiometric compounds, called van der Waals compounds. The effect of pressure is to modify the microscopic interactions and stabilise new structures. Remarkably, none of these van der Waals compounds have

Principal publication and authors
T. Plisson (a), G. Weck (a) and P. Loubeyre (a), *Phys. Rev. Lett.* **113**, 025702 (2014).
(a) CEA, DAM, DIF, Arpajon (France)

been observed at low temperatures in cryocrystals, which makes pressure a powerful driving force for self-assembly of molecular compounds.

Most of the compounds that have been observed so far under pressure, such as $NeHe_2$, $Ar(H_2)_2$, $CH_4(H_2)_2$, $Xe(O_2)_2$ crystallise in the form of Laves phases, *i.e.* analogous to intermetallic compounds and colloidal systems, the stability of which is explained in terms of binary crystals of hard sphere like particles. However, the van der Waals forces can also be anisotropic which, combined with packing constraints, may lead to more exotic structures. For example, in pure N_2, the quadrupole-quadrupole interaction between the N_2 molecules is responsible for a rich polymorphism under pressure.

In this study, we have discovered a new type of van der Waals compound in the N_2-Ne system at high pressure. This compound has the stoichiometry $(N_2)_6Ne_7$, with the structure of a clathrate-like insertion compound. It is the first van der Waals clathrate ever observed and it could open a route for the development of a new family of host-guest systems in high pressure molecular systems.

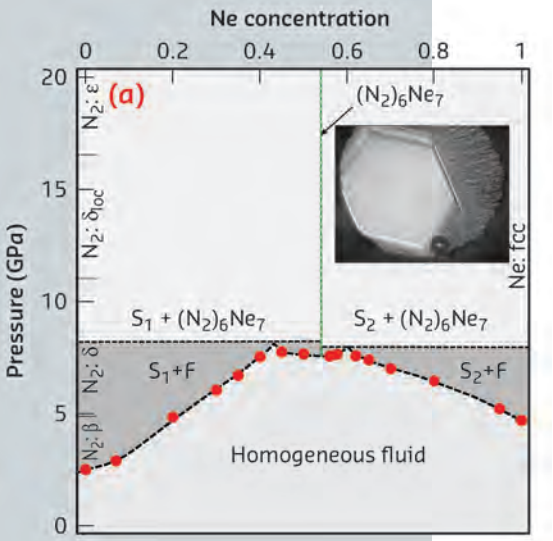

Fig. 85: Binary phase diagram of the N_2-Ne mixture at 296 K, plotted as pressure vs Ne concentration. S1 and S2 are the pure solids and F is the fluid phase. Inset: Photograph of a single crystal of $(N_2)_6Ne_7$ surrounded by a solid-solid phase separation, in the diamond anvil cell.

To unveil the existence of this stoichiometric compound, we performed a detailed measurement of the N_2-Ne binary phase diagram, at ambient temperature, by studying 16 different concentrations, as shown in **Figure 85**. The fluid mixtures were loaded in a diamond anvil cell. A ruby gauge was used to measure the pressure of the sample. The different phases were identified by Raman spectroscopy of the vibration modes of the N_2 molecule.

The sample was compressed to several gigaPascals, and the solidification was observed visually through the diamond anvils, using a microscope. The pressure at which the solid crystal disappears in the liquid is the melting pressure for a given concentration (red dots in **Figure 85**). The particular form of the binary phase diagram reveals the presence of a stoichiometric compound at 54 mol% concentration of neon, corresponding to the formula $(N_2)_6Ne_7$. At this pressure, congruent melting was observed and a solid with hexagonal structure was identified, as shown in the inset of **Figure 85**.

The structure of this compound was determined by single-crystal angular dispersive X-ray diffraction at beamline

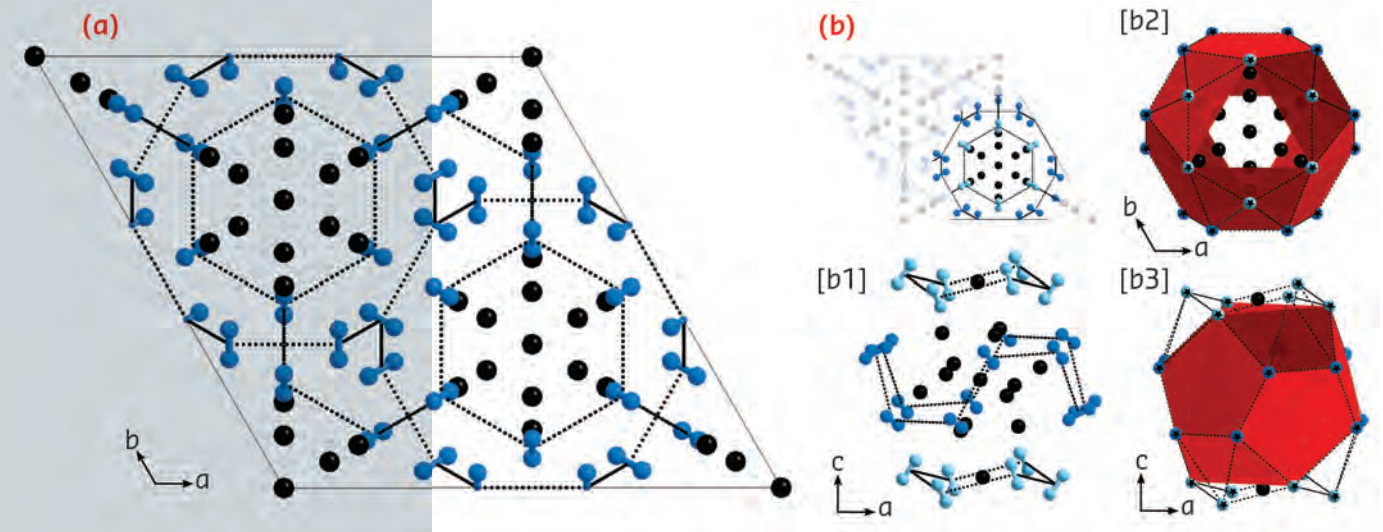

Fig. 86: Crystal structure of the $(N_2)_6Ne_7$ compound. Neon and nitrogen are represented by black and blue spheres respectively. The red planes show the surfaces supported by the centres of the N_2 molecules.

ID09A. The synthesis of a high quality single crystal, and the use of a high brilliance, monochromatic synchrotron beam optimised for diffraction at extreme conditions using diamond anvil cells was essential to the determination of the structure of $(N_2)_6Ne_7$. The diffraction signal was composed of 225 reflections, which were indexed to find that the structure is hexagonal with symmetry R-3m. The positions of the atoms were determined by direct methods and refined. The structure is shown in **Figure 86** The N_2 molecules surround the Ne atoms, forming cages with pentagonal faces, similar to the structures of clathrates. The fact that van der Waals interactions could drive the self-organisation of such a complex structure was unexpected. The prediction of this structure could be a challenging test for first principle calculations.

Such an exotic structure could also be used to stabilise new compounds synthesised at high pressure. For example, pure nitrogen was shown to polymerise at high pressure [1]. This polymeric single-bonded form is known to be a dense high-energy material that could be used as fuel, explosive or propellant. But it has not yet been recovered at ambient pressure. Constraining the geometry of the nitrogen molecules in such van der Waals compounds could change the conditions of polymerisation and the recovery of the polymeric compound at lower pressure. It could also serve as a pathway for the observation of other allotropic structures predicted theoretically, among which is an intriguing diamondoid structure formed by N_{10} cage units [2]. The compression of this compound to the megabar range is underway.

References
[1] M.I. Eremets, A.G. Gavriliuk, I.A.Trojan, D.A. Dzivenko and R. Boehler, *Nat. Mater.* **3**, 558 (2004).
[2] X. Wang *et al*, *Phys. Rev. Lett.* **109**, 175502 (2012).

EARTH AND PLANETARY SCIENCE

MELTING OF SUBDUCTED BASALT AT THE CORE-MANTLE BOUNDARY

Principal publication and authors
D. Andrault (a), G. Pesce (a), M.A. Bouhifd (a), N. Bolfan-Casanova (a), J.-M. Hénot (a) and M. Mezouar (b), *Science* **344**, 892-895 (2014).
(a) Laboratoire Magmas et Volcans, Université Blaise Pascal, CNRS, IRD, Clermont-Ferrand (France)
(b) ESRF

Seismological studies have demonstrated the complexity of the lowest 150-300 km-thick mantle layer, called the D" layer, situated just above the core-mantle boundary (CMB) [1] (see **Figure 87**). The anomalies detected could arise from various types of chemical or mineralogical heterogeneities including phase transitions in mantle minerals, chemical reactions with the outer core, presence of an ancient (crystallised) basal magma ocean and/or the deep descent of subducted slabs. Partial melting of the bulk mantle is often advocated to explain the seismic features, but it cannot explain the non-ubiquitous character of the ultra-low velocity zones (ULVZ). Partial melting would require a very hot core, higher than 4150 K [2,3], which is more than 1000 K above the mantle adiabat extrapolated to the CMB. Moreover, the hypothesis of a very hot core would be at odds with the current explanation for the existence of a geodynamo over prolonged geological periods.

In search of an alternative, researchers explored the melting properties of mid-oceanic ridge basalt (MORB), which can reach the lowermost mantle following subduction of oceanic crust. In the lower mantle, the MORB presents four coexisting phases: free silica, the Mg and Ca bearing silicate perovskites and a cage-type structure like calcium-ferrite. This mineralogy is radically different from the bulk mantle and, therefore, the melting properties should also be different. Due to the number of chemical elements, melting occurs progressively from the solidus, where the liquid contains a high concentration of incompatible elements, to the liquidus. The difference between solidus and liquidus can be of several 100 K at the CMB pressure of 135 GPa.

The difficulty of the experiments was therefore to determine the onset of melting using a laser heated diamond anvil cell at pressures of the CMB. The sample behaviour was followed continuously using *in situ* X-ray

diffraction at beamline **ID27**. Upon heating, we observed a sequence of events: crystallisation of the high-pressure phases; continuous grain growth; and then the sudden apparition of much larger spots on the CCD detector. These spots moved quickly and eventually disappeared, and randomly reappeared, as a function of time. The fast grain rotation indicates partial melting of the sample. At a pressure of ~80 GPa (corresponding to a mantle depth of ~1900 km), the solidus temperature of ~3200 K is similar to that of the bulk mantle (**Figure 88**). With pressure increased to 135 GPa, the MORB solidus increases to ~3800 K, whereas that of the bulk mantle increases to ~4150 K. Thus, the onset of melting in the MORB occurs at ~350 K below the mantle solidus.

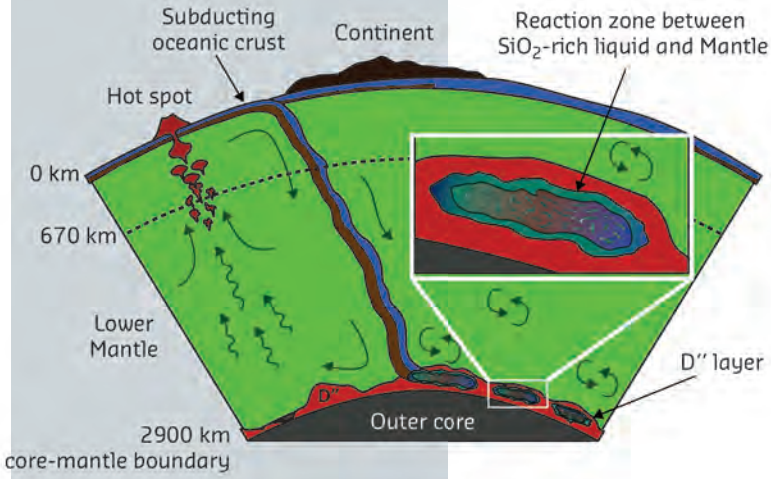

Fig. 87: Location of the D'' layer, between the Earth's core and lower mantle.

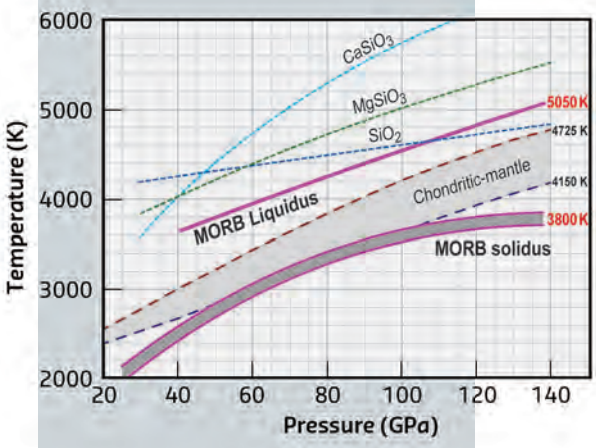

Fig. 88: The MORB solidus and liquidus compared with melting curves of the bulk (chondritic) mantle. At the core-mantle boundary, the MORB solidus reaches 3800 (±150) K. Its curvature is much more pronounced than that of a chondritic-type mantle [2], which induces a lower melting point for the MORB at 135 GPa, the core-mantle boundary pressure. The MORB solidus also plots 1000-1500 K below the melting curves of pure SiO_2 and $MgSiO_3$, as determined from shock wave experiments.

The flattening of the MORB solidus could be linked to a change in liquid composition with pressure. There are three indications of an increase of the SiO_2 content in the liquid with pressure during partial melting of MORB. First, the MORB solidus curve always plots 1000-1500 K below the lowest melting curve for pure $CaSiO_3$, $MgSiO_3$ or SiO_2 phases (**Figure 88**). Although SiO_2 is the most refractory phase at low pressures, it becomes the least refractory above 60 GPa. Second, we observe the total disappearance of the SiO_2 peaks above the solidus for pressures higher than 70 GPa, which indicates samples under-saturated in SiO_2 compared to the liquid composition. Third, the mineralogical and chemical analyses performed on the recovered samples (**Figure 89**) show higher SiO_2 content and presence of the high-pressure polymorph of SiO_2 (seifertite), while the surrounded rim of material is composed of bridgmanite, which is the MgO-bearing phase of the MORB lithology.

Following the hypothesis that the ULVZ of the lowermost mantle are associated with partial melting, our experimental results provide explanations for the seismological features. The SiO_2-rich liquid that is generated by MORB partial melting could either remain trapped in the subducted slab, producing the seismic anomalies, or solidify after reaction with the surrounding Mg-bearing mantle, which would result in a remixing of the subducted basalt in the lowermost mantle.

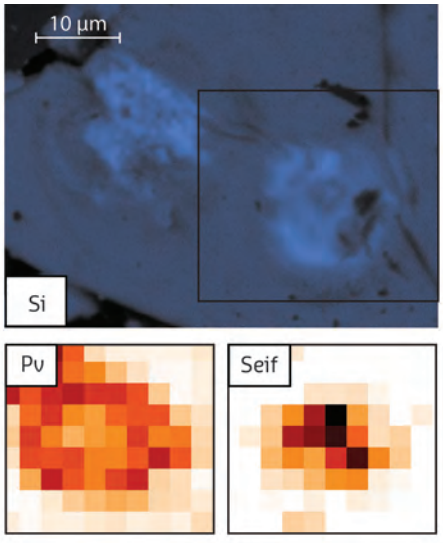

Fig. 89: Phase relations in the sample recovered after partial melting at 120 GPa. Mineralogical content (lower frames for Bridgmanite (Pv, left) and SiO_2-seifertite (right)) and Si chemical map (upper frame) were measured on the recovered samples by X-ray diffraction and scanning electron microscopy. They show higher SiO_2 content in the sample region corresponding to the quenched liquid.

References
[1] T. Lay, Q. Williams and E.J. Garnero, *Nature* **392**, 461-468 (1998).
[2] D. Andrault, *et al.*, *Earth and Planetary Science Letters* **304**, 251-259 (2011).
[3] G. Fiquet, *et al.*, *Science* **329**, 1516-1518 (2010).

BUOYANT MAGMAS TRIGGER SUPERVOLCANO ERUPTIONS

Principal publication and authors
W.J. Malfait (a), R. Seifert (a), S. Petitgirard (b), J.-P. Perrillat (c), M. Mezouar (b), T. Ota (d), E. Nakamura (d), P. Lerch (e) and C. Sanchez-Valle (a), *Nature Geosciences* **7**, 122-125 (2014).
(a) Institute for Geochemistry and Petrology, ETH Zurich (Switzerland)
(b) ESRF
(c) Laboratoire de Géologie de Lyon, Université Claude Bernard Lyon 1 and Ecole Normal Supérieure de Lyon, CNRS UMR 5276, Villeurbanne (France)
(d) Institute for Study of the Earth's Interior, Okayama University (Japan)
(e) Paul Scherrer Institute, Villigen (Switzerland)

Supervolcanoes are considered a rare but serious threat due to their destructive capacity only comparable to giant impacts [1]. Well-known supervolcanoes are located in the Yellowstone Caldera (USA), Lake Toba (Indonesia) and Lake Taupo (New Zealand), where the last supereruption occurred 26500 years ago. Supervolcano eruptions are explosive and eject more than 450 km^3 (or 10^{15} kg) of magma (*e.g.* La Garita, Yellowstone) compared to the mere 10 km^3 supplied by the largest conventional volcanic eruptions (*e.g.*, Pinatubo in 1991) [2]. Moreover, supereruptions have a major impact on global climate as the large volumes of emitted ashes and volcanic gasses (*e.g.* SO_2) raise the Earth's albedo and could decrease the global temperature by up to 10°C for over a decade.

In spite of their devastating impact, the triggering mechanisms for supereruptions have remained elusive until now. Processes occurring in conventional volcanic system are indeed not scalable to the much larger magma chambers beneath supervolcanoes (~ 5-10 km thick and up to 100 km wide). Because supervolcanoes are located in areas with high heat flux, the crust around their magma chambers is relatively hot and ductile. As a result, overpressure due to a change in volume, *e.g.* by magma recharge, volatile saturation or mush rejuvenation, is dissipated more efficiently in the plastic supervolcano magma chambers than in the more rigid magma chambers of conventional volcanoes [3]. Supervolcanoes therefore do not erupt very often (~1/100000 years on average, [1]).

In an alternative mechanism, magma buoyancy in large magma chambers potentially creates an overpressure sufficient for an eruption [3]. Contrary to the other plausible triggers, the buoyancy overpressure does not decrease upon wall rock deformation and expansion of the magma chamber. However, the viability of this mechanism could not be evaluated until now due to the lack of appropriate density data for the SiO_2-rich magmatic liquids that fed supereruptions.

We conducted experiments at beamline **ID27** to determine the density of dry and hydrous rhyolitic/granitic liquids (78 wt% SiO_2) using a Paris-Edinburgh press and a synchrotron X-ray absorption technique. Finely-powdered synthetic rhyolitic glasses with various H_2O contents (0, 4.5 and 7.7 wt% H_2O) were loaded into natural diamond cylinders and subjected to pressures (P) and temperatures (T) up to 3.6 GPa and 1950 K. After compression, the samples were heated until complete melting was confirmed by X-ray diffraction. The liquid density was determined *in situ* from the X-ray absorption contrast between the sample and the diamond cylinder used as container (**Figure 90**). The experimental densities were implemented in a model for the density of dry and hydrous granitic liquids at crustal and shallow upper mantle conditions (< 100 km depth) that allows the first evaluation of the buoyancy

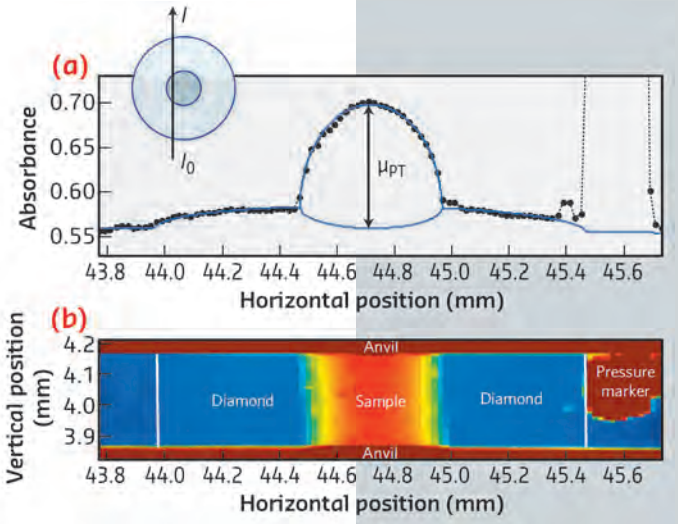

Fig. 90: *a) X-ray absorbance scan through the sample assembly (i.e., cylindrical diamond capsule and sample) as a function of the X-ray beam position in the horizontal direction (in mm) at 1.02 GPa - 1735 K (dotted line). The density (ρ_{PT}) is derived from the attenuation coefficient of the sample (μ_{PT}), obtained from the fit (blue line) to the measured absorbance profile. The strong absorption near 45.6 mm indicates the position of Pt-bearing pressure-temperature calibrants touching the outside of the diamond capsule. b) X-ray absorbance map of the gap between the anvils, reconstituted from horizontal scans collected at different vertical positions.*

References
[1] S. Self and S. Blake, *Elements* **4**, 41 (2008).
[2] B.G. Mason, D.M. Pyle and C. Oppenheimer, *Bull. Volcanol.* **66**, 735 (2004).
[3] A.M. Jellinek and D.J.A. DePaolo, *Bull. Volcanol.* **65**, 363-381 (2003).
[4] O. Bachmann and G.W. Bergantz, J. Petrol. **45**, 1565 (2004).

overpressure in supervolcano magma chambers.

For each melt composition and magma chamber conditions (*i.e.* thickness, degree of crystallisation and P-T), the density profiles (**Figure 91a**) and overpressures at the roof of the magma chamber (**Figure 91b**) were computed with our liquid density model and literature data for relevant mineral and volatile phases. Our results show that for magma chambers thicker than 5 km, if there are no volatiles, the buoyancy overpressure in the roof of the magma chamber is lower than the minimal critical overpressure (10 MPa) required to break the cap rock and to initiate the eruption. Therefore, magma buoyancy provides a background overpressure that can progressively increase by the addition of heat and/or magma during the evolution of a supervolcano and that primes the magma chamber for another (small) trigger or may ultimately lead to a supereruption by itself. The present results thus show that external triggers are not *a priori* required to start an eruption and that buoyancy alone may trigger a supereruption.

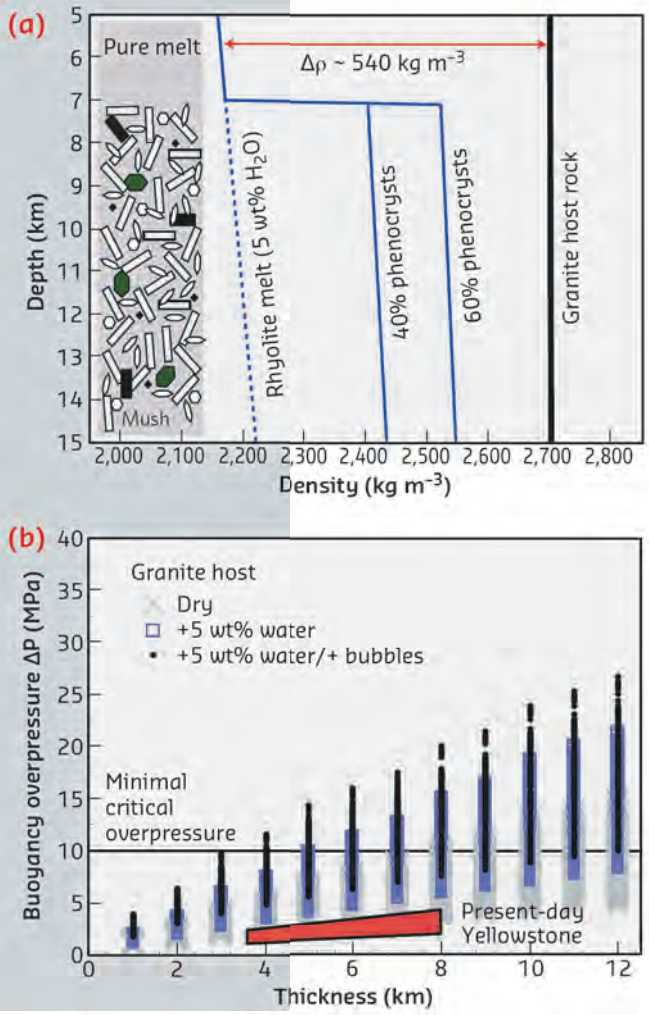

Fig. 91: a) Density profiles of a supervolcano magma chamber consisting of a 2 km thick granitic melt layer on top of 8 km of crystal mush (40 or 60% crystallinity) **[4]** and density contrast (Δρ) with the host rock. b) Buoyancy overpressure as a function of magma chamber thickness for a range of plausible chamber conditions; the red area denotes the overpressure for the present-day magma chamber conditions at Yellowstone (3.6-8 km thick, 68-90% crystallinity). In magma chambers thicker than 5 km, the buoyancy derived overpressure may exceed the critical overpressure (10-40 MPa) required for an eruption, even in the absence of volatile saturation.

GIANT PRESSURE-INDUCED VOLUME COLLAPSE IN THE PYRITE MINERAL MnS_2

Magnetism plays an important role in determining the properties of the minerals that make up Earth's crust and mantle **[1]**. This is due to the ubiquity of transition metals (notably Fe) with unpaired electrons. Under geological pressures, these may undergo abrupt volume collapses due to spin-state transitions, where the number of unpaired electrons is sharply reduced. This occurs when the crystal field splitting Δ, competes with Hund's rule and electronic Coulomb repulsion to determine the size of the magnetic moment. High pressure can thus make a high-spin (*e.g.*, S = 5/2) state unstable with respect to a low-spin state (*e.g.* S = 1/2). The primary driving force for this effect is an increase in Δ as the metal–ligand bond distances decrease. Many simple materials show pressure-induced spin state transitions, and volume collapses of $\Delta V \approx 5\%$ are regarded as notable. Understanding

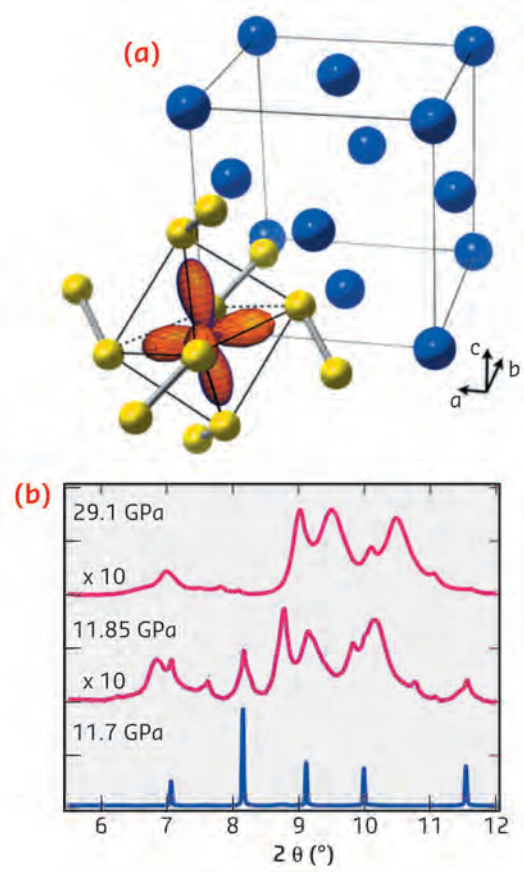

Fig. 92: a) Ambient pressure cubic structure of MnS_2, showing the *fcc* lattice of Mn sites (blue) and highlighting the valence e_g orbitals of one cation. b) Pressure dependence of diffraction data (**ID09A**) through the volume collapse, showing the formation of a disordered intermediate.

the mechanisms of such magnetically driven transitions, and predicting the high-pressure structures, is ultimately of great importance for modelling the Earth›s mantle in particular.

Using diamond anvil cells at **ID09A** and **ID27**, we discovered that a simple cubic manganese mineral (Hauerite, MnS_2) undergoes a truly giant 22% shrinkage of unit cell volume above 12 GPa. Instead of the expected transition between crystalline high and low-spin phases, compression induces the formation of a disordered intermediate (**Figure 92**). As we were unable to solve the high pressure structure from this data, we made use of recently developed *ab initio* structure searching methods implemented in the USPEX package [2], which predicted a new monoclinic polymorph. Using the recently commissioned online CO_2 laser heating at **ID27**, we were able to recrystallise the sample at 20 GPa. Indexing and Rietveld refinement confirmed the predicted structure (**Figure 93**). This contains a notable distortion, with neighbouring Mn atoms forming short bonds along one-dimensional chains of edge-sharing MnS_6 octahedra. Density functional theory calculations show that this structure is low spin S = 1/2, and that the remaining spin per site is occupied in chemical bonding. Magnetism is thus completely quenched in this phase.

Not only is the size of the volume collapse in MnS_2 much larger than that found in other minerals, it therefore also occurs by a new mechanism. Traditionally, the electronic and magnetic properties of oxides and sulphides have been explained using a so-called 'single-ion' model [3]. This takes into account the spin, charge and orbital degeneracies of isolated cations. The results presented here go beyond this simple picture, and show that molecule-like units can spontaneously emerge under pressure in otherwise ordinary continuous lattice materials. In MnS_2, the unpaired electrons on neighbouring cations form chemically bonded dimers, and it is this 'squeezing out' of magnetism which stabilises the giant increase in density of the new phase. Although its scarcity means that MnS_2 is geologically insignificant, similar phenomena might be found in more abundant minerals containing iso-electronic cations such as Fe^{3+}.

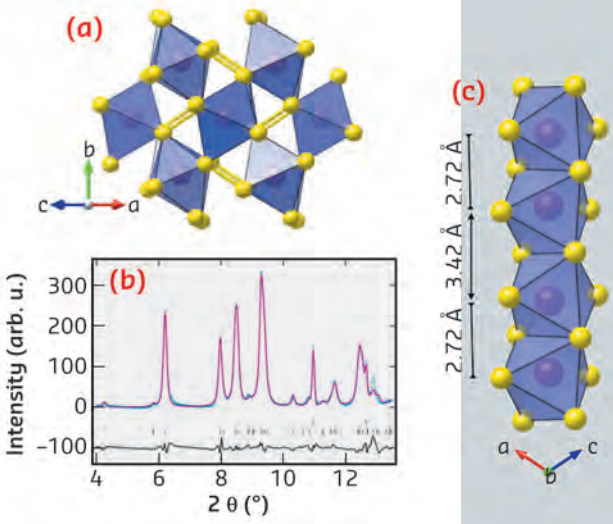

Fig. 93: a) High-pressure structure of MnS_2 as predicted using USPEX and as refined against the **ID27** diffraction data shown in b) at 20 GPa after laser heating. c) Perspective view of the high pressure structure showing the formation of short dimer bonds between neighbouring Mn cations in the edge-sharing chains. This viewpoint is perpendicular to that shown in a).

Principal publication and authors
S.A.J. Kimber (a), A. Salamat (a,b), S.R. Evans (a,c), H.O. Jeschke (d), K. Muthukumar (d), M. Tomić (d), F. Salvat-Pujol (d), R. Valenti (d), M.V. Kaisheva (e), I. Zizak (f) and T. Chatterji (g), *Proc. Nat. Acad. Sci.*, **111**, 5106 (2014).
(a) ESRF
(b) Lyman Laboratory of Physics, Harvard University, Cambridge (USA)
(c) Departement für Chemie und Biochemie, Universität Bern (Switzerland)
(d) Institut für Theoretische Physik, Goethe-Universität Frankfurt, Frankfurt am Main (Germany)
(e) School of Chemistry, University of Edinburgh (UK)
(f) Helmholtz-Zentrum Berlin für Materialien und Energie, Berliner Elektronenspeicherring-Gesellschaft für Synchrotronstrahlung-II, Berlin (Germany)
(g) Institut Max von Laue-Paul Langevin, Grenoble (France)

References
[1] R.E. Cohen, I.I. Mazin, *Science*, **275**, 654 (1997).
[2] C.W. Glass, A.R. Oganov and N. Hansen, *Comput. Phys. Commun*, **175**, 713 (2006).
[3] J.B. Goodenough, *Phys. Rev.*, **100**, 564 (1955).

STRUCTURAL BIOLOGY

With two new end-stations constructed and commissioned as part of the UPBL10 Upgrade project entering user operation, 2014 has seen both a major evolution in facilities available for Structural Biology at the ESRF and the coming to fruition of much hard work, spread over a number of years[1]. MASSIF-1 [ID30A-1] and MASSIF-3 [ID30A-3] provide new options for experiments in structural biology at ESRF.

Based around two ESRF-developed devices, the RoboDiff, which acts both as sample changer and goniometer and a high capacity dewar (HCD) that is capable of holding 240 SPINE standard sample holders, MASSIF-1 supplies for a new paradigm in structural biology: completely automatic, hands-off screening and/or data collection. Following a successful pilot study, such as service is now available to all our users and is proving extremely popular. MASSIF-3 is a fixed-energy end-station providing a highly intense (~2 x 10^{13} photons / second) microfocus (~15 µm diameter) X-ray beam at the sample position. This end-station is therefore ideal for the collection of diffraction data from microcrystals of biological macromolecules and, once the Eiger 4M detector associated with the end-station is operating at its full potential (750 Hz frame rate), will be an excellent vehicle for experiments exploiting the burgeoning technique of synchrotron serial crystallography (SSX).

The last element of the UPBL10 project will be put into place very shortly with the coming on stream of ID30B. This fully-tuneable end-station will offer both a high photon flux (~10^{13} photons/sec) and a variable spot size (20 to 200 µm^2) at the sample position. In its final configuration, foreseen for mid-2015, ID30B will also provide access to *in situ* (*i.e.* in crystallisation plate) screening and data collection.

While the UPBL10 project is nearing its end, the long-term evolution of the facilities available for structural biology will continue. Indeed, the recently published 'Orange Book' contains many ideas for future facilities and experiments that will be enabled by the ultra brilliant X-ray beams that will be produced following the Phase II Upgrade of ESRF.

Our beamlines will also evolve in the medium term. Even as this piece is being written the mirrors making up the focussing optics of ID23-2 are being replaced. This should give a new lease of life to this pioneering microfocus end-station prior to the completion of a technical design report (TDR) aimed at producing, in 2016, an upgraded ID23-2 with a beamsize 1 µm, or less, in diameter at the sample position. Additionally, ideas for improving the functionality and X-ray beam characteristics on the two MAD beamlines ID23-1 and ID29 are actively being considered. The provision at the ESRF of techniques complementary to macromolecular crystallography continues to evolve: upgrade of the sample environment at the ID29-S Cryobench microspectroscopy facility is planned while the BioSAXS beamline BM29 will soon benefit from the installation of a new, more user-friendly on-line HPLC set-up. This, coupled with a multi-technique sample environment, will greatly improve the information available during BioSAXS experiments.

A strength of the Structural Biology Group has been its ability to continue to operate existing experimental facilities while at the same time constructing and commissioning new ones. The past year is no exception to this rule. Indeed, the number of ESRF-based depositions in the Protein Data Bank remains very high and covers a broad range of structural biology research. The highlights presented here illustrate that membrane proteins, either transporters or receptors, remain major targets of the research carried out at the Structural Biology Group's beamlines as do studies aimed at understanding the molecular basis of disease. Concerning the latter, a particular highlight in 2014 was the elucidation, by Cusack and colleagues, of the crystal structures of the polymerases of bat-specific influenza A and human influenza B in complex with single stranded viral RNA promoter. Comparison of the two structures provides an atomic-level model of the mechanism of action of flu polymerases and may provide new insight into the design of anti-influenza drugs. The articles here also emphasise the increasing use of techniques (small-angle X-ray scattering, atomic force microscopy, *in cristallo* UV-visible or Raman spectroscopy) complementary to X-ray crystallography, a trend that is sure to grow in the coming years.

Finally, following a year's sabbatical leave Sean McSweeney and Elspeth Gordon officially resigned their positions at the ESRF in September 2014. As Head of the Structural Biology Group from 2000 to 2013, Sean's contribution to the success of the ESRF as an experimental resource for structural biology was extraordinary as was that of Elspeth in making use of synchrotron radiation an indispensible technique in the development of new pharmaceuticals. I'm sure that all readers of ESRF Highlights 2014 will want to join us in wishing Sean and Elspeth every success in their new ventures and in overcoming the challenges that lie ahead.

G. LEONARD
and **C. MUELLER DIECKMANN**

1 Although space does not allow acknowledgement of all those involved in the UPBL10 project, we would like to give a special mention here to technical staff of the Structural Biology Group (H. Caserotto, F. Dobias, T. Giraud, N. Guichard, M. Lentini, J. Soudarin, J. Surr), the staff of the EMBL Grenoble Outstation Synchrotron Instrumentation Group, the ESRF Beamline Control Unit (M. Guijarro, A. Beteva), the ESRF Data Analysis Unit (O. Svensson) and the staff of ESRF ISDD, particularly P. Theveneau and W. Schmid.

STRUCTURAL INSIGHTS INTO VIRAL RNA SYNTHESIS BY INFLUENZA POLYMERASE

Principal publications and authors
A. Pflug, D. Guilligay, S. Reich and S. Cusack, *Nature* **516**, 355–360 (2014); and S. Reich *et al.*, *Nature* **516**, 361–366 (2014).
European Molecular Biology Laboratory, Grenoble Outstation (France)

Influenza virus causes a highly contagious respiratory illness (the 'flu') to which everybody on the planet is susceptible. Viruses that infect humans can have three different origins. *Seasonal flu* causes annual epidemics and has a high public health and economic cost. The estimated global infection rate is 5%–10% in adults and 20%–30% in children and about 250 000 to 500 000 seasonal flu-related deaths occur each year worldwide, mainly amongst the very young, the elderly or the chronically ill. *Bird flu* is caused by highly pathogenic avian strains such as H5N1 and H7N9 (water birds are the natural reservoir for the virus), which through point mutations, are able to infect humans with up to 60% mortality, but as yet do not transmit between humans. *Pandemic flu* occurs when novel human strains are generated by recombination between avian and mammalian strains, often via an intermediate host such as the pig. This occurred in 1918, 1957, 1968 and, most recently, in 2009. Pandemics are unpredictable and potentially devastating. While vaccines can provide good protection against influenza, there is a need for effective anti-influenza drugs to treat severe cases and in the event of a dangerous pandemic where no vaccine is available.

The influenza virus genome comprises eight segments of negative sense, single stranded viral RNA (vRNA). Each segment is packaged in an individual ribonucleoprotein particle (RNP). RNPs contain one heterotrimeric RNA-dependent RNA polymerase, which is bound to the conserved 3' and 5' extremities of the vRNA (the 'promoter') and multiple copies of nucleoprotein. The viral polymerase both transcribes and replicates each genome segment. Transcription, which produces viral mRNA, occurs by a unique cap-snatching mechanism whereby the 5' cap-structure is cleaved from host cell mRNAs by an endonuclease and stitched onto the beginning of the viral transcript. Replication produces full-length copies of the genomic vRNA and proceeds via a complimentary cRNA intermediate. For many years we have been trying to obtain a high resolution crystal structure of the influenza polymerase in order to understand the distinct mechanisms of RNA synthesis and to enable structure-based drug design targeting this essential viral replication machine.

To overcome the problem of production of sufficient amounts of pure and active recombinant polymerase, we used a novel baculovirus vector, developed by I. Berger (EMBL), in which the three polymerase subunits are expressed as a fusion protein and post-translationally cleaved by a protease into separate pieces. Bat-specific influenza A (FluA) and human influenza B (FluB) polymerases were then co-crystallised with the vRNA promoter and the structures solved at 2.7 Å resolution using data collected at beamline **ID23-1**. These are the first structures of a complete polymerase from any negative strand RNA virus.

The three polymerase subunits, PA, PB1 and PB2 mutually stabilise each other through extensive and intricate interfaces (**Figure 94**). PB1 has a canonical polymerase fold, with a large, enclosed catalytic and RNA binding cavity connected to solvent by channels which allow nucleotide

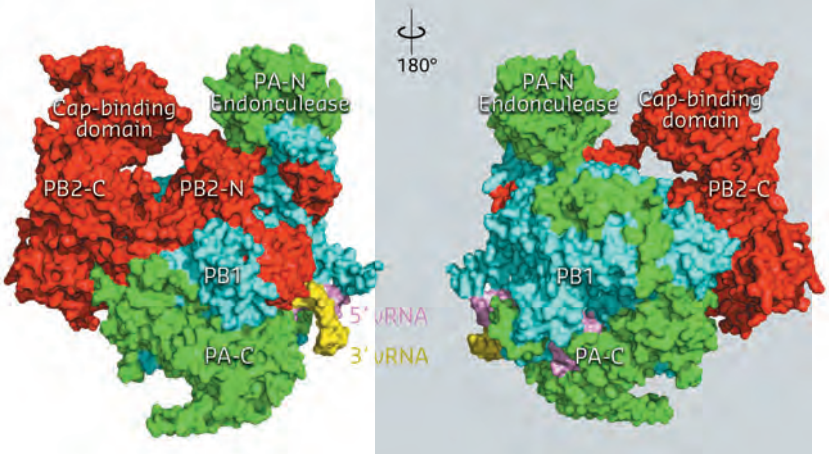

Fig. 94: Front and back views of the complete influenza polymerase with PA shown in green, PB1 in cyan and PB2 in red. The 3' and 5' ends of the viral RNA are shown in yellow and violet respectively.

triphosphate (NTP) entrance, template entrance and product exit. The domains involved in cap-snatching, the PA endonuclease domain and the PB2 cap-binding domain, form protrusions which face each other across a solvent channel. Ten nucleotides at the extreme 5′ end of the promoter form a compact stem-loop structure ('hook') which is bound in a pocket formed by PB1 and PA. The next four 5′ end nucleotides form canonical base-pairs with the distal part of the promoter 3′ end. The 3′ end proximal nucleotides interact with all three subunits and are directed towards the template entrance to the polymerase active site.

Comparing the FluA and FluB polymerase structures gives mechanistic insight into transcription and replication. In the FluA structure, an ordered priming loop suggests that influenza might initiate unprimed template replication by a similar mechanism to that seen for hepatitis C and Dengue virus polymerases. Interestingly, the FluA and FluB structures differ in the orientation of the PB2 cap-binding domain, suggesting a mechanism for cap-dependent transcription. In the FluA structure, the cap-binding site faces the PA endonuclease active site, a configuration compatible with cap-snatching. In the FluB structure, the cap-binding domain has rotated *in situ* by 70° and RNA-like residual extra electron density descends part way from the cap binding site towards the PB1 active site. Modelling this as RNA, its prolongation is compatible with the primer strand in known structures of other RNA polymerases bound to primer-template duplexes (**Figure 95**). The tight binding of the 5′ hook of the viral promoter to the polymerase is compatible with the role of this element in allosterically activating polymerase functions and in stalling transcription at the 5′ proximal oligo-U stretch on the vRNA leading to poly(A)-tail generation on the viral mRNA.

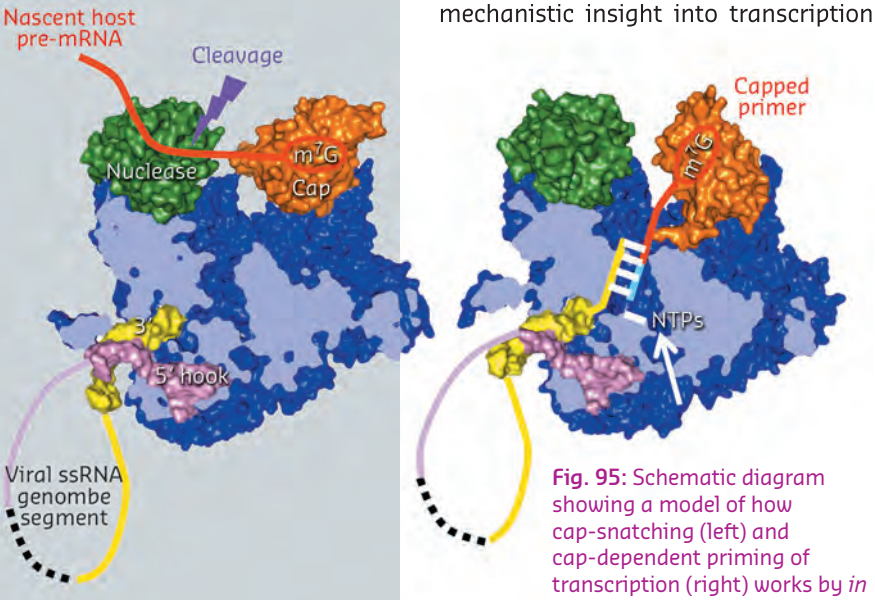

Fig. 95: Schematic diagram showing a model of how cap-snatching (left) and cap-dependent priming of transcription (right) works by *in situ* rotation of the cap-binding domain (orange).

These structures not only lay the basis for an atomic-level mechanistic understanding of the multiple functions of influenza polymerase but will also shed light on host-specific polymerase variants and open new opportunities for anti-influenza drug design.

Principal publication and authors
H. Takala (a, b), A. Björling (b), O. Berntsson (b), H. Lehtivuori (a), S. Niebling (b), M. Hoernke (b), I. Kosheleva (c), R. Henning (c), A. Menzel (d), J.A. Ihalainen (a) and S. Westenhoff (b), *Nature* **509**, *245-248 (2014).*
(a) University of Jyväskylä, Jyväskylä (Finland)
(b) University of Gothenburg (Sweden)
(c) University of Chicago (U.S.)
(d) Paul Scherrer Institut, Villigen (Switzerland)

LIGHT-INDUCED OPENING OF A PHYTOCHROME

All life on Earth is based on sunlight, and different organisms have developed multiple systems to detect and react to their light environment. Plants, bacteria, and several micro-organisms use light-sensitive proteins called phytochromes to control cellular functions in response to the changes in light. For example, a red/far-red light-absorbing bacterial phytochrome from *Deinococcus radiodurans* controls pigment production in response to light. The structures of several phytochromes have been solved in their resting state, but the structural details of their light activation have remained elusive [1]. Now, in a study conducted at the ESRF, the Swiss Light Source (SLS) and Advanced Photon Source (APS), we have assembled structural data on the activation mechanism of the phytochrome sensory module. These data provide exciting new insights into how light activates the protein. Our

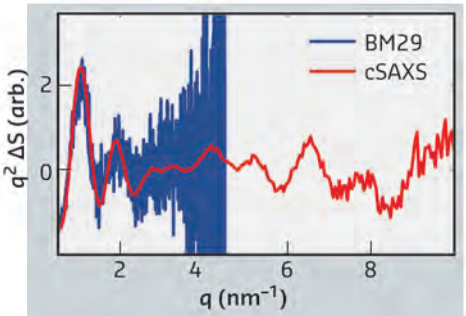

Fig. 96: Difference signals seen in light-induced SAXS (blue) and WAXS (red) scattering patterns from solutions of the phytochrome studied. The difference signals were calculated by subtracting the X-ray solution scattering pattern of the resting state from the solution scattering pattern of the active state and thus indicate structural changes between the states.

findings provide critical information for understanding these light-sensing proteins and set the basis for novel applications, *e.g.*, in agriculture.

In the studies described here, we aimed to reveal the structural details of a bacterial phytochrome from *D. radiodurans*. To attain this, we compared X-ray solution scattering data of the resting and activated forms of the protein. The data involved small X-ray scattering (SAXS) data from the ESRF beamline **BM29** and time-resolved solution X-ray data measured at SLS and APS in two states (**Figure 96**). This was achieved by switching the sample between the two states using flashes of different wavelengths of red light while the data were being collected. These SAXS data indicated large conformational changes in the protein upon activation.

After collecting the promising X-ray solution scattering data described above, we verified the exact structural changes between the states using X-ray crystallography. We managed to crystallise the photosensory module in two states: resting (Pr, red-absorbing) and active (Pfr, far-red absorbing) and collected diffraction data at ESRF beamline **ID23-1**. In both states the phytochrome appeared as a parallel dimer, as shown in **Figure 97**. However, the conformation of the dimers differed considerably between the states: the resting state adopts a "closed" configuration, the active state an "open" configuration in which the gap between the two subunits making up the dimer is opened by several nanometres.

In the structure of this phytochrome, an evolutionally highly conserved amino acid sequence forms a tongue-like structure (green in **Figure 97**). This tongue was shown to form a β-sheet structure in the resting state. Remarkably, the tongue adopted a completely different secondary structure in the activated state, taking up a shorter, α-helical conformation. The resulting shortening of the tongue by ~2.5 angstroms explain how the light-induced changes are relayed to

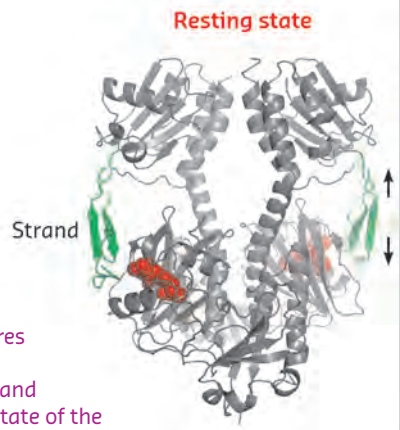

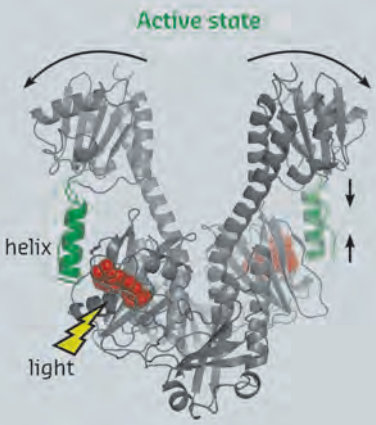

Fig. 97: Crystal structures of the resting and active state of the phytochrome fragment. The chromophore is shown in red and the tongue region of the protein is in green. The resting state was obtained by growing the crystals in complete darkness; the active state crystals needed sequential red light illumination to appear.

the rest of the phytochrome protein, and finally to the next proteins in the signalling cascade.

Our results have led to a comprehensive picture of the light-induced activation of the phytochrome. First, red light causes small conformational changes in the chromophore (red in **Figure 97**), which are amplified and transmitted to the rest of the protein. The tongue region of the phytochrome rearranges and shortens, which forces changes in the relative orientations of the rigid protein domains, leading to "opening" of the entire dimer structure. In this way a tiny change induced by absorption of a photon is amplified to a dramatic conformational rearrangement of the protein.

This finding sets the ground for the development of phytochrome-based applications and further studies in the field of phytochrome research **[2]**. Our next goal is to decipher how the structural signal changes the biochemical activity of the output region of the protein, which ignites signalling cascades within the cell. Naturally, this requires collecting more structural data on phytochromes.

References
[1] A.T. Ulijasz and R.D. Vierstra, *Curr Opin Plant Biol*. **14**, 498-506 (2011).
[2] A.W. Baker and K.T. Forest, *Nature*. **509**, 174-5 (2014).

Principal publication and authors
J.T. Grotwinkel, K. Wild, B. Segnitz and I. Sinning, *Science* **344**, 101-104 (2014).
Heidelberg University Biochemistry Center (BZH), Heidelberg (Germany)

THE "strong ARM" OF SRP68 SHAPES THE SIGNAL RECOGNITION PARTICLE

Targeted protein transport is a vital process for all cells. *A priori* targeting can occur while the protein is being synthesised (co-translational) or thereafter (post-translational) and each pathway depends on a dedicated machinery. In eukaryotic cells, membrane proteins and secreted proteins are co-translationally targeted to the endoplasmic reticulum (ER) by the universally conserved signal recognition particle (SRP) [1]. SRP recognises an N-terminal hydrophobic signal sequence within the nascent polypeptide chain, stalls the translation process, and upon interaction with the SRP receptor (SR), the ribosome–nascent chain complex (RNC) is docked onto the translocation channel (the Sec translocon) within the ER membrane. Here, protein biosynthesis resumes and the nascent chain is directly inserted into the ER membrane or translocates into the lumen of the ER. Eukaryotic SRP is a complex ribonucleoprotein particle consisting of six proteins assembled on a SRP RNA of 300 nucleotides (**Figure 98a**). SRP can be divided into two domains, the S domain, where the signal sequence binds, and the Alu domain, responsible for elongation arrest. In recent years, the molecular details of most SRP components have been determined with the beamlines at the ESRF playing a major role. However, it was only this year that structural information on SRP68, one of the largest, eukaryote specific components, became available.

SRP68 forms a heterodimer with SRP72 and the SRP68 RNA-binding domain (RBD) has been previously shown within the context of the RNC to bind to a three-way junction ([2], for review see [3]). While this binding site is quite distant from the Alu domain and the signal sequence binding protein SRP54, SRP68 was found to be essential for translation-arrest and protein translocation. We have now determined the X-ray structures of the human and a fungal SRP68-RBD domain both alone and in the context of the SRP S domain. Data were collected on the tuneable beamlines **ID23-1** and **ID29** and initial structure determination was performed by multi-wavelength anomalous dispersion (MAD) using selenomethionine labelled protein. The high brilliance of the beamlines was essential for obtaining superior data quality from the small and weakly diffracting crystals of the protein-RNA complex.

SRP68-RBD forms an unusual RNA-binding module resembling the purely α-helical tetratricopeptide repeat (TPR) fold (**Figure 98b**). The RBD exposes a highly positively charged surface, which tightly binds to an RNA three-way junction. While previous footprinting experiments accurately mapped the binding site on the SRP RNA, the consequences of the interaction were unexpected. SRP68-RBD remodels the SRP RNA on two levels and this remodelling elegantly explains previous structural and functional data. First, binding to the three-way junction induces a kink in S domain SRP RNA. When the new structure is fitted into the cryo-EM structure of the entire eukaryotic SRP/RNC complex, the "kinked" S domain is necessary to correctly explain the RNA density and to establish an important RNA-RNA contact between SRP and the ribosome (**Figure 99a**). Without SRP68 present to induce this contact, the Alu

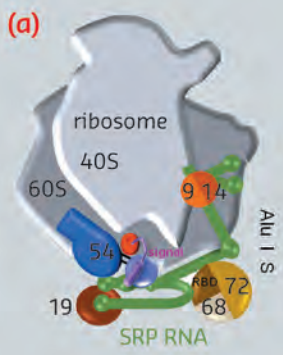

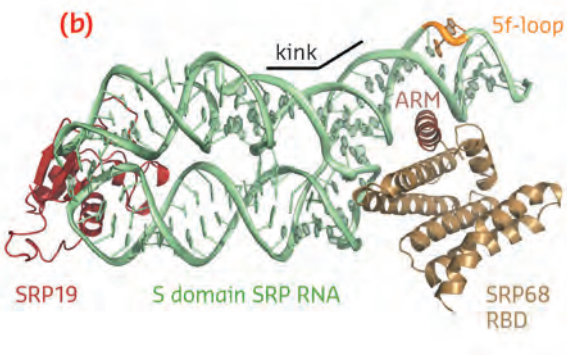

Fig. 98: Co-translational protein targeting by the signal recognition particle (SRP). a) Human SRP bound to the RNC. b) Ternary complex of SRP S domain including SRP19, SRP68-RBD, and SRP RNA

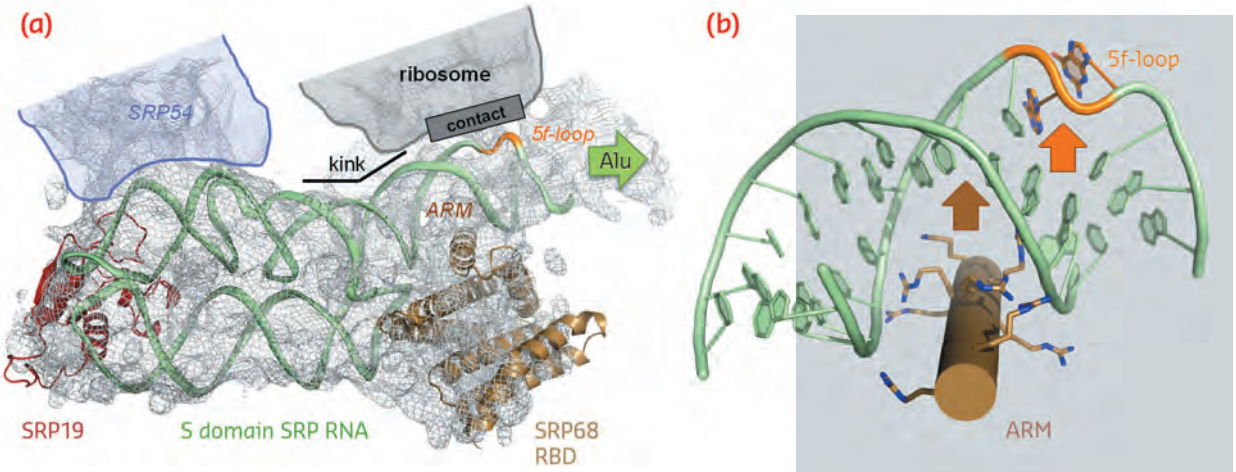

Fig. 99: SRP RNA remodelling by SRP68-RBD. a) SRP68-RBD induces a kink in SRP RNA necessary for contacting the ribosome. b) SRP68-RBD inserts an ARM into the major groove of SRP RNA and opens the 5f-loop.

domain could not, as already described 30 years ago, function in translation-arrest. Second, one α-helix of SRP68-RBD is inserted into the major groove of SRP RNA in the 5f-loop region next to the three-way junction (**Figures 98b** and **99b**). The major groove in RNA-helices is narrow and deep, and it needs a "strong arm" to open it. For this to happen, an arginine-rich motif (ARM) is inserted into the groove, and the 5f-loop is remodelled by bulging-out conserved unpaired nucleotides. It is these nucleotides that form the contact with ribosomal RNA (**Figure 99a**). A corresponding RNA-bulge in bacterial SRP RNA is essential for SRP RNA mediated GTPase activation of the SRP GTPases present in SRP and its SR **[4]**. GTPase activation is essential for driving the SRP cycle of co-translational targeting. Whether this mechanism also applies to the eukaryotic SRP system remains to be seen.

References
[1] P. Grudnik, G. Bange and I. Sinning, *Biol Chem* **390**, 775-782 (2009).
[2] M. Halic *et al., Nature* **427**, 808-814 (2004).
[3] K. Wild, M. Halic, I. Sinning and R. Beckmann, *Nat Struct Mol Biol* **11**, 1049-1053 (2004).
[4] G. Bange and I. Sinning, *Nat Struct Mol Biol* **20**, 776-780 (2013).

A PROMISCUOUS INTERMEDIATE UNDERLIES THE EVOLUTION OF SINGLE COPY TRANSCRIPTION FACTORS

A class of proteins known as transcription factors (TFs) is central to the evolution of organisms. TFs exert their control on the cell by binding specifically to DNA sequences and causing a cascade of downstream events to occur. A key question in the evolution of TFs is how they can evolve new DNA specificities. This is complicated by the fact that altering the target DNA sequence or the specificity of the transcription factor will in most cases change the binding properties of the TF towards its original target DNA sequence, which will in turn prevent the normal downstream events from occurring. A simple solution to this problem is the duplication of genes, followed by the evolution of new properties (most notably DNA binding specificity) of one copy of the gene. In this scenario, the organism will continue to survive because it has a working copy of both the DNA and TF, which frees the second copy of the TF to evolve new binding specificities. However, in cases where only a single copy of the gene exists in the cell, it is less obvious how changes can occur without deleterious effects. In this work, LEAFY, a generally single copy master regulator of floral development, was used as a model system. A key discovery which enabled this research was the identification of ancient forms of LEAFY from hornworts and algae. The DNA binding preferences of these proteins and other previously described forms from angiosperms and gymnosperms were determined using a technique called SELEX (Systematic Evolution of Ligands by EXponential

Principal publication and authors
C. Sayou (a), M. Monniaux (a), M.H. Nanao (b,c), E. Moyroud (a), S.F. Brockington (d), E. Thévenon (a), H. Chahtane (a), N. Warthmann (e), M. Melkonian (f), Y. Zhang (g), G.K.-S. Wong (g,h), D. Weigel (e), F. Parcy (a,i) and R. Dumas (a), *Science* **343**, 645-8 (2014).
(a) Laboratoire de Physiologie Cellulaire et Végétale (LPCV), Grenoble (France)
(b) European Molecular Biology Laboratory (EMBL), Grenoble (France)
(c) Unit of Virus Host-Cell Interactions, Université Grenoble Alpes–EMBL–CNRS, UMI 3265, Grenoble (France)
(d) Department of Plant Sciences, University of Cambridge (UK)
(e) Department of Molecular Biology, Max Planck Institute for Developmental Biology, Tübingen (Germany)
(f) Botanisches Institut, Lehrstuhl I, Universität zu Köln, Biozentrum Köln (Germany)
(g) Beijing Genomics Institute (BGI)–Shenzhen (China)
(h) Department of Biological Sciences, Department of Medicine, University of Alberta (Canada)
(i) Centre for Molecular Medicine and Therapeutics, Child and Family Research Institute, University of British Columbia (Canada)

enrichment). From the data obtained, in combination with classical biochemical binding assays, a "family tree" of DNA binding specificity could be assembled. The family tree showed that there are at least three different types of DNA recognition sites: types I, II and III.

Using the microfocus macromolecular crystallography beamline **ID23-2** [1] and a special data collection method to reduce radiation damage, the crystal structure of one of these family members (from moss) was determined, in complex with its preferred (type II) DNA sequence. When compared to an earlier structure of LEAFY in complex with a type I sequence [2], this structure revealed that an additional contact is made between the protein and DNA, and provided a molecular explanation for the altered DNA specificity compared to other LEAFY forms (**Figure 100**).

Equally important was the elucidation of the molecular determinants of primitive LEAFY binding to the type III motifs. Type III motifs differ dramatically from type I/II in that a central region in the recognised DNA is absent. Using SELEX, biochemical binding assays and the type I and type II LEAFY structures as a guide, it was shown that a region in the LEAFY protein of type I/II allows for binding to sequences with this central region (**Figure 101**). When this region is mutated (as in the hornwort and algal LEAFYs which bind type III sequences), LEAFY binds to type III sequences. With a molecular understanding of how, through evolution, LEAFY can bind to different sequences, the original question of how different DNA specificities in a single copy TF could be better addressed. Upon further analysis, the Hornwort LEAFY gene was shown to have structural characteristics of LEAFYs that should allow it to bind *both* type I/II and type III sequences. Biochemical assays were used to confirm this hypothesis experimentally and showed that this LEAFY is indeed promiscuous in its binding specificity. This seemingly simple finding has profound consequences for our understanding of how TFs could evolve different DNA specificities. In particular, such an intermediate state could have acted as an ancient evolutionary crossroad through which LEAFY developed into specialised "modern" forms. The reasons for the diversity of modern forms of LEAFY remain elusive, and are the subject of ongoing research.

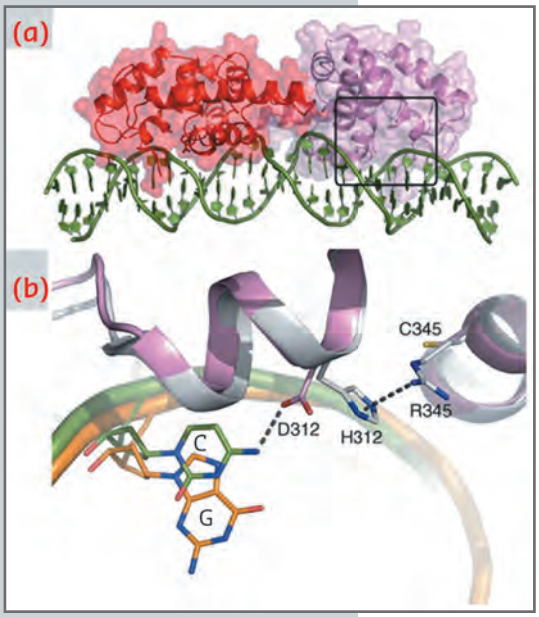

Fig. 100: Structural basis for type II specificity (PpLFY1-DBD), in comparison with type I (AtLFY-DBD). a) Overall structure of the moss LEAFY dimer bound to a type II DNA sequence. b) Superimposition of the structures of angiosperm (AtLFY-DBD, in grey) with its cognate DNA (orange) and moss (moss-DBD, in pink) with its cognate DNA (green).

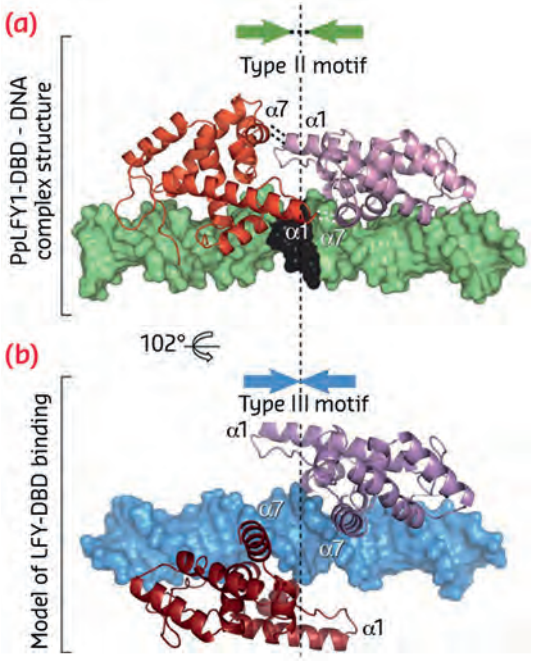

Fig. 101: a) Moss (PpLFY1)-LEAFY (in red and pink) bound to DNA (in green, except the black 3-bp spacer). Interactions between monomers (involving α helices α1 and α7) are shown with dashed lines. b) Modelled type III binding with DNA shown in blue. The dashed vertical line denotes the centre of the pseudopalindromic DNA sequence.

References

[1] D. Flot *et al.*, *J Synchrotron Radiat.* **17**, 107-18 (2010).

[2] C. Hamès *et al.*, EMBO J. **27**, 2628-37 (2008).

A TRANSPORTER CAUGHT IN THE ACT

Principal publication and authors
L. Malinauskaite (a), M. Quick (b,c), L. Reinhard (a,d), J.A. Lyons (a), H. Yano (b,e), J.A. Javitch (b,c), P. Nissen (a), *Nat Struct Mol Biol.* **21**, 1006-12 (2014).
(a) Aarhus University (Denmark)
(b) Columbia University College of Physicians and Surgeons, New York (USA)
(c) New York State Psychiatric Institute, New York (USA)
(d) Current address: Karolinska Institutet Stockholm (Sweden) and Karolinska Institutet, Hamburg (Germany)
(e) Current address: National Institutes of Health, Baltimore (USA)

Secondary transporters are membrane proteins that use the energy stored in electrochemical gradients (typically H^+ or Na^+) to drive antiport or symport of specific solutes. Their function is generally based on an "alternating access" mechanism [1] where the protein switches the orientation between outward- and inward-facing states. This mechanism allows a net transport and accumulation of solute determined by the driving gradient. Over the last 10 years, a wealth of structures of secondary transporters has emerged. However, information as to how transporters actually switch sides and release the driving ion is, in fact, scarce.

Classical examples of secondary transporters include the neurotransmitter-sodium symporters (NSSs) that perform an active re-uptake of molecules such as serotonin, dopamine and γ-aminobutyric acid (GABA). The signalling between neurons is achieved by the release of neurotransmitters into the synaptic cleft from the presynaptic neuron that activates receptors and signal transmission in the postsynaptic neuron. Based on the steep Na^+ gradient maintained by the Na^+, K^+-ATPase, the NSS family transporters perform an active re-uptake to terminate the signal and recycle the neurotransmitters to the presynaptic neuron. It is of particular interest to study the structure-function relationships of this family as they are implicated in various psychological and neurological disorders such as epilepsy, depression and schizophrenia. NSSs are also the key targets for pharmaceuticals including antipsychotics and antidepressants, and for psychostimulants such as cocaine and amphetamine.

Several crystal structures have been obtained of a bacterial member of the NSS family - the amino acid transporter LeuT from *Aquifex aeolicus*. These have captured the outward-open, sodium-bound state [2], the occluded outward-facing, substrate-bound state [3], and the inward-open apo state [2] and provide snapshots of the beginning and the end of the forward transport cycle. However, the mechanism of intracellular sodium release - where transport becomes coupled to the Na^+ gradient - has remained elusive.

We studied another bacterial model of the NSS family, the multihydrophobic amino acid transporter MhsT from *Bacillus halodurans*. Two crystal forms of this protein with bound L-tryptophan and sodium ions (diffraction data collected at ESRF beamline **ID23-2** and at Diamond Light Source) revealed the long-sought occluded, inward-facing state where sodium and substrate are primed for release to the cytoplasmic environment and highlights both the first steps of solvation of the driving sodium ion and the structural changes that have switched the transporter from an occluded outward- to an occluded inward-facing state. A unique feature was observed: an unwinding at the cytoplasmic end of the fifth transmembrane helix (TM5) allows solvent from the cytoplasm to enter the driving-ion binding site, which also changes from a trigonal pyramidal to an octahedral coordination with a cytoplasmic water molecule as the sixth ligand (**Figure 102**).

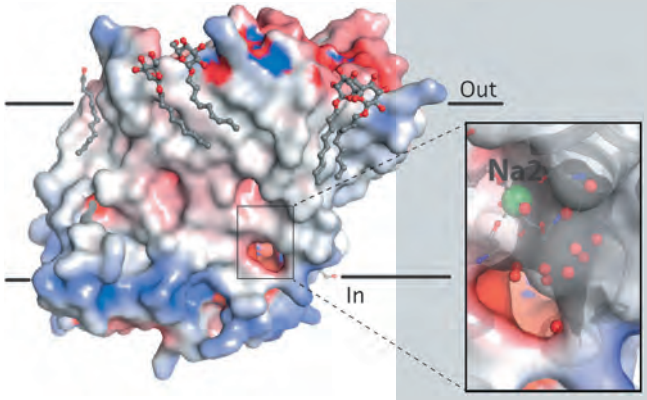

Fig. 102: The MhsT inward-facing occluded structure. The electrostatic surface is shown for MhsT. The close-up with a transparent surface shows a solvent-filled, cytoplasmic cavity that reaches the Na2 binding site. Associated detergent molecules are shown as ball-and-sticks, Na^+ as green spheres and water molecules as small red spheres (insert).

References
[1] O. Jardetzky, *Nature* **211**, 969-70 (1966).
[2] H. Krishnamurthy and E. Gouaux, *Nature* **481**, 469-74 (2012).
[3] A. Yamashita *et al.*, *Nature* **437**, 215-23 (2005).

The forward transport reaction can now be described for the NSS family (**Figure 103**): sodium binding at two sites stabilises the outward-open state [2], and allows substrate binding, which stimulates the transporter to occlude the substrate binding sites [3]. Subsequent closure of an extracellular, hydrophobic vestibule triggers unwinding, at the intracellular side, of TM5. This provides access of cytoplasmic water to the sodium site. This initiates sodium release to the low-sodium intracellular environment, possibly stimulated by a negative membrane potential. After the release of sodium the intracellular cavity opens for complete substrate release to occur [2]. Finally, the transporter switches back to an outward-open state through sodium-free return states, the structures of which are as yet unknown.

This new structure in the NSS cycle – caught in the act of exposing sodium to the intracellular environment - provides novel insight into NSS function and, perhaps, into how sodium-dependent transporters generally operate, and brings us closer to a complete picture of their transport mechanism and how this is regulated.

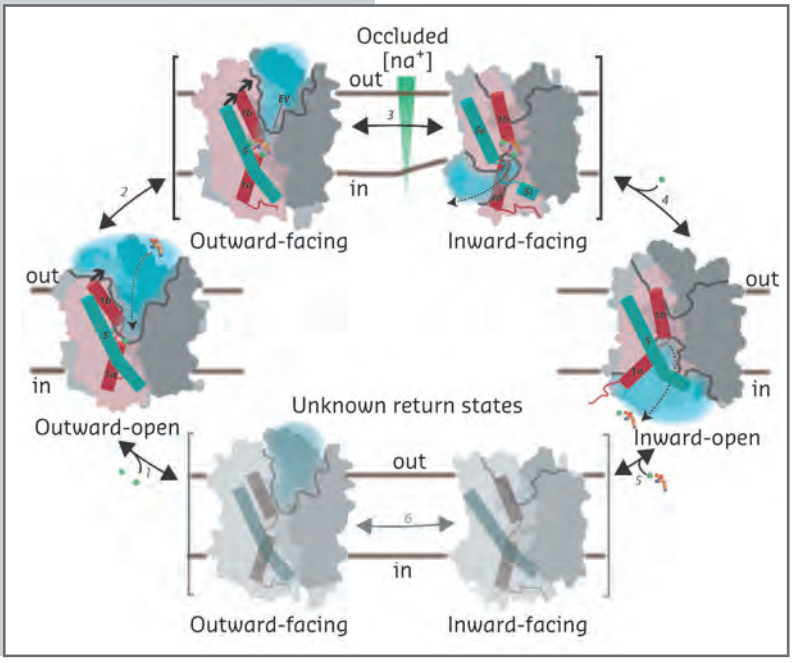

Fig. 103: Transport mechanism of the NSS family. Na^+ binding stabilises the outward-open state (*1*) and allows the substrate to bind (dashed arrow), triggering substrate site occlusion (*2*). Closure of a hydrophobic, extracellular vestibule (EV) stabilises the transition to an inward-facing state where TM5 unwinding provides a solvation pathway for the Na2 driving site (*3*). The helix unwinding provides an opportunity for Na^+ to escape to the intracellular low-sodium environment (*4*). Na^+ release from Na2 allows TM5 to reassume a helical structure and TM1a to swing out to release the substrate with Na^+ from the Na1 site in the inward-open state. Finally, the transporter switches back to the outward-open state via as yet unknown sodium-free return states (*5-6*). A scaffold domain of the transporter is shown in dark grey, a bundle domain in pink, half channel openings as grey lines, solvated regions by light blue shadows, TM1 as red and TM5 as cyan cylinders, Na^+ ions as green, and amino acid substrate in orange spheres. The membrane is indicated by straight, black lines.

STRUCTURE OF A MAMMALIAN SEROTONIN RECEPTOR REVEALED BY X-RAY CRYSTALLOGRAPHY

Principal publication and authors
G. Hassaine (a,b), C. Deluz (a), L. Grasso (a), R. Wyss (a), M.B. Tol (a), R. Hovius (a), A. Graff (c), H. Stahlberg (c), T. Tomizaki (d), A. Desmyter (e), C. Moreau (f), X.-D. Li (g), F. Poitevin (h), H. Vogel (a) and H. Nury (a,f), *Nature* **512**, 276-81 (2014).
(a) LCPPM, EPFL, Lausanne (Switzerland)
(b) Present address: Theranyx, Marseille (France)
(c) CCIN, Biozentrum, University of Basel (Switzerland)
(d) SLS, PSI, Villigen (Switzerland)
(e) AFMB, CNRS & Université Aix-Marseille, Marseille (France)
(f) Institut de Biologie Structurale, Grenoble (France)
(g) LBR, PSI, Villigen (Switzerland)
(h) DSM, Institut Pasteur & CNRS, Paris (France)

The complex mental capacities and motor behaviours of mammals rely on the evolution of nervous systems in which ligand-gated ion channels facilitate fast intercellular signalling. The Cys-loop receptor family encompasses pentameric ion channels such as the nicotinic acetylcholine and serotonin 5-HT3 (resp. GABA and Glycine) receptors which are cation- (resp. anion-) selective and promote excitatory (resp. inhibitory) signals. These receptors, targets of many psycho-active and therapeutic compounds, function as allosteric signal transducers whose conformational transitions, regulated by neurotransmitter binding, operate the gating of a channel that let ions flow through the plasma membrane. Each of their five subunits contains three domains: a β-sheet-rich extracellular domain comprising the ligand-binding site, an α-helical transmembrane

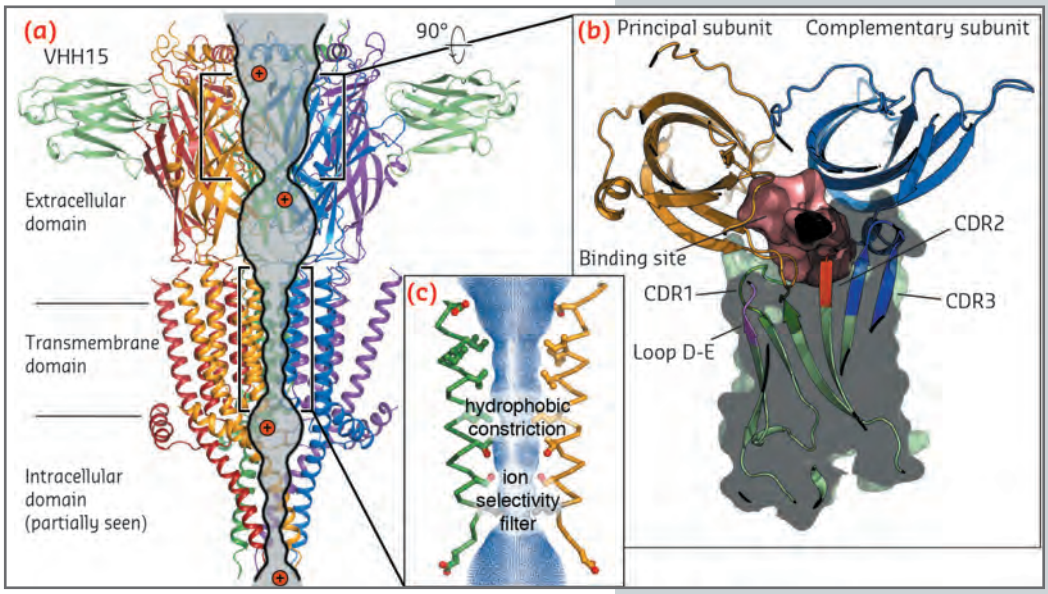

Fig. 104: a) View parallel to the membrane plane of the crystal structure of the split 5-HT3A receptor in complex with VHH15 in cartoon representation. Two out of the five VHH15 molecules observed are shown in pale green. The ion (pictured in red) permeation pathway is shown as a continuous solvent accessible volume (grey). b) Rotated view of the interface between two neighbouring extracellular domains and the solvent accessible volume (pink) representing the serotonin binding site. One VHH15 molecule (hidden in the main panel) is also displayed in cartoon and surface representation, highlighting the extensive interaction between its loops and the ligand-binding site. c) Close up of the transmembrane domain pore.

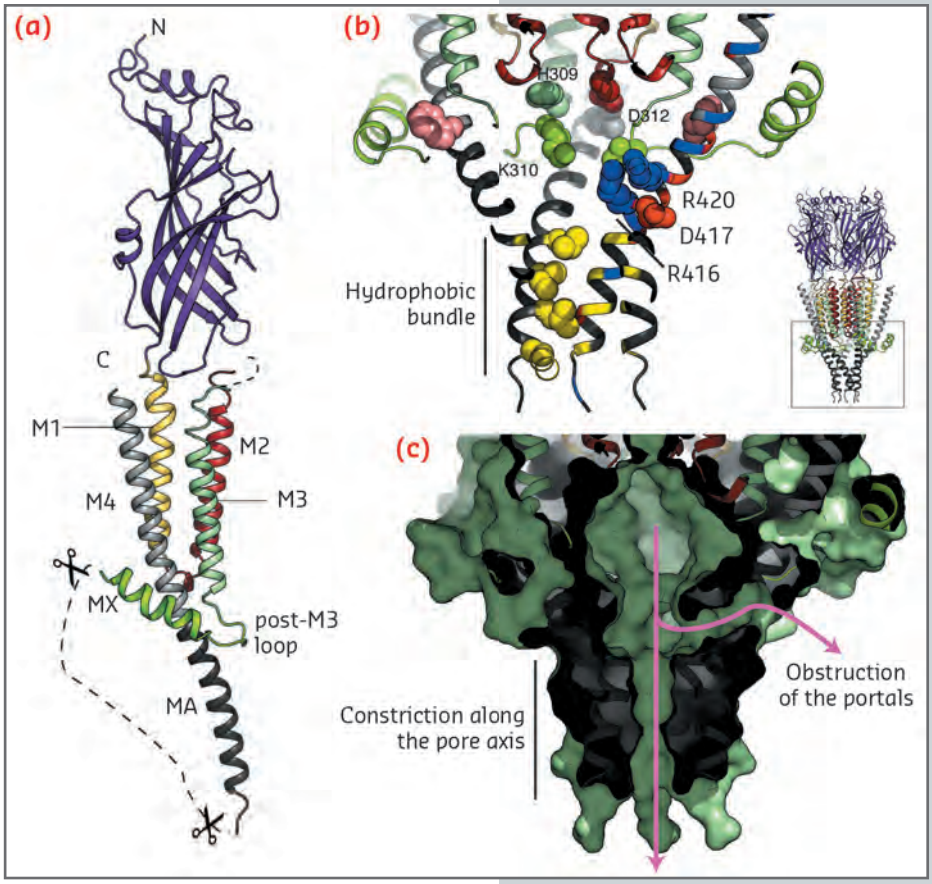

Fig. 105: a) View of one subunit of the split 5-HT3A receptor shown in cartoon representation. b) The intracellular domain. Key residues are shown as spheres. c) Same view, in surface representation, highlighting the vestibule and the two constricted ion exit pathways.

domain made of helices named M1 to M4, and an intracellular domain, a major determinant of gating kinetics and channel conductance. Even though structural knowledge of these receptors is rapidly increasing (see *e.g.* [1-2]), the latter domain, specific to metazoa, is absent in crystal structures derived thus far.

To further document the mechanistic details of the functional processes of pentameric ligand-gated ion channels, high-resolution structures of full-length mammalian receptors have to be solved. In an effort toward this goal, we crystallised a mouse homopentameric 5-HT3A receptor that retains a large part of its intracellular domain. The full-length receptor was expressed in HEK 293 cells [3]. First attempts yielded crystals diffracting X-rays only to 20 Å resolution and limited proteolysis experiments improved this limit to 7 Å. We eventually found that the Llama-derived single-chain antibody VHH15 formed a stable complex with the 5-HT3 receptor and crystals of this complex diffracted to 3.5 Å resolution at beamline **ID29**.

In these crystals, the 5-HT3 receptor subunits are arranged in pseudo five-fold symmetry around a central ion pathway perpendicular to the membrane plane (**Figure 104a**). The extracellular domain reveals the detailed anatomy of the serotonin binding-site capped by a VHH15 bound radially to the subunit interface (**Figure 104b**). The transmembrane domain delimits an aqueous pore lined by the M2 helices (**Figure 104c**), whose state (open or closed) cannot be

unambiguously defined without more dynamical information.

A portion of the intracellular domain structure is revealed in the crystal structure (**Figure 105a**): the post-M3 loop and the short MX helix clamp the helix MA, the latter a continuous extension of M4, and create a vestibule exposing charged residues on its inner surface that were identified as determinants of single channel conductance by mutagenesis studies (**Figure 105b**). Here, lateral ion pathways that might be formed between MA helices are blocked by the post-M3 loop and, further down, the MA helical hydrophobic bundle tightens, thus also constricting a possible exit pathway for ions (**Figure 105c**). Again, a more dynamical view of the receptor would be needed to gain further insight into ion permeation mechanism through the intracellular vestibule. The missing digested segment, between MX and MA, contains interaction sites for proteins modulating activity, assembly, trafficking and clustering.

The structure of the split 5-HT3 receptor shows a number of interesting features. Firstly, it reveals part of the intracellular domain, thus expanding the structural basis for understanding the operating mechanism of mammalian Cys-loop receptors. Secondly, our finding that a particular nanobody binds at the subunits' extracellular interface opens the possibility to specifically target Cys-loop receptor subtypes: a crucial challenge in developing new active compounds and in determining the crystal structures of pentameric ion channels.

References

[1] L. Sauguet *et al.*, *PNAS* **111**, 966-71 (2014).
[2] P. Miller and A.R. Aricescu, *Nature* **512**, 270-5 (2014).
[3] G. Hassaine *et al.*, *Biochim. Biophys. Acta* **1828**, 2544-52 (2013).

STRUCTURAL BASIS FOR NUCLEAR IMPORT OF SPLICING FACTORS

Principal publication and authors

G.N. Maertens (a), N.J. Cook (b), W. Wang (c), S. Hare (a), S.S. Gupta (a), I. Öztop (c), K.-E. Lee (d), V.E. Pye (b), O. Cosnefroy (b), A.P. Snijders (b), V.N. KewalRamani (b), A. Fassati (e), A. Engelman (c) and P. Cherepanov (a,b), *PNAS* **111**, 2728–2733 (2014).

(a) Division of Infectious Diseases, Imperial College London (UK)
(b) Clare Hall Laboratories, Cancer Research UK, London Research Institute, Potters Bar (UK)
(c) Department of Cancer Immunology and AIDS, Dana–Farber Cancer Institute, Boston (USA)
(d) HIV Drug Resistance Program, National Cancer Institute, Frederick (USA)
(e) Wohl Virion Centre and Medical Research Council Centre for Medical and Molecular Virology, Division of Infection and Immunity, University College London (UK)

The nuclear/cytoplasmic trafficking machinery that is essential for metazoan development and homeostasis, is often deregulated in cancer and can be hijacked by pathogens, such as HIV. The transport of macromolecules between cytoplasm and nucleus is orchestrated by nuclear import and export receptors. Referred to as importins and exportins, these proteins bind their cargos and translocate them across the nuclear pore complex. This process is regulated by Ran, a small GTPase, which partitions between cytoplasm and nucleus in the predominantly GDP- and GTP- bound form, respectively. Importins associate with their cargos in the cytoplasm, and the competitive binding to RanGTP induces them to release their cargos in the nucleus. Most nuclear import/export receptors belong to the β-karyopherin family of proteins of which 22 members encoded in the human genome. Typically, β-karyopherins bind their cargos directly, recognising a linear nuclear localisation or export signal, and/or a specific tertiary/quaternary structural feature. Small molecules targeting nuclear/cytoplasmic trafficking are currently being evaluated as cancer therapeutics.

One fundamentally important type of a nuclear localisation signal, comprising sequences rich in Arg-Ser dipeptides (known as RS domains), belongs to the family of Ser/Arg-rich (SR) proteins. These nuclear proteins also contain RNA recognition motif (RRM) domains and play essential roles in pre-mRNA splicing and 3´-processing, participating in transcription regulation, mRNA transport, translation and nonsense-mediated decay. The canonical splicing factors ASF/SF2 and SC35 are among the best-characterised SR proteins. RS domains are processively phosphorylated on their Ser residues by a set of dedicated kinases. This phosphorylation is thought to trigger import of SR proteins into the nucleus, where it is subsequently required for the spliceosome assembly. During pre-mRNA splicing and 3´-processing, RS domains are involved in establishing networks of protein-protein interactions.

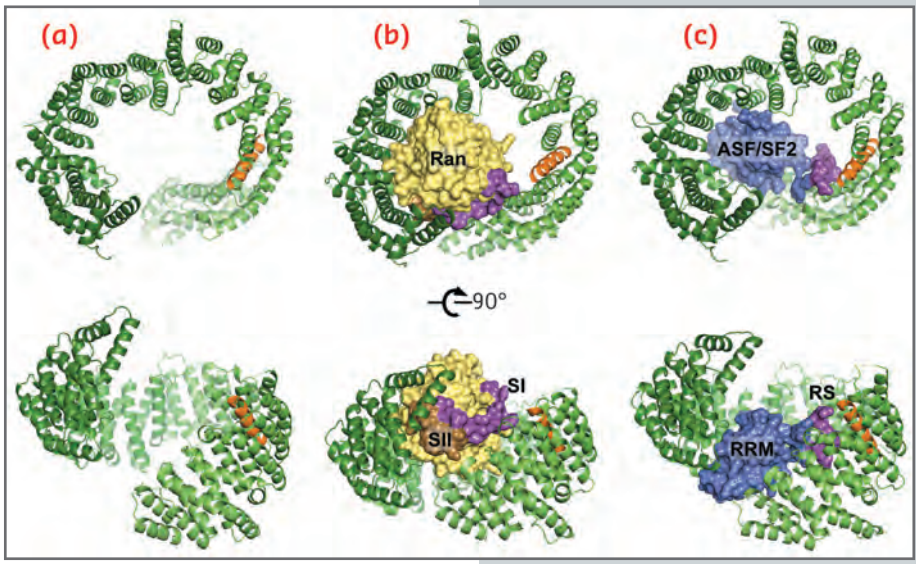

Fig. 106: Overview of the crystal structures of unliganded Tnpo3 (a), Tnpo3-RanGTP (b) and Tnpo3-ASF/SF2 (c) complexes. The structures were refined to 3.0, 3.4 and 2.6 Å resolution, respectively. Tnpo3 is shown as cartoons, while ASF/SF2 and Ran are shown in space-filling mode. Tnpo3 is coloured green, except the R-helix, which is shown in orange; Switch I (SI) and Switch II (SII) regions of Ran are shown in magenta and brown, respectively, with the remainder of the Ran structure shown in yellow; RRM2 and RS domains of ASF/SF2 are shown in blue and magenta, respectively.

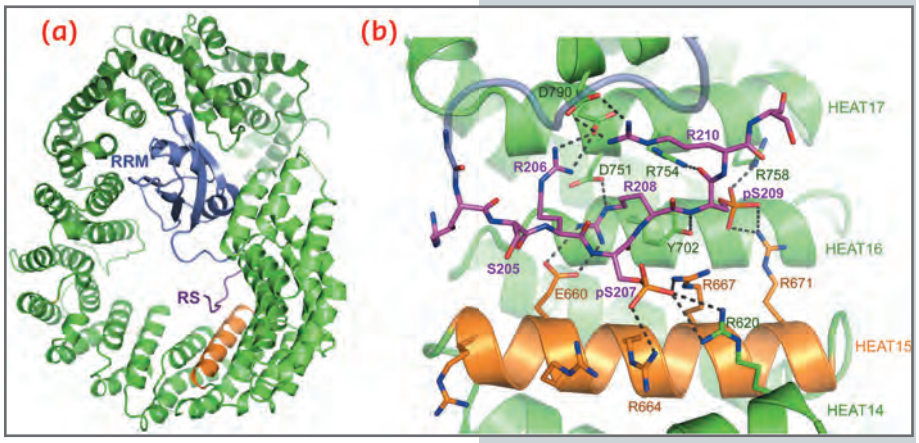

Fig. 107: Details of the structure of Tnpo3-ASF/SF2. a) Overview with both protein chains displayed as cartoons. The RRM2 and RS domains of ASF/SF2 and the R-helix of Tnpo3 are indicated. b) Details of the interface between Tnpo3 and the RS domain seen in the structure of ASF/SF2.

The human β-karyopherin Tnpo3 was shown to recognise the RS domains of ASF/SF2 and SC35 and execute their nuclear import. Likewise, Mtr10, the yeast version of Tnpo3, has long been known to facilitate nuclear import of splicing factors, but no atomic structural information on any of the Tnpo3 orthologs has been reported to date. Using data collected at beamlines **ID14-4** and **ID23-1,** we determined crystal structures of the human β-karyopherin in its three key function states: as a free protein, and as complexes with RanGTP and ASF/SF2 (**Figure 106**).

Tnpo3 is a highly flexible molecule, comprised of 20 HEAT repeats. The protein adopts an open circular/toroidal shape, with its N- and C-terminal arches facing each other (**Figure 106a**). The structure of the Tnpo3-ASF/SF2 complex revealed a tripartite protein-protein interface (**Figure 106c, 107a**), with the most important contacts involving the RS domain of the cargo. In its mode of binding to Tnpo3, the RS domain is reminiscent of Velcro tape, and its structure is then determined by the underlying Tnpo3 surface. Therefore, the interface is highly adaptable, aiding the β-karyopherin to accommodate highly degenerate RS domains. The inner helix of Tnpo3 HEAT repeat 15 (R-helix) projects an Arg side chain at each turn towards the concave surface of Tnpo3 and contributes to the phospho-Ser binding platform (**Figure 107b**). The phosphorylated RS domain forms a tight network of salt bridges with complementary Tnpo3 residues on and around the R-helix (**Figure 107b**).

The flexibility of Tnpo3 may allow it to bind a wide range of SR proteins and, furthermore, aid in their release upon engaging RanGTP in the nucleus. A close comparison of the structures of Tnpo3-ASF/SF2 and of Tnpo3-RanGTP (**Figure 106b**) revealed that the binding platforms for RanGTP and ASF/SF2 overlap on the concave surface of Tnpo3, with the Switch I region of Ran obstructing the approach of the RS domain to the R-helix. Collectively, these observations provide the structural basis for the dissociation of Tnpo3-cargo complexes via competitive binding of RanGTP upon nuclear entry.

THE CRYSTAL STRUCTURE OF HUMAN AQUAPORIN 2

Principal publication and authors
A. Frick (a), U. Kosinska-Eriksson (a), F. de Mattia (b), F. Öberg (a), K. Hedfalk (a), R. Neutze (a), W. de Grip (c), P.M.T. Deen (b) and S. Törnroth-Horsefield (a, d), *PNAS* **111**, 6305-6310 (2014)
(a) Department of Chemistry and Molecular Biology, University of Gothenburg (Sweden)
(b) Department of Physiology, Radboud University Medical Center, Nijmegen (The Netherlands)
(c) Department of Biochemistry, Radboud Institute for Molecular Life Sciences, Radboud University Medical Center, Nijmegen (The Netherlands)
(d) Department of Biochemistry and Structural Biology, Centre for Molecular Protein Science, Lund University (Sweden)

Maintenance of body water homeostasis is an essential part of human physiology. A key event in this is the kidney's ability to regulate urine volume in response to dehydration. This takes place in the collecting duct through the action of aquaporin 2 (AQP2), a membrane-bound water channel, in the apical membrane of the principal cells. Upon dehydration, AQP2 is moved from intracellular storage vesicles to the apical membrane, thereby increasing its water permeability. This process, which is known as trafficking, involves the pituitary hormone vasopressin, which stimulates phosphorylation of the AQP2 C-terminus, thereby triggering its translocation. Defective trafficking of human AQP2 leads to nephrogenic diabetes insipidus (NDI), a water balance disorder characterised by large urine volumes (up to 20 L/day) and subsequent dehydration [1].

We have solved the crystal structure of human AQP2 at 2.75 Å resolution using data collected at **ID14-4**. As seen in previous aquaporin structures, this reveals a tetrameric fold with each monomer comprising six transmembrane helices and two half-membrane spanning helices constituting a seventh pseudo-transmembrane segment (Figure 108). The water-translocating channel passes through the middle of each monomer in which water is transported in a single file while excluding ions and protons [2].

A striking difference between AQP2 and previous structures of mammalian aquaporins is the significant flexibility of the C-terminus. In particular, the C-terminal helix, which in previous aquaporin structures occupies a conserved position at the cytoplasmic interface, adopts four distinct new conformations (Figure 109a). In one monomer, the C-terminal helix interacts with the cytoplasmic interface of a symmetry-related AQP2 molecule (Figure 109b), thereby shielding four leucines aligned on the same side of the C-terminal helix from the cytoplasm. These leucine residues are responsible for the interaction between AQP2 and LIP5, a regulatory protein involved in targeting AQP2 for lysosomal degradation. The corresponding residues are also involved in the interaction between AQP0 and calmodulin [3]. We therefore suggest that exposed hydrophobic residues on the C-terminal helix are a common motif for protein-protein interactions amongst mammalian aquaporins.

An unexpected find in the AQP2 structure was the presence of two divalent cations per tetramer (Figure 109c), assigned as cadmium due to its presence during crystallisation, but likely to be replaced by calcium *in vivo*. The first binding site is located at the cytoplasmic interface between monomers A and D and causes a rearrangement of loop D, thereby exposing the binding pocket in which the C-terminal helix from the symmetry-related monomer binds (Figure 109b). The second calcium ion binds at the C-terminus and positions the C-terminal helix for this interaction. It thus seems that calcium ion binding may very well be important for protein-protein interactions involving the AQP2 C-terminus.

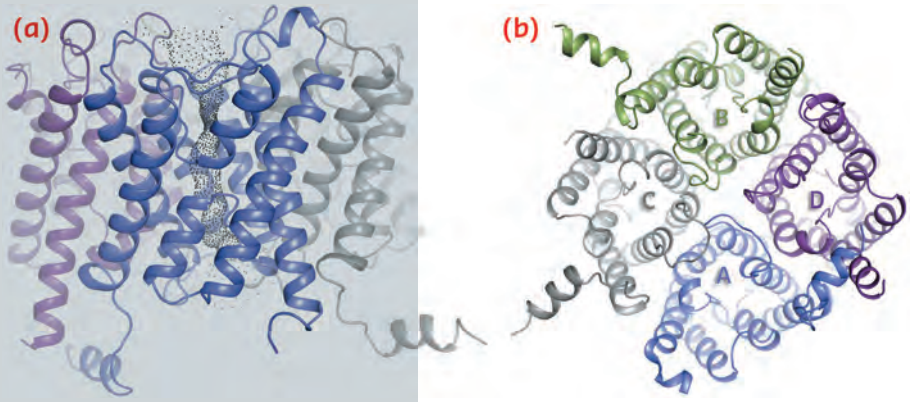

Fig. 108: Structure of the AQP2 tetramer viewed in the plane of the membrane (a) and from the cytoplasm (b).

Due to its role in NDI, AQP2 is the most clinically studied member of the aquaporin family. Over fifty different AQP2 point mutations have been identified in patients suffering from NDI, most of which cause endoplasmic reticulum (ER)-retention. By obtaining the structure of AQP2, we now have a structural framework to help us understand why these mutations cause disease thereby opening the possibility of finding new pharmacological treatments. Furthermore, the crystal structure provides a platform for exploring membrane protein cellular sorting in general, including how this is guided by protein-protein interactions and how misfolded proteins are recognised by the ER quality control.

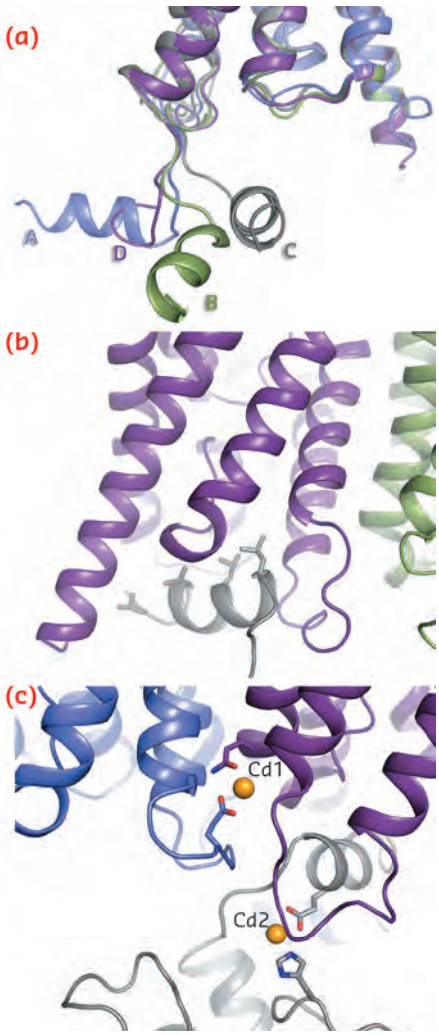

Fig. 109: Structural details of human AQP2. a) Overlay of four monomers showing the conformational variability of the C-terminus. b) Interaction between the C-terminal helix and the cytoplasmic interface of symmetry-related AQP2 molecules. c) Two cadmium ions can be seen per tetramer (Cd1 and Cd2) and are likely to represent calcium ion binding sites *in vivo*.

References
[1] P.M.T. Deen, M.A. Verdijk, N.V. Knoers, B. Wieringa, L.A. Monnens, C.H. van Os and B.A. van Oost, *Science* 264, 92-95 (1994).
[2] U. Kosinska Eriksson, G. Fischer, R. Friemann, G. Enkavi, E. Tajkorshid and R. Neutze, *Science* 340, 1346-1349 (2013)
[3] S.L. Reichow, D.M. Clemens, J.A. Freites, K.L. Nemeth-Calahan, M. Heyden, D.J. Tobias, J. E. Hall and T. Gonen, *Nat. Struct. Biol.* 20, 1085-1092 (2013).

STRUCTURAL ELUCIDATION OF MADS DOMAIN TRANSCRIPTION FACTOR SEPALLATA3

Virtually all terrestrial habitats are dominated by angiosperms, or flowering plants. However, angiosperms are a relatively recent step in evolution. Their success in colonising new habitats and superseding other species is due to the advent of a novel reproductive structure – the flower. Flowers are composed of four different organs: the sepals which protect the developing bud, the petals which are the showy organs that act as pollinator attractors, the stamen which are the male organs containing the pollen and the carpels which are the female organs and contain the ovules. The flower unites the male and female organs into one structure and encloses the seed. Flowering plants are not only the dominant type of land plants, but are also the primary source of food and habitat for all animals, including humans. The evolution of flowers has been the subject of speculation from the time of Charles Darwin who termed the dominant rise and diversification of flowering plants as "an abominable mystery" due to the lack of a smooth transition from non-flowering to flowering plants in the fossil record. With the sequencing of multiple genomes from basal angiosperms, gymnosperms and higher flowering plants, certain gene families that play a central role in the development

Principal publication and authors
S. Puranik (a), S. Acajjaoui (a), S. Conn (b), L. Costa (a), V. Conn (b), A. Vial (a), R. Marcellin (a,c), R. Melzer (d), E. Brown (a), D. Hart (e), G. Theißen (d), C.S. Silva (f), F. Parcy (f), R. Dumas (f), M. Nanao (g,h) and C. Zubieta (a,f,i), *The Plant Cell* **26**, 3606-3615 (2014).
(a) ESRF
(b) SA Pathology and the University of South Australia, Adelaide (Australia)
(c) Faculté des Sciences de Montpellier (France)
(d) Friedrich Schiller University, Jena (Germany)
(e) Université Grenoble Alpes, CNRS, Integrated Structural Biology Grenoble, UVHCI, Unité Mixte Internationale 3265, UMS 3518 Grenoble (France)
(f) LPCV, Grenoble (France)
(g) EMBL, Grenoble (France)
(h) UVHCI, Université Grenoble Alpes-EMBL-CNRS, Grenoble (France)
(i) CEA, DSV, iRTSV, Grenoble (France)

and evolution of the flower have been identified. Our research focuses on one such family of high-level regulators called the MADS transcription factor (TF) family, that orchestrates flower development. We are interested in understanding the molecular mechanisms of the MADS family and how these proteins are able to control complex reproductive functions.

Unlike animals which have only a few MADS family members, plants have greatly expanded and diversified the family during evolution. MADS TFs play significant roles in all aspects of plant life from seed germination to fruit and flower development. One of the most central members of the MADS family is SEPALLATA3 (SEP3). SEP3 is able to form over 50 different complexes with other MADS proteins and has roles in virtually all aspects of plant reproduction including the establishment of the floral meristem, the development of all floral organs and fruit ripening [1]. SEP3-containing protein complexes are postulated to bind DNA at multiple binding sites resulting in DNA loops that are important for downstream gene expression and/or repression [2]. Some of our recent work investigated the molecular mechanisms of SEP3 function. Using a combination of structural techniques, including X-ray crystallography and atomic force microscopy (AFM), we determined how SEP3 is able to form different protein-protein complexes and directly demonstrated DNA looping following SEP3 tetramer formation.

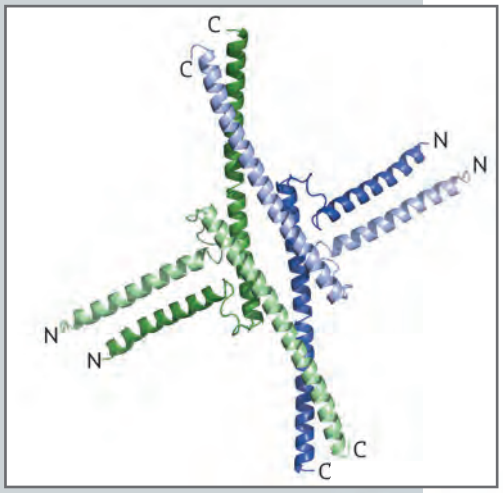

Fig. 110: SEP3 tetramer depicted as a cartoon with each monomer coloured differently. For each monomer, the N and C termini are labelled.

The 2.5 Å resolution crystal structure of the SEP3 oligomerisation domain was determined from diffraction data obtained at beamline **ID14-4**. This is the first structure for a plant MADS transcription factor and demonstrates novel dimerisation and tetramerisation interfaces formed by amphipathic α–helices. **Figure 110** shows that the protein monomer folds into two amphipathic α–helices separated by a rigid kink region, that the dimer is formed via hydrophobic interactions from helix 1 and helix 2 and that the tetramerisation interface is more limited, relying on hydrophobic residues contributed by the C-terminal portion of helix 2. Mutagenesis studies have confirmed the importance of these residues to the tetramerisation of the protein. To study the full-length protein, AFM was performed in collaboration with F. Comin and L. Costa of the ESRF Surface Science Laboratory. These experiments directly demonstrate SEP3-DNA binding. **Figure 111** shows a SEP3 tetramer binding two adjacent DNA-binding sites leading to the formation of a DNA loop. This ability is lost when the C-terminal portion of helix 2 is deleted.

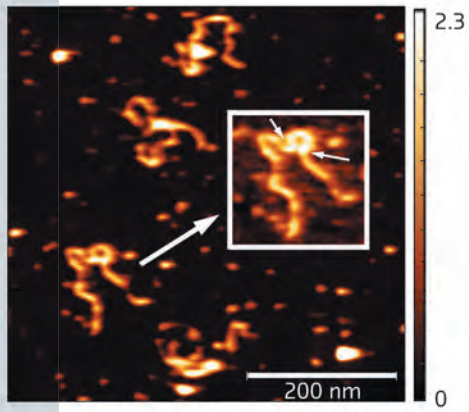

Fig. 111: AFM results showing full length SEP3 in complex with a 1-kb DNA fragment containing two SEP3 binding sites. The inset clearly shows that SEP3 tetramer binding to two adjacent DNA-binding sites (indicated by arrows) leads to formation of a DNA loop.

These results provide the first structural basis for MADS domain transcription factor function. The novel dimerisation and tetramerisation interfaces present two independent protein-protein interaction surfaces, allowing the proper binding of many different partners for both dimer and tetramer formation. We are currently developing and testing predictive models for MADS domain TF function based on our structural studies of SEP3 using an integrated biophysical and genetic approach. As a long-term goal, these studies will help us to tune the function of MADS TFs in plants and to alter different reproductive pathways and structures in a predictable manner.

References

[1] R.G.H Immink, I.A. Tonaco, S Folter, A Shchennikova, A.DJ. Dijk, J. Busscher-Lange and J.W. Borst, *Genome Biology* **10**, R24 (2009).

[2] R. Melzer, W. Verelst and G. Theissen, *Nucleic Acids Res.* **37**, 144-157 (2009).

TRACKING THE BACTERIAL IMMUNE SYSTEM

Principal publication and authors
S.G. Wong (a), and A. Dessen (a,b), *Nature Comm.* **5**, 4917 (2014).
(a) Institut de Biologie Structurale (IBS), CNRS, CEA, Univ. Grenoble (France)
(b) Brazilian National Laboratory for Biosciences (LNBio), Campinas (Brazil)

Alpha-2-macroglobulins (A2Ms) are plasma proteins that trap and inhibit a broad range of proteases and are major components of the eukaryotic innate immune system. Their main functions include clearing pathogenic or parasitic proteases from circulation, as well as blocking proteases that participate in inflammatory and blood clotting events. A2Ms are composed of ~180 kDa subunits that generally associate into oligomeric forms. The human form, for example, is a tetramer (thus, a 720 kDa protein). Despite it being believed that these molecules existed uniquely in metazoans, A2M-like proteins were recently identified in pathogenically invasive bacteria as well as in species that colonise plants, fish, and insects [1], suggesting that bacteria could also require 'protection' from proteases secreted by the target host or by other organisms competing for nutrients or space.

Bacterial A2Ms are monomeric molecules located in the periplasm of the cell, thus right underneath the outer membrane, where they are believed to provide protection to the cell upon membrane breach [2]. This occurs by trapping external proteases through a covalent interaction with a thioester bond buried within a hydrophobic environment inside the inactive macroglobulin. In the test tube, activation of the thioester can be mimicked by a small molecule called methylamine. Our paper reports the crystal structures and the characterisation of the alpha-2 macroglobulin from the human pathogen *Salmonella typhimurium* (StA2M) in different states of thioester activation. Diffraction data were collected at beamlines **ID29** and **ID23-2**, and solution scattering data at beamline **BM29**. The crystal structures revealed thirteen domains (**Figure 112**), whose arrangement displays high similarity to proteins involved in eukaryotic immune defense, such as complement C3. The crystal structure of (StA2M) in complex with methylamine confirms that the small molecule can attack the thioester bond without engendering conformational modification of the macroglobulin. Interestingly, the thioester motif is stabilised by a structural lock provided by Tyr1175, a residue which is present only in A2Ms of bacterial species. The necessity for this 'lock', which guarantees that the thioester remains entrenched (and protected from hydrolysis) within the macroglobulin in the absence of a target protease, is potentially linked to the fact that bacterial A2Ms are monomeric, and thus structurally simplistic, when compared to their oligomeric eukaryotic counterparts. Human A2M, for example, entraps target proteases in a central cage-like structure formed by its four monomers. In StA2M a Y1175G mutation opens this lock. Here, the thioester region is unprotected, the covalent thioester bond is broken, and the macroglobulin is unable to trap proteases. Our structural and mechanistic studies thus not only pinpoint how bacteria can inhibit protease attack during infection or colonisation, but also indicate that bacteria have developed a rudimentary innate immune system whose mechanism mimics that of eukaryotes.

Fig. 112: Schematic arrangement of the *S. typhimurium* A2M, which comprises over 1600 residues that fold mostly into β-sheet-carrying domains. The only exception is the thioester domain (TED), which is mostly helical (blue), and harbours the thioester bond that attacks target proteases.

References
[1] A. Budd, S. Blandin, E. Levashina and T.J. Gibson, *Genome Biol* 5, R38 (2004).
[2] N. Doan and G.W. Gettins, *J Biol Chem* 283, 28747-28756 (2008).

CRYSTAL STRUCTURE OF A COMMON GPCR-BINDING INTERFACE FOR G-PROTEIN AND ARRESTIN

Principle publication and authors
M. Szczepek (a,b), F. Beyrière (a), K.P. Hofmann (a), M. Elgeti (a), R. Kazmin (a), A. Rose (a), F.J. Bartl (a), D. von Stetten (c), M. Heck (a), M.E. Sommer (a), P.W. Hildebrand (a) and P. Scheerer (a,b), *Nature Communications* **5**, 4801 (2014).
(a) Institute of Medical Physics and Biophysics, Charité - Universitätsmedizin Berlin (Germany)
(b) Institute of Medical Physics and Biophysics, Group Protein X-ray Crystallography and Signal Transduction, Charité - Universitätsmedizin Berlin (Germany)
(c) ESRF

The large family of G-protein-coupled receptors (GPCRs) controls various sensory and physiological responses and is thus a major focus of research and of interest for medical drug targets. These receptors bind a variety of ligands (*e.g.* light-depending retinal, hormones, opioids, odorants, peptides, neurotransmitters) and communicate such extracellular signals into the cell by coupling to intracellular heterotrimeric G-proteins (Gαβγ) and arrestins (**Figure 113**) **[1]**. In G-protein-signalling, the Gα C-terminus (GαCT) binds to a cytoplasmic crevice formed in the agonist-bound active receptor **[2,3]**, eventually catalysing GDP/GTP exchange in the Gα-subunit (1). Another binding partner is arrestin, whose canonical role is to stop signalling by blocking receptor coupling to G-proteins, or to initiate arrestin-dependent signalling by bringing together other signalling proteins. In our studies, we have addressed the question of how arrestins employ the cytoplasmic crevice within the 7 transmembrane (TM) bundle of the active receptor for the high-affinity interaction necessary to block G-protein binding or stimulate arrestin mediated signalling **[4,5]**. This work was motivated by our observation of a consensus sequence motif, (E/D)

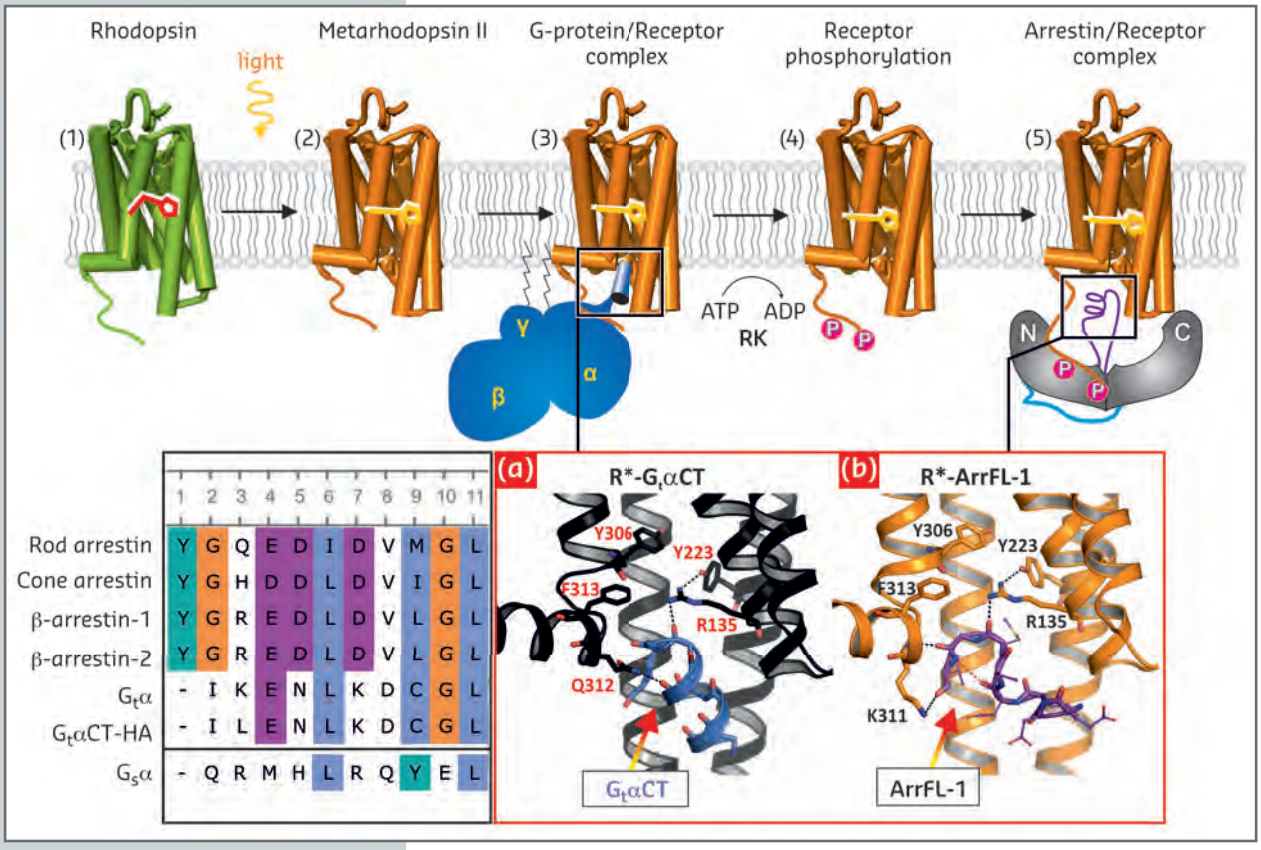

Fig. 113: Overview of rhodopsin signal transduction and deactivation. (1) Dark-state bovine rhodopsin with inverse agonist 11-*cis*-retinal. (2) Light-activation and formation of metarhodopsin II with agonist all-*trans*-retinal. (3) Coupling to the G-protein. (4) Phosphorylation of the activated receptor by its specific kinase. (5) Arrestin binding to the phosphorylated receptor. Inset (left): Sequence alignment of a proposed common sequence motif: rod photoreceptor arrestin (Arr1; residues 68–77), cone photoreceptor arrestin (Arr4; 63–72), β-arrestin-1 (Arr2; 64–73), β-arrestin-2 (Arr3; 65–74), wildtype $G_t\alpha$CT (340–349), high-affinity variant $G_t\alpha$CT-HA (340–349), $G_s\alpha$ (385–394). Inset (right): View of the cytoplasmic receptor crevice from the crystal structures depicted as ribbon-stick diagrams of a), R*- $G_t\alpha$CT (coloured in black-blue, PDB entry 3DQB, **[2]**) and b) R*- ArrFL-1 (coloured in orange-purple, PDB entry 4PXF, **[6]**).

x(I/L)xxxGL (**Figure 113**, inset left), which is conserved in $G_t\alpha$CT of the G_i/G_t-family and the "finger loop" (ArrFL) from the central crest region of all four subgroups of arrestin [6].

We have used protein X-ray crystallography, Fourier-transform-infrared spectroscopy, functional competition assays and UV-Vis absorption spectroscopy on solutions ("Extra-Meta II assay") and on crystals (at beamline **ID29S** – The Cryobench) to gain insight into how an active receptor binds to ArrFL. Firstly, we co-crystallised the active receptor rhodopsin R* (as light-activated metarhodopsin II or as the active form of the apo-protein opsin, Ops* [1,2,3,6]) with three different ArrFL peptides derived from rod photoreceptor arrestin, β-arrestin-1 and β-arrestin-2. The crystal structure of active rhodopsin with a peptide analogue derived from ArrFL-1 (rod photoreceptor arrestin), was solved at 2.75 Å resolution using diffraction data collected at beamline **ID29**. ArrFL binds to the cytoplasmic crevice of R* with a similar reverse turn structure as observed for the C-terminal $G_t\alpha$CT [2]. In both cases, a hydrogen bond is formed between the ArrFL-1 reverse turn and Arg135 from the highly conserved E(D)RY motif of R*.

To verify the functional relevance of the observed peptide binding to the receptor crevice, we applied three different functional assays to native disc membranes filled with rhodopsin. These functional experiments showed similar R* binding properties of G_i/G_t and ArrFL peptides. The key player, Arg135, essential for receptor activation and G-protein-coupling, has also a decisive role in arrestin binding (**Figure 113**, right). However, significant differences between ArrFL and $G_t\alpha$CT are seen at the rim of the receptor crevice. In ArrFL-1, the interaction with TM5/6 is partially replaced by interactions with TM7/H8 (specifically to the conserved NPxxY$(x)_{5,6}$F motif) and directed towards the intracellular loop 2 (CL2).

Overall, the crystal structure indicates a general mechanism of arrestin binding and the remarkable homology seen between $G_t\alpha$CT and ArrFL suggests that the (E/D)x(I/L)xxxGL motif evolved in both G-protein and arrestin to allow recognition and interaction with the same binding crevice presented by the active GPCR [6]. Despite these similarities, we also identified pronounced differences, namely a larger hydrophobic interaction surface in the case of $G_t\alpha$CT, which may contribute to the distinct biological functions of G-proteins and arrestin.

References
[1] K.P. Hofmann *et al.*, *Trends Biochem Sci.* **34**, 540-552 (2009).
[2] P. Scheerer *et al.*, *Nature* **455**, 497-502 (2008).
[3] H.-W. Choe *et al.*, *Nature* **471**, 651-655 (2011).
[4] A.K. Shukla *et al.*, *Nature* **497**, 137-141 (2013).
[5] Y.J. Kim *et al.*, *Nature* **497**, 142-146 (2013).
[6] M. Szczepek *et al.*, *Nature Communications* **5**, 4801 (2014).

INSIGHT INTO AN INTERMEDIATE STEP IN O_2-DEPENDENT CATALYSIS

The unambiguous identification of reaction intermediates is one of the most challenging tasks in structural enzymology. Although peroxide intermediates are likely to be formed in many reactions involving molecular oxygen (O_2), their structural identification has so far proven elusive. Here, X-ray crystallography combined with online *in-crystallo* Raman spectroscopy at beamline **ID29** and radiation damage effects have provided direct evidence for a C5(*S*)-(hydro) peroxide intermediate in a cofactor-free oxidase reaction that also allowed the visualisation of the reactive enzyme-substrate-O_2 complex.

Uricase (UOX) is the archetypal cofactor-independent oxidase [1]. It catalyses the breakdown of uric acid to 5-hydroxyisourate. A recombinant version of UOX finds therapeutic application to aid uric acid clearance in paediatric and adult cancer patients and for gout treatment. To investigate the step involving dioxygen in UOX-mediated catalysis, we employed 9-methyl uric acid (MUA). When anaerobic UOX:MUA co-crystals are exposed to O_2, electron density maps at 1.3 Å resolution unambiguously reveal that MUA converts into its C5(*S*)-peroxo derivative (5-PMUA) (**Figure 114a**). 5-PMUA is sp^3 hybridised at carbon C5.

Principal publication and authors
S. Bui (a), D. von Stetten (b), P.G. Jambrina (c), T. Prangé (d), N. Colloc'h (e), D. De Sanctis (b), A. Royant (b,f), E. Rosta (c) and R.A. Steiner (a), *Angew.Chem.Int.Ed.* **53**, 13710–13714 (2014).
(a) Randall Division of Cell and Molecular Biophysics, King's College London (UK)
(b) ESRF
(c) Dept. of Chemistry, King's College London (UK)
(d) LCRB, UMR 8015-Université Paris Descartes-CNRS (France)
(e) ISTCT, UMR 6301–UCBN–CNRS–CEA-Normandie Université (France)
(f) IBS, Grenoble (France)

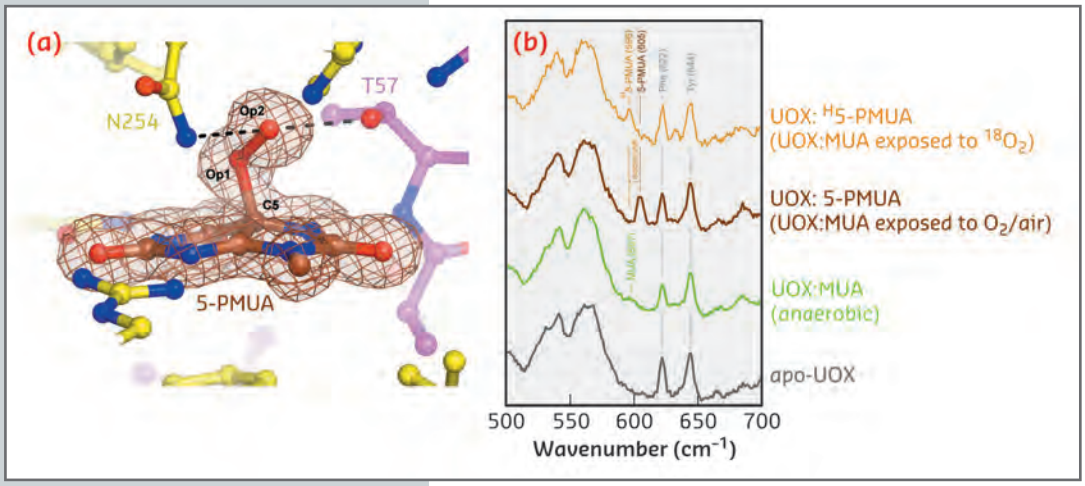

Fig. 114: *a*) The UOX:5-PMUA complex formed by reacting UOX:MUA crystals grown in anaerobic conditions with air. Electron density is shown for 5-PMUA. Hydrogen bonds involving the peroxo atoms are shown by broken lines. b) *In-crystallo* Raman spectra of *apo*-UOX (grey), anaerobic UOX:MUA (green), UOX:5-PMUA (brown), and UOX:H5-PMUA (gold). H5-PMUA (H for heavy) refers to MUA reacted with $^{18}O_2$.

The peroxo Op1-Op2 bond is 1.47 Å long, whilst the length of the C5-Op1 bond refines to 1.51 Å.

Non-resonant Raman spectra recorded from crystals of substrate-free UOX, anaerobic UOX:MUA and UOX:5-PMUA complexes are very similar overall. However, the region centred around 600 cm^{-1} exhibits changes sensitive to the chemistry of the oxygenation reaction (**Figure 114b**). Upon MUA peroxidation, a distinct band develops at 605 cm^{-1} (brown trace), whilst the shoulder at 597 cm^{-1} for the UOX:MUA complex (green) disappears. Neither band is present in the spectrum of substrate-free UOX (grey) indicating that they arise from the bound organic molecules. Furthermore, the 605 cm^{-1} band could be selectively shifted by carrying out MUA peroxidation with $^{18}O_2$ (shift to 596 cm^{-1}, $\Delta\tilde{\nu}$= –9 cm^{-1}, gold), thus confirming that this band specifically involves Raman modes with contributions from the peroxide oxygen atoms. Quantum mechanics/molecular mechanics (QM/MM) calculations at the MP2/6-31+G* level of theory predict a band at 600 cm^{-1} (experimental 605 cm^{-1}) for the 5-PMUA hydroperoxide resulting from a set of modes involving C5-Op1 bond stretching and C5-Op1-Op2 bending coupled to ring distortions. The theory further predicts a -9 cm^{-1} isotope shift (experimental -9 cm^{-1}) for 5-PMUA featuring ^{18}Op1 and ^{18}Op2 peroxide oxygen atoms. Overall, the calculations agree remarkably well with the experiment identifying the 605 cm^{-1} 5-PMUA Raman band as a 'signature' for its peroxide state.

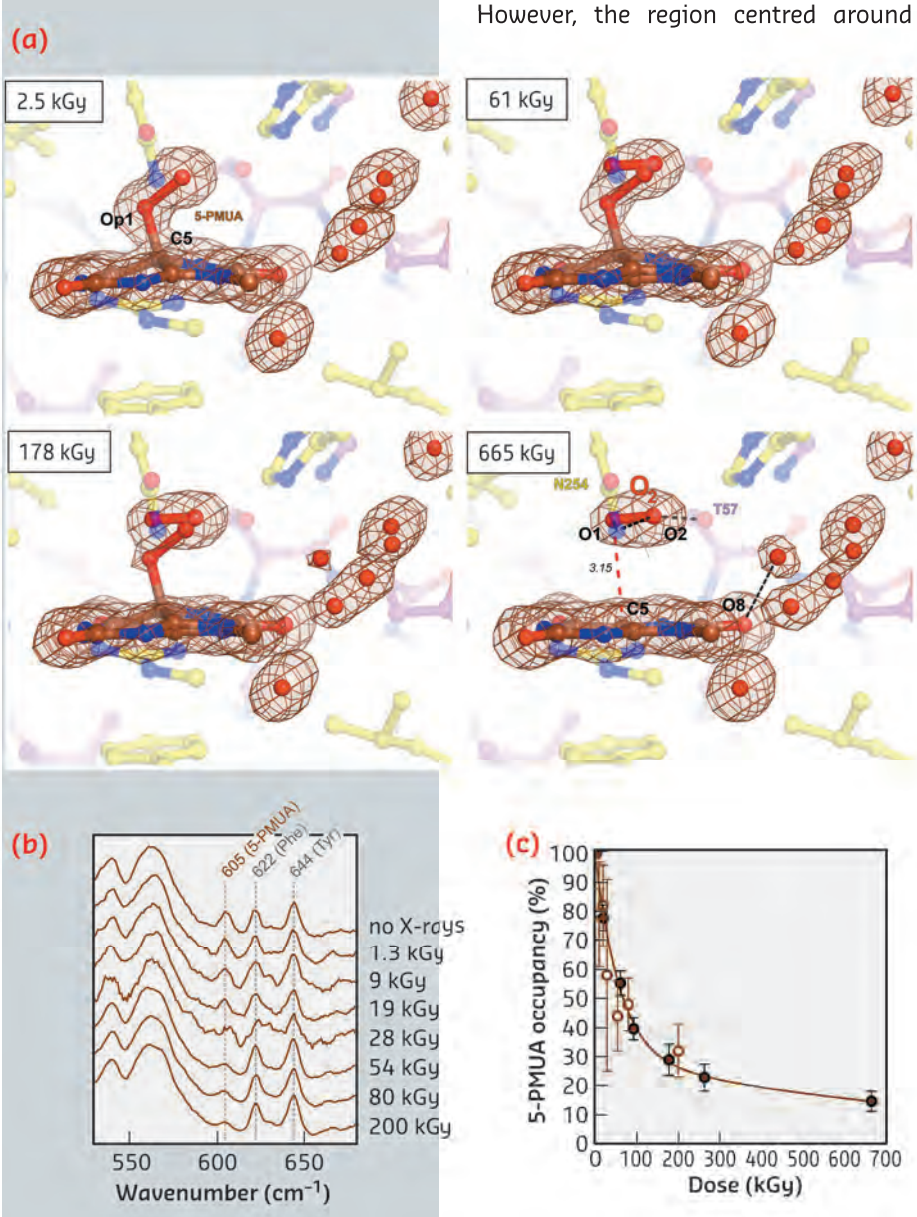

Fig. 115: *a*) Dose-stamped snapshots for UOX:5-PMUA radiolysis. Electron density is shown for the organic moieties and solvent molecules in close proximity. b) Online *in-crystallo* Raman spectroscopy reveals the specific dose-dependent decrease of the 605 cm^{-1} 5-PMUA 'fingerprint band'. c) 5-PMUA decay is biphasic suggesting a mechanism of peroxide regeneration. 5-PMUA occupancies from crystallographic refinement are shown as filled circles. Open circles are 5-PMUA occupancies estimated from the integration of the 605 cm^{-1} Raman band.

Exposure to X-rays can lead to specific modifications in proteins and nucleic acids, including bond rupture. We observed that the C5-Op1 bond is susceptible to selective radiolysis at very low X-ray doses. We tracked this quantitatively using on line Raman-assisted crystallography by performing multiple data collections interspersed by spectrophotometric measurements on a single UOX:5-PMUA crystal. The dose-dependent rupture of the C5-Op1 bond is accompanied by the loss of Sp3 hybridisation at C5 leading to a planar organic structure (**Figure 115a** 2.5-655 kGy). Concomitantly, a diatomic molecule with a shorter bond length (1.2 Å) than the original peroxide is liberated and trapped above it. We interpreted the elongated electron density as molecular oxygen as reactive oxygen species are likely transiently formed in the process and are expected to rapidly convert to the more stable O_2 molecule. Dioxygen adopts a well-defined position and orientation above the flat organic molecule. The O_2 molecular axis lies parallel to the plane at a distance of 3.15 Å and is rotated by 15° as compared to the original Op1-Op2 peroxide bond (**Figure 115a**).

Online Raman analysis shows that peroxide rupture causes the height of the 605 cm^{-1} 'signature band' to selectively decrease in a dose-dependent manner (**Figure 115b**), consistent with our QM/MM calculations that assign this band to the stretching of the C5-Op1 bond. The dose-dependent 5-PMUA occupancy from crystallographic refinement at near-atomic resolution is in excellent agreement with its orthogonal estimation from the integration of the 605 cm^{-1} Raman signal (**Figure 115c**). 5-PMUA decay follows a biphasic profile. This is not consistent with a simple peroxide decomposition process. The observed decay can be rationalised assuming a pathway of peroxide regeneration acting alongside its decomposition. We have fitted this process kinetically.

Our multi-technique investigation offers unambiguous evidence for a C5-peroxide intermediate in cofactor-free UOX catalysis. Peroxide radiolysis followed by online Raman-assisted X-ray crystallography afforded exquisite insight into the elusive reactants' configuration leading to the peroxo intermediate. The latter is suggested to be formed by a radical recombination process.

References
[1] S. Fetzner and R.A. Steiner, *Appl. Microbiol. Biotechnol.* **86**, 791-804 (2010).

SHAPING THE EARLY EVENT OF PRION FORMATION

The conversion of the cellular prion protein (PrP^C) into its misfolded and amyloidogenic isoform, denoted as prion or PrP^{Sc}, is the central event in prion diseases which affect humans and animals. In prion biology, unravelling the molecular mechanisms leading the conversion process whereby α-helical motifs are replaced by β-sheet secondary structures is of utmost importance.

The structure of human PrP^C consists of a disordered N-terminal part (residue 23-127) and a structured C-terminal domain (residue 128-228) (**Figure 116**). The insoluble and heterogeneous nature of PrP^{Sc} makes its structural characterization extremely difficult. The N-terminal region of PrP^C features a palindromic sequence (AGAAAAGA) which can lead to the formation of neurotoxic fibrils enriched in β-sheet motifs. Experimental evidence also supports the idea that the palindromic sequence plays a critical role for prion generation and transmissibility. However, the intrinsic flexibility of this N-terminal region has hampered efforts to obtain atomic information on the structural features of the palindromic sequence.

In this study, we used nanobodies (Nb) to solve the first structures of the full-length HuPrP and its

Principal publication and authors
R.N.N. Abskharon (a, b, c), G. Giachin (d, e), A. Wohlkonig (a, b), S.H. Soror (a, b, f), E. Pardon (a, b), G. Legname (d) and J. Steyaert (a, b), *J Am. Chem. Soc.* **136**, 937-944 (2014).
(a) Structural Biology Brussels, Vrije Universiteit Brussel (Belgium)
(b) Structural Biology Research Center, VIB, Brussels (Belgium)
(c) National Institute of Oceanography and Fisheries (NIOF), Cairo (Egypt)
(d) Department of Neuroscience, Laboratory of Prion Biology, Scuola Internazionale Superiore di Studi Avanzati (SISSA), Trieste (Italy)
(e) Present address: ESRF.
(f) Center of Excellence, Helwan Structure Biology Research, Faculty of Pharmacy, Helwan University, Cairo (Egypt)

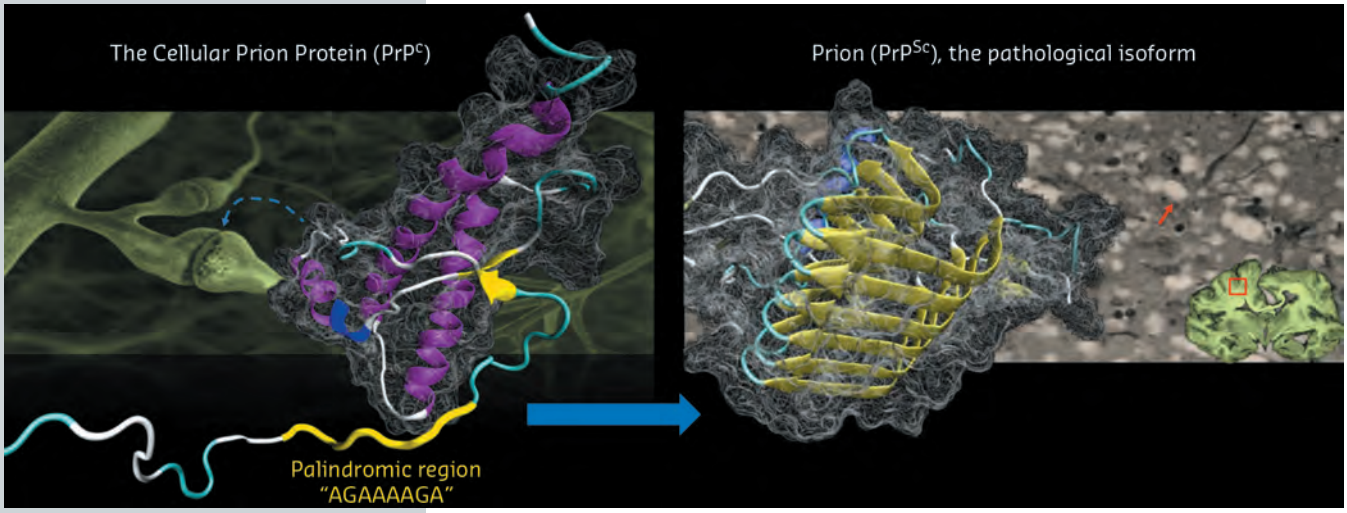

Fig. 116: Structural conversion of the cellular prion protein (PrP^{C}) to its pathological isoform, denoted as prion or PrP^{Sc}. PrP^{C} is mostly involved in synaptic functions. PrP^{Sc} causes prion diseases such as Creutzfeldt-Jakob disease in humans which is characterised by spongiform neurodegeneration (arrow) in the brain.

C-terminal truncated version by X-ray crystallography. Nb are small (15 kDa) and stable single-domain fragments harbouring the full antigen-binding capacity of the original heavy chain–only antibodies that naturally occur in camelids. Collective efforts of several laboratories have demonstrated that Nbs are exquisite chaperones for crystallising complex biological systems such as membrane proteins, transient multiprotein assemblies, transient conformational states and intrinsically disordered proteins [1].

In complex with this Nb, the total amount of structured polypeptide (125 amino acids of antibody and 108 amino acids of the prion protein) rises to 71% as against 52% for free HuPrP, thus providing a much better starting point for crystallisation. The high-resolution X-ray crystal structures (obtained using data collected at beamline **BM30A**) of two HuPrPs in complex with a selective nanobody (Nb484) revealed a novel structural feature. While the segment from residues 128 to 225 shares a fold that is very similar to the corresponding NMR HuPrP structures, the binding of Nb484 to a region adjacent to the first β-sheet (β1) unveils key structural features of the hydrophobic segment from residues 117 to 128, which had remained unresolved in all the PrP structures published so far.

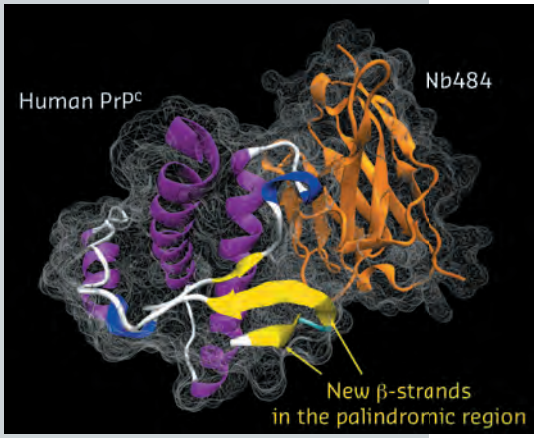

Fig. 117: Crystal structure of the human PrP^{C} in complex with a nanobody (Nb484) with the newly formed β-strands in the palindromic region highlighted.

In our X-ray structures, the sequence including the palindromic motif arranges in a novel β-strand we denoted as β0 (residues 118–122), which folds into a three-stranded antiparallel β-sheet with β1 and β2 (**Figure 117**). The same structural arrangement was observed in both crystal structures, suggesting that it does not result from crystal packing but might have major biological implications for prion conversion. Edges of regular β-sheets are inherently aggregation-prone because the motif for H-bonding with any other β-strand is available. From our structures, it appears that the exposed edge of the short β1 strand observed in all previous PrP structures serves as an intra-molecular nucleus for edge-to-edge β aggregation of part of the palindromic sequence to form the β0 strand. The propensity of the palindromic sequence to engage in such β-structures strongly indicates that this motif mediates β-enrichment in the PrP^{C} monomer as one of the early events in the PrP^{C} to PrP^{Sc} conversion.

Here, we show that Nb-assisted crystallography is a powerful tool for unveiling local structural features of intrinsically disordered proteins. Our data provide structural evidence that the palindromic motif of HuPrPs is important as a dynamic site for

β-sheet structural conversion in prion formation. The structures we solved also support the hypothesis that the conserved palindromic sequence mediates β-enrichment in the PrP^C monomers as one of the early events in prion formation. Moreover, crystals of the full-length human PrP in complex with Nb484 are amenable to soaking experiments to study the interactions of small molecules with the flexible region of HuPrP [1].

References
[1] E. Pardon *et al.*, *Nat Protoc* **9**, 674-93 (2014).

A MOLECULAR CALIPER FOR METERED HORMONE RESPONSE

Principal publication and authors
D.R. Boer (a,b), A. Freire-Rios (c), W.A.M. van den Berg (c), T. Saaki (c), I.W. Manfield (d), S. Kepinski (d), I. Lopez-Vidrieo (e), J.M. Franco-Zorrilla (e), S.C. de Vries (c), R. Solano (e), D. Weijers (c) and M. Coll (a,b), *Cell* **156,** 577-589 (2014).
(a) Institiute for Research in Biomedicine, Barcelona (Spain)
(b) Institut de Biologia Molecular de Barcelona (Spain)
(c) Laboratory of Biochemistry, Wageningen University (Netherlands)
(d) Faculty of Biological Sciences, University of Leeds (UK)
(e) Centro Nacional de Biotecnologia, Madrid (Spain)

Hormones trigger a variety of responses to control growth, development and physiology. Understanding the molecular underpinnings of specificity is a key challenge in biology. The plant signalling molecule auxin is central for growth and development and controls a wide range of processes, including embryogenesis and flower development [1]. Here, we report a molecular mechanism for the generation of diversity and specificity in auxin response.

Auxin is recognised by nuclear receptors, promoting degradation of inhibitor proteins and consequent activation of DNA-binding auxin response factors (ARFs), that control transcription of thousands of genes to bring about a multitude of developmental responses. In the past, we had shown that variations in the ARF family in the higher plant *Arabidopsis thaliana* largely determine auxin response specificity [2]. For the present research, our biological and structural biology teams joined forces to determine the structural underpinnings of functional diversity within the ARF family.

Crystallographic analysis using beamlines **ID14-1** and **ID14-4** revealed that ARF proteins bind DNA as dimers, and let us identify the essential protein-DNA contacts. We then used a range of biochemical and *in vivo* methods to show that these protein-DNA contacts are indeed essential for DNA binding and function in mediating auxin response and that ARF protein dimerisation is critical for function as it allows high-affinity cooperative binding to complex DNA elements. These elements are composed of inverted repeats of a binding motif with a spacer in between the two motifs.

When comparing two highly divergent ARF proteins, we found them to adopt almost identical structures (**Figure 118**). Likewise, when we determined the DNA-binding preference of ARF monomer proteins, the intrinsic specificity was the same. Thus, neither overall structure, nor intrinsic DNA binding specificity can explain the different biological functions of these two ARF proteins. As the binding of ARF dimers to complex motifs is not only determined by DNA-binding amino acids but also by protein-protein interactions, we tested the hypothesis that ARFs could differ in the spacing tolerated between the two DNA motifs. We found that ARFs differed in this property. While ARF1 could bind with high affinity to complex elements with a spacer of 7 or 8 bases, ARF5 could also bind to motifs with spacing of 5, 6 or 9 bases (**Figure 119**). Thus, our work reveals a mechanism for DNA-binding specificity within a transcription factor family that is based upon proteins acting as "calipers". The overall structure of dimers determines the setting of the caliper, and thus the distance between two sites.

This work now offers a new framework for understanding specificity in plant hormone response and opens many new avenues for future investigations. Of particular interest would be

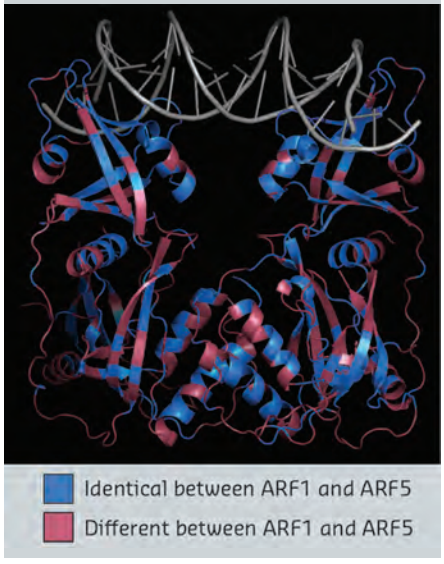

Fig. 118: Structure of *Arabidopsis thaliana* ARF1 protein dimer in complex with DNA oligonucleotide with two inverted binding motifs. Residues are coloured according to whether they are identical (blue) or different (magenta) between ARF1 and ARF5.

References
[1] S. Vanneste and J. Friml, *Cell* **136,** 1005-1016 (2009).
[2] E.H. Rademacher, A.S. Lokerse, A. Schlereth, C.I. Llavata-Peris, M. Bayer, M. Kientz, A. Freire-Rios, J.W. Borst, W. Lukowitz, G. Jürgens and D. Weijers, *Dev. Cell* **22,** 211-222 (2012).

to discover: how a caliper-based mechanisms is leveraged in living cells to recognise specific genes, how the ARF caliper can be tuned by co-factors and, perhaps most importantly, how this caliper mechanism evolved to increase the complexity of the auxin response.

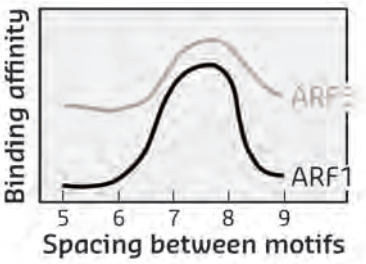

Fig. 119: Affinity of DNA binding by ARF1 and ARF5 depends on the space between the two inverted binding motifs.

STRUCTURES OF PI4KIIIβ COMPLEXES SHOW HOW THE ENZYME RECRUITS Rab11 WITH ITS EFFECTORS

Principal publication and authors
J.E. Burke (a,b), A.J. Inglis (a), O. Perisic (a), G.R. Masson (a), S.H. McLaughlin (a), F. Rutaganira (c), K.M. Shokat (c), R.L. Williams (a), *Science* **344**, 1035-1038 (2014).
(a) MRC Laboratory of Molecular Biology, Cambridge Biomedical Campus (UK)
(b) Department of Biochemistry and Microbiology, University of Victoria (Canada)
(c) Howard Hughes Medical Institute and Department of Cellular and Molecular Pharmacology, UCSF, San Francisco (USA)

References
[1] N. Altan-Bonnet and T. Balla, *Trends Biochem Sci* **37**, 293–302 (2012).

Four mammalian enzymes phosphorylate the lipid phosphatidylinositol to produce phosphatidylinositol 4-phosphate (PI4P). One of these enzymes, PI4KIIIβ, is enlisted by a range of RNA viruses, including hepatitis C virus and enteroviruses to form PI4P-enriched viral replication organelles [1] and several compounds inhibit enteroviral replication by targeting cellular PI4KIIIβ. PI4KIIIβ is also important in the malarial life cycle, and inhibitors of the *P. falciparum* PI4KIIIβ are potent anti-malarial agents.

In addition to producing PI4P, PI4KIIIβ is also required for the recruitment of both the small GTPase Rab11 and its downstream effectors. To understand the structure and dynamics of PI4KIIIβ, we have employed a combination of X-ray crystallography carried out at beamlines **ID23-2** and **ID29** with hydrogen-deuterium exchange mass spectrometry (HDX-MS) carried out at the MRC-LMB HDX-MS facility. The HDX-MS analysis of PI4KIIIβ identified intrinsically disordered regions in the enzyme and removal of these regions enabled crystallisation of the enzyme in a complex with Rab11. The structure of the complex shows that PI4KIIIβ has a catalytic domain that resembles the phosphatidylinositol 3-kinases (PI3Ks) and that it interacts with Rab11 using a helical solenoid domain N-terminal to the kinase domain (Figure 120). These crystal contacts were confirmed in solution by HDX-MS.

PI4KIIIβ interacts with Rab11 in a contact that includes a unique direct interaction with the Rab11 GTP nucleotide, and this contact leaves the switch regions of the Rab11 largely free to interact with Rab11 effectors (see inset, Figure 120). It is the nucleotide-dependent change in conformation of these switch regions that is essential for the signalling role of Rab11. This suggests that PI4KIIIβ might be able to bind Rab11 while it, in turn, binds to its effectors. This was confirmed by a low-resolution structure of a complex of PI4KIIIβ with Rab11 and the dimeric Rab11-binding domain (RBD) of the FIP3 Rab11 effector. These structures may provide the basis for design of PI4KIIIβ inhibitors for anti-viral and anti-malarial applications.

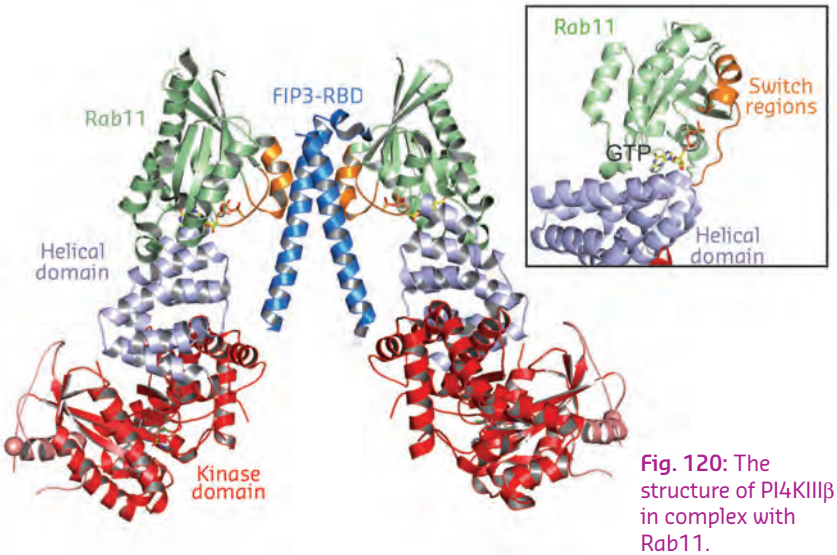

Fig. 120: The structure of PI4KIIIβ in complex with Rab11.

STRUCTURE OF MATERIALS

The development of new technologies plays a fundamental role in meeting major societal challenges. New advanced materials and devices such as rechargeable batteries, catalytic materials, etc. form part of this development. The complexity of these heterogeneous devices can only be studied adequately by a combination of experimental methods, in order to reveal the interplay between the microscopic material properties and the macroscopic device performance. The following structure of materials highlights demonstrate the utility of synchrotron X-ray characterisation techniques for the study of both real devices under operating conditions and idealised model systems under precisely controlled environments.

The past year was again especially busy for the Structure of Materials Group. ID01 has now been reconstructed as the upgrade beamline project UPBL1, Diffraction imaging for nanoanalysis. The first coherent diffraction nano-imaging user experiments were carried out at the end of the year taking advantage of the enhanced nanofocus and coherence capabilities of this long beamline. Through optimisation of the source and the geometry of the monochromator, an increase of the coherent flux by a factor of 5 has been obtained right from the first startup of the beamline. Further optical elements will be added in 2015 allowing versatile optimisation of the total flux and beam size over a wide energy range. The high resolution powder diffraction beamline moved from ID31 to ID22 at the beginning of 2014 and it returned to user operation at the beginning of the summer. The flux has increased by a factor of 2.5 due to the reduced horizontal divergence at a high-β sector and its energy range now reaches 80 keV. Later this year, ID22 users will be able to benefit from the large area detector for complementary studies and from the new high-resolution diffractometer allowing future developments for enhanced detector systems.

The construction of upgrade beamline project UPBL2, the high energy beamline for buried interface structures and materials processing, started at ID31 in January 2014. The lead hutches are now ready and installation of the beamline components will soon commence. This long beamline with nanofocus capabilities extended to high photon energies will carry out the first user experiments in autumn 2015. The final beamline to be rebuilt in the current Phase I of the Upgrade Programme is ID15. At the moment, the old lead hutches are to be demolished, and by the end of 2015 the new hutches will be ready for the high pressure diffraction branch (relocation of ID09A) and for the material chemistry and engineering materials science branch. Due to the canting of the straight section, these two branches are independent.

The new buildings constructed during the first phase of the upgrade resulted in an increase in space available for the structure of materials group. In particular, an electrochemistry laboratory, under the responsibility of the ID03 team but open to all the users, is now operational in the new Lab and Office Building (LOB). In particular, it houses a new glove box dedicated to studies of Li batteries partly funded by the BM26-Dubble and BM1-Swiss Norwegian beamlines. The LOB also hosts a catalyst laboratory, providing new opportunities for materials chemistry studies at ESRF. Furthermore, a nanoscope instrument to exploit high energy nanofocus beams at ID11 will be ready later this year.

The beamline performance improvements already mentioned in addition to better detectors constitute a revolutionary enhancement in performance. This, together with the development of side laboratories should open a new chapter in the structure of materials studies at the ESRF and make it possible to attract an even greater community of users from both academia and industry.

V. HONKIMÄKI

ARTIFICIAL GRAPHENE MADE OF SEMICONDUCTOR QUANTUM DOTS

Principal publication and authors
M.P. Boneschanscher (a), W.H. Evers (b), J.J. Geuchies (a), T. Altantzis (c), B.Goris (c), F.T. Rabouw (a), S.A.P. Van Rossum (a), H.S.J. van der Zant (b), L.D.A. Siebbeles (b), G. Van Tendeloo (c), I. Swart (a), J. Hilhorst (d), A.V. Petukhov (a), S. Bals (c) and D. Vanmaekelbergh (a), *Science* **344**, 1377-1380 (2014).
(a) Debye Institute for Nanomaterials Science, Utrecht University (The Netherlands)
(b) Opto-electronic Materials, Kavli Institute, Delft University of Technology (The Netherlands)
(c) Electron Microscopy for Materials Science (EMAT), University of Antwerp (Belgium)
(d) ESRF

Quantum dot superlattices are structures that can be formed through the self-assembly of colloidal semiconductor nanocrystals, which are nanoparticles with size-dependent properties [1]. Many applications have been envisioned for quantum dot superlattices, ranging from solar cells and transistors to LEDs. The properties of such systems depend both on the properties of the constituent particles and on the structure of the superlattice. The novel effects related to the formation of a superstructure remain to be addressed experimentally.

One particular superlattice with very interesting properties is the honeycomb superlattice [2]. It resembles the wonder material graphene, but instead of having carbon atoms at the edges of its honeycomb, it has PbSe or CdSe nanocrystals, which are fused together into a single-crystalline sheet. Theory predicts this material to have properties similar to those of graphene, such as very high charge carrier mobility, which could be conveniently modified by an electric field. In addition, courtesy of its semiconductor building blocks, the electronic properties can be further tuned by the quantum dot composition and size, making the "artificial graphene" very interesting for applications in the electronics industry [3].

Oriented attachment is a specific method for the preparation of such superlattices from the nanocrystal building blocks. In oriented attachment, nanocrystals fuse together through atomically matched bond formation between two specific facets. Precise control of nanocrystal and ligand concentration as well as temperature enabled the synthesis of large area, defect free honeycomb superlattices. The formation of these systems is remarkable, given that several demanding conditions must be fulfilled. The nanocrystal building blocks must be nearly monodisperse in size and shape, and attachment should occur with atomic accuracy, between a geometrically defined subset of nanocrystal facets.

The nanocrystal building blocks have the shape of a truncated cube, approaching that of a rhombicuboctahedron, implying that the nanocrystals are terminated with {100}, {110} and {111} facets. Characterising the honeycomb superlattice with high-angle annular dark field (HAADF) scanning transmission electron microscopy (STEM) combined with electron diffraction reveals that the <111> axis of the nanocrystals is perpendicular to the substrate and that the structure is single crystalline, having all nanocrystals aligned similarly (**Figure 121a,b**). There are three models which fulfil this condition: a trigonal model, where the nanocrystals attach via {110} facets, a tetrahedral model where they attach via {111} facets and an octahedral model where they attach via {100} facets (see **Figure 121c,d**).

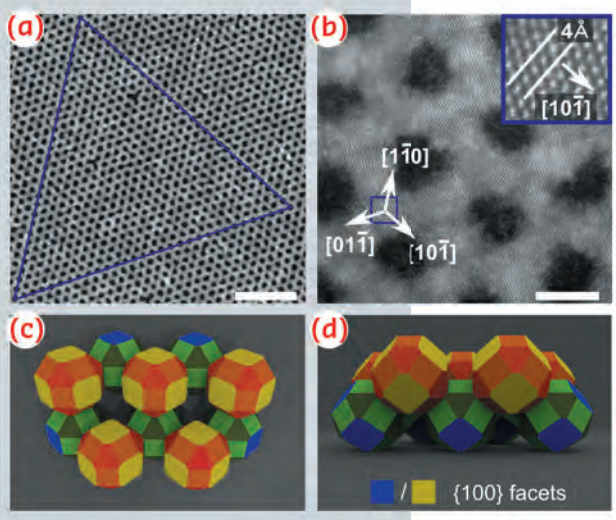

Fig. 121: Single-crystalline PbSe honeycomb structures created by means of oriented attachment. a) HAADF-STEM image of the honeycomb structure (bright on a dark background). The equilateral triangle shows the long-range ordering of the structure. Scale bar, 50 nm. b) High-resolution HAADF-STEM image showing that the ⟨111⟩ NC axes are perpendicular to the honeycomb plane and three of the ⟨110⟩ axes are perpendicular to the (c) and (d) models of the honeycomb structure, with truncated cubes as nanocrystals. The two inequivalent sites in the honeycomb lattice are indicated by yellow/red and blue/green NCs. c) and d) are the top and side view of the octahedral structure, respectively.

These models appear similar from the top, but have a very different 3-dimensional structure. The trigonal structure is flat, exactly like graphene, whereas the tetrahedral and octahedral structures are buckled comparable to the silicene structure.

The HAADF-STEM images combined with the electron diffraction show that the <110> axes are perpendicular to the superstructure bonds, ruling out the possibility of the trigonal structure (where the <110> axes are parallel to the nanocrystal bonds). In addition, these images show increased scattering strength on the nanocrystal bonds, indicating a larger-than-average thickness of the structure at these positions which originate from the out-of-plane bonding of the honeycomb structure. Scanning tunnelling microscopy (STM) measurements showed that the honeycomb structure is indeed buckled. However in STM, the topography is a complicated convolution of the superlattice topography and the tip shape, so no quantitative height data could be extracted. A next-nearest neighbour distance of nanocrystals at the same height could reliably be extracted, which on average is 8.5 ± 0.8 nm.

To further study the long-range order, grazing incidence small-angle X-ray scattering (GISAXS) experiments were performed at **ID01** (**Figure 122a,b**). The scattering pattern shows diffraction rods arising from the hexagonal symmetry of the honeycomb structure, with the expected relative positions of 1 : √3 : 2 : √7. The extracted hole-hole distance of the honeycomb structure, corresponding to the next-nearest neighbour (NNN) distance, is 8.5 nm, which is in agreement with the STM measurements.

To distinguish between the tetrahedral and octahedral model, electron tomography was performed. Slices through the reconstructed tomogram perpendicular to the substrate indicate that the nanocrystals in the honeycomb unit cell are located on different heights. Subsequently, automated particle detection was performed on a region of interest to extract important parameters, such as bond angle, bond length and NNN

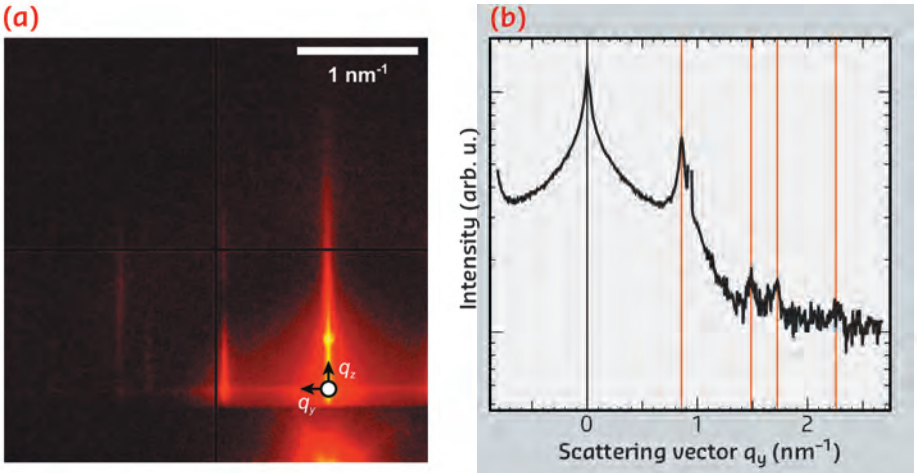

Fig. 122: a) GISAXS pattern of a honeycomb structure on top of a Si(100) substrate obtained at ID01. b) Line trace in the horizontal direction indicated in (a). Red lines mark diffraction peaks with relative positions of 1 : √3 : 2 : √7 arising from the hexagonal symmetry of the honeycomb lattice.

bond length. The obtained bond length of 95° ± 5° shows that the honeycomb structure is of the octahedral type, with bonds between {100} facets. The bond length was found to be 13% larger than the original nanocrystal diameter, indicating neck formation between the nanoparticles in the superlattice.

It has been predicted that honeycomb semiconductors of zinc blend compounds (such as CdSe) show a truly new electronic band structure. The PbSe honeycomb structure is changed into CdSe via a cation exchange reaction, which has been confirmed by means of energy dispersive X-ray spectroscopy. Combining this with HAADF-STEM and electron diffraction showed that the Se anion lattice is preserved with respect to the honeycomb periodicity.

These results show that the honeycomb lattice, which is buckled and of octahedral symmetry, can be made on a liquid surface, and can subsequently be transformed into a material of interest via cation exchange. A next step in this research will be the *in situ* measurements of the formation of this remarkable type of crystal.

References
[1] W.H. Evers *et al.*, *Nano Lett.* **13**, 2317 (2013).
[2] M.P. Boneschanscher *et al.*, *Science* **344**, 1377 (2014).
[3] E. Kalesaki *et al.*, *Phys. Rev. X* **4**, 011010 (2014).

Principal publication and authors
Z. Ristanović (a), J.P. Hofmann (a), U. Deka (a), T.U. Schülli (b), M. Rohnke (c), A.M. Beale (a) and B.M. Weckhuysen (a), *Angew. Chem. Int. Ed.* **52**, 13382 –13386 (2013).
(a) Inorganic Chemistry and Catalysis, Utrecht University (The Netherlands)
(b) ESRF
(c) Institute of Physical Chemistry, Justus-Liebig-University Giessen (Germany)

CRYSTALLOGRAPHIC ARCHITECTURE OF A SINGLE ZEOLITE ZSM-5 CRYSTAL

Zeolites represent a very important class of natural and synthetic aluminosilicate materials with a wide range of applications including ion-exchange, adsorption and catalysis. The size and topology of zeolite cages and channels is determined by a highly crystalline 3-D porous network that consists of the Si-O tetrahedra. Substitution of Al for Si atoms in the crystalline structure leads to the formation of acidic sites that can catalyse a broad range of chemical reactions. This particular combination of Al-related acidic sites and shape-selective properties defined by their narrow pores (< 0.8 nm) makes zeolite catalysts a workhorse in numerous large-scale industrial processes.

Zeolite ZSM-5 is one of the most abundantly used solid acid catalysts in oil refining and petrochemical industries. To understand the catalytic performance of this material, large coffin-shape zeolite crystals (100 × 20 × 20 μm^3) have frequently been investigated as model systems [1]. The crystals have been used in numerous micro-spectroscopic studies due to their well-defined structure and suitable size. They consist of at least 6 intergrown subunits (**Figure 123**) that may differ in their crystallographic orientation making the crystal properties highly anisotropic. Therefore one of the intriguing questions related to the structure and reactivity of zeolite ZSM-5 crystals is the precise orientation of the porous network in individual subunits and their impact on uptake and diffusion of guest molecules. This question has been mostly studied using a number of optical microscopy techniques providing only indirect evidence of the crystallographic orientation of the subunits.

Using highly focused X-rays at **ID01,** we conducted a micro-X-ray diffraction (μ-XRD) crystallographic imaging study of a single zeolite ZSM-5 crystal. Individual zeolite ZSM-5 crystals were mapped using an X-ray beam (8.5 keV) focused down to a size of 1 × 2 μm^2. To minimise the footprint of the beam, we recorded higher order Bragg reflections in the range of 2θ > 70° (**Figure 123a**). The *a* and *b* lattice parameters of zeolite ZSM-5 are almost identical, which enables reliable identification of the crystalline phases based on distinct splitting of the higher order (16 0 0) and (0 16 0) reflections. Using those reflections, we further reconstructed diffraction intensity maps with lateral resolution of 2 μm and determined crystallographic orientation of the individual subunits. The results indicate 90° intergrowth structure of a zeolite ZSM-5 crystal, meaning that the top and bottom subunits have a 90° rotated crystal lattice as compared to the remaining subunits (**Figure 123b**). This implies that the direction of the straight and sinusoidal pores changes depending on the subunits, therefore having an impact on uneven uptake of guest molecules.

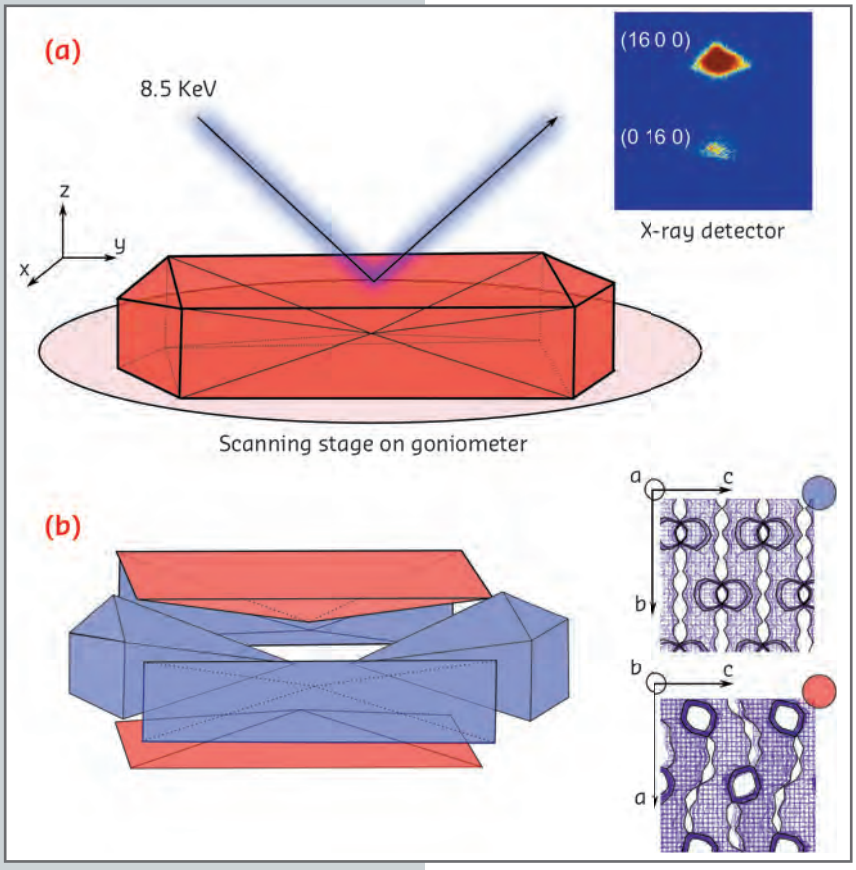

Fig. 123: a) Schematic of the μ-XRD imaging approach. b) Intergrowth structure of the zeolite ZSM-5 crystal and the crystallographic orientation of each subunit (colour-coded).

The high angular and spatial resolution of the technique also enables subtle changes in the lattice parameters to be resolved. It was possible to map the distortion of the crystal lattice spatially along the crystal *x* and *y* axes (**Figure 124**). The results point towards a very small, but detectable 0.02 Å expansion of the unit cell from the centre of the crystal towards the edges. This is explained by a macroscopic gradient in the concentration of Al atoms and consequently the heterogeneous distribution of acidic sites. As a result of this gradient, inner regions of the zeolite crystal are Si-rich, while Al atoms mostly concentrate in the outer crystalline layer near the surface – a phenomenon that to the best of our knowledge has never been crystallographically substantiated (**Figure 124b**).

With the method demonstrated here, it is possible to look at the crystalline structure not only of a single zeolite crystal – but also at any advanced crystalline material where structural and chemical gradients play an important role. In addition, hard X-ray diffraction provides an ideal tool to study chemical processes *in situ*, where one could benefit from the well-defined model systems, such as zeolite ZSM-5 crystals. Using a combination of μ-XRD and a wide range of micro-spectroscopic techniques, it is now possible to elucidate the structure-performance relationship for numerous processes that take place within functional materials.

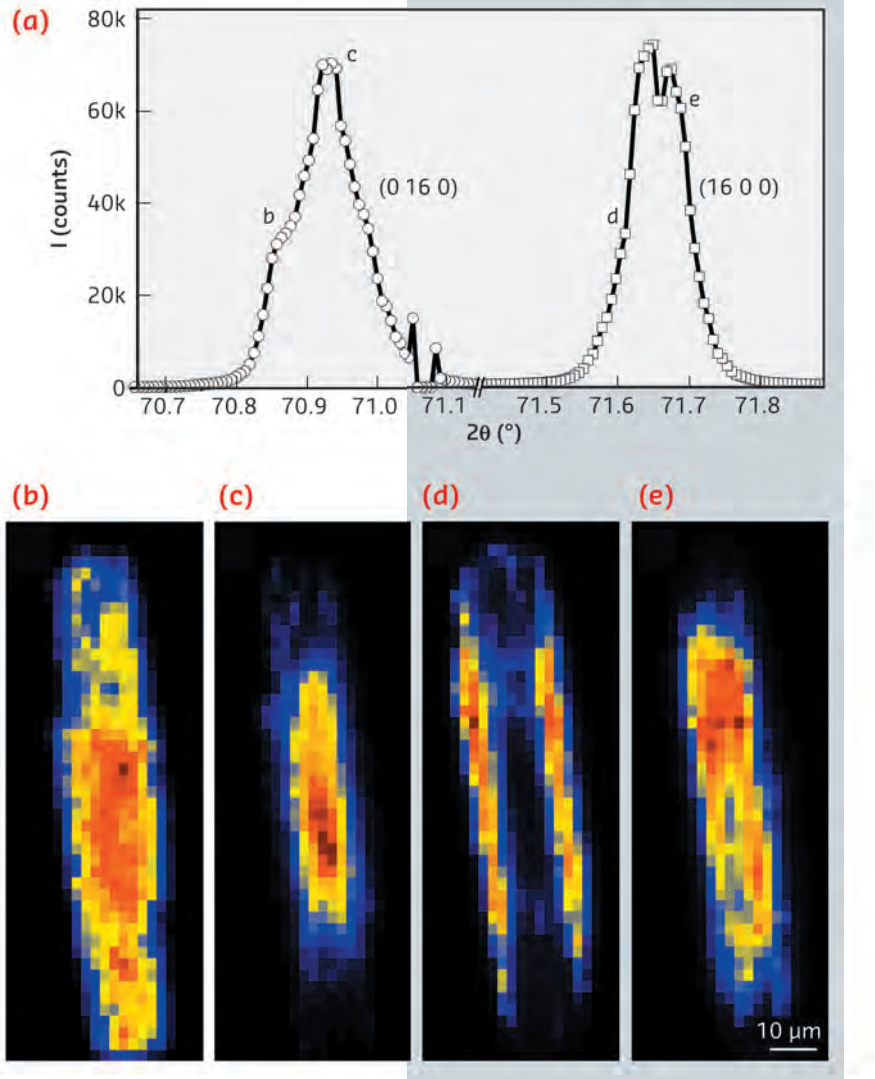

Fig. 124: a) Fine structure of the reconstructed single (x, y) pixel diffractograms, measured for the (16 0 0) and (0 16 0) Bragg reflections. b-e) Corresponding μ-XRD intensity maps of the Bragg peaks integrated for the 2θ regions as indicated in (a).

References
[1] L. Karwacki, M.H.F. Kox, D.A. Matthijs de Winter, M.R. Drury, J.D. Meeldijk, E. Stavitski, W. Schmidt, M. Mertens, P. Cubillas, N. John, *et al.*, *Nat. Mater.* **8**, 959–965 (2009).

GENERATION OF SURFACE STEPS ON Pt(9 7 7) INDUCED BY THE CATALYTIC OXIDATION OF CO

Atoms at surfaces have fewer neighbours than atoms in the bulk (typically 9 vs 12) and consequently they have "unsaturated" chemical bonds. Atoms at surface steps (see **Figure 125**) have even more "dangling" bonds (seven neighbours only) and due to this, they might be key actors in surface chemical reactions in catalysis. This simple idea was proposed in 1925 and since that time it has been investigated extensively. Atoms at steps have been found to dissociate molecules such as N_2, CO or molecules with C-C bonds; in most cases this has been determined using ultra-high vacuum techniques. However, chemical reactions are more complicated

Principal publication and authors
O. Balmes (a), G. Prevot (b), X. Torrelles (c), E. Lundgren (d) and S. Ferrer (c,e), *Journal of Catalysis* **309**, 33–37 (2014).
(a) ESRF
(b) Institut des NanoSciences de Paris, UMR CNRS 7588, Université Pierre et Marie Curie-Paris 6 (France)
(c) Institut de Ciència de Materials, CSIC, Bellaterra (Spain)
(d) Department of Synchrotron Radiation Research, Institute of Physics, Lund University (Sweden)
(e) ALBA Light Source, Cerdanyola del Valles (Spain)

References

[1] R. van Rijn *et al., Rev, Sci. Instrum.* **81,** 014101 (2010).

than the adsorption and dissociation process and many studies have set out to question the simple picture of "more step atoms implies more reactivity". This was the case for several reports dealing with CO oxidation to CO_2.

We investigated the oxidation of CO at beamline **ID03** using a single crystal surface of platinum as the catalyst. This crystal has a periodical array of steps (see **Figure 125**), which generates specific diffraction features.

Figure 125b shows a portion of the diffracted intensity. The diffuse lines at H = 16 and 18 designated as CTR (crystal truncation rod) arise from the step array, whereas the intense peaks (red colour) arise from the diffraction of bulk atoms, of no interest here. The diffuse lines marked {111} indicate that the crystal surface also has regions with (111) symmetry, therefore not all areas are stepped as depicted in the figure. Regions with (111) symmetry occur because the 977 surface is not very stable and in some places the steps bunch together generating (111) microfacets.

By measuring the intensities of the CTR and of the {111} diffuse lines, we were able to monitor the evolution of the concentration of steps at the surface during the reaction.

We used a specially designed reactor **[1]** that allows the diffracted intensities and the reaction product to be measured simultaneously while the reaction $2CO + O_2 = 2CO_2$ was occurring. The proportion of the reactants was measured with the experimental variable $R = P_{CO} / P_{O2}$, the ratio of the partial pressures. R = 2 corresponds to the stoichiometric proportion and R < 2, R > 2 to oxygen rich or oxygen deficient proportions. The total pressure $PCO + PCO_2$ = 200 mbar and the reaction temperature was around 490°C. The amount of CO_2 produced was monitored with a gas spectrometer.

We found that, at a given temperature, the production of CO_2 was maximum for R = 2 and that the maximum reactivity was associated with a maximum density of steps. Values of R other than 2 resulted in lower CO_2 production and fewer steps in the Pt surface. Some of these observations are presented in **Figure 126**.

These results illustrate that the morphology of the catalyst changes with the reaction conditions. When the reactivity is high, the number of steps is also high, whereas when the reactivity is low, the number of steps decreases and the proportion of (111) microfacets increases. The catalyst is not a passive spectator of the reaction, rather the contrary, it transforms itself to optimise the reaction rate by increasing its proportion of step atoms. Thus, the atoms at the steps do appear to be a key ingredient for a high reaction rate.

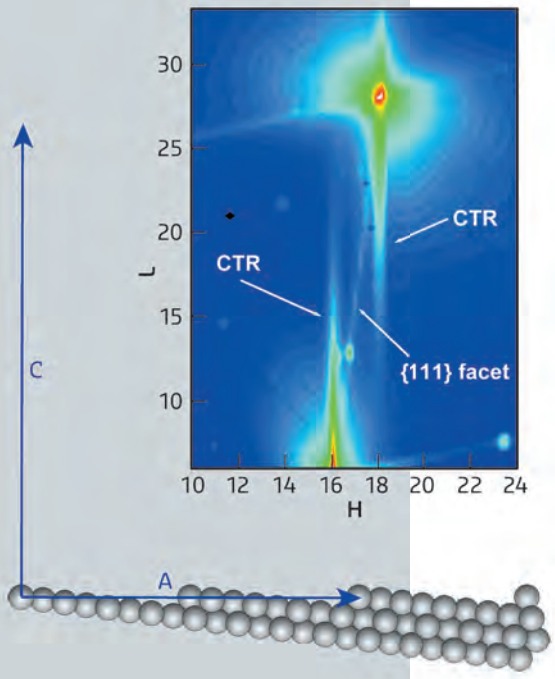

Fig. 125: a) Side view of the 977 surface showing step and terrace atoms. b) A portion of reciprocal space diffraction pattern. The diffuse CTR lines arise from the monoatomic steps and the {111} diffuse inclined line from (111) microfacets.

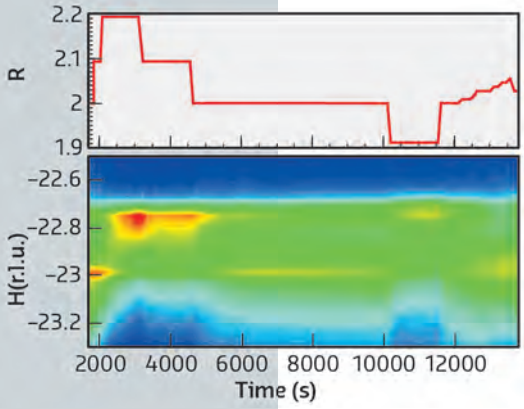

Fig. 126: Temporal variation of the proportion of the reactants (upper panel) and the corresponding changes in reciprocal space (lower panel). The intensity at H = –23 arises from steps and that at ~ –22.7 from (111) microfacets. At the start of the experiment (R = 2, stoichiometric mixture), the intensity from the monoatomic steps is pronounced (red indicates high intensity) and it fades out when the gas mixture is made CO rich, while the intensity from the facets that was initially low (green) clearly develops. When the gas mixture is set back to the stoichiometric proportion (near t = 5000 s), the intensity from the steps increases again (yellow segment), while that of the facets strongly decreases. Subsequent change to an oxygen rich mixture (t ≅ 10,000 s) results again in a decrease in the intensity from the steps in favour of the facets. Finally, the intensity from the steps reappears when the gas mixture is returned to the stoichiometric value.

POSITIVE THERMAL EXPANSION OF GRAPHENE ON ITS SUBSTRATE

Principal publication and authors
F. Jean (a,b), T. Zou (c), N. Blanc (a,b), R. Felici (d), J. Coraux (a,b) and G. Renaud (c), *Phys. Rev. B* **88**, 165406 (2013).
(a) Université Grenoble Alpes, Inst. NEEL, Grenoble (France)
(b) CNRS, Inst NEEL, Grenoble (France)
(c) CEA-UJF, INAC, SP2M, Grenoble (France)
(d) ESRF

Graphene (a single sheet of graphite) is expected to exhibit unusual mechanical properties related to its atomic thickness. In a free-standing form, graphene is predicted to have a negative thermal expansion below a few 100 K, *i.e.* its lattice parameter should decrease as temperature increases (see ref. [1] and references therein). This behaviour is associated with the activation of out-of-plane vibrations when graphene is in a free-standing form. Whether such vibrations are still active when graphene rests on a substrate is unknown. To shed some light on this matter, we have studied graphene grown *in situ* on iridium. Graphene is known to have a weak interaction with this substrate.

We performed a series of *in situ* temperature-dependent high resolution surface X-ray diffraction experiments, from 10 to 1300 K, at beamlines **BM32** and **ID03**, with high quality graphene. The graphene was prepared *in situ* on a (111)-terminated iridium crystal by chemical vapour deposition under ultra-high vacuum [2] to minimise the contribution from contaminants.

We found that graphene on its substrate exhibits no negative thermal expansion coefficient in the broad temperature range that we explored (**Figure 127**). The weak graphene-metal interaction indeed forces graphene's lattice parameter to follow the temperature dependence of the metal lattice parameter.

The lattice properties of the two materials are distinctive, and this shows up as graphene becomes unlocked from the metal lattice at a certain threshold, corresponding to a situation when the in-plane compressive (upon cooling down) elastic energy overcomes the sum of the binding and bending energies of graphene on iridium. Graphene forms linear delaminations: wrinkles several micrometres-long and a few nanometres-high that can be observed with a microscope.

The transition between the two regimes – graphene locked and unlocked on its substrate – gives rise to a hysteretic change of graphene's lattice parameter. Remarkably, after becoming unlocked from the substrate, graphene locks onto it again, adopting another, well-defined epitaxial relationship. At high temperature, this relationship approaches a coincidence of 21 carbon atoms with 19 iridium atoms, which is of high order, while at low temperature, the relationship is of lower order, with 10 carbon atoms matching 9 iridium atoms (**Figure 128**).

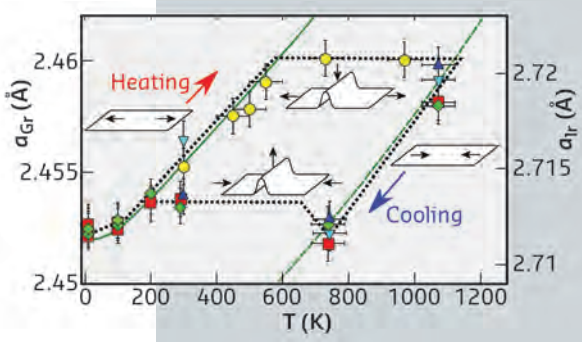

Fig. 127: Graphene lattice parameter (a_{Gr}, left axis) as a function of temperature. The different symbols refer to different samples prepared under the same conditions. The lattice parameter of the substrate (a_{Ir}, right axis, same steps as left axis) as a function of temperature is also displayed as a solid green line. The dotted green is the same curve shifted to pass through the graphene data points. The cartoons show the appearance/disappearance of wrinkles in graphene, which merely compresses and expands in their absence.

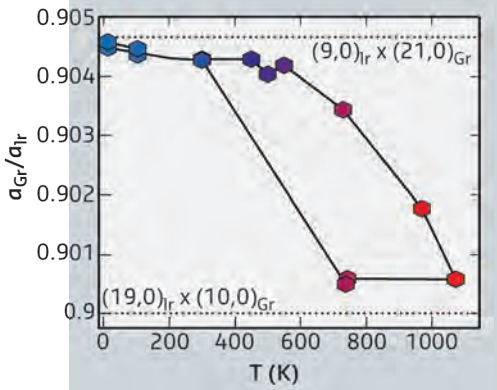

Fig. 128: Ratio of the graphene to iridium lattice parameters as a function of temperature. Dotted lines highlight low- and high-order lattice coincidences (commensurabilities).

References
[1] Y. Magnin, G. D. Förster, F. Rabilloud, F. Calvo, A. Zappelli and C. Bichara. *J. Phys.: Condens. Matter* **26**, 185401 (2014).
[2] J. Coraux, A.T. N'Diaye, C. Busse and T. Michely. *Nano Lett.* **8**, 565 (2008).

Principal publication and authors
T. Rosenthal (a), P. Urban (b), K. Nimmrich (a), L. Schenk (a), J. de Boor (c), C. Stiewe (c) and O. Oeckler (b), *Chem. Mater.* **26**, 2567-2578 (2014).
(a) Department of Chemistry, LMU Munich (Germany)
(b) Faculty of Chemistry and Mineralogy, Leipzig University (Germany)
(c) German Aerospace Center, Cologne (Germany)

MULTINARY THERMOELECTRICS – A CHALLENGE FOR CRYSTAL STRUCTURE DETERMINATION

The conversion of thermal into electrical energy is an important goal for better energy efficiency by means of waste-heat recovery. Modern thermoelectric materials render this conversion possible and gained worldwide interest because of their high 'thermoelectric figures of merit' *ZT*, which depend on the thermal (κ) and electrical (σ) conductivity, the Seebeck coefficient (*S*) and the temperature (*T*): $ZT = (S^2\sigma/\kappa)T$. State-of-the-art bulk materials often contain a mixture of elements with very low scattering contrast like Pb and Bi or Ag, Sn, Sb and Te [1], which often share atomic sites in the corresponding crystal structures. These elements can reliably be distinguished by the effect of anomalous dispersion at absorption edges, where the dispersion correction term $\Delta f'$ is large and strongly modifies the atomic form factor $f(\lambda,\theta) = f^0(\sin\theta/\lambda) + \Delta f'(\lambda) + i\Delta f''(\lambda)$. These correction terms can be determined directly at the beamline: $\Delta f''(\lambda)$ is calculated from X-ray fluorescence and $\Delta f'(\lambda)$ can be derived from it. The scattering contrast between neighbouring elements in the periodic table can be enhanced by up to 8 electrons [2].

Beamline **ID11** is ideally suited to high-resolution single crystal diffraction because of its stable beam and small band pass. A fluorescence detector for the determination of dispersion correction terms as well as a furnace for high-temperature measurements are integral parts of the setup used to refine the element distribution and structural changes in $Ge_2Sb_2Te_5$ as a function of temperature [3]. This material is well known as a fast phase-change material for data storage. Its stable phase consists of tetradymite-like distorted rocksalt-type slabs which are terminated by Te-atom layers and separated by van der Waals gaps (**Figure 129**). The element distribution changes very little upon heating, but instead the GeTe-like layers detach reversibly from the slab. In addition, this class of materials turned out to exhibit very promising thermoelectric properties which led to many substitution experiments to further enhance the efficiency of energy conversion.

$Ge_{\sim 5}Sb_2(Te_{0.13}Se_{0.87})_{\sim 8}$, for example, crystallises in a highly disordered rocksalt-type structure. TEM investigations revealed that the vacancies tend to order in parallel non-equidistant defect planes (111). This involves fourfold twinning and stacking disorder, which is also corroborated by diffuse streaks in the diffraction patterns obtained at beamline **ID11** (**Figure 130**). Semi-quantitative information on the real structure can be drawn by comparing the diffraction patterns of crystals with different compositions $(GeTe)_nSb_2(Se_xTe_{1-x})_3$

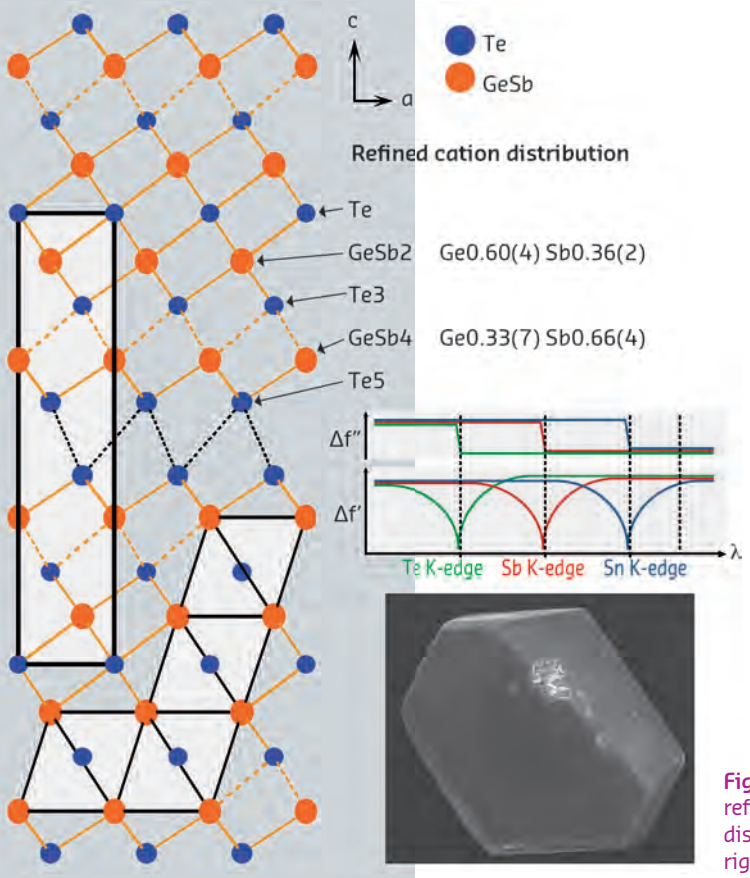

Fig. 129: Room-temperature structure of $Ge_2Sb_2Te_5$ (left) with refined element distribution (top right); the principal trend of the dispersion correction terms is sketched (middle right); bottom right: SEM image of the crystal investigated.

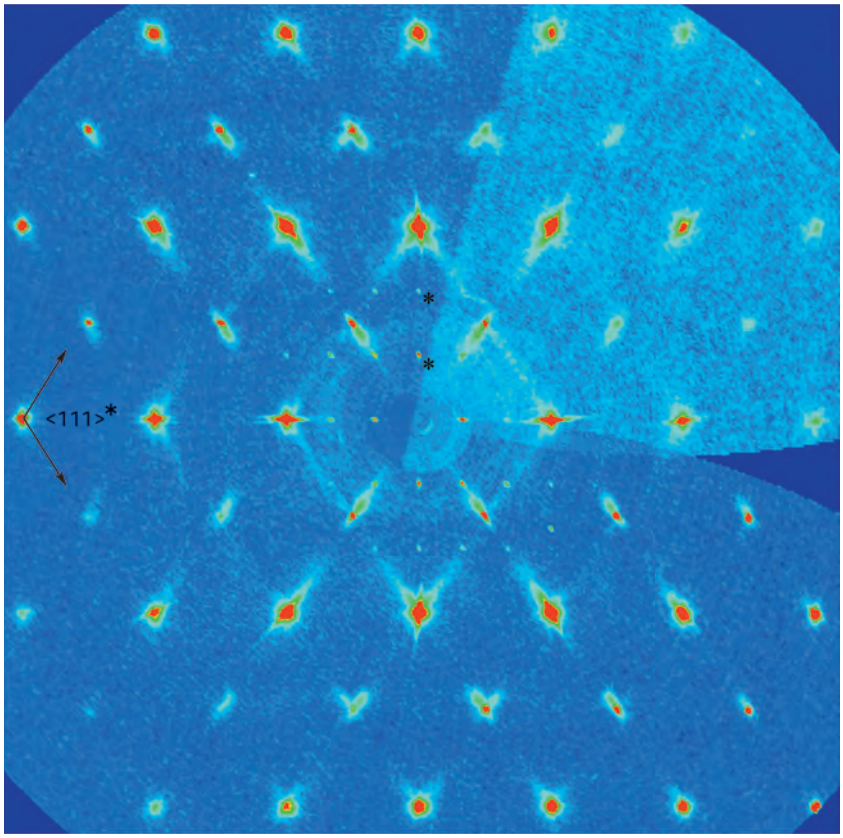

Fig. 130: Reciprocal lattice section (*hhl*) from a crystal of $Ge_{\sim 5}Sb_2(Te_{0.13}Se_{0.87})_{\sim 8}$; note the diffuse scattering running along <111>* (λ/3 reflections are marked with asterisks).

and simulated patterns. The most promising thermoelectric properties (*ZT* = 1.2 at 425°C) were found for n = 7 and x = 0.2. Furthermore, the refinement of the atom distribution in long-range ordered layered compounds like $Ge_{0.6}Sn_{0.4}Sb_2Te_4$ **[4]** yields clear statements concerning the most probable local structures in disordered compounds. Occupancy factors on sites shared by Sn, Sb and Te, impossible to distinguish using laboratory X-ray sources, could be determined in a joint refinement on five datasets (three at the K-edges of Sn, Sb and Te, one further off-edge synchrotron and one laboratory dataset).

In conclusion, the use of anomalous dispersion is a unique way to reliably determine structures of promising thermoelectric materials that contain several elements with a low scattering contrast. *In situ* investigations and the refinement of site occupancies of mixed sites are easily possible.

References
[1] L.-D. Zhao, V.P. Dravid and M.G. Kanatzidis, *Energy Environ. Sci.* **7**, 251-268 (2014).
[2] S. Welzmiller, P. Urban, F. Fahrnbauer, L. Erra and O. Oeckler, *J. Appl. Crystallogr.* **46**, 769-778 (2013).
[3] P. Urban, M.N. Schneider, L. Erra, S. Welzmiller, F. Fahrnbauer and O. Oeckler, *CrystEngComm* **15**, 4823-4829 (2013).
[4] S. Welzmiller, T. Rosenthal, P. Ganter, L. Neudert, F. Fahrnbauer, P. Urban, C. Stiewe, J. de Boor and O. Oeckler, *Dalton Trans.* **43**, 10529-10540 (2014).

DISCOVERY OF AN UNEXPECTED LI-ION BATTERY CHARGING MECHANISM

The revolution of personal electronics and rise of electronic mobility is made possible by the increasing energy densities of Li-ion batteries. Lithium, which is the third lightest element, is a relatively small ion with a very strong tendency to give away its outer electron. As a consequence, large numbers of lithium ions can be stored at high potential in electrode materials such as $LiFePO_4$, making lithium-ion batteries at least three times more powerful than the traditional nickel-cadmium and nickel metal hydride varieties. One of the main restrictions of today's Li-ion batteries is the poor kinetics of the phase transitions taking place in the electrodes upon Li-ion

Principal publication and authors
X. Zhang (a), M. van Hulzen (a), D.P. Singh (a), A. Brownrigg (b), J.P. Wright (b), N.H. van Dijk (a) and M. Wagemaker (a), *Nano Letters* **14**, 2279-2285 (2014).
(a) Department of Radiation Science and Technology, Delft University of Technology (The Netherlands)
(b) ESRF

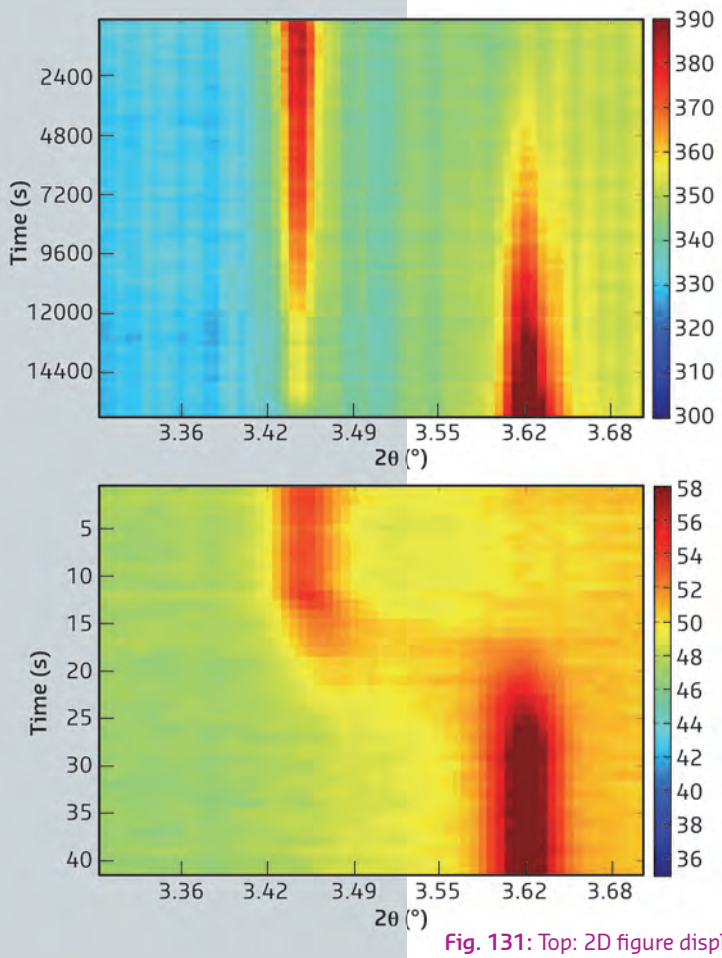

Fig. 131: Top: 2D figure displaying the time evolution of the {200} reflection during slow charging (5 hours). Bottom: 2D figure displaying the time evolution of the {200} reflection during fast charging (1 minute).

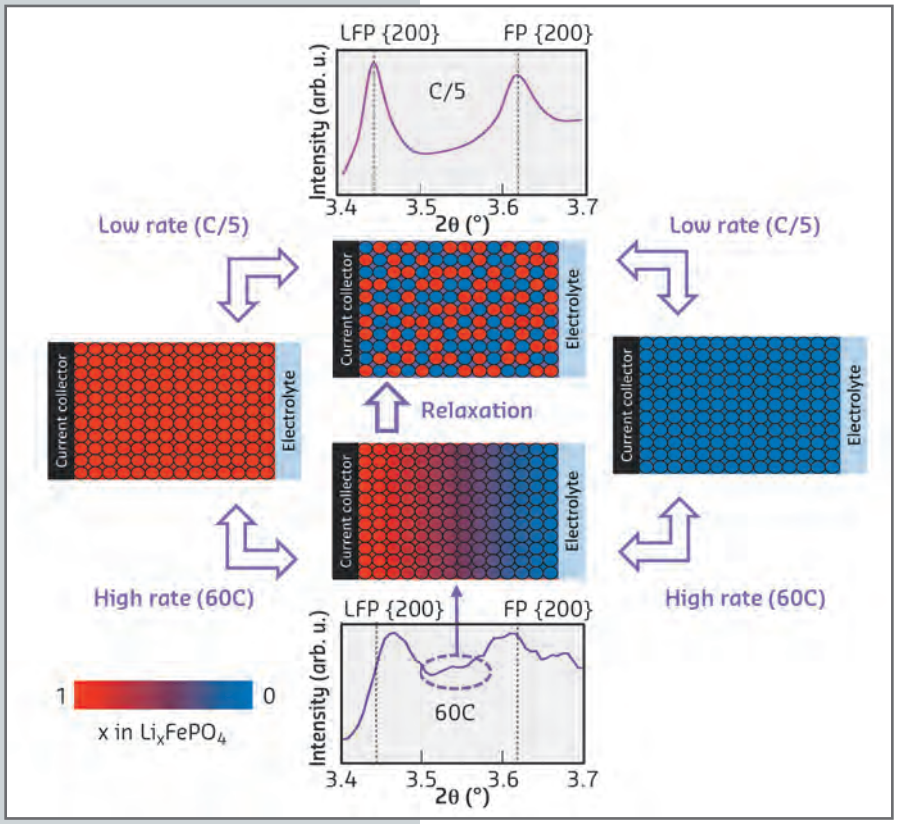

Fig. 132: Model for the phase distribution in $LiFePO_4$ electrodes at high and low rates and upon relaxation. At a low rate of 5 hours (C/5) the electrode is near equilibrium and no significant Li concentrations/overpotentials exist throughout the electrode. At high charge rate (60C corresponding to 1 minute charging) the potential gradient locally causes the bypassing of the first-order phase transition and the appearance of the solid-solution compositions that are observed.

insertion and extraction. The impact of defects, particle size and charging rates on the phase transitions in Li-ion battery electrode materials have already been studied intensively, but *in situ* X-ray diffraction experiments at beamline ID11 have now allowed us to study the chemistry of $LiFePO_4$ batteries during very fast cycling rates for the first time. This effectively made it possible to watch lithium atoms enter and exit the electrodes in real time. We have observed that at high charge and discharge rates, the electrode phase transitions can be bypassed – thereby enhancing the transport of lithium ions through otherwise poorly Li-ion conducting electrode material.

Electrode materials for Li-ion batteries like $LiFePO_4$ store lithium via a reversible first-order phase transition between $LiFePO_4$ and $FePO_4$, which is associated with a reduction in the *a*-axis lattice parameter. Diffraction during slow charging (5 hours) of the battery demonstrates this phase transition by the gradual disappearance of the {200} reflection of $LiFePO_4$ and the appearance of the {200} reflection of $FePO_4$, shown in the top part of **Figure 131**. In contrast, during fast charging (1 minute) the {200} reflection gradually shifts from the Li-rich phase position ($LiFePO_4$) towards the Li-poor position ($FePO_4$) showing a considerable intensity between the two end positions, indicating a different phase transition mechanism. The intensity distribution between the $FePO_4$ and $LiFePO_4$ {200} reflections implies that the phase transition progresses via a distribution of lattice parameters, gradually converting $LiFePO_4$ to $FePO_4$. This demonstrates that the dynamic fast charging conditions induce a solid solution transition rather than the thermodynamically predicted first-order phase transition with a

phase coexistence of two well defined individual phases.

The *in situ* fast charging diffraction indicates that only a small fraction of the electrode is actively transforming, consistent with the existence of a Li-ion concentration/potential gradient. The consequence is that the electrode material localised at the gradient experiences an overpotential, absent near equilibrium conditions, that drives the solid-solution transformation. This condition moves like a wave through the electrode as illustrated in **Figure 132**, transforming the complete electrode. Interrupting the fast charging will allow the system to relax towards equilibrium where, in contrast, the phase transition appears to occur randomly throughout the electrode. From previous research [1], we know that the occurrence of a reacting phase front at high rates indicates that the Li-ion transport in the electrodes limits faster (dis)charging.

Interestingly, the observed bypassing of the first-order phase transition is accompanied by a decrease in internal resistance of the battery. This demonstrates that the solid-state charge transport can be enhanced by the external charge conditions. Against intuition, this may indicate that charging and discharging at higher rates may be beneficial for a battery's efficiency and cycle lifetime. In addition, we have learned that the key to even faster charging is the Li-ion transport in the electrolyte located in the pores of the electrode, which we can improve by smart design of the electrode morphology. Currently, we are analysing the phase transitions in individual electrode grains in different battery systems under varying charge/discharge conditions, aiming to better understand the nucleation mechanisms, and the development of improved high-performance energy storage in batteries.

References
[1] D.P. Singh *et al.*, *Advanced Energy Materials* **3**, 572-578 (2013).

MECHANOCHEMICAL SYNTHESIS OF PHARMACEUTICAL COCRYSTALS MONITORED BY REAL-TIME *in situ* POWDER X-RAY DIFFRACTION

Principal publication and authors
I. Halasz (a), A. Puškarić (a), S.A.J. Kimber (b), P.J. Beldon (c), A.M. Belenguer (c), F. Adams (d), V. Honkimäki (b), R.E. Dinnebier (d), B. Patel (c), W. Jones (c), V. Štrukil (e) and T. Friščić (e), *Angewandte Chemie, International Edition* **52**, 11538-11541 (2013)
(a) Ruđer Bošković Institute, Zagreb (Croatia)
(b) ESRF
(c) Department of Chemistry, University of Cambridge (UK)
(d) Max-Planck-Institute for Solid State Research, Stuttgart (Germany)
(e) Department of Chemistry and FRQNT Centre for Green Chemistry and Catalysis, McGill University (Canada)

Mechanochemical synthesis, *i.e.* chemical synthesis by milling or grinding, is a leading methodology for environmentally-friendly, 'green' synthesis. However, one of the most established and valuable applications of milling is screening for new solid forms of active pharmaceutical ingredients (APIs): cocrystals, polymorphs or salts [1]. Discovery of new cocrystals is one of the principal pursuits in modern drug development, as cocrystals represent an exciting opportunity to improve physicochemical properties of the API (solubility, bioavailability, tableting) and represent tremendous value in intellectual property development. The application of mechanochemistry in screening for cocrystals is based on the ability of neat and liquid-assisted grinding (LAG) to rapidly explore cocrystal formation without interference from problems of solubility, solvolysis or thermal instability, inherent to other cocrystal discovery strategies.

Despite its broad synthetic potential and the widespread presence of milling in industrial processing, mechanisms of mechanochemical reactions are almost unknown. This is most likely due to a general inability to directly observe the course of chemical reactions and phase transformations. Until recently, the only means to follow changes in composition of mechanochemical reactions has been by stepwise analysis, *i.e.* by periodically interrupting the milling process and analysing the reaction mixture. Such an approach is, however, very poorly informative or even misleading as the samples transform before analysis due to relaxation, recrystallisation, desolvation or simply moisture absorption.

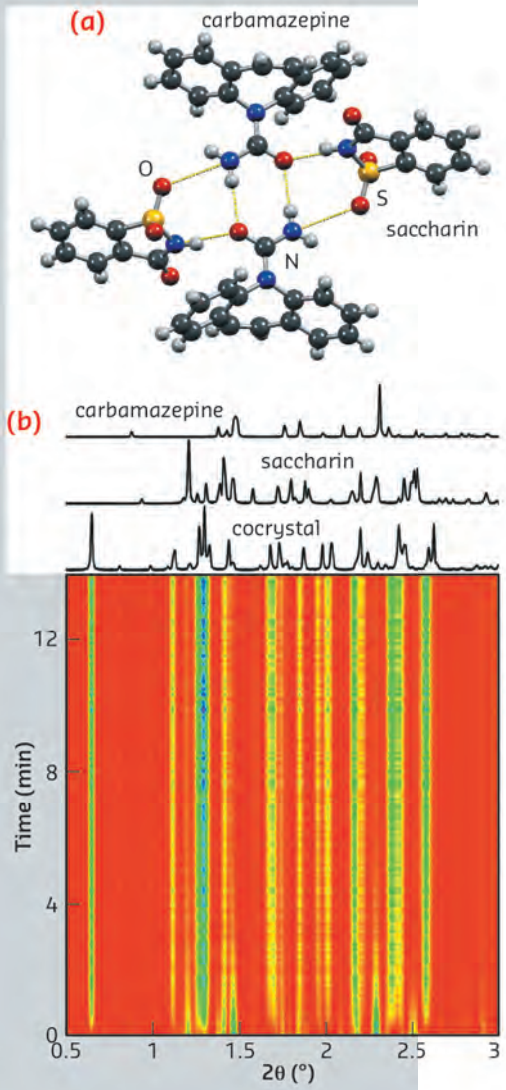

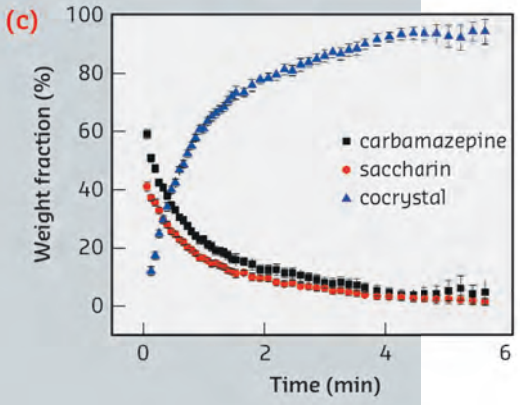

Fig. 133: a) Fragment of the crystal structure of the pharmaceutical cocrystal of carbamazepine and saccharin. b) Time-resolved X-ray diffractogram for the LAG cocrystallisation of saccharin and carbamazepine. c) reaction course obtained *via* Rietveld analysis.

In collaboration with ESRF scientists, we have recently developed the first technique for direct, real-time and *in situ* monitoring of structural and chemical transformations during milling using X-ray powder diffraction. This technique was first introduced for monitoring the transformations of strongly diffracting inorganic oxides into metal-organic materials [2].

In continuation, we extend the experimental design to monitor mechanochemical complexation of poorly scattering organic solids, as encountered in the formation of pharmaceutical cocrystals. The required signal-to-noise ratio was achieved by performing the experiment in a milling vessel made of non-crystalline, poorly scattering Perspex (poly(methyl)metacrylate). The first application of this new technique for monitoring pharmaceutical cocrystallisation was on an archetypal pharmaceutical cocrystal consisting of carbamazepine and saccharin (**Figure 133**). Reaction monitoring demonstrated their amorphisation upon neat milling, while milling in the presence of a catalytic liquid additive (liquid-assisted grinding, LAG) led to rapid cocrystal formation observable by changes in intensities of characteristic reflections for each phase. This revealed a clear difference between neat and liquid-assisted approaches for solid-state molecular complexation, and demonstrated the unexpectedly high rate of mechanochemical reactions, leading to complete conversions in 2 minutes (**Figure 133**).

We also explored the mechanochemical cocrystallisation of nicotinamide (vitamin B_3) with suberic acid, a model pharmaceutical system known to encompass materials with different stoichiometric composition. In this system, *in situ* cocrystallisation monitoring revealed complex, multi-step mechanisms involving short-lived and metastable materials not observable by other means. Milling cocrystallisation of nicotinamide and suberic acid in a 2:1 respective stoichiometric ratio yielded the expected cocrystal over 40 min, but only through the formation of an intermediate cocrystal containing the two components in a 1:1 ratio. Replacing the slower neat milling with much faster LAG revealed the formation of the final product cocrystal within about 5 minutes. Again, the reaction involved the 1:1 cocrystal as an intermediate which, this time, lasted only for 3 minutes (**Figure 134**).

Monitoring of the LAG reaction also revealed another short-lived intermediate appearing about 1 minute

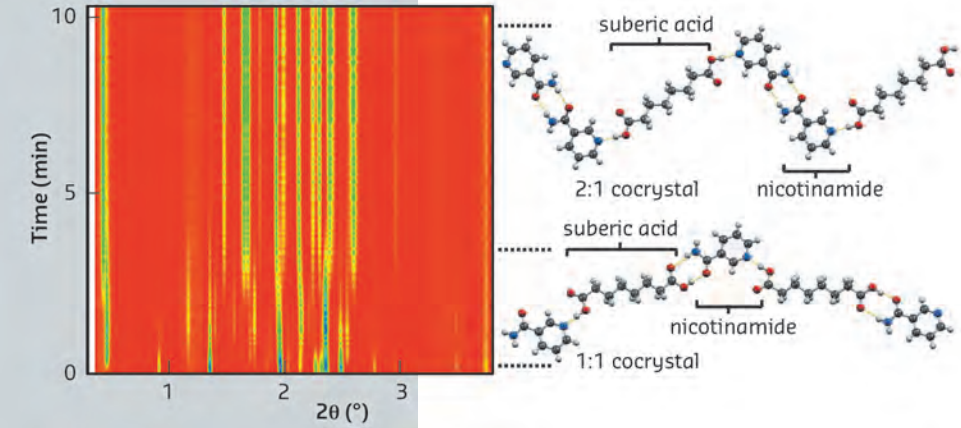

Fig. 134: Time-resolved diffractogram for LAG cocrystallisation of suberic acid with nicotinamide, indicating a multi-step mechanism involving the formation of different cocrystals.

into milling. This novel intermediate has never previously been observed in studies of this well-known model pharmaceutical system and, although it could not be characterised structurally, *in situ* monitoring now allowed it to be prepared under conventional laboratory conditions.

The presented methodology provided the first *in situ* and real-time insight into the course of mechanochemical formation of pharmaceutical cocrystals, immediately demonstrating the unexpected speed of the process, possibility of multi-step reaction mechanisms, as well as the formation of intermediate phases that have previously not been observed. The latter is a particularly exciting development, as it demonstrates the value of *in situ* monitoring not only as a tool for the academic investigation of reaction mechanisms, but also for the discovery of new, potentially commercially valuable, solid forms of APIs.

References
[1] A. Delori, T. Friščić and W. Jones *CrystEngComm* **14**, 2350-2362 (2012).
[2] T. Friščić, I. Halasz, P. J. Beldon, A. M. Belenguer, F. Adams, S. A. J. Kimber, V. Honkimäki and R. E. Dinnebier *Nature Chem.* **5**, 66-73 (2013).

TIME-RESOLVED X-RAY DIFFRACTION WITH ENHANCED SENSITIVITY

X-ray diffraction (XRD) is a powerful method to determine the structure and the structural changes of materials. An advantage of XRD is that it allows the observation of all XRD visible phases simultaneously within a complex multiphase material. When using synchrotron radiation, the information is obtained in a snapshot, *i.e.* with high time resolution. In the case of supported precious metal based catalysts, used for example to control the emissions of automotive engines, XRD provides information on the precious metal particles and the metal oxide support(s). Chemical reactions at the heart of the abatement of pollutants (NO_x, CO and hydrocarbons) occur mainly on the precious metal nano-particles. The function of the metal oxide is to provide stability against severe reaction conditions. For example, CeO_2 is responsible for maintaining metal nano-particles in an oxidised state, thus retarding their growth which otherwise leads to loss of the catalytic function. Strongly X-ray absorbing materials like CeO_2 are difficult to analyse by X-ray absorption spectroscopy (XAS) with high time resolution. On the one hand, the strong absorption of X-rays by the metal oxides hinders detection of the low loaded active metals (Pt, Pd, Rh) and fluorescence based detection is often required. As a result, high time resolution is still an issue. High energy XRD is suitable to circumvent the inherent problems of XAS but is still limited by its intrinsic detection limit. Metal nano-particles are visible by XRD only if dispersion is low and the metal content high. Typically, detection is limited to ca. 3 nm particle size for high loaded metals.

At beamline **ID15B,** we have used high energy XRD in combination with a modulation approach and lock-in amplification based on phase sensitive detection (PSD) [1] to follow redox processes on technologically relevant materials. A 2 wt% $Pd/Ce_{0.6}Zr_{0.4}O_2$ catalyst is subjected to repeated and equally long pulses of CO and O_2 at 573 K

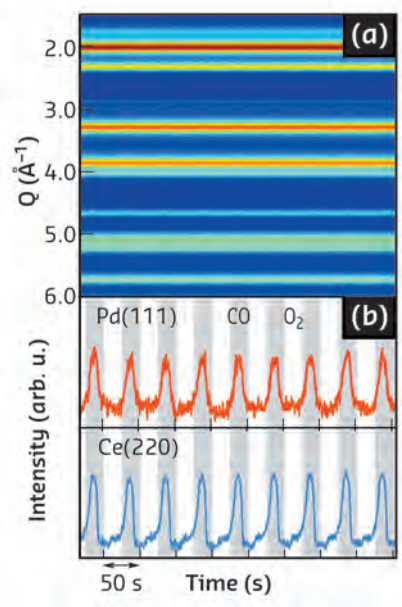

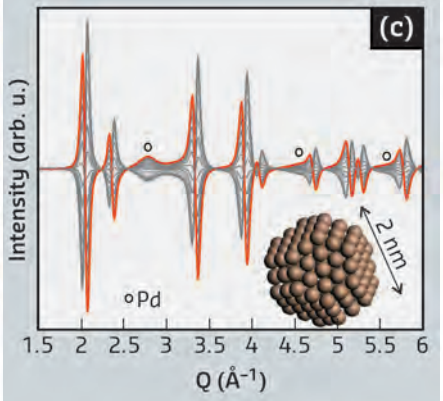

Fig. 135: Time-resolved XRD data. a) Colour map representation. b) Temporal responses of the XRD reflections. c) Phase-resolved data.

Principal publication and authors
D. Ferri (a), M.A. Newton (b), M. Di Michiel (b), G.L. Chiarello (c,d), S. Yoon (c) Y. Lu (c) and J. Andrieux (b,e), *Angew. Chemie Int. Ed.* **53**, 8890–8894 (2014).
(a) Paul Scherrer Institut (Switzerland)
(b) ESRF
(c) Empa, Swiss Federal Laboratories for Materials Science and Technology (Switzerland)
(d) Present address: Università degli Studi di Milano (Italy)
(e) Present address: Université de Lyon (France)

while XRD acquisition is performed at 500 ms/pattern. A combined XRD/DRIFTS/MS setup was used for this purpose [2]. After averaging, the set of time-resolved XRD patterns was analysed by PSD, which provided a new dataset containing information only on the species that changed dynamically during the modulation experiment.

Figure 135 shows that the time-resolved XRD data contain little or no information on any structural change induced by the modulation experiment. Features that could be associated with Pd or PdO nano-phases are absent as expected from the low metal loading and the absence of long range order that are at the base of the peculiar catalytic activity of such nano-entities. In marked contrast, the corresponding phase-resolved data obtained by PSD show two sub-sets of reflections signifying that structural changes occurred during the experiment. The first one is characterised by a differential profile (both by intensity and 2θ variation) and is associated with expansion and contraction of the Ce component upon reduction of Ce^{4+} (in CO) and oxidation of Ce^{3+} (in O_2). The very small (0.11%) and reversible change of d spacing is associated with the capacity of CeO_2 to exchange oxygen with the environment under reducing conditions. The second sub-set entails only an intensity change with equally reversible behaviour. The position of this sub-set of reflections coincides with the XRD pattern of fcc Pd. Estimation of the crystallite size by the Scherrer formula provides Pd particles of <2 nm that become visible only after application of PSD. This size estimate is supported by simulation of particles in the range 1-5 nm. The temporal behaviour of the two datasets demonstrates that evolution of the structural change within $Ce_{0.6}Zr_{0.4}O_2$ and reduction-oxidation of the Pd component occur quasi simultaneously. Also, the function of Ce^{3+}/Ce^{4+} becomes clear in the appearance of the Pd(111) reflection in the PSD data. This shows that reduction of Pd is retarded until the very end of the reducing pulse as a result of the intimate contact of the $Ce_{0.6}Zr_{0.4}O_2$ and Pd phases.

Therefore, we have demonstrated that a greater detail of the redox kinetics of a complex material can be obtained by the combination of high energy XRD, the modulation approach and PSD. Subtle changes associated with metal nano-particles can be made visible using a bulk analysis method. Such enhanced insights should be achievable in all systems that involve functional materials where reversible cycling is possible for one or more of the intrinsic process variables.

References

[1] D. Baurecht, U.P. Fringeli, *Rev. Sci. Instr.* **72**, 3782 (2001); D. Ferri, M.A Newton, M. Di Michiel, S. Yoon, G.L. Chiarello, V. Marchionni, S.K. Matam, M.H. Aguirre, A. Weidenkaff, F. Wen and J. Gieshoff, *PCCP* **15**, 8629 (2013).

[2] M.A. Newton, M. Di Michiel, A. Kubacka and M. Fernàndez-Garcià, *J. Am. Chem. Soc.* **132**, 4540 (2010).

REVEALING RAPID DYNAMICS IN WELD SOLIDIFICATION

Principal publication and authors

W.U. Mirihanage (a), M. Di Michiel (b), A. Reiten (a), L. Arnberg (c), H.B. Dong (d) and R.H. Mathiesen (a), *Acta Materialia* **68**, 159–168 (2014).

(a) Department of Physics, Norwegian University of Science and Technology, Trondheim (Norway)

(b) ESRF

(c) Department of Materials Science and Engineering, Norwegian University of Science and Technology, Trondheim (Norway)

(d) Department of Engineering, University of Leicester (UK)

Welding is considered the most important and economical material processing route for joining metals. Welds are employed extensively to fabricate components and structures ranging from tiny electronic chips to massive ships and even for components operated under critical and demanding conditions such as in nuclear reactors. In fusion welding, metals coalesce via extremely rapid solidification processes which are critical to the structural integrity of the weld and often the origin of catastrophic weld failures. Enhanced insight on weld solidification is vital to prevent losses of lives and property [1], yet the inherent complexity, high temperatures and the rapidness of the welding processes make direct experimental investigations extremely demanding [2].

Polychromatic X-ray diffraction has been used in time resolved studies of rapid solidification microstructure

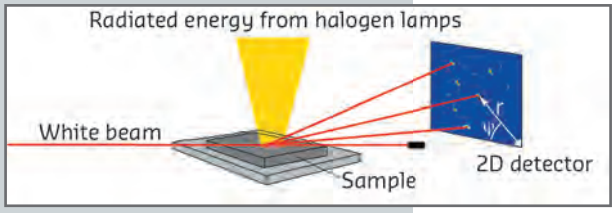

Fig. 136: Schematic experimental setup.

evolution *in situ* during spot welding at beamline **ID15A**. Austenitic steel samples 2 mm thick were placed with the surface normal tilted 0.035 rad from the vertical axis towards an incident 50-150 keV white beam, and defined by upstream apertures to a cross section of 1 x 0.1 mm^2 (H x V) at the sample. Weld pools of ~5.0 mm diameter and <1.5 mm depth were formed in a few seconds by focused radiation from halogen lamps. Solidification was initiated by powering off the lamps, and completed within 1.5 s. 2D data was collected in reflection geometry at 1.0 kHz frame rate with a PCO. dimax® CMOS equipped with an image intensifier, see **Figure 136**.

In the chosen experimental geometry, scattered intensities stemmed from the topmost ~140 µm of the weld pool, with the most prominent growth mode detected corresponding to columnar dendritic grains growing in the surface-near layer from the pool periphery towards the weld centre. In addition to crystal growth, a remarkable angular motion of diffraction spots were observed at the early growth stages, typically 3 - 4 orders of magnitude larger than that associated with thermal contraction of the solid at cooling rates of 3-400 K/s. Grain rotation is presumably driven by substantial melt convection in the pool. It is well known that very strong convection currents may arise during welding due to the extreme thermo-solutal conditions that apply, and a crude calculation indicate that flow velocities up to ~ 0.4 m/s can be expected in the fully molten pool for the case reported here.

The data have been processed in terms of integrated diffraction spot intensities and angular positions to allow for information to be extracted on the growth of individual columnar crystals, overall solid fraction evolution and accompanying grain rotation dynamics (**Figure 137 *a*, *b***). Correlation between the temporal evolutions in integrated intensities, grain motions and 2D diffraction spot areas pointed towards columnar crystal tilting at their attaching roots as the predominant mode of grain motion, and, by further data analysis, the tilting motion could be expressed in terms of metric velocities at the crystal tips. As illustrated in **Figure 137c**, when growth and tilting rates at the columnar tips are compared, crystal growth velocities and tilting velocities are found to be of the same order of magnitude, especially in the earlier stages of solidification. Thus, solute pile-up ahead of the columnar front should be effectively removed not only by strong convection, but also by tilting, such that growth at this stage should be substantially different from situations where only melt convection and diffusion are present.

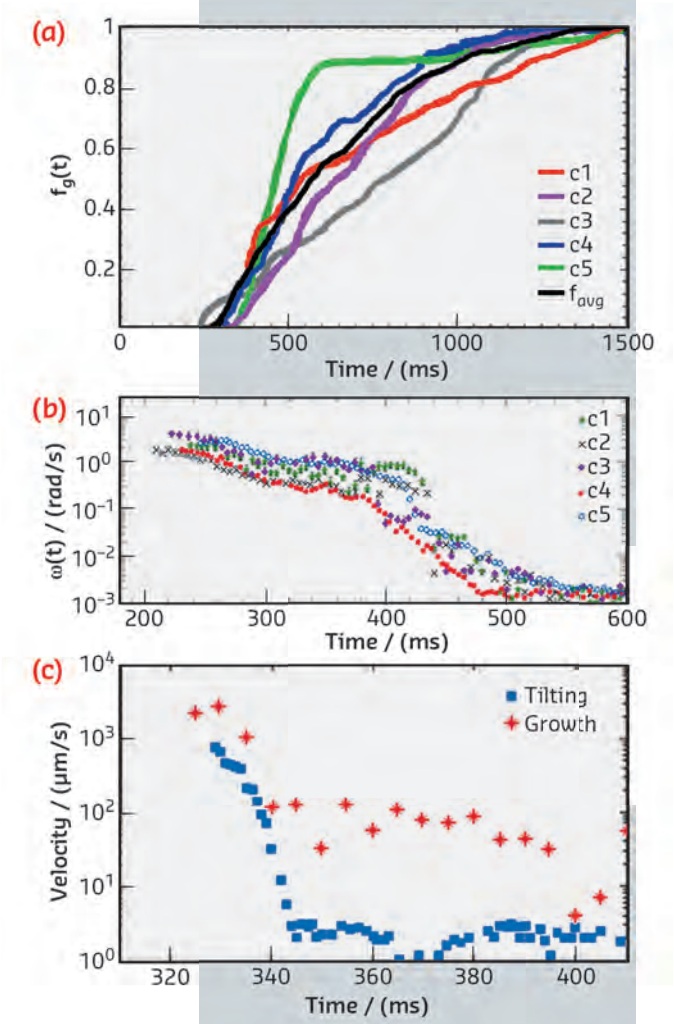

Fig. 137: *a*) Columnar (c) crystal volume evolution, c1-c5 denotes 5 different crystals, and f_{avg} presents the overall solid volume fraction. b) time-evolution of angular velocities for crystals c1-c5. c) evolution of growth and tilting velocities for one representative columnar crystal.

Experimental data both in terms of individual grain growth and motion are novel in the case of welding or similar rapid solidification processing, and will be very useful for benchmarking of more realistic simulation models. Grain tilting has not been incorporated into present simulation models, although its presence may be quite readily recognised. Thus, the experimental results serve to stress that both melt flow and liquid to solid momentum transfer have to be addressed and accounted for in future theoretical work and simulation models for welding. Furthermore, quite similar experimental setups could be employed in the future for fast *in situ* XRD studies of real welding processes or other fast phase transformations under extreme conditions.

References
[1] S.A. David and T. DebRoy, *Science* **257**, 497 (1992).
[2] M. Yonamura *et al.*, *J. App. Physics* **107**, 013523 (2010).

Principal publication and authors
A. Zorko (a, b) O. Adamopoulos (c), M. Komelj (a), D. Arčon (a, d) and A. Lappas (c), *Nat. Commun.* **5**, 3222 (2014).
(a) Jožef Stefan Institute, Ljubljana (Slovenia)
(b) EN—FIST Centre of Excellence, Ljubljana (Slovenia)
(c) Institute of Electronic Structure and Laser, Foundation for Research and Technology—Hellas, Heraklion (Greece)
(d) Faculty of Mathematics and Physics, University of Ljubljana (Slovenia)

ON THE INHOMOGENEOUS GROUND STATE OF A TRIANGULAR ANTIFERROMAGNET

In condensed matter, phase separation breaking the translational symmetry of a Hamiltonian on a local scale is particularly intriguing, as it regularly appears in chemically homogeneous systems [1]. This is related to some fundamental functional properties of materials, such as colossal magnetoresistance of manganites, giant electrostriction of relaxors, and possibly even high-T_c superconductivity [1]. According to a conventional paradigm, electronic charge plays the leading role in promoting phase-separated states when competing phases are present. Also, quenched disorder – random deviations from perfect system's uniformity – is generally required for the stabilisation of such states. However, in spin systems that are geometrically frustrated, a novel mechanism leading to spatial instabilities could be at play even in the absence of charge degrees of freedom and in the clean limit. In such spin lattices, geometrical constraints prefer exotic degenerate ground states over conventionally ordered magnetic states. We have identified a novel kind of phase-separated state in the triangular antiferromagnet α-$NaMnO_2$, where the interplay of geometrical frustration and a structural instability of the lattice leads to a magnetostructural inhomogeneity at the nanoscale.

The investigated compound α-$NaMnO_2$ is well known for its intriguing magnetic and structural properties [2]. It orders magnetically at T_N = 45 K, but diffuse neutron magnetic scattering, characteristic of short-range spin correlations, remains present down to the lowest temperatures. The coexistence of such scattering with sharp magnetic Bragg peaks is a clear indication of a magnetically inhomogeneous ground state intrinsic to α-$NaMnO_2$. Moreover, large and highly anisotropic microstrains in the crystal structure above T_N suggest structural inhomogeneities. Based on the analysis of the neutron powder diffraction patterns, the microstrains were reported to grow with decreasing temperature that should eventually result in a monoclinic-to-triclinic structural phase transition, occurring simultaneously with the magnetic ordering [2].

We have studied the alleged structural changes in α-$NaMnO_2$ at beamline **ID31** (now ID22). The enhanced resolution of the synchrotron X-ray diffraction compared to previous neutron studies has revealed that a bulk structural transition is impeded, in sharp contrast to the isostructural $CuMnO_2$ compound, where such magnetic-order-induced improper ferroelastic transition indeed occurs at T_N = 65 K (**Figure 138**). A characteristic symmetry-lowering peak splitting is missing in α-$NaMnO_2$, although the reflections exhibit sizeable anisotropic broadening with decreasing temperature (**Figure 138**). Moreover, a peculiar asymmetric line shape developed below T_N that cannot be adequately modelled by the high-temperature monoclinic crystal structure (**Figure 138**). Regularly

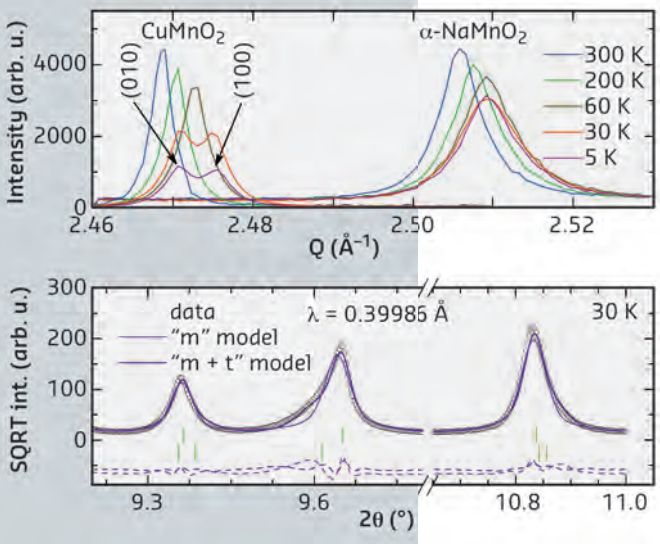

Fig. 138: Upper panel: Bragg-peak splitting witnesses the presence ($CuMnO_2$) and absence (α-$NaMnO_2$) of a structural phase transition. Lower panel: Rietveld fit of the synchrotron X-ray powder diffraction (XRD) profile of α-$NaMnO_2$ in the inhomogeneous phase, with the monoclinic ("m") only and a combined monoclinic and triclinic ("m + t") models.

observed structural defects, such as twin boundaries and stacking faults, fail to account for the measured peak-shapes. Therefore, a more complex parameterisation of the structural model was required. A two-phase model incorporating the monoclinic and triclinic phase offers a significantly improved Rietveld refinement (**Figure 138**). This implies the presence of randomly distributed nanoscale inhomogeneities, pertaining to the minority triclinic phase that grows at the expense of the majority monoclinic phase.

Such a nanoscale structural inhomogeneity is further supported by an electronic inhomogeneity. The latter has been witnessed in α-$NaMnO_2$ by our local-probe magnetic investigations, incorporating both nuclear magnetic resonance (NMR) and muon spin relaxation (mSR) techniques. These have unambiguously demonstrated a nanoscopic coexistence of two different magnetic environments that can be explained by a model of triclinic magnetic defects in the form of dispersed nano-sized islands, with the magnetic order reversed at the interfaces with the monoclinic matrix (**Figure 139**).

We suggest that the newly discovered magnetostructural phase separation in α-$NaMnO_2$ is a consequence of the system's tendency to remove magnetic degeneracy associated with the geometrically frustrated triangular spin lattice (**Figure 139**). The associated magnetic-exchange energy gain due to the monoclinic-to-triclinic distortion is compensated by the increase of the elastic energy. The resulting near-degenerate monoclinic and triclinic structures, as suggested by *ab initio* calculations, can then lead to nanoscale phase separation even in the limit of zero quenched disorder.

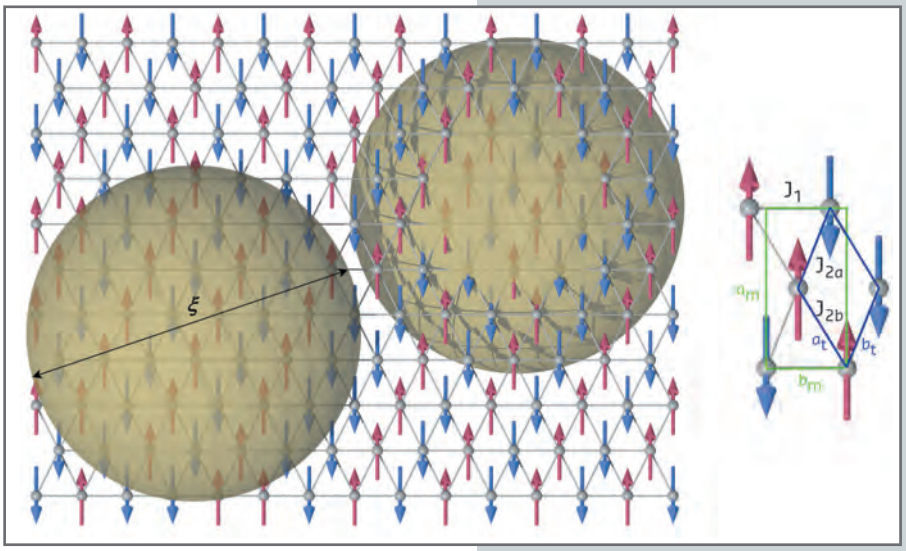

Fig. 139: Left: Illustration of the magnetostructurally inhomogeneous ground state of α-$NaMnO_2$. Right: Local structural deformation from the monoclinic (m) to triclinic (t) symmetry pertinent to the defect (sphere) regions.

References
[1] E. Dagotto, *Science* **309**, 257–262 (2005).
[2] M. Giot *et al.*, *Phys. Rev. Lett.* **99**, 247211 (2007).

In situ MONITORING OF "JUMPING CRYSTALS" BY X-RAY POWDER DIFFRACTION

Certain crystals, when taken over a phase transition, are capable of self-actuation, jumping, exploding, bending or changing their physical appearance, thus presenting a novel platform for clean and effective conversion of thermal energy to mechanical work **[1–3]**. These thermosalient crystals, in the near future, might also find other applications, such as smart medical devices and implants, artificial muscles, actuators, sensors, electromechanical devices, to name but a few.

This extremely rare phenomenon of "jumping crystals" was noticed in the 1980s and remained poorly understood ever since. Etter and Siedle reported that when crystals of (phenylazophenyl) palladium hexafluoroacetylacetonate (PHA) are heated, they "literally fly off the hot stage" **[4]**. This impressive dynamic effect is captured in **Figure 140**. Although this system could help to understand how ordered matter responds to extreme internal pressures and performs locomotion, the

Principal publication and authors
M.K. Panda (a), T. Runčevski (b), S.C. Sahoo (a), A.A. Belik (c), N.K. Nath (d), R.E. Dinnebier (b) and P. Naumov (a), *Nature Communications* **5**, 4811 (2014).
(a) New York University Abu Dhabi, Abu Dhabi (United Arab Emirates)
(b) Max Planck Institute for Solid State Research, Stuttgart (Germany)
(c) National Institute for Materials Science, Tsukuba (Japan)

References

[1] Ž. Skoko, S. Zamir, P. Naumov and J. Bernstein, *J. Am. Chem. Soc.* **132**, 14191 (2010).

[2] S.C. Sahoo, S.B. Sinha, M.S.R.N. Kiran, U. Ramamurty, A. Dericioglu, M.C. Reddy and P. Naumov, *J. Am. Chem. Soc.* **135**, 13843 (2013).

[3] S.C. Sahoo, M. Panda, N.K. Nath and P. Naumov, *J. Am. Chem. Soc.* **135**, 12241 (2013).

[4] M.C. Etter and A.R. Siedle, *J. Am. Chem. Soc.* **105**, 641 (1983).

relationships between the structural, mechanistic and kinematic aspects of this system have remained unknown.

When single crystals of PHA jump, they increase their mosaicity and disintegrate, thwarting the crystal structure solution by single crystal diffraction. The macroscopic disintegration of single crystals is all but an obstacle for powder diffraction (XRPD), and this method was used to investigate the system in greater detail. A laboratory XRPD study revealed as many as 5 polymorphs between 98 and 388 K (a record for the largest number of polymorphs of an organometallic compound). Our crystallographic, thermogravimetric, microscopic and spectroscopic analyses revealed that when heated, crystals of form alpha undergo two subsequent phase transformations: alpha–to–gamma, which is accompanied by jumping of the crystals, and gamma–to–beta, which is not thermosalient. Determination of the crystal structure of form gamma was crucial to understand the jumping effect in PHA. This phase was found to exist in a triple mixture with alpha and beta (**Figure 141**). Moreover, the relative amounts of the phases were found to change under isothermal conditions.

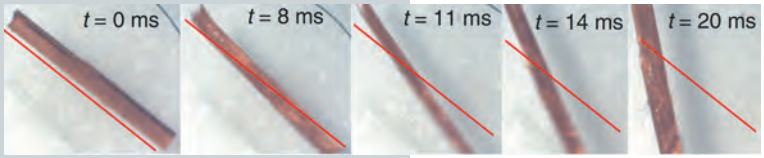

Fig. 140: Snapshots (taken at frequency 10^3 s^{-1}) of the kinematic effect of hopping of PHA crystals.

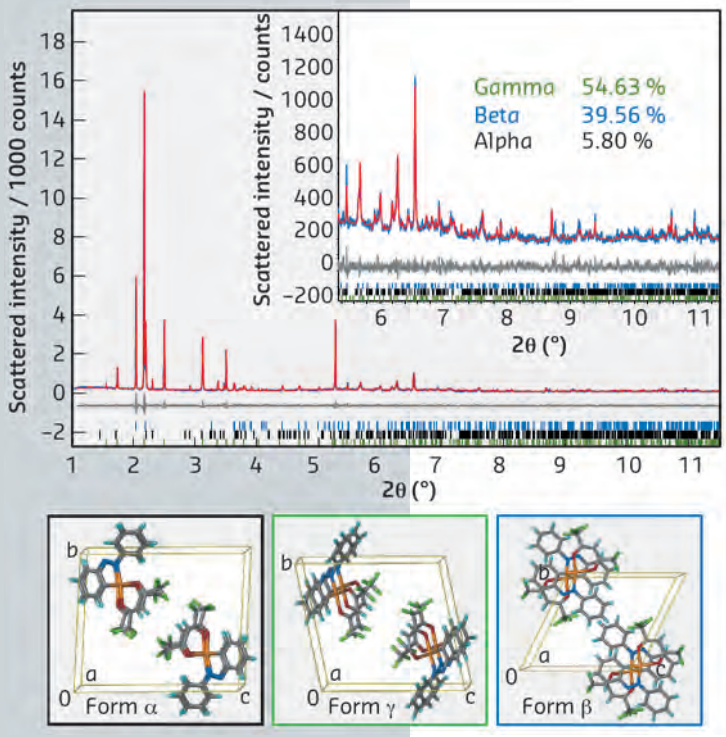

Fig. 141: Rietveld plot of a three-phase refinement of PHA polymorphs used to detail the crystal structure of the gamma form, which is relevant to the thermosalient behaviour. The crystal packing diagrams of forms alpha, gamma and beta are given in the lower panels.

When dealing with crystal structures of metastable species, it is necessary that the data are collected at the same (or preferably lower) timescale relative to the lifespan of the metastable structures. Laboratory XRPD data, of suitable quality for *ab initio* crystal structure solution, requires hours for collection, thus conventional X-ray sources could not be applied to study this system. The high-resolution diffraction data collected at beamline **ID31** (now ID22), with a time-resolution of 3 minutes per powder pattern, made this complicated system amenable to structural investigations (**Figure 141**).

The crystal structures of forms alpha and beta were already known **[4]**. The solution of the structure of form gamma provided us with a unique possibility to follow the structural changes on the alpha-gamma-beta phase transitions and to relate them to the thermosalient effect. During the phase transition accompanied by jumping, layers of molecules in form alpha slide atop each other, which results in slanting of the columns of stacked molecules that generates immense internal strain, which is released in form of forceful jumps of the crystals and phase transformation into form gamma. In the second phase transition, alternating layers of molecules in form gamma slide in opposite directions and interdigitate into the thermodynamically stable head-to-tail stacking pattern of form beta.

The detailed crystallographic study of this intriguing "jumping crystal" phenomenon was only possible by using high-intensity and high-resolution synchrotron radiation. The PHA research project once again demonstrated the necessity of acquiring high-resolution diffraction data in frontier studies of novel materials.

PUSHING CRYSTALLOGRAPHY ACROSS THE NUCLEATION BARRIER

Principal publication and authors
C. Tyrsted (a), N. Lock (a), K.M.Ø. Jensen (a,b), M. Christensen (a), E.D. Bøjesen (a), H. Emerich (c), G. Vaughan (d), S.J.L. Billinge (b) and B.B. Iversen (a), IUCr-J **1**, 165-171 (2014).
(a) Center for Materials Crystallography, Department of Chemistry, and iNANO, Aarhus University (Denmark)
(b) Department of Applied Physics and Applied Mathematics, Columbia University, New York (USA)
(c) SNBL, ESRF
(d) ESRF

The century-old technique of X-ray diffraction continues to become ever more important for materials characterisation, laying the foundation for many scientific and technological advances in academia and industry alike. The rapid progress in X-ray diffraction methods has made it possible for researchers to routinely identify known materials and solve the structures of previously unknown compounds. The key requirement being that the material exhibits a crystalline long range ordering of the atomic lattice, the prerequisite for Bragg diffraction. Digging into the world of nanoscience, the coherent atomic domains of materials become ever smaller, challenging the condition for Bragg diffraction. This has meant that crystallography was often disregarded in the structural characterisation of amorphous, liquid and extremely nanocrystalline systems. However, this perception is quickly changing, partly owing to the further development and growing use of total scattering experiments and pair distribution function (PDF) analysis [1].

In material science, it is a grand challenge to understand the atomic ordering of materials during synthesis. By knowing the mechanism of crystal formation it may be possible to control it, thereby tailoring desired materials. This is especially a keen interest in the field of solvothermal synthesis [2], where crystalline materials often form from dissolved chemical species or otherwise disordered gel systems. While the evolution of the growing crystalline particles themselves may be followed by diffraction, a barrier is met when trying to understand the local structures existing at the point of nucleation or the stage(s) preceding it.

In this study, total X-ray scattering in combination with X-ray absorption spectroscopy was used in an attempt to further the understanding of the formation of yttria-stabilised zirconia nanoparticles during solvothermal processing. Under these conditions (methanol-based solution at T = 275°C and P = 250 bar), dissolved Zr^{4+} and Y^{3+} species are transformed into crystalline $Zr_{1-x}Y_xO_{2-\delta}$ nanoparticles in a matter of minutes. Visually, the system may be observed to change from a translucent solution to an apparent gel-like structure upon nucleation, steadily densifying with prolonged hydrothermal processing. Therefore, three different structural stages likely exist during different points in this process: 1) pre-nucleation molecular species, 2) a disordered amorphous network and 3) an ordered crystal lattice. The experimental PDF's representing these different structural stages are shown in **Figure 142**. Only the third structural stage exhibits Bragg diffraction, the first two stages giving rise to diffuse scattering alone, excluding the use of standard Bragg crystallography. Nonetheless, total scattering clearly proves the existence of distinct local atomic structuring in all three stages spanning further than the first immediate coordination shell.

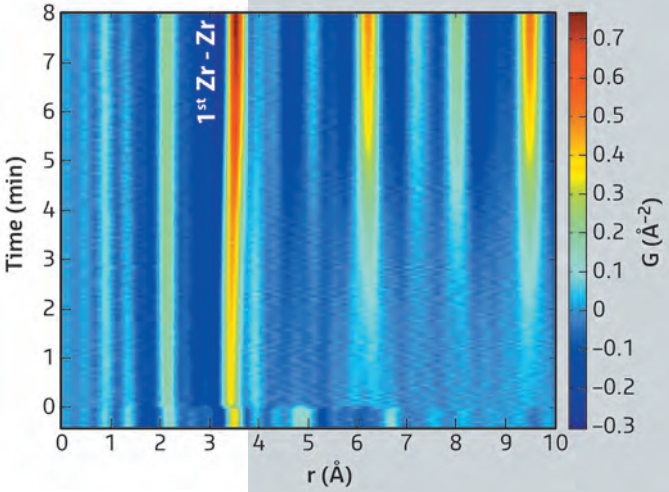

Fig. 142: Local atomic ordering as revealed by total scattering. (d) Time-resolved view of the local structural region (0–10 A°) of the PDF.

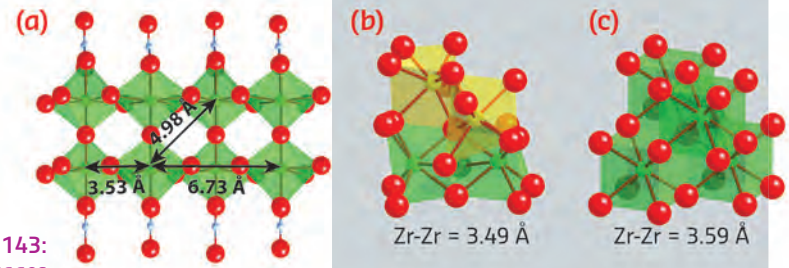

Fig. 143: Structural stages observed during yttria-stabilised zirconia formation. (a) Proposed solution species structure. (b) Amorphous network structure. (c) Mature cubic crystalline structure of YSZ.

The structures found to best describe these structural stages are shown in Figure 143. The local structure found in the pre-nucleation stage is proposed to consist of polymeric zirconia species, formed during dissolution or present in the solid precursor from the beginning. At the point of nucleation, the data indicate that the polymeric species are rapidly fragmented into smaller species which cluster together and precipitate out as an amorphous network. The atomic network of the precipitate is not entirely randomised despite the apparent chaotic nucleation process, but has a local ordering which may be described as monoclinic in nature. The local bonding environment of the precipitate is therefore not too far from the cubic lattice structure of the end product, yet lacks the correct long range topology. Over time, bond reforming ensures that the local domains order within themselves and in relation to each other thereby forming the desired cubic lattice structure.

Numerous simplified models exist to describe crystal nucleation and growth phenomena. The present study provides the first experimental atomistic insight into the very complex chemical processes that take place during crystallisation, and the total scattering technique provides a new approach to truly understanding nanomaterial formation.

References

[1] T. Egami and S.J.L. Billinge. *Underneath the Bragg peaks: structural analysis of complex materials*. Vol. 16. Newnes (2012).

[2] K.M. Jensen, C. Tyrsted, M. Bremholm and B.B. Iversen, *ChemSusChem* **7**, 1594-1611 (2014).

ILLUMINATING THE PHYSICAL PROCESS OF CATALYST DEACTIVATION

Principal publication and authors

A.M. Beale (a,b,c), E.K. Gibson (b,c), M.G. O'Brien (a), S.D.M. Jacques (c,d), R.J. Cernik (d), M. di Michiel (e), P.B. Cobden (f), O. Pirgon-Galin (f), L. van de Water (g), M.J. Watson (g) and B.M. Weckhuysen (a), *J. Catal.* **314**, 94 (2014).

(a) Inorganic Chemistry and Catalysis, Debye Institute for Nanomaterials Science, Utrecht University (The Netherlands)

(b) Department of Chemistry, University College London (UK)

(c) UK Catalysis Hub, Research Complex at Harwell, Rutherford Appleton Laboratory, Didcot (UK)

(d) School of Materials, University of Manchester (UK)

(e) ESRF

(f) Energy Research Centre of the Netherlands (ECN), Petten (The Netherlands)

(g) Johnson Matthey Technology Centre, Billingham (UK)

Synchrotron-based X-ray diffraction computed tomography (XRD-CT) is a technique developed at the ESRF for the purpose of revealing detailed chemical compositional information in solid materials in 2 and 3 spatial dimensions [1]. Much of this 'chemical imaging' has focused on the study of pre-shaped catalyst bodies often as a function of time. Here we demonstrate how the technique has been used to understand the importance of spatial variation during the process of sulfur-induced solid-state deactivation of low temperature $Cu/ZnO/Al_2O_3$ water-gas shift catalysts.

Catalyst deactivation by sulfur poisoning is a common problem for a wide range of catalytic processes and which is likely to become more problematic as the chemical industry moves from relatively clean feeds, such as natural gas and crude oil, to alternative feedstocks, such as bitumen tars and some forms of biomass. Cu/ZnO catalysts represent the industrial standard for the production of methanol and the water–gas shift (WGS) reaction. The catalysts are however very susceptible to sulfur poisoning (ZnO for example is often used as a 'sulfur scrubber'). However the process by which sulfur poisons these catalysts is still up for debate. It is thought that sulfur, in the form of either H_2S or similar compounds, accumulates on the surface of the metallic Cu species blocking the active sites or else induces a phase transformation of the Cu and ZnO into the respective sulfides and oxy-sulfides. Since catalysts are used in pre-shaped forms, *i.e.* as millimetre-sized catalyst bodies, to understand deactivation in real catalyst samples needs consideration of the spatial perspective in order to assess macroscopic effects leading to catalyst deactivation. XRD-CT is ideal for assessing crystalline phase distribution at the μm scale, whereas XAFS/XRD mapping can be used to determine the relative importance of poisoning via sulfur adsorption vs. solid-state transformation of the active Cu/ZnO phase(s) into sulfide phases.

Sulfur, in the form of H_2S, was added to the catalytic feed during the WGS reaction and the results of the XRD-CT data recorded as a function of increasing sulfur concentration are given in Figure 144. The initial crystallline Cu and ZnO phases disappear with increasing $[H_2S]$ in the feed and both phases lose intensity and 'shrink'

towards the core of the body. New sulfide phases evolve on the outside, while the increasing [H_2S] leads to a thicker sulfide shell. Consequently, the thicker the sulfide shell, the greater the loss in catalytic activity. In the sample poisoned using 500 ppm H_2S, over 80% of the cylinder volume is converted into sulfide-containing phases and almost all catalytic activity is lost.

Whilst XRD-CT is able to identify the distribution of crystalline components over the 2D cross-section, it is insensitive to the presence of small amounts of adsorbed sulfur species on the surface of metallic Cu, which may block the active site. For this purpose, a chemical map derived from the fitting of the Cu-NN (nearest neighbour) contribution from XAFS spectroscopy on a section of the microtomed catalyst is given in **Figure 145**. The main Cu nearest neighbour component is < 2 Å at the core and > 2.1 Å towards the edge, consistent with the presence of CuO at the core and CuS at the edge. There was no clear evidence for the presence of either Cu-S or Zn-S phases in the centre of the sample [2].

The formation of sulfide phases at the sample edges is highly detrimental to the catalytic activity of the sample since the catalyst deactivates before all Cu/ZnO has been lost. Although industrial $Cu/ZnO/Al_2O_3$ catalysts are unlikely to see anything like the amount of H_2S used in this study, the tendency for Cu and Zn to adsorb S does mean that, over time, sulfide phases will accrue in much the same way as observed here. Clearly it is important to consider the spatial component when trying to determine the structure-activity relationships in real heterogeneous catalyst samples with imaging methods critical for such purposes.

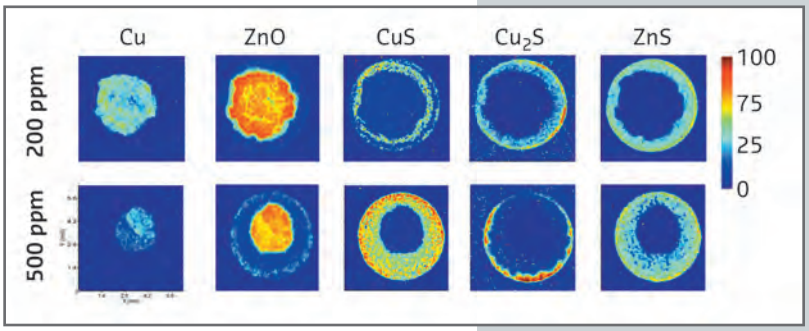

Fig. 144: 2D XRD intensity colour maps for various crystalline phases (top) after two concentrations of H_2S (left) were introduced in the WGS reactant feed. Right – colour scale map.

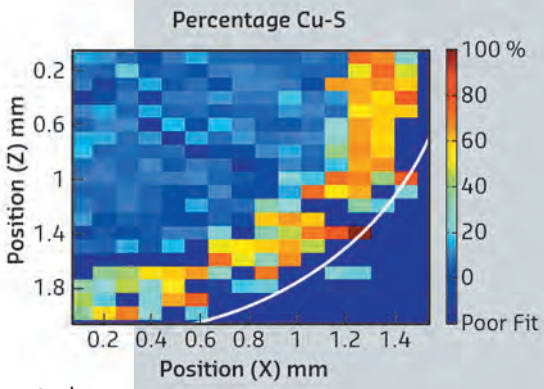

Fig. 145: Derived composition data from the Cu-'O' bond distance map of a microtomed cross-section of a Cu/ZnO/Al_2O_3 catalyst body treated with 200 ppm H_2S. Right – colour scale map.

References
[1] A.M. Beale, S.D.M. Jacques, E.K. Gibson and M. Di Michiel, *Coord. Chem. Rev.* **277**, 208 (2014).
[2] A.M. Beale, E.K. Gibson, M.G. O'Brien, S.D.M. Jacques, R.J. Cernik, M. di Michiel, P.B. Cobden, O. Pirgon-Galin, L. van de Water, M.J. Watson and B.M. Weckhuysen, *J. Catal.* **314**, 94 (2014).

SHORT-RANGE CORRELATIONS IN MAGNETITE ABOVE THE VERWEY TEMPERATURE

Magnetite, Fe_3O_4, is the first magnetic material discovered and utilised by mankind in Ancient Greece, yet it still attracts attention due to its puzzling properties. Discovered in the first half of the twentieth century, the Verwey transition in magnetite [1] remains one of the most intriguing phenomena in solid-state physics. Magnetite is a ferrimagnet with an anomalously high Curie temperature T_C = 850 K. Hence, it is viewed as an ideal candidate for room-temperature spintronic applications. It crystalises in the inverse spinel cubic structure, with two types of Fe sites: the tetrahedral A sites and the octahedral B ones. At T_V = 124 K, a first-order phase transition occurs as the electric conductivity drops by two orders of magnitude with the simultaneous change of the crystal structure from the cubic to monoclinic symmetry and with

Principal publication and authors
A. Bosak (a), D. Chernyshov (b), M. Hoesch (c), P. Piekarz (d), M. Le Tacon (e), M. Krisch (a), A. Kozłowski (f), A.M. Oleś (e,g) and K. Parlinski (g), *Phys. Rev. X* 4, 011040 (2014).
(a) ESRF
(b) SNBL, ESRF
(c) Diamond Light Source, Didcot (UK)
(d) Institute of Nuclear Physics, Polish Academy of Sciences, Kraków (Poland)
(e) Max-Planck-Institut für Festkörperforschung, Stuttgart (Germany)
(f) AGH-University of Science and Technology, Kraków (Poland)
(g) Marian Smoluchowski Institute of Physics, Jagellonian University, Kraków (Poland)

References
[1] E.J.W. Verwey, *Nature* **144**, 327 (1939).
[2] A. Faber, in *Spectroscopy Techniques*, B. Richards, H. Evans (Eds.), Oxford University Press, New York, 1-34 (1999).

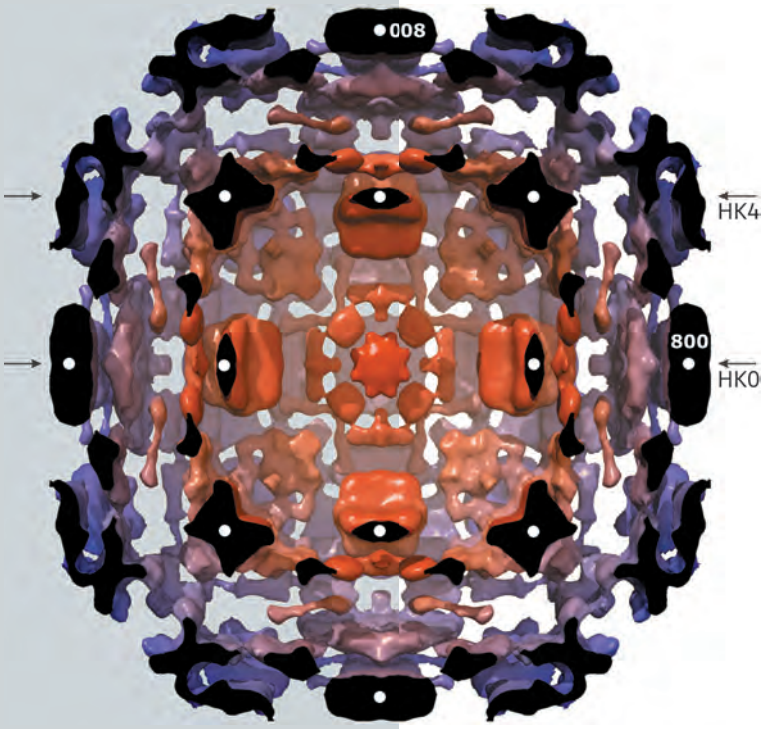

Fig. 146: Isosurface representation of diffuse scattering in magnetite slightly above T_V. Colour represents the distance to the (000) node; diffuse clouds in the proximity of weak Bragg spots have been removed. The half-space above the H0L plane has also been removed. White circles mark strong Bragg reflections in the H0L plane, and arrows denote HK0 and HK4 cuts perpendicular to the image plane.

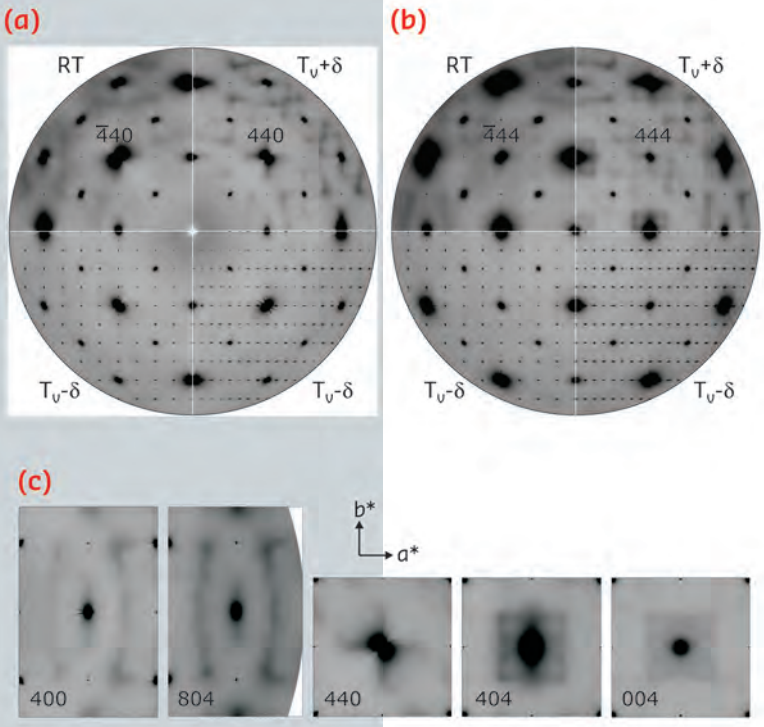

Fig. 147: Diffuse scattering in magnetite at variable temperature. Magnetite reciprocal space cuts HK0 (a) and HK4 (b) are shown at room temperature (RT), slightly above (T_V + δ) and below (T_V − δ) the Verwey transition, with δ ~ 2.5 K. Left-hand bottom panels: Sections perpendicular to the cell doubling direction. Right-hand bottom panels: sections parallel to the cell doubling direction. Selected regions of interest (see text) are shown in (c) together with the unit cell vectors a* and b*. Cubic m3m (above T_V) and tetragonal 4/mmm (below T_V) Laue symmetries have been applied.

spectacular anomalies in practically all physical characteristics. The low-temperature structure of magnetite, as deduced from recent studies, was identified to be of monoclinic Cc space group symmetry, with a complex displacement pattern [2]. This suggests that electron localisation, responsible for the dramatically increased resistivity, appears in basic three-Fe-site units, called "trimerons".

With the use of a state-of-the-art large area detector (PILATUS 6M), a detailed three-dimensional (3D) reciprocal space mapping can be performed, revealing an extremely rich diffuse scattering pattern (**Figure 146**), inherited from the complex low-temperature structure below the Verwey transition. Even at room temperature, which is considerably higher than the 124 K transition temperature, electrons appear to be correlated over relatively large length scales (**Figure 147**). The characteristic length estimated from the width of diffuse features varies from ~2 unit cells (u.c.) of the prototype cubic structure at T_V+2.5 K to a value slightly larger than ~1 u.c. at room temperature. Thus, the ordering pattern cannot be reduced to the trimeron features, but rather to complexes of trimerons. Therefore, our study supports the polaron picture, and we can state that its structure is in reality much more complex than ever expected previously. We were able to associate some characteristic experimental features with the topology of the Fermi surface of magnetite. While the structure of the low-temperature phase was frequently considered as a key to the understanding of the Verwey transition, our work indicates that the diffuse scattering pattern *above* the transition actually encodes some key information.

ENABLING TECHNOLOGIES

By definition, enabling technologies provide the means to generate significant leaps in performance and capabilities of our facility and therefore underpin every aspect of the ESRF's scientific activity. In this context, 2014 saw the concomitant execution of Phase I of the Upgrade Programme and the development of Phase II. Together with the facility operation, these two deliverables represented a real challenge in terms of resource management and scheduling. On the one hand several UPBLs went through various stages of completion, while on the other hand an in-depth reflection on the future scientific instrumentation and accelerator technology was carried out. The majority of the ESRF beamlines are expected to reap immediate performance benefits from the improved source and in many cases, novel instrumentation will be needed. The Orange Book provides a comprehensive overview of the ESRF's strategy for developing future beamline instrumentation and infrastructure, driven by the new storage ring's capacities.

A successful enabling technology programme is not limited to scientific instrumentation and in fact involves a very broad range of engineering areas. The content of this chapter on "Enabling Technologies" exemplifies this variety and touches a multitude of topics, all key in the current and future operation of the ESRF. The constantly growing sophistication of state-of-the-art instrumentation together with the very high expectations of our User Communities requires a holistic strategy involving many different factors that together determine the overall performance and reliability of the facility. All ESRF divisions, and in particular the two technical divisions, ISDD and TID, collaborate together to deploy state-of-the-art technologies taking into account the challenging trade-off between performance, cost, and maintenance effort.

The two first articles illustrate the impact that new cryo-cooling techniques and automation have on the new macromolecular crystallography beamlines. The third article emphasises the impact of our long-standing effort to develop generic solutions for beamline instrumentation. Similarly the fourth article recalls the importance of accurate modelling to optimise the performance of light converters that can be integrated into high spatial resolution X-ray detectors. The fifth article describes the helium recovery network, which has a significant financial impact on the use of liquid helium at the beamlines, thus making it a sustainable operation. The last article describes the implementation of the new Internet addressing scheme IPv6 for all institutes on the EPN Science Campus enabling Internet connectivity compliant and performing with countries and laboratories having adopted this new standard.

R. DIMPER and J. SUSINI

Principal publication and authors
P. van der Linden, F. Dobias, H. Vitoux, U. Kapp, J. Jacobs, S. Mc Sweeney, C. Mueller-Dieckmann and P. Carpentier, *J. Appl. Cryst.* **47**, 584 (2014).
ESRF

HIGH PRESSURE COOLING OF BIOLOGICAL CRYSTALS WITHOUT CRYOPROTECTION

Most diffraction data for biological crystals is recorded at cryogenic temperatures to reduce the secondary radiation damages and thereby extend the life-time of samples in X-rays. However, crystals need to be cryo-protected prior to being cryo-cooled to avoid solvent crystallisation and its subsequent spoiling of the experimental results: the loss of diffraction orders and of diffraction quality. To a lesser extent, the cryo-protection process also has its own undesirable effects: (1) crystals are slightly destabilised during the short soaking passage in the cryosolution and extremely fragile crystals may dissolve regardless of the cryo-agent type, (2) the vitrification of solvent into low density amorphous (LDA) ice at ambient pressure produces a mechanical stress that increases the mosaicity of crystals, and (3) cryo-molecules may bind and disturb proteins possibly even at their active sites. The search for optimum cryoprotectant conditions which aim to limit these drawbacks is so time-consuming for usually a poor improvement that crystallographers often prefer to simply use glycerol. Therefore, we investigated alternative cooling methods to eliminate the need for cryoprotection in an attempt to circumvent this issue. High pressure cooling is one of the most effective of these techniques and consists of flash-cooling cryoprotectant-free biological crystals down to 77 K under 2 kbar of helium pressure (**Figure 148a**) [1]. During this thermodynamical process, the crystals are frozen in their non-protected mother liquor which is directly transformed into high density amorphous (HDA) ice under the effect of pressure, avoiding water crystallisation and its destructive effects. Advantageously, the cryoprotectant-free HDA matrix limits the augmentation of the mosaicity which results from the LDA-ice expansion, eliminating the unwanted effects that are associated with the presence of cryo-agents, and thus preserves crystals close to their native state. High pressure cooling has proven to be systematically applicable to all kinds of biological crystals regardless of the protein's nature, the solvent content or the crystallisation conditions. Moreover, the method has recently been extended to cryopreserve hydrated bacteria for imaging experiments [2]. In addition, pressure is a key thermodynamic parameter as important as temperature in studies of macromolecules. Indeed, pressure allows the energy landscape of proteins to be explored, providing access to different conformational substates that cannot be studied in any other manner (active site conformations or reaction coordinates). Therefore, this technique has potential to address many essential biological issues.

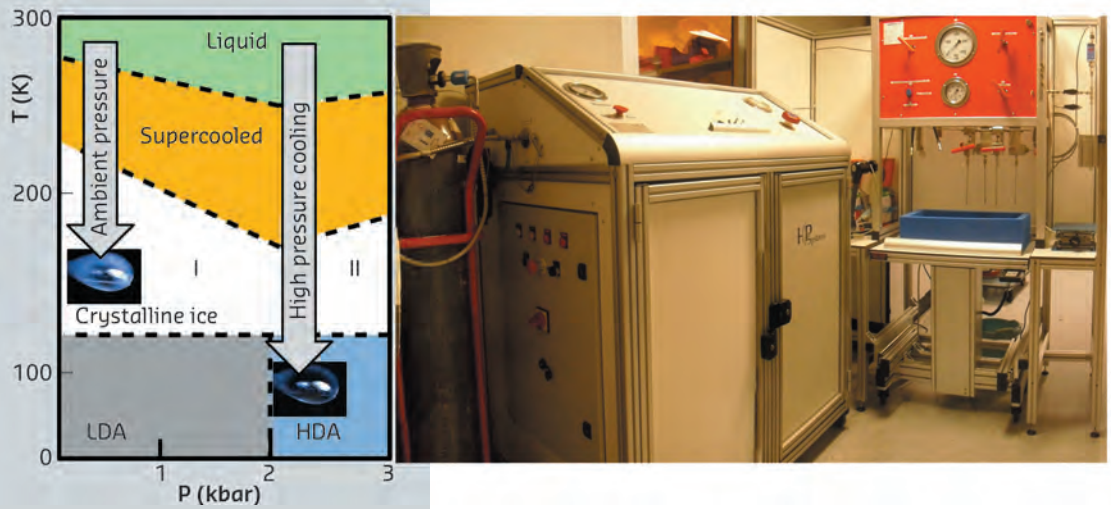

Fig. 148: *a*) Phase diagram of water. Unprotected crystals cooled at ambient pressure (AP-cooled) produce crystalline ice. At high pressure the solvent is transformed into HDA-ice. b) High pressure cooling installation at beamline ID23.

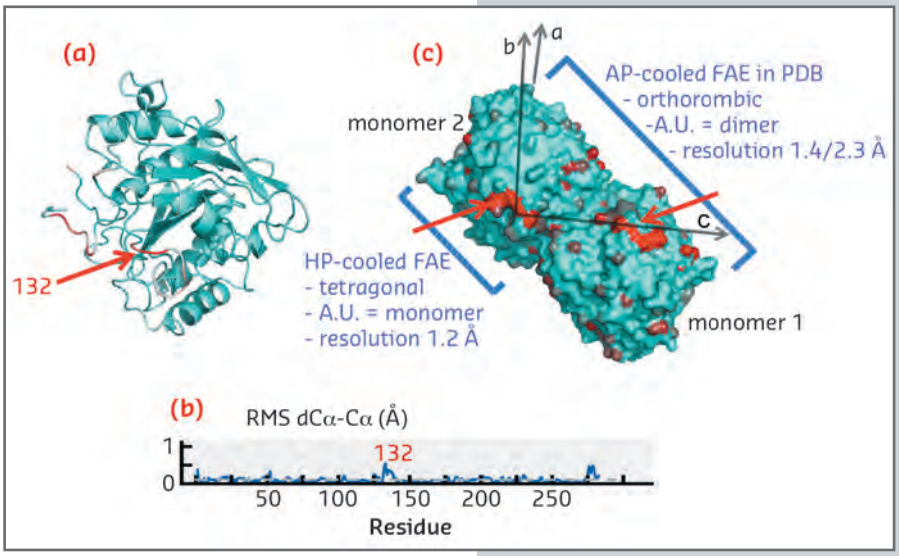

Fig. 149: a) Ribbon representation of the structure of the HP-cooled protein FEA, largest structural displacements are represented in red (loop 132). b) Root mean square displacement of the HP-cooled FEA versus residue number. c) Crystallographic packing of FAE in surface representation (monomer/dimer).

Until now, users have been put off by this difficult approach reserved for specialists, which needs heavy instruments of low productivity to combine high pressures with cryogenic temperatures. We have designed an automated high pressure cooling instrument and developed a concomitant methodology and ancillary equipment, paying particular attention to the user-friendliness and throughput (**Figure 148b**). The computer controlled system is theoretically capable of processing 30 samples per hour. The throughput bottleneck now mainly depends on classical sample handling operations of crystallographers facilitated by a new pluggable SPINE compatible sample-holder and its associated toolkit (*i.e.* crystal fishing, recovery and mounting/dismounting). Optionally, during the high pressure cooling procedure, the pressurisation bench can be switched to a noble gas circuit to produce xenon or krypton heavy atom derivatives for anomalous phasing purposes. In practice, the machine is capable of vitrifying nanolitres of aqueous solution with only 5% glycerol for cryopreserving dilute biological objects. Moreover, the method is particularly effective for cooling biological crystals that are totally free of cryoprotectant since the ingredients of the mother liquor are sufficient to act as antifreeze agents. The methodology was successfully validated with a series of test crystals (lysozyme, insulin, thaumathin, FEA, proteinase-K and thermolysin). Following this, nearly a thousand users' crystals have been processed. The resulting structures are relatively isomorphous to their counterparts in the PDB, since the pressure induced structural changes are limited to flexible loops at the proteins surfaces while their structured cores are relatively pressure insensitive. High pressure cooled FAE is a meaningful example, revealing a pressure induced modification that concerns only a single loop at the dimer interface, but this simple modification results surprisingly in a superior crystalline quality: a transition to a higher symmetry, a higher resolution, lower B-factors and a lower mosaicity (**Figure 149**).

The apparatus is installed in the laboratory associated with beamline **ID23**, and a high pressure cooling service is now offered to the ESRF structural biology user community for appropriate projects.

References
[1] C.U. Kim, R. Kapfer and S.M. Gruner, *Acta Cryst.* **D61**, 881 (2005).
[2] E. Lima, Y. Chushkin, P. van der Linden, C. Un Kim, F. Zontone, P. Carpentier, S.M. Gruner, and P. Pernot, *Phys. Rev.* **E90**, 042713 (2014).

MXCuBE2 DEFINES A NEW PARADIGM IN MACROMOLECULAR CRYSTALLOGRAPHY BEAMLINE CONTROL

Authors
M. Oscarsson, M. Guijarro, A. Beteva, S. Monaco, O. Svensson, G. Leonard and D. de Sanctis.

Macromolecular crystallography (MX) beamlines have been undergoing an increasing evolution in automation, with constant improvements in robotics for sample handling, development of high accuracy multiaxis diffractometers, and faster and more sensitive X-ray detectors

based on pixel technologies. This evolution has resulted in both an increase in the productivity and an improvement in the quality of diffraction data collected. Moreover, the advent of microfocus beamlines has made it possible to collect data from microcrystals or from the best diffracting part of any crystal. However, developments in instrumentation have not been the only driving force behind the increase in scientific productivity of MX beamlines: The simultaneous development of laboratory information management systems (LIMS) [1], automatic pipelines for data collection [2] and reduction [3], and software for beamline control has also been an essential contributor as it has allowed researchers to perform increasingly complex experiments and to link these both to exhaustive metadata descriptions and to automated data analysis.

MXCuBE (Macromolecular Crystallography Customised Beamline Environment), is a beamline control graphical user interface (GUI) for MX experiments [4] that was initially developed at the ESRF. The first version of MXCuBE was released in 2005, and since then it has become the preferred data-acquisition software for structural biologists at many synchrotron sites, providing a platform for modern high-throughput MX that also allowed users to carry out experiments remotely. In particular, the MXCuBE GUI provided the user with an intuitive means of interacting with beamline components by using graphical icons and visual indicators rather than text-based interfaces. MXCuBE2 is a completely upgraded version of MXCuBE, its development and recent deployment has been driven by the new requirements of next-generation MX experiments at synchrotron sources.

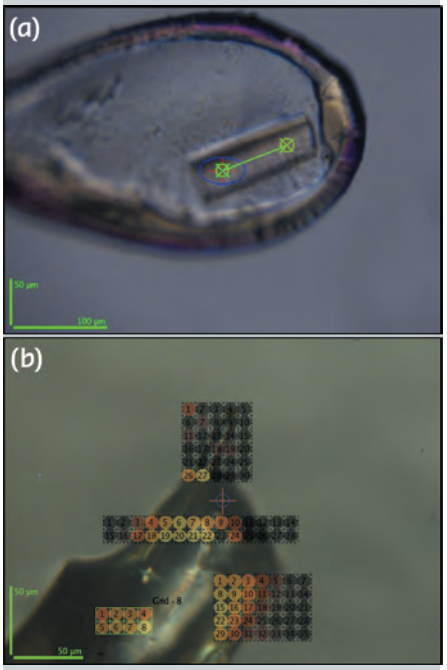

Fig. 150: (a) MXCuBE2 offers improved interaction with the sample thus facilitating advanced experiments, such as a helical scan in continuous mode (4dscan). Diffraction data are collected while rotating and translating the crystal along the line defined. (b) A new mesh drawing tool permits the drawing of a different grid using the beam size as unit. After analysis, scores are reported directly on screen.

MXCuBE2 is built on a level of hardware abstraction that permits its adaptation to any kind of hardware environment and its interfacing with a variety of low-level control systems, thus making it compatible with most components of any synchrotron-based MX facility. Like its predecessor, MXCuBE2 offers users the same look-and-feel to its interface despite controlling different hardware, and it allows users to drive experiments from a single module that controls sample handler, diffractometer, detector and all other beamline components. In this manner, it allows users to focus on samples and experiments, without having to have a specific knowledge of how the hardware is going to carry out the instructions. Compared to that of MXCuBE, the appearance of MXCuBE2 has been simplified in order to permit a closer interaction with the sample under study while, at the same time, providing a growing number of new tools for experiment design and execution. In particular, MXCuBE2 provides an improved and more user-friendly environment for complicated multi-crystal/multi-position MX experiments performing them in a modular, logical and automatic fashion. It also offers both the possibility of performing routine experiments and of accessing the advanced parameters and functionalities required for more complicated tasks through a single, unified GUI. MXCuBE2 can thus be used both to drive completely automatic data collection at the ID30A MASSIF beamlines and, for example, in specific experiments exploiting microbeams. To facilitate the latter, MXCuBE2 allows the storage of different positions on a single sample that are then either used for data collection with an X-ray beam of a defined size or to define areas on the sample that are to be characterised prior to full diffraction data collection. MXCuBE2 also facilitates experiments involving complex experimental phasing protocols, such as inverse beam geometry, interleaved multi-wavelength experiments and multi-positional data collection. The new tools available in MXCuBE2 also include much-improved line and mesh scan protocols and, coupled with improved motor control via ICEPAP modules, faster helical data collection based on 4d scans [5] (**Figure 150**)

and workflows for the collection of partial data sets from many samples contained on the same sample support.

MXCuBE2 is now developed as a joint effort - the MXCuBE Collaboration - between the ESRF, other European synchrotron sites [SOLEIL, EMBL@PETRAIII, BESSY and MAXLAB] and the Cambridge-based computer software company Global Phasing Ltd. Developments of the ISPyB LIMS [1] are keeping pace with the improved environment for experiment execution that MXCuBE2 provides. As the development of ISPyB will also soon be the subject of a collaboration agreement between the ESRF and other synchrotron sites, the future of the MXCuBE/ISPyB combination as *the* software environment for MX experiments seems assured for many years to come.

References
[1] S. Delagenière *et al.*, *Bioinformatics* **27**, 3186-92 (2011).
[2] S. Brockhauser, *Acta Cryst.* **D68**, 975-984 (2012).
[3] S. Monaco *et al.*, *J. Appl. Cryst.* **46**, 804-810 (2013).
[4] J. Gabadinho *et al.*, *J. Synchrotron Rad.* **17**, 700-707 (2010).
[5] D. de Sanctis *et al.*, *J. Synchrotron Rad.* **19**, 455-461 (2012).

GENERIC SOLUTIONS EASE THE WAY FOR PHASE I UPGRADE BEAMLINES

Authors
T. Mairs, R. Barrett, Y. Dabin, P. Fajardo, A. Goetz and P. Marion, representing the many engineers and technicians of the ISDD who worked on the generic solutions.
ESRF

In 2009, the ESRF took on the challenge of designing, installing and commissioning nine upgrade beamline projects (UPBL), renovating four beamlines and moving three beamlines. Eighteen endstations of considerable complexity, in comparison with existing beamlines, were to be completed in the six years of the upgrade Phase I using existing technical staff. A strategy of using standard and generic building blocks to construct the beam delivery and detection systems yielded significant technical and financial advantages, leaving time to develop *ad hoc* sample environment and manipulation instrumentation.

Advantages to generic solutions:
- Technical staff are interchangeable between projects as the technology adopted is similar leading to easier maintenance, lower ownership costs and quicker commissioning.
- High performance is obtained thanks to intense design and testing efforts invested to optimise and characterise the first units of each generic block, which then benefits all the devices using this block.
- Design and development time is considerably shorter. A more collaborative approach to design work is fostered due to multiple use of the same technology.
- Cheaper and more efficient procurement due to increased quantities of component building blocks with appropriate sub-contractors being identified early in the development phase.
- The combined performance of the beamlines and accelerator can be optimised due to the global view and know-how of the engineers and technical staff over the whole ESRF complex.

There are several minor disadvantages such as:
- Longer design and production time for the first device of the generic family.
- Less freedom for beamline scientists and engineers to choose their individually-preferred and specifically tailored solutions.

Generic solutions at the ESRF originated from the time of the installation of the first beamlines in the 1990's. Then, being the first third generation synchrotron source, the ESRF was obliged to develop a large proportion of its instrumentation in-house as industrial suppliers had not enough experience to produce cutting-edge designs. This initial investment in our in-house engineering and the early adoption of standard components such as primary and secondary slits, fluorescent screens, attenuators, beamshutters, DPAP motor controllers, SPEC, TACO, Kohzu monochromators, etc., allowed the first beamlines to be installed and commissioned efficiently. As the source performance improved and increased in power in

the late 1990's, these initial, rather basic, components, which were essentially identical for all beamlines, were gradually replaced with higher performance versions either for standard devices (*e.g.* primary slits and attenuators) or by generic variants that were tailored or adapted to individual beamline requirements.

A generic solution is considered to be an instrument that can be made up of building blocks which have already been used and tested beforehand with a number of relatively small changes introduced for the particular beamline. A typical example of this would be the ESRF UHV compatible beamviewers that have evolved from their initial concepts starting in 1993 to a stable design in 2012. These devices are particularly being used during the commissioning phase of beamlines, and hence, large quantities were foreseen for Phase 1 of the upgrade (**Figure 151**).

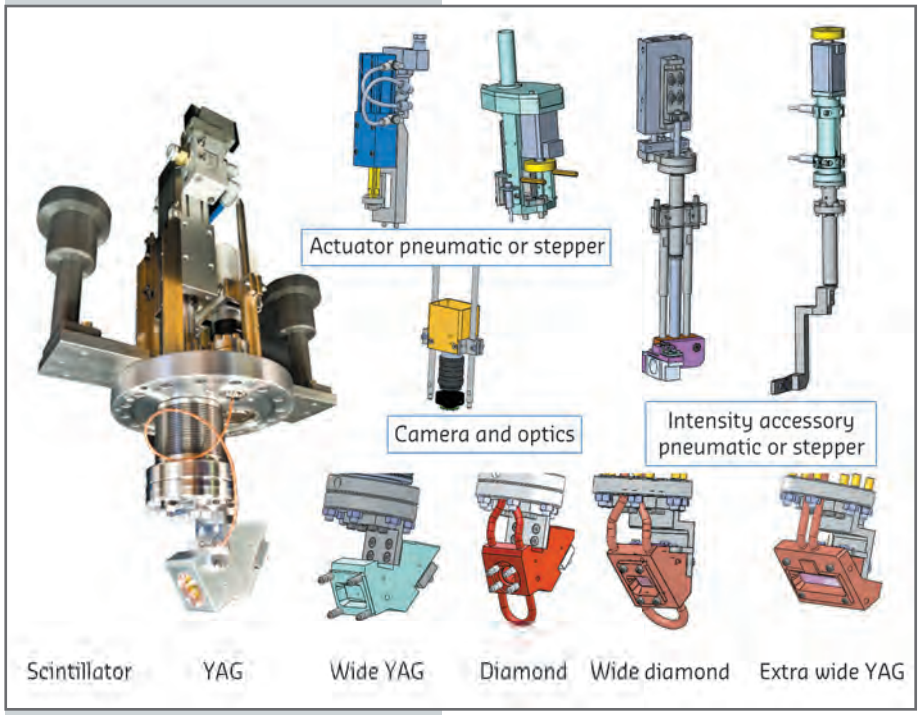

Fig. 151: UHV Beam viewers.

Fig. 152: Generic solutions.

The beamviewers consist of the following building blocks:

- Camera and focusing optics
- Scintillator and holder
- Positioning device to bring the viewer into or out of the beam
- Vacuum chamber
- Software to read, analyse and display the images

Basic imaging cameras are evolving quickly and the necessity to choose a standard camera for Phase 1 beamlines was identified early on. An Ethernet GigE camera was chosen and implemented in a number of different ESRF devices. The scintillator and its holder depend on the beam characteristics (white/pink/monochromatic, size and position) and consequently each beamline is able to choose either a standard configuration or one adapted to its needs. Two methods of positioning the device in the beam are available either pneumatically or using a stepper motor driven actuator. Integration of the device is specific to the beamline, and hence, the vacuum chamber is designed on an *ad hoc* basis. The ESRF software group is confronted daily with integrating images into beamline control so the beamviewers naturally benefit from LIMA (Library for image acquisition) developed as a generic solution for reading cameras. A total of more than 50 devices from this family have been installed during the Phase 1 beamline programme.

The catalogue of generic solutions has continued to grow during Phase 1, which started with some high performance ESRF solutions ranging from opto-mechanics such as dynamic benders for KB mirror systems and precision jacks through more general mechanics such as hexapods and positioning technology (**Figure 152**). The generic approach extended to control instrumentation such as

IcePAP motor controllers or MUSST acquisition modules, Xray detectors such as the FReLoN cameras and the first generations of Maxipix devices. and software solutions with libraries (PyFAI), applications (MxCube, PyMCA), and complete toolboxes (TANGO). In addition, all generic software is open source and has been shared with a large number of sites in Europe and the rest of the world.

These generic solutions have been extensively used during the upgrade and are now complemented among others by:

- Opto-mechanics: A range of white beam and monochromatic beam transfocators, fixed radius nano focusing KB systems, white beam mirror assemblies and multilayer monochromators.
- Mechanics: Improved hexapods.
- Diagnostics and detectors: extended range of focused beam viewers, new high resolution scintillator screens or CdTe based Maxipix detectors.
- Control electronics: continued improvements of IcePAP motor controllers and 100 MHz voltage-to-frequency converters.
- Software: TANGO, LIMA, MxCube, PyFAI, PyMCA, e-motion, graphical user interfaces, workflows, metadata and archive databases.

MODELLING OF THE MTF PERFORMANCE OF HIGH SPATIAL RESOLUTION X-RAY DETECTORS

Authors
F. Riva (a,b), P.A. Douissard (a), T. Martin (a) and C. Dujardin (b).
(a) ESRF
(b) ILM, Université Lyon 1-CNRS (France)

X-ray detectors for high spatial resolution imaging are mainly based on indirect detection. The detector consists of a converter screen made of a scintillating material, light microscopy optics and an imaging sensor (CCD or CMOS). The scintillating screen converts part of the absorbed X-rays into a visible light image, which is projected onto the CCD by means of the optics (**Figure 153**). The performance of the detector is strongly influenced by the properties of the converter screen, which include X-ray absorption, spread of energy deposition, scintillation yield and emission wavelength.

To obtain detectors with micrometre and sub-micrometre spatial resolution, thin (1-50 µm) single crystal film (SCF) scintillators are required.

At the ESRF, X-ray imaging applications regularly make use of energies up to 120 keV. At relatively high energies, the efficiency of the detector is reduced dramatically because of the weak absorption of the converter screen. For example, at 20 keV a 5 µm thick scintillator of gadolinium gallium garnet (GGG) absorbs only 10% of the incident photons. Furthermore, the low stopping power degrades the spatial resolution because of the energy deposition spread in the converter screen.

At the ESRF, GGG and LSO (lutetium orthosilicate) scintillators are produced by liquid phase epitaxy (LPE). Additionally, the development of new scintillating materials is currently being investigated: the goal is to improve the contradictory compromise between absorption and spatial resolution, thereby increasing the detection efficiency while keeping a good image contrast even at high energy. The development of a new kind of scintillating screen by LPE is time consuming and expensive. Therefore, we developed a "simulation tool" able

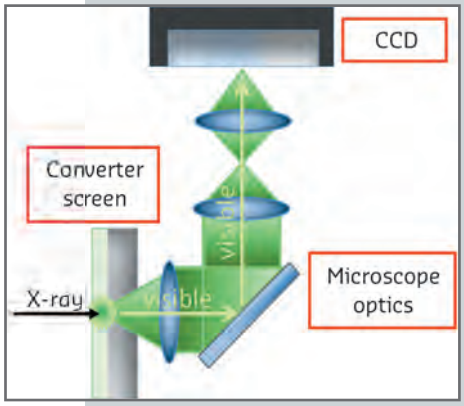

Fig. 153: Schematic of a detector for high spatial resolution based on indirect detection.

References

[1] S. Agostinelli *et al.*, *Nuclear Instruments and Methods A* **506**, 250-303 (2003).

[2] H.H. Hopkins, *Proc. R. Soc. Lond. A* **231**, 91-103 (1955).

[3] Slanted Edge MTF: http://rsb.info.nih.gov/ij/plugins/se-mtf/index.html

to predict the optimal combination of scintillating screen (in terms of thickness, composition and substrate) and visible light optics for different energy ranges. The aim of these simulations is to guide the choice of the materials that will be developed by LPE.

We combined a Monte Carlo approach using Geant4 Monte Carlo toolkit [1] for the energy deposition leading to light emission with analytical calculations for the optical collection. The energy spread in the converter screen is described by Monte Carlo simulations in which a monochromatic X-ray pencil beam hits the scintillator, generating secondary X-rays and electrons. To quantify the spatial resolution, we estimated from the spatial distribution of the deposited energy the linear spread function (LSF). We also calculated the modulation transfer function (MTF) corresponding to the LSF in the frequency domain: this function gives the contrast as function of the spatial frequency.

However the intrinsic MTF of the converter screen does not describe the ultimate resolution of the detector completely: the visible light still needs to be projected on a CCD by means of microscope optics. The optics magnify the image, reducing the real pixel size of the CCD, with the consequence that it can degrade the resolution because of the combination between the depth of field of the optics and the thickness of the scintillator. This means that part of the visible image produced in the screen will be projected on the image sensor as a defocused image, creating a blur in the final image. To include this effect, we applied analytical equations describing the optics to the MTF of the converter screen obtained by Monte Carlo simulations [2].

We validated our model experimentally at beamline BM05, using the slanted edge method [3] to investigate the spatial resolution of the detector in a variety of configurations. In Figure 154a we show the excellent agreement between experimental MTF and the simulated MTF obtained at 15 keV. The microscope optic has a numerical aperture of 0.4 and it was combined with various scintillators: LSO grown by LPE on YbSO substrate (ytterbium orthosilicate), yttrium and lutetium aluminium garnet (LuAG and YAG) bulk single crystals grown by the Czochralski technique. The thickness of the scintillators ranges from 11.8 µm to 500 µm. In Figure 154b, the same model is used to simulate the MTF at 55 keV: gadolinium aluminum perovskite (GAP), a candidate material for the development by LPE, is compared to LSO and GGG, both currently used at ESRF. Simulations show that GAP could improve the spatial resolution compared to the available screens in the energy range higher than the gadolinium k-edge.

A model for indirect detection has been developed and validated with experimental data. The agreement with experiment is very good and we are confident that our model can be used for optimisation of detectors, helping to estimate the spatial resolution for different configurations of the detector for various experimental conditions. Additionally, it gives important information about the improvements that could be obtained regarding resolution and efficiency using a new scintillator or a new detector configuration as well as the crucial role of the substrate when the ultimate resolution is desired.

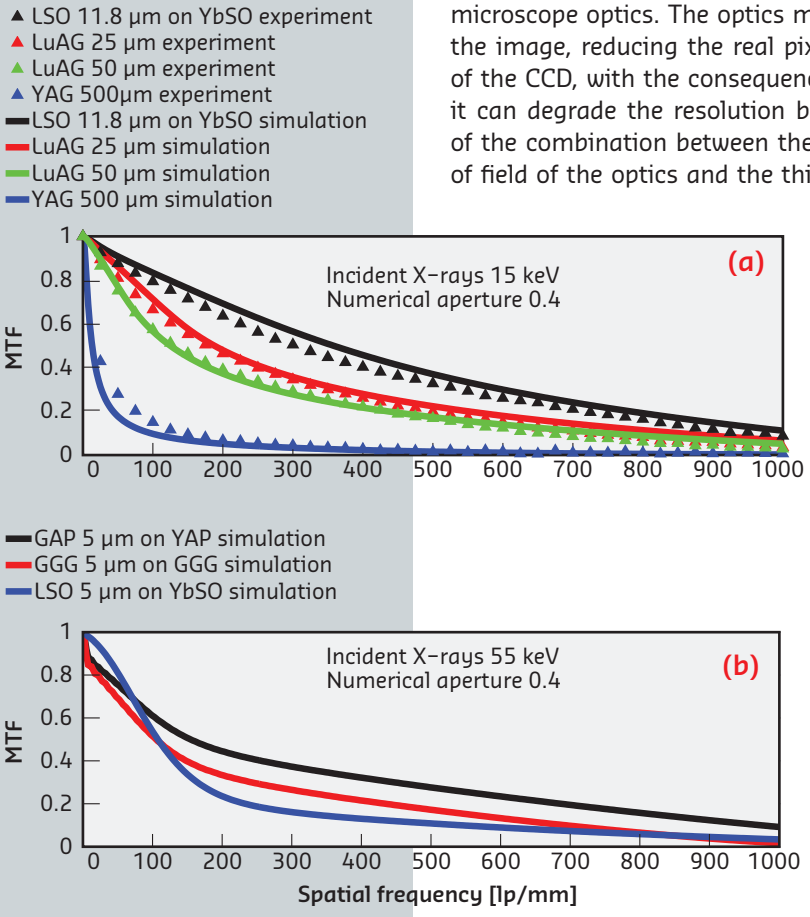

Fig. 154: Contrast as a function of the spatial frequency (MTF): a) X-rays 15 keV, experimental data and simulations; b) X-rays 55 keV, simulations for different materials.

THE ESRF HELIUM NETWORK

Authors
F. Favier, G. Guernet and T. Marchial.
ESRF

Helium is the second-lightest element in the Universe (seven times lighter than air), it has the lowest boiling-point, the lowest liquefaction temperature (-269°C) and, unlike any other element, helium will remain liquid down to absolute zero at ambient pressures. Its thermal conductivity and transmission of speed of sound are superior to that of all other gasses (save hydrogen). It is also the least water-soluble of all gasses. Colourless, odourless and non-toxic, helium is particularly chemically inert and ranks as the second least reactive noble gas, after neon. The remarkable properties of this gas have led to its widespread use in both liquid and gas forms.

In industry, helium is used to inflate airships and weather balloons. It provides a protective atmosphere in the manufacture of integrated circuits, screens, and in arc welding procedures. Helium can be used as a leak detector in vacuum equipment or in high pressure tanks, or to determine water tightness in food packaging. In science, helium is an integral element in cryogenic procedures for cooling or for experiments that require extremely low temperatures (supra conductors). It is also used in optics for its refraction index and in the aeronautics industry, laser systems and leisure activities (inflating balloons).

Helium is an irreplaceable but non renewable gas. It is the most abundant element in the universe, second only to hydrogen, but it is much rarer on earth. There is no synthesising method capable of producing helium except for nuclear fusion. Helium is a sub-product of natural gas that contains it from some parts per million to several percent. Helium-producing countries are USA (78%), Algeria, Qatar, Russia and Poland.

In 1996, the US passed a law which diminished the return on investment of recycling helium; the law stated that the US National Helium Reserve, which is kept in a disused underground gas field in Texas – by far the biggest store of helium in the world – must all be sold off by 2015, irrespective of the market price. The ESRF applies a standard practise for distribution and recovery of helium. ESRF benefits from compressed gas storage facilities at the ILL and the liquefaction services available at the CNRS and the CEA. Liquid helium is supplied by the CEA or CNRS in 100 dewars. Users connect the dewars to the equipment to be cooled (cryostats) then connect the gas outlet to the helium recovery network (50 mm stainless steel tube), running for 1.5 km around the storage ring and to the ILL.

An individual meter on each beamline makes it possible to control the volume of gas transferred over the network. This low pressure gas (about 30 mbar) is fed back into the ILL system where it is stored in a buffer tank (volume 20 000 *l*) then compressed into bottles at about 200 bars. The compressed gas is then transported to one of the liquefaction centres in either the CEA or CNRS, where it goes through a drying and purification process at low temperature (77 K, -196°C) to separate oxygen, nitrogen and water vapour. It is then re-liquefied (passage from gas

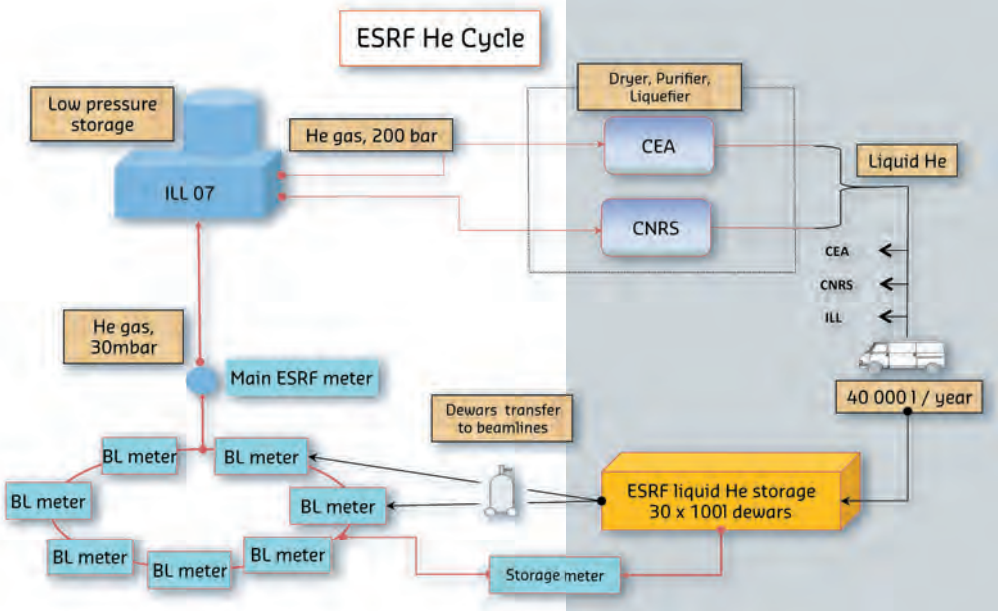

Fig. 155: The helium recovery process at the ESRF.

phase to liquid phase) to fill the dewars which come back again to supply the ESRF experiments (Figure 155).

The ESRF's consumption of liquid helium is about 40 000 per year with a recovery rate of over 70% (see Figure 156). An analysis of the recovery rate shows that it can vary between 50 and 80% depending on the month and the year. The major factors causing helium loss are evaporation (about 10%) and accidental loss (leaks on experimental pipes, poor connections). Nonetheless, in case of an important contamination of the recovered gas (*e.g.* introduction of air), the global volume of recovered helium is affected because the correct functioning of the liquefier is linked to the purity of the gas (at very low temperatures solidified gas particles can cause damage).

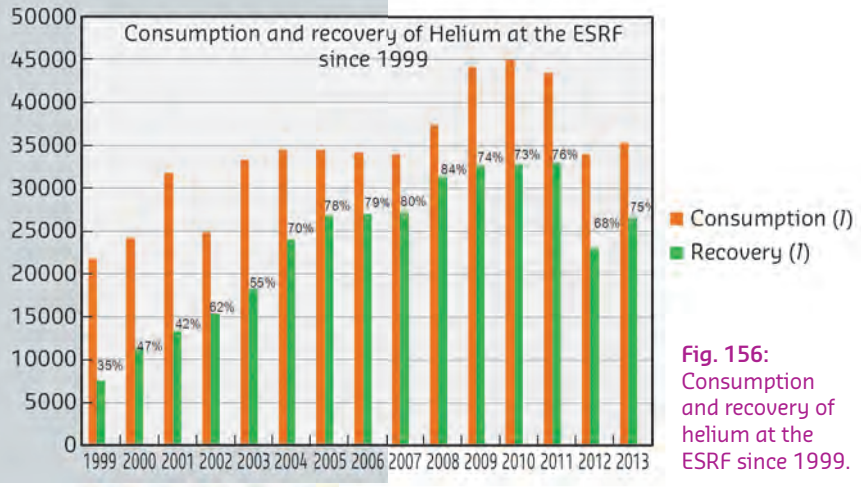

Fig. 156: Consumption and recovery of helium at the ESRF since 1999.

Adhering to simple procedures reduces loss and improves the recovery rate. Dewars pending use are systematically connected to the recovery network; dewars must be returned rapidly after use at a cold temperature, *i.e.* not completely empty. The tightness of the connections between the dewars and the experiment and the recovery network must be checked. Indications on the recovery meter should be checked against consumption. A significant difference could indicate a leak or contamination by ambient air and a local contamination could shutdown the whole of the ESRF recovery network.

IPv6 - PREPARING THE INTERNET CONNECTIVITY OF THE FUTURE

Authors
F. Calvelo Vazquez and B. Lebayle.
ESRF

The Internet Protocol (IP) is the main communication protocol in the Internet for relaying packets across networks and version 6 (IPv6) is the latest version [1]. IPv6 was developed by the Internet Engineering Task Force (IETF) to deal with the long-anticipated problem of IPv4 address exhaustion.

The depletion of IPv4 addresses was foreseen as long ago as the late 1980s. With the rapid growth of the Internet after commercialisation in the 1990s, the democratisation of Internet access in the developed world, the increasing use of mobile devices and buildings or home automation, the initial over-allocation managed by the Internet Assigned Numbers Authority (IANA) and by five Regional Internet Registries (RIR), and the inefficient address use by companies, are some of the reasons that have contributed to accelerate address consumption.

The top-level exhaustion occurred on 31 January 2011. Just three months later, on 15 April 2011, the APNIC (Asia-Pacific region) was the first RIR to run out of their free IPv4 address pool (Figure 157).

By 1998, the Internet Engineering Task Force had formalised the successor protocol IPv6. IPv6 uses a 128-bit address, allowing 2^{128}, or approximately 3.4×10^{38} addresses, or about 10^{29} times as many as IPv4, which uses 32-bit addresses and provides approximately 4.3 billion addresses. IPv6 offers a virtually inexhaustible number of addresses and paves the way for connecting ubiquitous devices to the Internet, a trend lately branded as the "Internet of Things" where uniquely identifiable embedded computing devices are connected within the existing *Internet* infrastructure.

IPv6 is intended to replace IPv4, which still represents 95% of the Internet traffic worldwide. At the beginning of 2013, the percentage of users reaching Google services with IPv6 was just a little bit above 1% [2]. This shows the slow adoption of IPv6 by major Internet Service Providers (ISPs), home networking equipment manufacturers and companies around the world.

IPv4 and IPv6 protocols are not designed to be interoperable, complicating the transition to IPv6. However, several IPv6 transition mechanisms have been devised to permit communication between IPv4 and IPv6 hosts.

The "IPv6 Task Force France" (TTF) was created by the French Senate in 2002 to regroup main service providers and industrial actors to promote the use of IPv6 in France. It is part of the initiative launched by the European Commission to coordinate all IPv6 Task Forces in Europe.

Efforts made by the government and some other institutions that were involved have proved fruitful as France is currently among the top 20 countries using IPv6 (rated as fourteenth in the global classification).

RENATER [3], our National telecommunications network for Technology, Education and Research, is currently connecting more than 1000 sites (institutions, universities and French organisations), but only 174 of them have already applied for an IPv6 prefix. Furthermore, only 118 have already broadcast their prefix to the rest of the world. Rhône-Alpes is one of the most active regions just behind Île-de-France.

At the ESRF, IPv6 will not replace IPv4 in the short term. Instead both protocols must co-exist on the Internet for several years. Being IPv6 ready is important for sites like ESRF to guarantee that data transfers are not slowed down by heavy protocol translations. However, progressing towards the implementation of this new Internet protocol standard was a long and complicated procedure for the EPN-campus. There were significant hurdles to overcome; organisational as well as technical. Discussions on this subject between the different EPN participants started only in April 2013. IPv6 has a significant impact for the System Administrators of the campus laboratories because of some new features and default behaviours. In fact System Administrators have to learn a completely new internet protocol. Once administrative formalities to obtain the new IPv6 address space had been settled, there was still a long road ahead for EPN institutes to implement the new prefix assigned by RENATER: give external visibility to our new prefix through our metropolitan network (TIGRE), find new partners supporting the Domain Name Service (DNS), adapt several hardware and software components to support this protocol, and make an address plan to share this IPv6 prefix between the four institutes taking part: ESRF, ILL, EMBL, IBS.

The last component to be dealt with was the upgrade of the common EPN-site firewall. Discussions with different suppliers of security systems started as early as May 2013. But nonetheless, finding companies with sufficient experience of this kind of deployment over IPv6 was challenging. Finally, on 20 October 2014 everything was in place and the migration was performed with only 43 seconds of service interruption. Today, the firewall is able to support new security features over the dual IPv4 and IPv6 stack.

The ESRF is now ready for the next generation of Internet services based on IPv6!

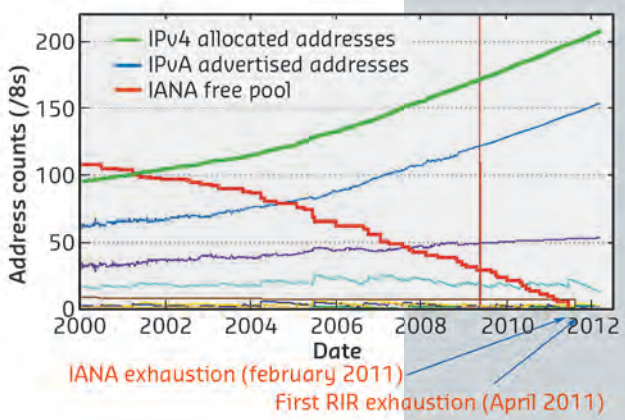

Fig. 157: Exhaustion of IPv4 addresses.

References
[1] Wikipedia entry on IPv6: http://en.wikipedia.org/wiki/IPv6
[2] Google's statistics: http://www.google.com/intl/en/ipv6/statistics.html
[3] RENATER: https://www.renater.fr

The Accelerator and Source Division (ASD) is in charge of the production of synchrotron light from the ESRF's 6 GeV storage ring. We have continued our efforts to ensure reliable operation during 2014. Indeed, during the year, 5399.20 hours of beam was delivered, representing an accelerator availability of 99.11% and beating the all-time ESRF record of 99.04% in 2009.

As well as providing beam to users, with 2014 marking the end of Phase I of the Upgrade Programme, the Division has completed or is in a very advanced stage of completion of major upgrades of several subsystems of the accelerator complex, including:

- Upgrade of the RF system with solid state amplifiers (completed)
- Development and installation of new higher order mode (HOM)-damped cavities (completed)
- Development and installation of improved electron beam position monitoring system and a fast orbit feedback system (completed)
- Extension of the straight sections from 5 m to 6 m (completed)
- Installation of canted straight sections (completed)
- Installation of one 7 m straight section (completed)
- Implementation of top-up mode capability (in progress)

This year was also a crucial year for the future of the Phase II Accelerator Upgrade, and a lot of time was dedicated to presenting our ideas, studies and designs to the Accelerator Project Advisory Committee (APAC), which was held in January, May, September and October. Following positive reports from the APAC in May, the project was approved and launched by the ESRF Council in June 2014. The upgrade will see the implementation of a new lattice for the storage ring to reduce the natural horizontal emittance from 4 nm to about 134 pm, thus greatly increasing the brilliance and coherence of the beam.

In addition to our work on Phase I and Phase II, we also hosted the 22nd annual European Synchrotron Light Source (ESLS) workshop in November. Thirty-five representatives from fifteen European light sources spent two days at the ESRF discussing the status of their institutes operational performance as well as future upgrade projects. We were pleased to note that the accelerator lattice concept developed at the ESRF is being adopted by many other world-leading synchrotron facilities.

After a busy but fruitful year, we entered the execution phase of the Phase II Upgrade Programme on 1st January 2015 and work on the project is now in full swing.

P. RAIMONDI

BEAM PARAMETERS OF THE STORAGE RING

Table 1 presents a summary of the characteristics of the storage ring electron beam.

Table 2 gives the main optic functions, electron beam size and divergence at various source points. For insertion device source points, the beta functions, dispersion, sizes and divergences are calculated in the middle of the straight section. For bending magnets, two representative source points have been selected for each type (even or odd cell number) of magnet, corresponding to magnetic fields of 0.4 T and 0.85 T. These points differ by the observation angles, of respectively 3 and 9 mrad from the entrance of the magnet.

Energy	[GeV]	6.04
Maximum current	[mA]	200
Horizontal emittance	[nm]	4
Vertical emittance	[pm]	4
Revolution frequency	[kHz]	355
Number of bunches		1 to 992
Time between bunches	[ns]	2.82 to 2816

Table 1: Principal characteristics of the electron beam.

Electron beam profiles are Gaussian and the size and divergence are presented in terms of rms values. The associated full width at half maximum sizes and divergences are 2.35 times higher. Horizontal electron beam sizes and divergences are given for the multibunch filling modes and apply to almost all filling patterns, except when the current per bunch is larger than 4.5 mA, for which a slightly larger size and divergence are attained because of the increased energy spread of the electron beam.

Vertical electron beam sizes and divergences are given for a vertical

		Even ID (ID2, ID6...)	Odd ID (ID1, ID3...)	Even BM (ID2, ID6...) 3 mrad	Even BM (ID2, ID6...) 9 mrad	Odd BM (ID1, ID3...) 3 mrad	Odd BM (ID1, ID3...) 9 mrad
Magnetic field	[T]	Variable	Variable	0.4	0.85	0.4	0.85
Horiz. Beta function	[m]	37.6	0.35	1.33	1.06	2.12	1.61
Horiz. Dispersion	[m]	0.134	0.031	0.062	0.051	0.089	0.075
Horiz. rms e- beam size	[µm]	413	50	99	85	132	113
Horiz. rms e- divergence	[µrad]	10	107	116	114	104	99
Vert. Beta function	[m]	2.95	2.97	41.7	42.0	32.1	32.2
Vert. rms e- beam size	[µm]	3.4	3.4	12.9	13.0	11.3	11.4
Vert. rms e- divergence	[µrad]	1.17	1.16	0.50	0.50	0.36	0.36

Table 2: Beta functions, dispersion, rms beam size and divergence at the various source points.

emittance of 4 pm, which is now the standard for 2 x 1/3 and 7/8+1 filling modes. The vertical sizes and divergences are about 1.4 times larger in uniform filling mode (due to ion effects, which are partially corrected by the use of a vertical bunch-by-bunch feedback). To increase the lifetime of the stored beam, the vertical beam sizes and divergences are deliberately increased by about a factor of 4 in the 16-bunch, 4-bunch and hybrid filling patterns.

The lifetime, bunch length and energy spread mainly depend on the filling pattern. These are given in **Table 3** for a few representative patterns. Note that in 16-bunch and 4-bunch filling patterns, the energy spread and bunch length decay with the current (the value indicated in the table corresponds to the maximum current). The bunch lengths are given for the usual radiofrequency accelerating voltage of 9 MV (8 MV for 16-bunch and 4-bunch).

Filling pattern		Uniform	7/8 + 1	Hybrid	16-bunch	4-bunch
Number of bunches		992	870+1	24x8+1	16	4
Maximum current	[mA]	200	200	200	90	40
Lifetime	[h]	50	45	30	16	9
Rms energy spread	[%]	0.11	0.11	0.11	0.12	0.16
Rms bunch length	[ps]	20	20	25	48	55

Table 3: Current, lifetime, bunch length and energy spread for a selection of filling modes.

SUMMARY OF ACCELERATOR OPERATION

Last year was a record-breaking year for accelerator operation, seeing 5399.20 out of 5487.5 planned hours of beam delivered to Users in 2014 (excluding shifts for radiation and personal safety system tests). This excellent figure represents an accelerator availability of 99.11%, which beats the all-time ESRF record of 99.04% in 2009. This was achieved through a rapid resolution of failures, of which only a few were significant long failures. The longest of these was in May and lasted just over four hours.

Similarly, the mean time between failures (MTBF) of 105.5 hours is the second best MTBF ever obtained at the ESRF (the record is 107.8 hours in 2011). In April, during the second

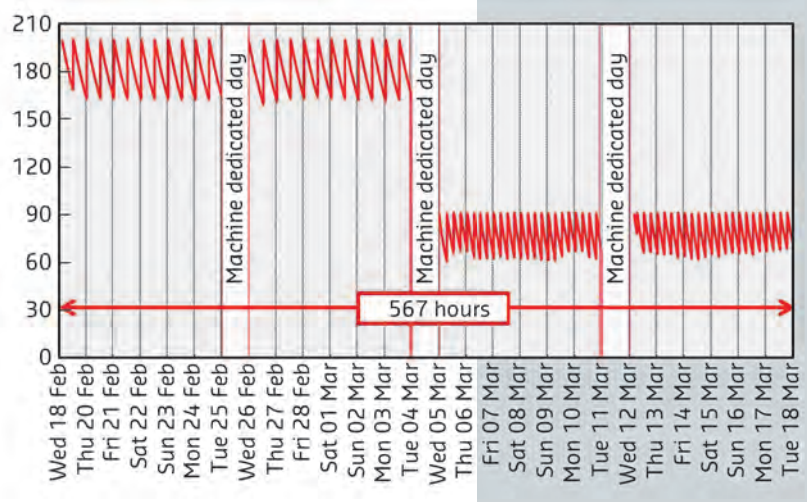

Fig. 158: Uninterrupted beam delivery for 567 hours in 7/8+1 and 16-bunch filling modes during weeks 5, 6, 7 and 8 (RUN 2014-01).

RUN NUMBER	2014-01	2014-02	2014-03	2014-04	2014-05	TOTAL 2014
Start	17/01/2014	28/03/2014	06/06/2014	22/08/2014	17/10/2014	
End	19/03/2014	27/05/2014	30/07/20147	08/10/2014	17/12/2014	
Total number of shifts	183	180	162	141	183	**849**
Number of USM shifts	146.44	147	131.13	113.25	148.13	**685.94**
Beam available for users (h)	1158.70	1153.30	1031.50	892.40	1163.30	**5399.20**
Availability	**99.50%**	**98.95%**	**98.87%**	**99.38%**	**98.90%**	**99.11%**
Dead time for failures	0.5%	1.1%	1.1%	0.6%	1.1%	**0.89%**
Dead time for refills	0.6%	0.9%	0.5%	0.9%	0.7%	**0.72%**
Average intensity (mA)	153	133	179	99	151	**95.4**
Number of failures	10	14	10	9	9	**52**
Mean time between failures (h)	117.2	84	104.9	100.7	131.7	**105.5**
Mean duration of a failure (h)	0.6	0.9	1.2	0.6	1.4	**0.94**

Table 4: Overview of storage ring operation in 2014.

run of the year, six beam trips during the same week reduced the MTBF. This was due to an unfortunate series of events. Once these problems had been solved, a noticeable absence of repetitive events (especially during Runs 1, 3 and 5 when the MTBF greatly exceeded 100 hours) resulted in 14 out of 37 weeks where beam was delivered without any interruptions, including one period of four weeks (see **Figure 158**) and two periods of 288 hours (*i.e.* two consecutive weeks) without a single beam interruption. A summary of operation is presented in **Table 4**.

FILLING PATTERNS

The distribution of filling modes (**Figure 159**) has not drastically evolved over the last four years, since the 7/8+1 filling mode was introduced. This mode remains the best compromise for users who need intensity and/or time-structure. The uniform mode remains mainly for the specific experiments on one beamline.

During machine-dedicated time, several shifts were carried with participation of the beamlines to assess top-up in 16-bunch mode, testing refills every 10, 20 and 30 minutes. Many scientists expressed their enthusiasm thanks to the excellent results obtained. More details are presented in a later section.

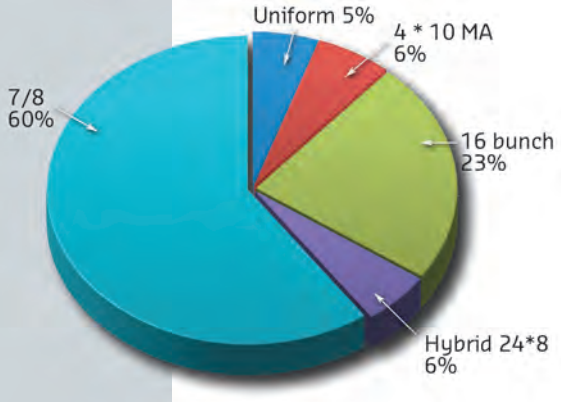

Fig. 159: Distribution of filling modes in 2014.

COMPLETION OF THE TECHNICAL DESIGN STUDY FOR THE NEW STORAGE RING

In 2014, the ASD completed the technical design study (TDS) of the Phase II Accelerator Upgrade. The upgrade is focused on greatly improving the brightness of the source by decreasing the natural horizontal equilibrium emittance of the storage ring from the current 4 nm to about 134 pm. This will be possible by replacing the present 32 double-bend achromat arcs with a much more compact lattice based on a hybrid 7-bend arc achromat (**Figure 160**). The smaller emittance, together with a shorter-period, smaller-gap undulators and new beamline optics, optimised to take full advantage of the new source, will allow a general improvement in performance by a factor of 100 or more.

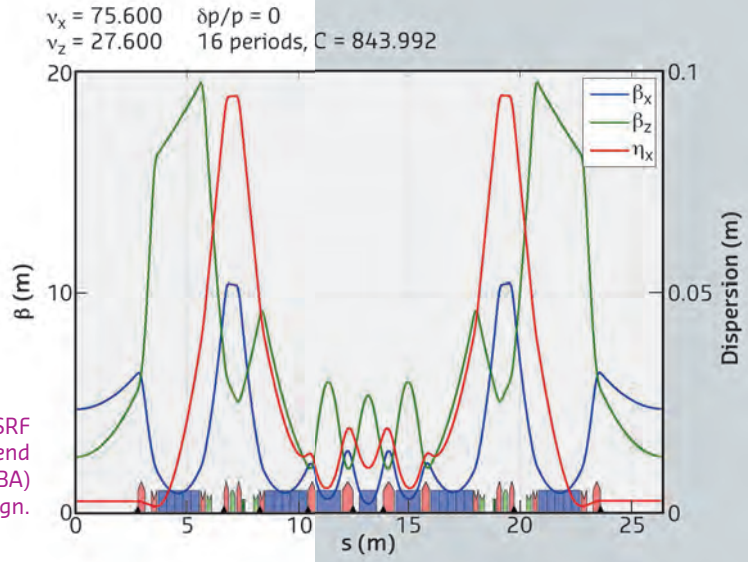

Fig. 160: The ESRF hybrid multi-bend achromat (HMBA) lattice design.

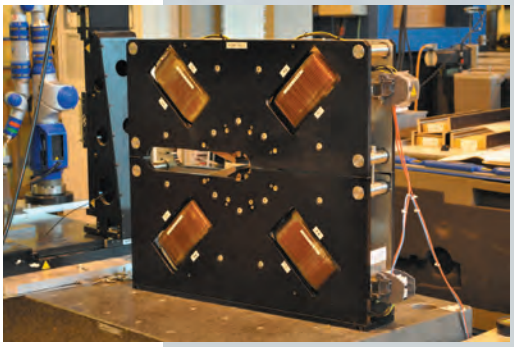

Fig. 161: The prototype octupole for the new lattice, delivered in October 2014.

The sources for the bending magnet beamlines will be replaced by three-pole wigglers, resulting in a comparable increase in brightness and flexibility of the X-ray spectra for these beamlines too. The lattice and the engineering designs are well advanced and the magnetic designs are already at the prototyping stage. A prototype octupole was delivered in October 2014 (see **Figure 161**). Two prototypes of the permanent magnet dipoles with longitudinal gradients have been constructed and a third is planned for 2015. A high-gradient quadrupole prototype is currently under construction and prototypes for a combined dipole-quadrupole and a sextupole are foreseen for 2015. The first magnetic designs for the correctors have been completed and the engineering designs will be done in 2015.

In May 2014, the Accelerator Project Advisory Committee (APAC), appointed by the Council, reviewed and produced a very positive report on the overall feasibility of the project. The TDS, together with their report was submitted to the June meeting of the Council, which subsequently gave its approval to the project. The execution phase was officially launched on 1st January 2015.

PERMANENT MAGNET DIPOLES FOR THE ACCELERATOR UPGRADE

The new magnet lattice for the accelerator upgrade includes 128 dipoles with longitudinal field gradients contributing to the reduction of the horizontal emittance of the electron beam. The use of permanent magnet technology was found to be suitable for building these dipoles for compactness and economical reasons. Each dipole magnet consists of a series of five short

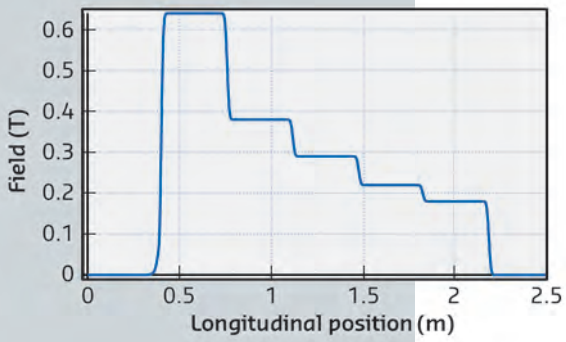

modules with different field amplitudes, ranging from 0.65 T to 0.17 T (see **Figure 162**).

Fig. 162: Typical magnetic field along a dipole with a longitudinal field gradient.

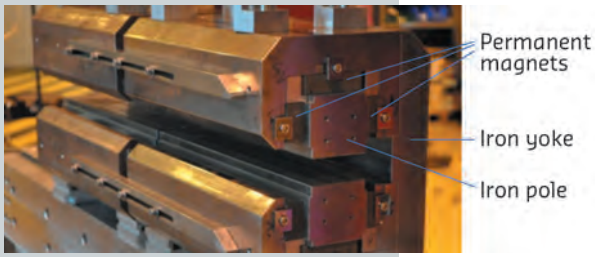

Fig. 163: Prototype dipoles with longitudinal field gradient under study (two modules).

The Sm2C017 permanent magnet material was chosen to ensure adequate temperature stability and long-term stability with respect to radiation-induced demagnetisation. The development of permanent magnet structures was initiated in 2013-2014 with the construction of several types of modules. Each module has a length of 350 mm and a transverse size of 190 mm (horizontal) and 240 mm (vertical) with a typical weight of 85 kg. The magnetic structure is based on a C-shape design with solid iron poles and a yoke driving the magnetic field from permanent magnets in the 25 mm gap. **Figure 163** shows an assembly of two modules under study. The magnetic measurement results are in very good agreement with the simulation.

PROGRESS IN THE TOP-UP OPERATION PROJECT

To reduce the heat load variation on the beamline optics, the implementation of top-up operation is under preparation. This mode of operation will be beneficial for the 16-bunch mode by reducing the current variation and also by allowing delivery at low vertical emittance. A new cleaning technique has been developed for this project and is now routinely used during user service mode (USM) for the 16bunch and hybrid modes. This reduces the strong vertical blow-up just after injection from 2 nm to only a few pm. The development of bunch cleaning in the booster is progressing and will benefit from the upgrade of the injector, in particular, the new booster power supply system operating at 4 Hz, which is under development for the dipole and quadrupole magnets.

Top-up in 16-bunch mode has been tested successfully (**Figure 164**). The reliability of the storage ring was validated with 90 mA average current in 16bunch mode, refilled every 10 minutes over a period of several hours, with no disturbance; all parameters were even more stable in this configuration. Radioprotection aspects are satisfactory (injection is routinely performed with the front end open) but a formal agreement from the authorities for such operation in USM is still needed. Large horizontal orbit perturbations are still being induced during injection, mainly by the injection kickers and injection septa. Solutions using feed-forward corrections have been successfully developed and should be implemented for routine operation (see dedicated paragraph). An injection sequencer has been developed in order to automatically manage the equipment and to optimise electrical consumption. Using this tool, injection is now done in top-up in less than 30 seconds.

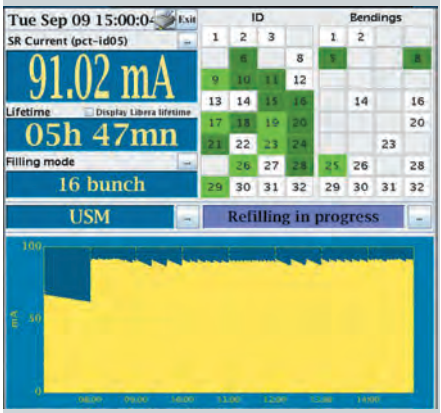

Fig. 164: Synopsis of eight hours of top-up tests with beamlines in September 2014.

The top-up frequency is a crucial parameter for this project. The first top-up tests with users at the beamlines were carried out in September 2013 and May 2014 in 16-bunch mode, with a refill every 5, 10, 20 and 30 minutes. The main feedback from the beamlines was that it had not been possible to move the mechanics during the top-

up sequences, preventing them from taking maximum advantage from top-up operation. This was due to a restriction on an ID device server, which was then removed in time for the next tests.

In September, a third top-up shift – also in 16-bunch mode – was carried out with 23 beamlines. This time it had been possible for the beamlines to move their mechanics and the lowest gap of 6 mm was obtained at ID09 and ID11 in-vacuum devices, while ID15 obtained 6.5 mm. The beamline feedback was positive, showing a general improvement in the stability of all the X-ray beam parameters. The beamlines could be operated without interruption during injections and were unable to detect the exact moment when refills had been carried out.

Nevertheless, detailed analysis and tests still have to be completed for the most sensitive beamlines. Further user tests are planned for early 2015. There remains much to do in order to ensure reliability of equipment before top-up operation can be put into routine service but the benefits for most users are clear.

NEW STORAGE RING BPM PROTOTYPES TESTED WITH BEAM

The development of 6 mm-button UHV feed-throughs is making very good progress; a total of 27 buttons were delivered in the spring and tested successfully. During the August 2014 shutdown, a test beam position monitor (BPM) chamber was installed in the ID25 straight section (**Figure 165**). Three BPMs were connected to the Libera BPM electronics and the test BPM chamber itself placed on a motorised translation table allowing +/-3 mm displacement in both planes, to enable RF signals to be checked with stored beam and to carry out detailed verification of the beam position measurements obtained. A second chamber with different buttons will shortly be installed and tested.

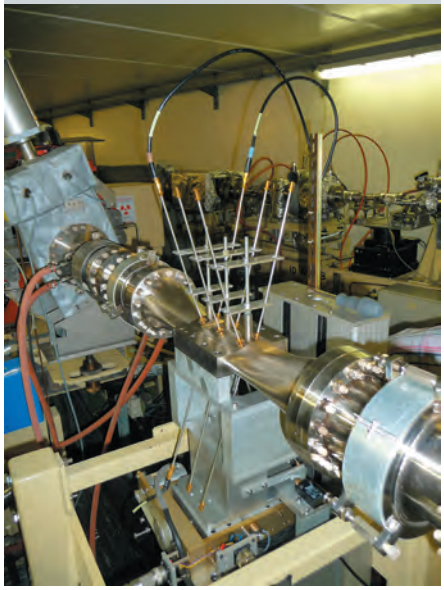

Fig. 165: The test BPM chamber installed at ID25.

NEW BOOSTER BPM ELECTRONICS

Following the goal to modernise the 25-year-old electronics for the RF signal acquisition and processing of the booster BPM system, two prototypes, called Libera Spark, have been tested under various beam filling modes in the booster and they have shown their potential for precise beam position monitoring. After satisfactory testing, a contract for the delivery of a further 81 units was signed and these were delivered in November 2014. The installation of these Sparks in the booster has now started and 10 units were successfully commissioned in December. The full conversion to the new BPM system is expected to be finished by the end of February 2015. An agreement has been reached on specifications and a price for an advanced version of this device that opens up various applications in the injector and the storage ring.

NEW VERTICAL BEAM HALO MONITOR

The halo monitor measures the electron population along the vertical beam profile at 0.5 mm to 6 mm from the central core of the electron beam, using X-rays emitted from the first dipole in cell 7. Following initial commissioning at the beginning of the year, the halo monitor was further optimised with more rigorous lead shielding for its detector and the choice of CMOS camera technology, which has greater resistance to radiation. The tungsten blade has also been modified to give more calibration possibilities. A device server records halo measurements at a frequency of 1 Hz and stores them in a database (**Figure 166**). Such recordings show the very strong sensitivity of this diagnostic device to vacuum conditions and to any variation of Touschek scattering conditions. It is a new and novel addition to our range of diagnostic instruments dedicated to electron beam loss phenomena.

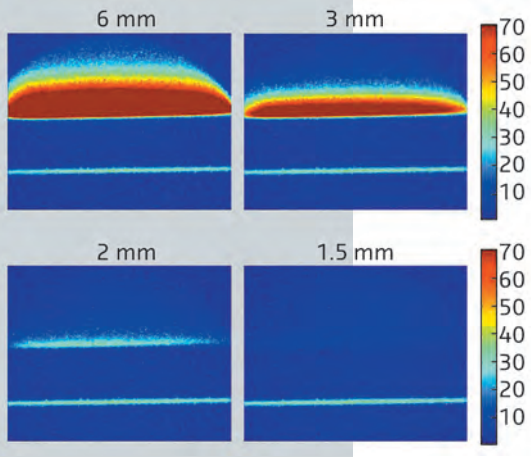

Fig. 166: Images from the halo monitor for four vertical scraper positions. In the lower part of each image, one can observe that the beam core is shielded while the halo signal disappears progressively.

NEW PICOSECOND TIME-RESOLUTION STREAK CAMERA

The new visible light streak camera was delivered to the ASD optical laboratory in January 2014. The results obtained from various tests were satisfactory and in line with the theoretically predicted shortest bunch length at zero bunch current. Since its installation, the Streak camera has been used in several MDT studies, such as HOM instability and also for beam dynamics studies relating the RF voltage to beam phase, bunch length and lifetime. After initial setup for each experiment, the streak camera can be controlled and read from the control room.

NEW BUNCH CLEANING METHOD FOR THE BOOSTER

A new method of time-gated cleaning was implemented in 2013, using the bunch-by-bunch feedback system. However, since cleaning is performed after injection into the storage ring, it won't be compatible with the future top-up mode of operation, as the time interval between injections will become much smaller. Therefore, in 2014, a new system was implemented

to perform bunch cleaning 5 to 10 milliseconds after injection in the booster. This has been upgraded by the addition of a system generating the excitation frequency of the parasitic bunches more accurately. Now that the transverse resonant frequency of the beam is tracked precisely, the cleaning efficiency should be stable at each injection. Measurements taken in the autumn of the efficiency of the booster cleaning showed that adequate cleaning is generally achieved for most injection shots. Future work will aim to increase the reproducibility of the system.

DAMPING OF THE HORIZONTAL OSCILLATION OF THE STORAGE RING STORED BEAM CAUSED BY INJECTION

The firing of the pulsed magnets of the injection system (kickers and septum) is the cause of horizontal and vertical transient orbit distortion or beam position oscillation. Various factors contribute to this disturbance including non-closure of the injection bump during kicker rise and fall, a slight tilt of the kickers, septum magnet field leakage and asymmetry. The horizontal disturbance is the largest, but is expressed in the relative increase of the beam emittance, whereas the vertical disturbance is more significant since the vertical nominal emittance is much smaller. Solutions are underway to tackle each source of disturbance.

We have implemented a system that damps the horizontal betatron oscillation by applying a correction signal over nine turns using a 0.6 MHz bandwidth magnet driven by a 400 W amplifier. The system was tested at the end of 2013 and proved to be effective, dividing the amplitude of the horizontal betatron oscillation induced during the rise and fall time of the kickers by three (**Figure 167**).

At the end of 2014, an orbit correction system cancelling the horizontal orbit distortion caused by the septum leakage was also implemented, using a set of fast corrector magnets and amplifiers that were originally part of the old fast orbit correction system. A signal with the same shape as the beam position signal recorded when the correction was not active was used to drive the amplifier input in a feed-forward scheme. The first test of the system demonstrated a very effective cancellation of this orbit distortion (**Figure 168**). A similar set of vertical correctors was added during the December 2014 shutdown and the system will be operated in USM in 2015.

We aim to suppress the vertical betatron oscillation due to the kickers' tilt by mechanically trimming the tilt of the kickers according to the result of turn-by-turn position measurements done following the firing of the kickers. A first set of tilt corrections will be applied during the shutdown in January 2015.

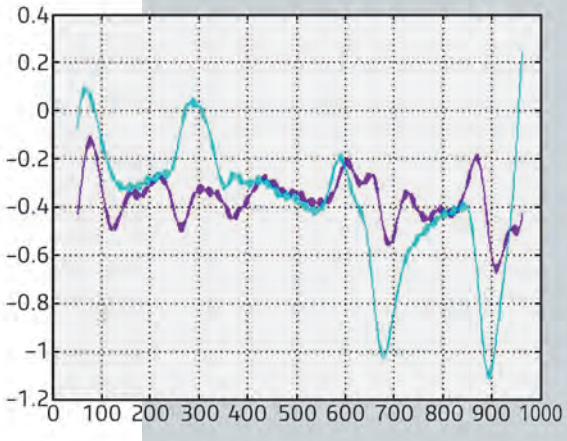

Fig. 167: Non-damped (purple) versus damped (blue) horizontal oscillations over turn 7 to turn 10 after injection, for all bunches, showing the effect of the feed-forward damping.

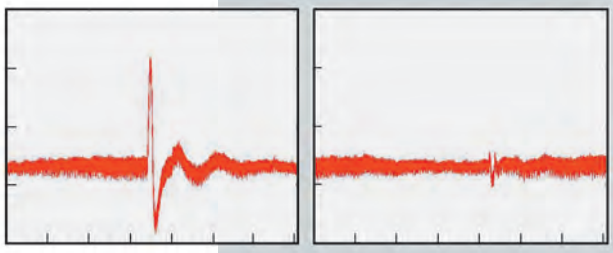

Fig. 168: Effect of the septum field leak on the horizontal beam position without (left) and with (right) the orbit correction system activated. Scale: Vertical: 0.5 mm/div, Horizontal: 10 ms/div.

UPDATE ON THE NEW HOM-DAMPED CAVITIES IN THE STORAGE RING POWERED BY 150 kW RF SOLID STATE AMPLIFIERS

In 2013, three new RF HOM-damped cavities were installed in cell 23, the last being put in place during the December shutdown and powered in January 2014. The first two cavities performed well throughout 2014. They were operated in USM at the nominal voltage of 0.5 MV with 80 kW input power at a stored beam current of 200 mA. During machine studies, these cavities were tested with up to 150 kW incident power by increasing their voltage to 0.65 MV and adjusting their phase to increase their beam loading. Following the discovery of an air leak in the third cavity, it was removed from the ring for repair in December 2014. The manufacture of 12 additional HOM-damped cavities by RI is progressing well and the delivery is foreseen during the course of 2015.

The four 150 kW solid state amplifiers (SSAs) installed in the booster in 2012, and the three SSAs installed in the storage ring in 2013, are all performing well. In October 2014, the supplier retrofitted the four booster SSAs with non-flame-propagating cables, bringing them in line with the three storage ring SSAs.

The implementation of the in-house 75 kW prototype RF SSA, which uses a cavity combiner to combine the power from 132 ESRF-developed 700 W RF power modules, is in progress. This came within the remit of work package WP7 of the EU/CRISP project, which ended in September 2014. Over the course of the project, it was decided to develop an integrated system comprising fully planar RF circuits that are coupled directly to the cavity combiner instead of connecting existing RF modules available from industry by means of coaxial cables. This resulted in an extremely compact solution that will allow cost effective industrial production. A 12 kW prototype with 18 connected modules was successfully tested, and power tests of the 75 kW prototype are scheduled for the second half of 2015.

ID STRAIGHT SECTIONS

The required undulator segments for the upgrade of ID1 have been installed and are in operation. The new 2.5 m-long helical undulator will be installed in March 2015 in the ID32 straight section. Most of the work is now focused on ID31 and ID15. A high-performance cryogenic permanent magnet undulator is under construction at ID31. The undulator will be installed in the middle of the 5 m-long straight section to reach a minimum gap of 4.5 mm. Its installation will take place before mid-2015. At ID15, the straight section will be modified with a canting scheme in 2015. A required short, high-field wiggler has been designed and the associated components are under procurement. The modification of the straight section and a new insertion device layout will be completed before the end of 2015.

MEMBERS AND ASSOCIATE COUNTRIES

(AS OF JANUARY 2015)

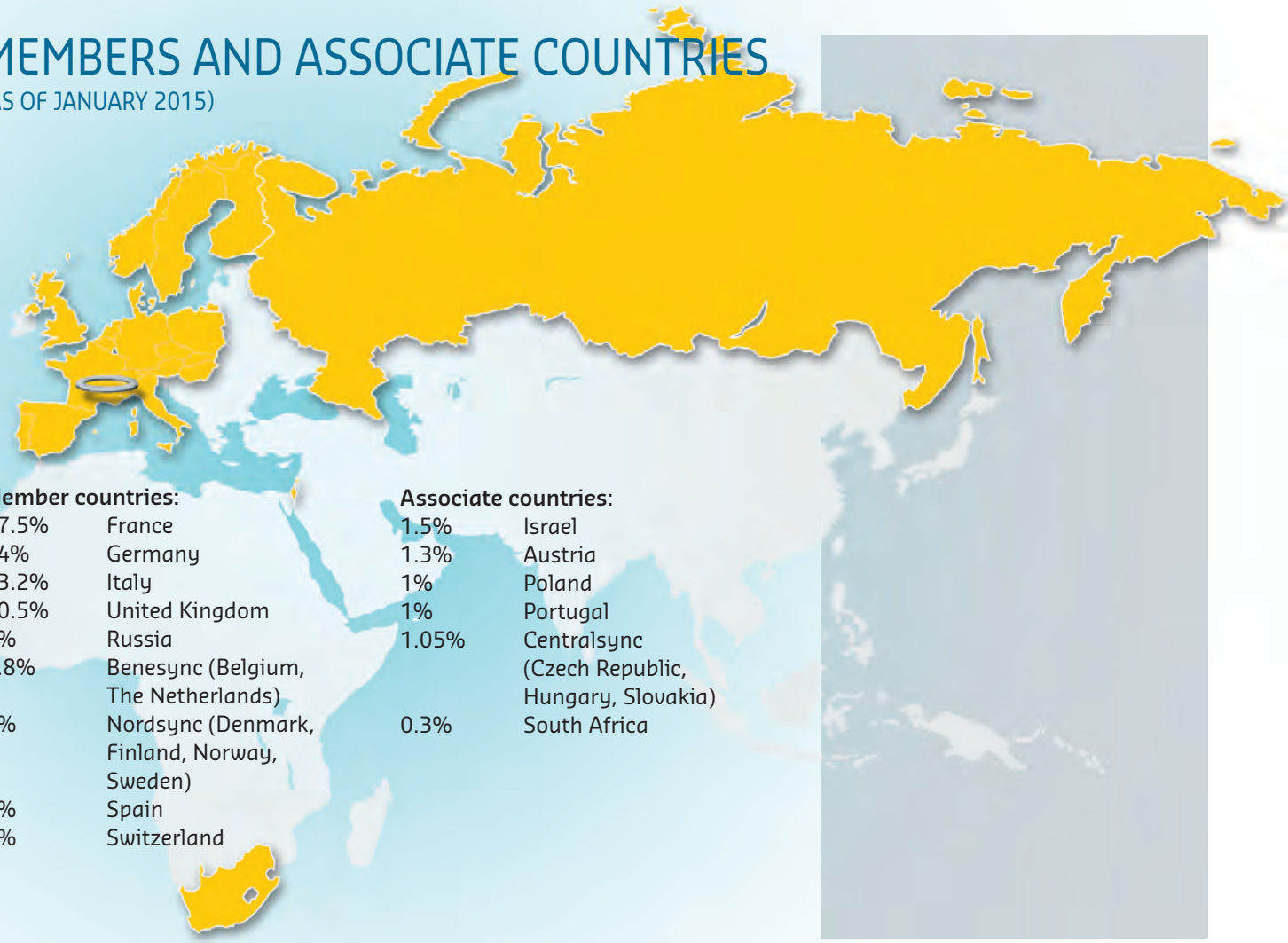

Member countries:

27.5%	France
24%	Germany
13.2%	Italy
10.5%	United Kingdom
6%	Russia
5.8%	Benesync (Belgium, The Netherlands)
5%	Nordsync (Denmark, Finland, Norway, Sweden)
4%	Spain
4%	Switzerland

Associate countries:

1.5%	Israel
1.3%	Austria
1%	Poland
1%	Portugal
1.05%	Centralsync (Czech Republic, Hungary, Slovakia)
0.3%	South Africa

THE BEAMLINES

Details of the public ESRF beamlines as well as those operated by Collaborating Research Groups (CRG) are given in **Tables 5** and **6**. **Figure 169** shows the location of the beamlines in the experimental halls.

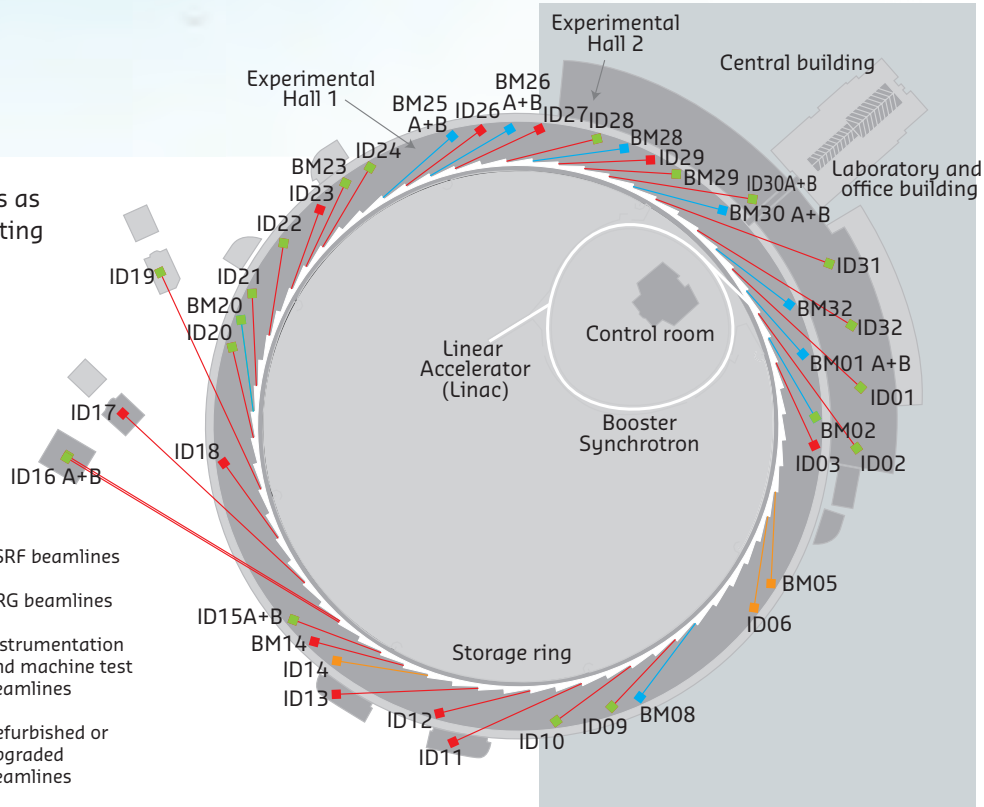

Fig. 169: Experimental hall showing location of the beamlines (public and CRG beamlines).

SOURCE POSITION	NUMBER OF INDEPENDENT END-STATIONS	BEAMLINE NAME	STATUS	
ID01	1	Microdiffraction imaging	Operational	since 12/14
ID02	1	Time-resolved ultra-small-angle X-ray scattering	Operational	since 07/14
ID03	1	Surface diffraction	Operational	since 09/94
ID06	0.3	Large volume press	Operational	since 10/13
ID08	1	Dragon	Closed	since 10/13
ID09	1	White beam	Operational	since 09/94
ID10	1	Soft interfaces and coherent scattering	Operational	since 06/12
ID11	1	Materials science	Operational	since 09/94
ID12	1	Circular polarisation	Operational	since 01/95
ID13	1	Microfocus	Operational	since 09/94
ID15A	1	High energy diffraction	Closed	since 01/15
ID15B	1	High energy inelastic scattering	Closed	since 01/15
ID16A	1	Nano-imaging	Operational	from 05/14
ID16B	1	Nano-analysis	Operational	from 04/14
ID17	1	Medical	Operational	since 05/97
ID18	1	Nuclear scattering	Operational	since 01/96
ID19	1	Topography and tomography	Operational	since 06/96
ID20	1	Inelastic X-ray Scattering	Operational	since 06/13
ID21	1	X-ray microscopy / IR Spectroscopy	Operational	since 12/97
ID22	1	High resolution powder diffraction	Operational	since 05/14
ID23	2	Macromolecular crystallography MAD	Operational	since 06/04
		Macromolecular crystallography microfocus	Operational	since 09/05
ID24	1	Dispersive EXAFS	Operational	since 02/96
ID26	1	X-ray absorption and emission	Operational	since 11/97
ID27	1	High pressure	Operational	since 02/05
ID28	1	Inelastic scattering II	Operational	since 12/98
ID29	1	Multiwavelength anomalous diffraction	Operational	since 01/00
ID30A	1	Macromolecular crystallography	Operational	since 12/4
ID31	1	Powder diffraction	Closed	since 01/14
ID32	1	Soft X-ray spectroscopy	Operational	since 11/14
BM14	1	Macromolecular crystallography (MAD)	Operational	since 01/10
BM23	1	X-ray absorption spectroscopy	Operational	since 03/11
BM29	1	Bio SAXS	Operational	since 06/12
Operational in 2015:				
ID30B	1	Macromolecular crystallography	Operational	from 01/15
ID31	1	High energy	Operational	from 08/15

Table 5: List of the ESRF public beamlines.

SOURCE POSITION	NUMBER OF INDEPENDENT END-STATIONS	BEAMLINE NAME	FIELD OF RESEARCH	STATUS
BM01	2	Swiss-Norwegian BL	X-ray absorption & diffraction	Operational since 01/95
BM02	1	D2AM (French)	Materials science	Operational since 09/94
BM08	1	Gilda (Italian)	X-ray absorption & diffraction	Operational since 09/94
BM20	1	ROBL (German)	Radiochemistry & ion beam physics	Operational since 09/98
BM25	2	SPLINE (Spanish)	X-ray absorption & diffraction	Operational since 04/05
BM26	2	DUBBLE (Dutch/Belgian)	Small-angle scattering	Operational since 12/98
			EXAFS	Operational since 06/01
BM28	1	XMAS (British)	Magnetic scattering	Operational since 04/98
BM30	2	FIP (French)	Protein crystallography	Operational since 02/99
		FAME (French)	EXAFS	Operational since 08/02
BM32	1	IF (French)	Interfaces	Operational since 09/94

Table 6: List of the Collaborating Research Group beamlines.

USER OPERATION

Following 20 years of successful operation for scientific users (September 1994 to September 2014), we look back on user operation at the facility over the past year 2014. The ESRF has been back in full user operation for the majority of users since 2013, but Phase I of the Upgrade Programme continues and several beamlines were either fully or partially closed during 2014 for upgrade. ID01 (UPBL1) and ID32 (UPBL7) were closed for almost the whole year, taking their first user experiments in December 2014; ID31 has been closed for upgrade for the whole year and the new upgrade beamline ID22 opened in May 2014 (UPBL2); ID02 (UPBL9a) was re-opened more than half way through the year while new beamlines ID16A-NI and ID16B-NA were also only partially open (UPBL4); ID14 closed and one of the new MX beamlines, ID30A-1, opened half way through the year (UPBL10). In total, the equivalent of around 23.3 ESRF publicly funded beamlines (out of an optimum of 29.5 in the portfolio) and 9 CRG beamlines were available for users in 2014. **Figure 170** shows the number of applications for beamtime received since 2008. Despite the heavy construction programme and the unavailability of a non-negligible number of beamlines, 2014 saw the highest ever number of proposals submitted to the ESRF in its history. This shows that the user interest in the ESRF has not diminished in any way and is, at the moment, even stronger than in the past.

Proposals for experiments are selected and beamtime allocations are made through peer review. As in previous years, beamtime for 2014 was allocated based on recommendations made by review committees of specialists, for the most part from European countries, Israel and South Africa. A new structure has been in place since 2013 for the proposal review process, with beamline-based committees allowing all proposals received for a particular beamline to be assessed by the same review committee. This gives the committees a better overall view of all the projects proposed for a single beamline, and allows them greater flexibility to optimise the selection of proposals awarded beamtime for each beamline. Proposals for experiments in 2014 were reviewed by 10 review committees grouping the following beamlines of similar techniques or activities:

- C01 (ID01, ID03, BM25B, BM32)
- C02 (ID11, ID15A, ID15B, ID22)
- C03 (ID12, ID20, ID26, ID32, BM28)
- C04 (ID24, BM01B, BM08, BM20, BM23, BM25A, BM26A, BM30B)
- C05 (ID06-LVP, ID09A, ID18, ID27, ID28, BM01A)
- C06 (ID17, ID19)
- C07 (ID16A&B, ID21)
- C08 (ID02, ID13, BM26B)
- C09 (ID09B, ID10, BM02)
- C10 (Structural Biology Beamlines).

The scientific areas of the ESRF research activities reviewed by these ten committees are shown in **Table 7**.

In September 2014, an 11th review committee C11 was created and the beamlines reviewed by committees C03 and C04 were redistributed so that some of those beamlines are now reviewed by C11. This modification concerns beamtime allocation for 2015 and so will be described in more detail in next year's report concerning 2015 operation.

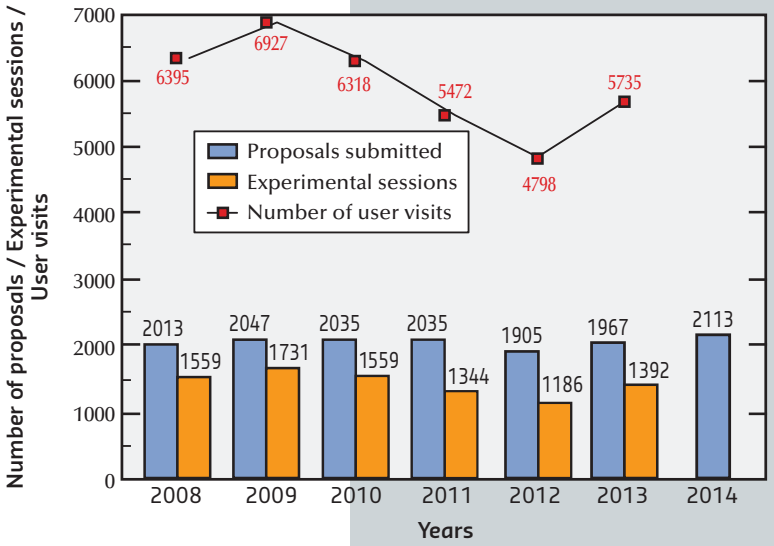

Fig. 170: Numbers of applications for beamtime, experimental sessions and user visits, 2008 to 2014. N.B. Final numbers of experimental sessions and user visits for 2014 were not available at the time of going to press.

Table 7: Number of shifts of beamtime requested and allocated for user experiments, year 2014.

Scientific field	Total shifts requested	Total shifts allocated
Chemistry	4 338	1 775
Earth Sciences	1 835	819
Environment	832	249
Hard Condensed Matter Science	9 380	3 165
Cultural Heritage	332	144
Life Sciences	1 423	549
Applied Materials Science	5 055	1 652
Medicine	1 058	465
Engineering	237	117
Methods & Instrumentation	492	201
Structural Biology	3 061	2 077
Soft Condensed Matter	3 157	1 077
Totals	**31 200**	**12 290**

The review committees met twice during the year, around six weeks after the deadlines for submission of proposals (1 September 2013 and 1 March 2014). They reviewed 2113 applications for beamtime, and selected 864 (40.9%), which were then scheduled for experiments.

Requests for beamtime in 2014, which is scheduled in shifts of 8 hours, totalled 31 200 shifts or 249 600 hours, of which 12 290 shifts or 98 320 hours (39.4%) were allocated. The distribution of shifts requested and allocated, by scientific area, is shown in **Table 7**.

The breakdown of shifts delivered for experiments by scientific area in the first half of 2014 is shown in **Figure 171**. This same period saw 2667 visits by scientists to the ESRF under the user programme, to carry out 643 experiments. Overall, the number of users in each experimental team averaged just over 4 persons as in all previous years, and the average duration of an experimental session was 9 shifts. This can be further broken down to show an average duration of 3 shifts for MX experiments and 14 shifts for non-MX experiments. The annual number of experimental sessions and user visits since 2008 is shown in **Figure 170**. The effect of the reduction in beamtime available in 2011 and 2012 due to the long shutdown is clearly visible, and even though the figures for 2013 show the return to something close to pre-shutdown user operation, the unavailability of the remaining upgrade beamlines due to the ongoing Phase I programme means that, for the time being, the number of experimental sessions and user visits is still slowly growing back towards its optimum level. This will also be the case for 2014 due to the upgrade beamline work listed at the beginning of this report, but once all beamlines are running towards the end of 2015 the trends suggest that we may return to a higher level of usage than before, despite the permanent closure of two beamlines since 2010.

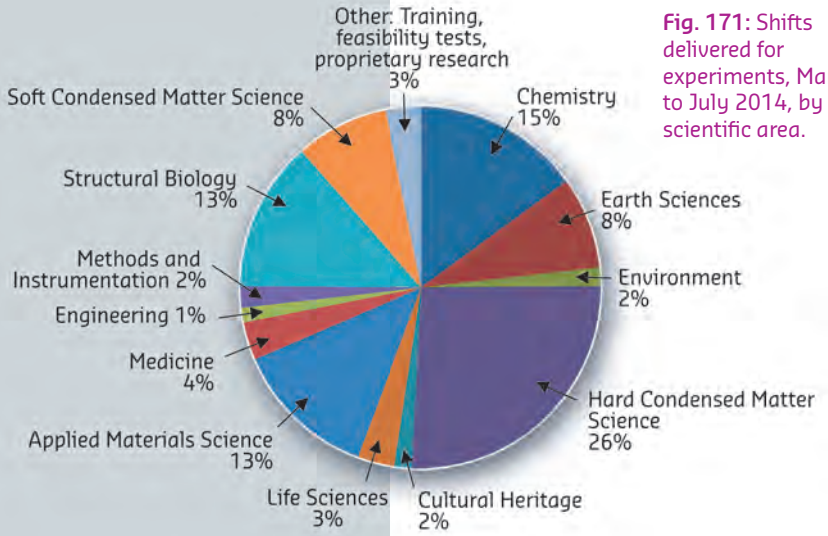

Fig. 171: Shifts delivered for experiments, March to July 2014, by scientific area.

One of the new upgrade beamlines that came online in 2014 is MX beamline ID30A-1, also known as MASSIF-1, which is the first beamline in Europe to offer fully automatic hands-off screening and data collection for structural biology. Users do not come to the beamline but instead send their samples, which are automatically analysed. This analysis can include the collection of full diffraction datasets, and is carried out based on information supplied by the user via the ISpyB LIMS for structural biology beamlines.

One of the principle measurable output parameters of the ESRF is the number and quality of publications accepted in peer-reviewed journals. The number of publications rose continuously over the past years to reach a plateau of just under 1900 publications per year, corresponding to the maximum operation level of the ESRF before the Upgrade Programme, as shown in **Figure 172**. Despite the 6 month shutdown between 2011 and 2012 for the construction of the new EX2 experimental hall, the number of publications has not fallen in any significant way. These are excellent figures, with a publication output

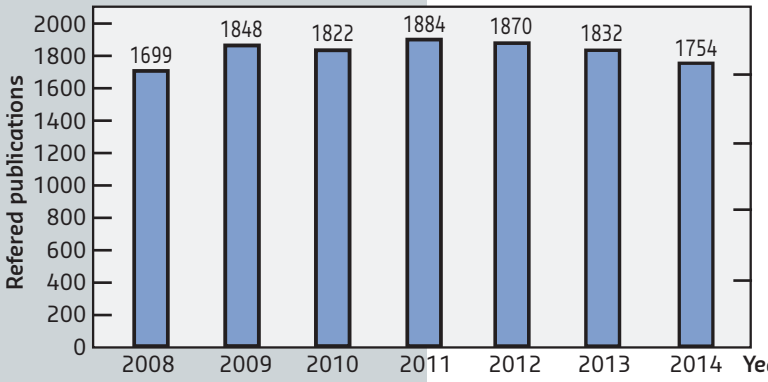

Fig. 172: Numbers of publications appearing in refereed journals reporting on data collected either partially or totally at the ESRF, 2008 to 2014.

systematically on a level of well over one publication per experimental session. The year 2014 promises to be highly fruitful, with 1754 publications registered so far in the ILL/ESRF Library database, which is higher than the 2013 figure at this same time last year. Since the ESRF began user operation back in 1994, a total of 25148 publications have been accepted in peer-reviewed journals. Of these, nearly 300 every year are published in high impact factor journals.

User responses to questionnaires show once again that the ESRF continues to maintain its excellent reputation concerning the assistance and service given by scientists and support staff on beamlines, and travel and administrative arrangements, in addition to the quality both of the beam and of the experimental stations. Facilities on site, such as preparation laboratories, the Guesthouse and a canteen open 7 days a week, also make an important contribution to the quality of user support.

ADMINISTRATION AND FINANCE

Expenditure and income 2013

Expenditure		kEuro	Income	kEuro
Accelerator and Source			2013 Members' contributions	84 981.0
Personnel		6 181.0	Funds carried forward from 2012	843.0
Recurrent		1 801.1	Building costs provision	1000.0
Operating costs	*1 723.4*		Other income	
Other recurrent costs	*77.7*		Scientific Associates	5 408.0
Capital		5 366.0	Sale of beamtime	1 588.0
Accelerator and Source developments	*5 366.0*		Compensatory funds	2 005.0
Beamlines, experiments and in-house research			Scientific collaboration and Special projects	8 232.0
Personnel		18 232.3	Pre-financing	4 744.0
Recurrent		5 716.1	Pre-financing carried forward to 2014	5 560.0
Operating costs	*1 462.5*			
Other Recurrent costs	*4 253.6*			
Capital		13 698.9		
Beamline developments	*13 695.6*			
Beamline refurbishment	*3.3*			
Technical and administrative supports				
Personnel		28 562.5		
Recurrent		12 220.7		
Capital		16 498.1		
Industrial and commercial activity				
Personnel		428.9		
Recurrent		68.7		
Unexpended committed funds				
Funds carried forward to 2014		5 586.0		
Total		**114 360.0**	**Total**	**114 360.0**

Revised expenditure and income budget for 2014

Expenditure		kEuro	Income	kEuro
Accelerator and Source			2014 Members' contributions	86 863
Personnel		6 193	Funds carried forward from 2013	5 586
Recurrent		1 546	Building costs provision	315
Operating costs	*1 466*		Other income	
Other recurrent costs	*80*		Scientific Associates	6 103
Capital		6 026	Sale of beamtime	1 310
Accelerator and Source developments	*6 026*		Compensatory funds	3 912
Beamlines, experiments and in-house research			Scientific collaboration and Special projects	4 149
Personnel		18 983	Pre-financing	–5 995
Recurrent		4 861		
Operating costs	*918*			
Other Recurrent costs	*3 943*			
Capital		13 992		
Beamline developments	*13 992*			
Technical and administrative supports				
Personnel		28 726		
Recurrent		13 156		
Capital		8 235		
Industrial and commercial activity				
Personnel		422		
Recurrent		103		
Total		**102 243**	**Total**	**102 243**

Expenditure 2013 by nature of expenditure

	kEuro
PERSONNEL	
ESRF staff	51 450.9
External temporary staff	51.1
Other personnel costs	1 902.8
RECURRENT	
Consumables	7 637.6
Services	9 790.3
Other recurrent costs	2 378.7
CAPITAL	
Buildings, infrastructure	12 328.0
Lab. and Workshops	1 979.3
Accelator and Source incl. ID's and FEs	5 366.0
Beamlines, Experiments	13 698.9
Computing Infrastructure	2 129.8
Other Capital costs	61.0
Unexpended committed funds	
Funds carried forward to 2014	5 586.0
Total	**114 360.0**

Revised budget for 2014 by nature of expenditure

	kEuro
PERSONNEL	
ESRF staff	52 249
External temporary staff	60
Other personnel costs	2 015
RECURRENT	
Consumables	7 355
Services	9 863
Other recurrent costs	2 448
CAPITAL	
Buildings, infrastructure	4 181
Lab. and Workshops	2 932
Accelator and Source incl. ID's and FEs	6 026
Beamlines, Experiments	13 992
Computing Infrastructure	1 036
Other Capital costs	86
Total	**102 243**

The budget for 2014 includes additional contributions from Members and Scientific Associates of 13 971 kEUR dedicated to the Upgrade Programme. The Upgrade expenditure budget amounts to a total of 27 427 kEUR including 13 891 kEUR of ESRF operating budget.

2014 manpower *(posts filled on 31/12/2014)*

	Scientists, Engineers, Senior Administrators	Technicians and Administrative Staff	PhD Students	Total
Staff on regular positions				
Accelerator and Source*	36	42	1	79
Beamlines, instruments and experiments*	233	88	21	342
General technical services	29	52		81
Directorate, administration and central services	37	53		90
Sub-total	*335*	*235*	*22*	*592*
Other positions				
Short term contracts	35			35
Staff under "contrats de professionnalisation"		33		33
European Union grants				0
Temporary workers				0
Total	**370**	**268**	**22**	**660**
Scientific collaborators and consultants	*6*			*6*

** Including scientific staff on time limited contracts.*

ORGANISATION CHART OF THE ESRF

(AS OF JANUARY 2015)

Administrative and Finance Committee
Chairperson: A-M. Hundere

Council
Chairperson: B. Girard
up to 3 delegates per Contracting Party

Science Advisory Committee
Chairperson: D. McMorrow

Machine Advisory Committee
Chairperson: R. Walker

Director General
F. Sette

DG's Services:
- Head of DG's Office/Secretary of Council: I. Echeverria
- Communication Group
- Business Development Office
- Internal Auditor
- Safety Group

Beam Time Allocation Panels
C01 (ID01, ID03, BM25B, BM32) Chairperson: A. Stierle
C02 (ID11, ID15A, ID15B, ID22) Chairperson: A. Beale
C03 (ID12, ID20, ID26, ID32, BM28) Chairperson: H. Tjeng
C04 (ID24, BM23, BM01B, BM08, BM20, BM25A, BM26A, BM30B) Chairperson: C. Lamberti
C05 (ID06-LVP, ID09A, ID18, ID27, ID28, BM01A) Chairperson: U. Schwarz
C06 (ID17, ID19) Chairperson: A. Olivo
C07 (ID16A, ID16B, ID21) Chairperson: I. Fairchild
C08 (ID02, ID13, BM26B) Chairperson: P. Stepanek
C09 (ID09B, ID10, BM02) Chairperson: A. Plech
C10 (Structural Biology Beamlines) Chairperson: M. Czjzek

ACCELERATOR AND SOURCE
Director: P. Raimondi

- Beam dynamics and applications
- Power supplies
- Insertion devices
- Front-ends
- Radio frequency and linac
- Diagnostics
- Operation
- Secretariat

ADMINISTRATION
Director: L-J. Sánchez Ortiz

- Personnel
- Finance
- Purchasing

- Joint ILL/ESRF
- Medical service
- Joint ILL/ESRF
- Library

EXPERIMENTS

Director: J. Susini

Beamline groups:
- Structural biology
- Structure of soft matter
- X-ray imaging

Director: H. Reichert

Beamline groups:
- Dynamics and extreme conditions
- Electronic structure and magnetism
- Structure of materials

Scientific infrastructure
- Theory
- User office
- CRG liaison
- Secretariat

INSTRUMENTATION SERVICES AND DEVELOPMENT DIVISION
Acting Head: A. Barrett

- Advanced analysis and modeling
- Detector and electronics
- Software
- X-ray optics
- Mechanical engineering

TECHNICAL INFRASTRUCTURE DIVISION
Head: R. Dimper

- Management information systems and web
- Systems and communication
- Buildings and infrastructure
- EX2/CPER project team
- Survey and alignment
- Vacuum

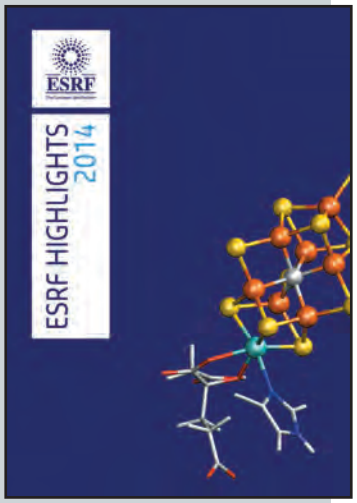

Cover
Cover design by M. Scandella featuring the image "The $MoFe_7S_9C$ cluster in a nitrogenase enzyme active site" by R. Bjornsson from the article *HERFD XAS reveals a Mo(III) in the nitrogenase active site*, R. Bjornsson *et al.*, p22.
Back cover, thumbnail images: X.B. Zeng *et al.*, p36; S. Cusack *et al.*, p81; M. Moretti-Sala *et al.*, p12.

We gratefully acknowledge the help of:

C. Argoud, T. Baudoin, B. Boulanger, K. Clugnet, M. Cotte, E. Dancer, R. Dimper, I. Echeverría, S. Gerlier, L. Graham, V. Honkimaki, A. Joly, A. Kaprolat, M. Krisch, G. Leonard, C. Mueller-Dieckmann, C. Mary, J. McCarthy, T. Narayanan, S. Pascarelli, P. Raimondi, H. Reichert, S. Rio, M. Scandella, F. Sette, L. Stone, J. Susini and all the users and staff who have contributed to this edition of the Highlights.

Editor
G. Admans
Layout
Pixel Project
Printing
Imprimerie du Pont de Claix

Communication Group
ESRF
CS40220
38043 Grenoble Cedex 9 • France
Tel. +33 (0)4 76 88 20 56
Fax. +33 (0)4 76 88 25 42
http://www.esrf.eu

The European Synchrotron
CS 40220 - F38043 Grenoble Cedex 9, France
www.esrf.eu